2009-01-14

Development and Implementation of Diagnostics for Unsteady Small-scale Plasma Plumes

James Michael Partridge
Worcester Polytechnic Institute

DEVELOPMENT AND IMPLEMENTATION OF DIAGNOSTICS
FOR UNSTEADY SMALL-SCALE PLASMA PLUMES

By

James M. Partridge

A Dissertation

Submitted to the Faculty

of the

WORCESTER POLYTECHNIC INSTITUTE

In partial fulfillment of the requirements for the

Degree of Doctor of Philosophy

In

Mechanical Engineering

By

September, 2008

APPROVED:

Dr. Nikolaos A. Gatsonis, Advisor
Professor, Mechanical Engineering Department

Dr. John J. Blandino, Committee Member
Associate Professor, Mechanical Engineering Department

Dr. Cosme Furlong, Committee Member
Assistant Professor, Mechanical Engineering Department

Dr. Peter S. Rostler, Committee Member
Busek Co. Inc., Natick, MA

Dr. James J. Szabo, Jr., Committee Member
Busek Co. Inc., Natick, MA

Dr. Jerold W. Emhoff, Committee Member
The Johns Hopkins University Applied Physics Laboratory, Laurel, MD

Dr. Mark W. Richman, Graduate Committee Representative
Associate Professor, Mechanical Engineering Department

Abstract

This research seeks to increase the applicable range and sensitivity of Triple Langmuir Probes (TLPs) and Retarding Potential Analyzers (RPAs) in the characterization of sub-centimeter scale, unsteady plasmas found in micropropulsion and other non-propulsive applications. The validation of these plasma diagnostics is accomplished by their implementation in the plume of a Micro Liquid-fed Pulsed Thruster (MiLiPulT) prototype developed and MEMS fabricated by the Johns Hopkins University Applied Physics Laboratory.

A current-mode TLP (CM-TLP) theory of operation for the thin-sheath and the transitional regimes is expanded to include the Orbital Motion Limited regime applicable to low density plasmas. An optimized CM-TLP bias circuit employing operational amplifiers in both a differential amplifier configuration as well as a voltage follower configuration has been developed to adequately amplify current signals in instances where traditional current measuring techniques are no longer valid. This research also encompasses novel sub-microampere signal amplification in the presence of substantial common-mode noise as well as several a priori electromagnetic interference elimination and filtering techniques. The CM-TLP wires used in the experiments were designed with a radius of 37.5 μm and a length of 5 mm. Measurements were taken in the plume of the MiLiPulT at 2.0 cm, 6.0 cm and 10.0 cm downstream of the exit using a linear translation stage. Reduced electron temperature and electron number density profiles for a set of filtered CM-TLP raw currents are presented. The results indicate increased accuracy due to successful amplification of CM-TLP current signals at the risk of op-amp saturation due to inherent electrical noise of the plasma source.

This research also includes the experimental validation of two new and distinct collimating RPA design types. Specifically, these design improvements include a 406 μm

diameter single channel bore and a multi-channel plate (MCP) consisting of sixty-four 2 μm diameter bores, respectively. Both of these collimators relax the Debye length constraints within the electrode series and increase the instrument's range while minimizing the presence of space charge limitations. The single channel needle also has the added advantage of providing a relatively small cross-section to the incident plasma, thus minimizing pressure gradients and shock effects inherent to bulkier instrumentation. Experimental results obtained in the plume of the MiLiPulT are benchmarked against those of a traditional gridded RPA (having a 650 μm grid wire gap) and are reduced using an iterative fuzzy logic algorithm. Modifications to the classical RPA current collection theory include a thorough treatment of geometrical flux limitations due to an electrically floating cylindrical channel of high diameter to length aspect ratio. The differences between true and effective RPA collimating channel transparencies in the presence of a Maxwellian plasma are also addressed.

Acknowledgements

First and foremost, I wish to thank my advisor, Professor Gatsonis, for the incredible opportunities and for encouraging me to extend beyond my preconceived notions of my abilities. Thank you kindly, professor, for always providing sound guidance and for always making sure I had the proper equipment, software, and materials. I'd also like to thank professors Blandino, Richman, and Furlong for serving on my dissertation committee, as well as for their ingenuity and advice over the past several years. I am indebted to the following wonderful people at WPI: Barbara Furhman, Barbara Edilberti, Pam St. Louis, Gloria Boudreau, Erica Tolles, Dr. Martha Cyr, Dr. Michael Demetriou, Tracey Coatzee, Randy Robinson, and Sia Najafi. I'd also be remiss if I didn't thank my labmates Anton Spirkin and Ryan Chamberlin for their impeccable wit, both academic and otherwise.

Special thanks are warranted to Daniel Simon and Jerold Emhoff at the John Hopkins University Applied Physics Laboratory for the development and use of the Micro Liquid Pulsed Plasma Thruster (MiLiPulT). As one of my outside committee members, Jerry was also able to offer both his time and expertise during the defense process.

I owe several people at Busek, Co., Inc. in Natick, MA a debt of gratitude for their technical aptitude, dedication, and vision. Many thanks are owed towards two of my outside committee members, James Szabo and Peter Rostler, first for the chance to work on such innovative research topics, and secondly for their technical intuition. Peter's suggestion to use operational amplifiers for Langmuir probe signal amplification was invaluable. I am grateful to both Larry Byrne and Jurg Zwhalen for their expertise pertaining to Langmuir probes, the MiLiPulT, and the bell jar vacuum system. There are also many other employees at Busek who provided me with plenty of their valuable time to answer my incessant questions, and to show

me how to *properly* use various equipment. They are, in no particular order: Charles Freeman, Jim Johnston, Chris Grenier, Kurt Hohmann, Seth McElhinney, Tom Roy, Bruce Pote, John Duggan, Mike Robin, and Lynn Olsen. I would also especially like to thank Vlad Hruby for the opportunity to perform much of this research at Busek, Co. Inc.

I also wish to thank my mother Paula and my sister Kristen for always believing in me and for providing several sanity checks, as well as my father Ron for his unparalleled work ethic and vast expertise on many subjects.

I attribute my early interest in both mathematics and the sciences to each of my grandparents in a unique way and I earnestly dedicate this work to them: To Gloria, for the love of all things flight related; to Malcolm, for the attention to detail; to Mary, who taught me integer division among countless other lessons; and finally to Charlie, for the slide rule mentality.

This work would have seemed significantly more complicated to me had it not been for Allison, my sounding board and voice of reason. Thank you, Alli, for your understanding and patience.

Recognition and gratitude are also owed to the Burgess family for their acceptance, the Pi group for the distractions, Erik and John for the music, Russ for the sarcasm, Craig and Christine for the jokes, Matt for the clarity, Kurt for the inspiration, Mike for the interest, and Xavier for the motivation.

Finally, to all of my friends and family I have not mentioned by name, thanks for helping me to convert potential energy into kinetic.

This research was partially supported through the teaching assistantships provided by the Department of Mechanical Engineering at Worcester Polytechnic Institute.

Table of Contents

List of Figures

List of Tables

Nomenclature

A = exposed probe area
$\mathbf{A}$ = least squares derivative matrix
a = channel flux integration distance
A_{cs} = cross-sectional area
a_n = error function approximation coefficient
AR = angular resolution
dA = channel entrance differential Element
dA' = channel exit differential element
$\mathbf{B}$ = magnetic induction
b_0 = collision cross section parameter
$\mathbf{C}$ = peculiar velocity vector
C = peculiar speed, loss mechanism constant
$\mathbf{c}$ = total velocity vector
c = total speed
$\mathbf{c}_{\mathrm{mode}}$ = mode velocity
$\mathbf{c}_0$ = mean velocity vector
c_0 = mean speed
CpA = channels per area
$\mathbb{C}_s$ = Boltzmann collision term for species s
$\mathbf{D}$ = electric displacement
D = diameter to length ratio
d = diameter, TLP distance from source
D = diameter to length ratio
$d_{\mathrm{grid},\perp}$ = grid wire gap
d_p = TLP probe diameter
d_{plume} = plume diameter
d_s = sheath diameter
$\mathbf{E}$ = electric field
e = electron species subscript
E_{cap} = capacitive energy
E_{eff} = effective energy corresponding to ϕ_{eff}
$\mathbf{F}_s$ = force on species s
f = frequency, floating potential subscript
f_s = distribution function
f_{co} = corner frequency
g = gravitational constant
H^+ = hydrogen ion species subscript
h_{impact} = impact parameter
H_0 = amplification ratio
H_0^* = true amplification ratio
I = current
i = ion species subscript
I^* = TLP current ratio
I_{bit} = impulse bit
I_{cp} = collector plate current
I_n = TLP current of probe wire n
$I_{s,sat}$ = saturation current of species s
IPD = incident power density
I_{sp} = specific impulse
$\mathbf{j}$ = charge density
J_{s0} = TLP parameter for species s
K = permeability
k = Boltzmann constant
Kn_{s_1,s_2} = Knudsen number of species s_1 and s_2
L = collision length, TLP probe length
l = length
L_c = characteristic length
L_{grid} = grid spacing
$L_{\text{p-source}}$ = distance between source and probe p
m = mass, slope
$\dot{m}$ = mass flow rate
$\bar{m}_{loss}$ = average mass loss per pulse
m_s = mass of species s

$\hat{n}$ = unit normal vector
$\dot{N}_s$ = number flux of species s
n_s = number density of species s
N_{cc} = number flux without wall collisions
N_{cr} = number flux with wall collisions
dN = number of particles in a phase space element
O^+ = oxygen ion species subscript
p = probe subscript, pressure
p_{MCP} = microchannel spacing
p_{approach} = distance of closest approach
p_{impact} = impact pressure
P_s = probe wire for species s
Q = fluxal quantity
$\bar{Q}_{mn}$ = collision cross section between species m and n
q = charge
QLP = subscript pertaining to the QLP
$\mathbf{r}$ = position vector
r = radius
R^2 = sum of square residuals
R_m = measurement resistor
R_n = resistance value of resistor n
r_p = probe radius
RPA = subscript pertaining to the RPA
$\vec{S}$ = speed ratio vector
S_s = speed ratio of species s
s = pertaining to species s or space potential, TLP probe spacing
SD = shield density
SE = shield effectiveness
T = thrust
t = time, thickness, error function approximation coefficient
t_{grid} = grid thickness
$t_{\text{grid,wire}}$ = grid wire thickness
TLP = subscript pertaining to the TLP
T_s = temperature of species s
t_p = tip effect
TPD = transmitted power density
u = flux integral substitution variable
u_{exhaust} = exhaust velocity
u_l = upper limit function for flux integral
V = effective potential ratio, voltage
V_m = measured voltage drop
V_s = voltage of species s
v_{eff} = effective velocity corresponding to ϕ_{eff}
$d^3\text{v}$ = volume of velocity space Element
W = weight
w = Clausing probability function
X = normalized channel length
x = distance, arbitrary variable
x_n = stoichiometric coefficient
$d\vec{x}$ = least squares difference vector
dx_i = least squares difference
Y = arbitrary integration variable
Z_s = degree of charge for species s
α = TLP theory coefficient, RPA-plasma flow alignment angle
α_s = species concentration of species s
β = inverse of most probable ion velocity, TLP theory coefficient
Γ = flux, gamma function
γ_s = specific heat ratio for species s
$\partial_{m,n}$ = spatial resolution in direction m of probe n
Δn = uncertainty coefficient of n
ε_0 = permittivity of free space
ζ = arbitrary integration angle
η = efficiency, Patterson flux component, energy ratio

θ = probe, plume polar angle, elevation angle
θ_{MCP} = MCP geometric acceptance Angle
θ_{plume} = plume divergence angle
Λ_{mn} = Coulomb logarithm parameter between species m and n
λ_0 = modified Debye shield length
λ_D = Debye length
λ_i = least squares arbitrary parameter
λ_{s_1,s_2} = mean free path of species s_1 and s_2
$d\vec{\lambda}$ = least squares change vector
$d\lambda_i$ = least squares change
μ_0 = permeability of free space
ν_{mn} = collision frequency between species m and n
$\vec{\Xi}$ = total velocity ratio vector
ξ = radius to Debye length ratio, error function variable
ρ_s = density of species s
ρ_0 = charge density
τ = channel exit flux integration distance
τ_1 = distance between channel exit location and exit wall
ϕ = effective potential, azimuthal angle, cylindrical flux integration angle
ϕ_{eff} = effective retarding potential
ϕ_{ERE} = electron retarding electrode potential
ϕ_{FE} = floating electrode potential
ϕ_{initial} = particle potential at infinity
ϕ_{IRE} = ion retarding electrode potential
ϕ_{mn} = potential difference between probe states m and n
ϕ_{probe} = probe potential for orbital motion analysis
ϕ_{SESE} = secondary electron suppression electrode potential
φ = Langmuir probe-plasma flow alignment angle, channel flux integration angle
φ_1 = channel flux entrance location to exit wall angle
χ = Patterson flux component
χ_C = collimating transmission fraction
χ_{grid} = grid transmission fraction
$\chi_{\text{grid,total}}$ = grid series transmission fraction
χ_{MCP} = MCP transmission fraction
χ_s = ionization fraction of species s
$\vec{\Psi}$ = peculiar velocity ratio vector
Ψ = Patterson flux component
$\{u, v, w\}$ = total velocity components
$\{u_0, v_0, w_0\}$ drift velocity components
$\{U, V, W\}$ peculiar velocity components
$\{\hat{u}, \hat{v}, \hat{w}\}$ = velocity space unit normal Vectors
$\{x, y, z\}$ = Cartesian coordinate system axes
$\{\hat{\text{x}}, \hat{\text{y}}, \hat{\text{z}}\}$ = Cartesian unit normal vectors
$\{y', z'\}$ = Channel exit alternative planar coordinate system
$\parallel$ = parallel subscript
$\perp$ = perpendicular subscript

Chapter 1: Introduction

The development and optimization of electric propulsion (EP) devices and other plasma processing applications is heavily dependent on accurate and robust diagnostic methods. The physical processes occurring within these devices, in addition to the collision and transport mechanisms throughout their plumes, are not yet fully understood (Fridman & Kennedy, 2004). Yet mission requirements of satellites and deep space missions alike are obliging the optimization of plasma thrusters and placing an emphasis on the repeatability and the reliability of thruster performance (Simon et al., 2006). The scaling of thruster dimensions and power input marks a continued need for increasing the range of applicability for even the most basic plasma energy diagnostic tool. However, as these instruments are scaled down accordingly, certain manufacturing and operational limits are approached. While recent advances in microelectromechanical systems (MEMS) fabrication techniques and electrical discharge machining may allow for smaller diagnostics to be built, these devices will still be limited by the requirement of having sufficient surface area to collect a measurable current signal. Possible arcing, Paschen discharging, and other substrate/surface breakdown phenomena occur between electrodes more readily as the distance between them decreases (Djogo & Osmokrovic, 1989). Most importantly, the operational theory and fundamental assumptions associated with the operation of these diagnostics may simply no longer apply if either the source or the instrument is overtly changed.

Most plasma probe designs and their accompanying theories of operation are predicated on initial assumptions about the anticipated plasma properties which are to be measured. It therefore becomes necessary to quantify the applicability, physical dimensions, and other constraining diagnostic parameters in relation to these macroscopic properties. Relevant

properties include but are not limited to plasma species concentration, ion and electron number densities, ion excitation, ion and electron temperature, plasma drift velocity, plasma thermal velocity, ionization fraction, plasma potential, and collisional parameters. Dimensional analysis of these parameters yields several dimensionless groups, perhaps the most relevant of which is the Knudsen number, which is defined by the ratio of the mean free path λ_{s_1,s_2} (average distance between collisions for two given species s_1 and s_2) to a characteristic length L_c (usually a probe dimension or thruster channel length) and is expressed as

$$Kn = \frac{\lambda_{s_1,s_2}}{L_c}. \tag{1.1}$$

The Knudsen number is an effective indicator of the flow regime, as well as the validity of a collisionless assumption relative to probe length and diameter (Gatsonis et al., 2004). The Debye length is another important characteristic measurement of a plasma and is defined as

$$\lambda_D = \sqrt{\frac{kT_e}{4\pi q^2 n_e}} \tag{1.2}$$

where k is the Boltzmann constant, T_e is the electron temperature, q is the electron charge, and n_e is the electron temperature (Mitchner & Kruger, 1973). While the Debye length physically represents the distance beyond which electric screening occurs, it is a means to gauge the overall scale of the plasma. Atmospheric plasmas tend towards macroscopic Debye lengths due to their relatively low number densities, while plasma plumes from common EP sources can yield micro- and nano-scale Debye lengths (Boenig, 1982). Regardless, the Debye length number estimations are critical to the sizing and data reduction methods of several relevant diagnostic devices.

Two such devices, the Triple Langmuir Probe (TLP) and the Retarding Potential Analyzer (RPA), if sized and applied correctly, can each provide detailed information as to the

instantaneous state of the plasma. Consisting of three parallel exposed wires, TLPs are in some cases overly constrained. The diameters and lengths of the exposed probe wires are limited by the anticipated Debye lengths and Knudsen numbers of the plasma to be measured. Conversely, the exposed wires must also have sufficient surface area in order to collect a measurable current signal (Eckman, et al., 2001). The applicable TLP theory of operation is then determined by the ratio of probe radius to Debye length (Gatsonis et al., 2004). Similarly, the electrode spacing and entrance area of RPAs are constrained by the anticipated lower bound of the Debye length, leading to possible fabrication and signal strength concerns when these estimates are on the order of a few microns (Hutchinson, 2002). Additionally, the geometric fluxal expressions associated with single-channel RPAs assume a free-molecular regime in the case of $Kn > 10$ (Patterson, 1971). These relationships will be described in more detail in Chapter 2.

Untested RPA and TLP design improvements should therefore be scrutinized and calibrated on EP devices which have been proven to produce relatively desirable number densities ($1\text{x}10^{17}\ \text{m}^{-3} \leq n_i \leq 1\text{x}10^{20}\ \text{m}^{-3}$) while offering minimal unexpected behavior.

Pulsed Plasma Thrusters (PPTs) are an example of one such device, which have been successfully implemented on several spacecraft beginning in the early 1970s (Guman & Nathanson, 1970). While the essential technology dates as far back as the 1960s, a renewed interest in PPTs stemmed from the Earth Observing-1 (EO-1) spacecraft in the 1990s and continues to this day (Pencil & Kamhawi, 2003). The flight-proven reliability and inherent scalability of PPT technology makes these devices an attractive option for both primary maneuvering and attitude control of nanosatellite (<10 kg) and picosatellite (<1 kg) constellation missions (Simon et al, 2006).

PPTs lend themselves well to miniaturization, as the technology behind these thrusters can be scaled due to the lack of moving parts and a separate propellant storage and feed system. They are relatively light weight and offer high specific impulse with a small impulse bit. Valves are not required for either solid- or liquid-fed PPTs, and they require only one power supply for overvoltage operation or at most two power supplies for trigger and sustain operation. PPTs are an ideal candidate for missions involving station keeping, drag compensation, and other maneuvering requiring precision impulse control (Igarashi et al., 2001). PPT miniaturization efforts have previously encompassed rectangular geometry PPTs in addition to coaxial PPT design types (Antonsen et al., 1999). Researchers at the Johns Hopkins University Applied Physics Laboratory (JHU/APL) have developed a micro liquid-fed pulsed plasma thruster (MiLiPulT) in a dual effort to demonstrate MEMS fabrication as an effective means of micro thruster fabrication and to validate water as an effective PPT propellant (Simon & Land III, 2005).

This dissertation involves the development and implementation of a TLP in current-mode operation as well as two collimating RPAs suitable for unsteady, small-scale, noisy plasmas found in micropropulsion and other non-propulsive applications. The validation of these plasma diagnostics is accomplished by their implementation in a plasma plume that shares such characteristics, specifically the JHU/APL MiLiPulT. Since much of the preexisting probe theory and post-processing of plume data no longer applies as a result of the diagnostic design improvements, additional signal processing and data reduction methods must also be developed and authenticated. Accordingly, this dissertation is motivated by the following goals:

- The first goal entails the development and implementation of a TLP in current-mode operation particularly tailored for small-scale, high-density, unsteady, noisy, plasma

plumes and represents a significant improvement over the original design of Gatsonis et al. (2004a; 2004b).

- The first objective is to review, and where applicable, expand the TLP current-collection theory presented in Gatsonis et al. (2004a) and implement improvements on the current data-reduction methods. The contributions involve the review of the applicability of the orbital motion limited assumptions for a probe with an infinite sheath diameter to supplement the regimes anticipated in micropropulsion plumes.
- The second objective is to develop the proper current signal amplification methods and RFI/EMI common-mode noise reduction and elimination techniques. The desired product is a reliable TLP bias circuit consisting of passive electrical components to provide an accurate and optimal current amplification ratio. This new bias circuit would thereby increase the applicability of standard TLP and quadruple Langmuir probe (QLP) investigations.
- The third objective involves the validation of the TLP design by implementation in the plume of a MiLiPulT. Signal validation includes current summation, current ratio monitoring, polarity reversal, and comparison with data obtained using standard TLP bias circuitry.

- The second goal entails the development of two distinct, collimating RPA designs in the form of a collimating single channel and a low-transparency micro-channel plate (MCP) suitable for small-scale, high-density, unsteady, noisy, plasma plumes.
    - The first objective involves the extension of the RPA current collection theory for gridded RPAs and the treatment of geometric flux limitations for cylindrical

collimating channels (Kelley, 1989; Patterson, 1971). The extension of these theories towards both the collimating and ion retarding effects of the two new RPA designs (Partridge, 2005).

- The second objective includes the validation of both collimating RPA designs by implementation in the plume of a MiLiPulT and comparison with a traditional gridded RPA. Plume data reduction results are compared for both a nonlinear least squares analysis for the classical RPA current collection theory as well as for fuzzy logic iterative methods for the collimating current collection theory.

This chapter begins with a survey of miniaturized EP devices, followed by a review of pulsed plasma thrusters and the diagnostics used in their characterization. A description of the MiLiPulT is also presented. This chapter concludes with the detailed description of the research objectives and approaches.

1.1 Small-Scale Plasmas

Mission requirements for nanosatellite (<10 kg) and picosatellite (<1 kg) clusters mark a continued need for increased thruster precision and reliability. Satellite attitude control and general station-keeping (i.e. drag makeup) for such satellites are typically provided by a wide variety of small-scale plasma thrusters. Additional micropropulsion applications could eventually include orbit transfers, plane changes, and constellation rearrangements. The impulse bits necessary to achieve such precise maneuvers (as yet impossible for picosatellites) would need to be as low as 10^{-2} μN-s by conservative estimates. A May 2003 workshop sponsored by the DARPA Microsystems Technology Office (MTO) determined that micropropulsion devices

for picosatellites could achieve specific impulses greater than 8000 s and thrust to power ratios above 100 μN/W by 2013. Four main priorities for micropropulsion research and development as recommended by the MTO meeting included the reduction of overall thruster system dry mass, power efficiency improvement, the divergence of design between both high thrust and high specific impulse thrusters, and the need for new and innovative fabrication techniques (Simon & Land, 2003). A summary of relevant micropropulsion devices and their relevant thruster performance characteristics, plume sizes, and time scales are listed in Table 1. A time scale of continuous operation in this chart typically indicates a constant thrust source, one that is usually tested for one or more hours of operation, and in most cases for more than thousands of hours of operation. Initial plume sizes were calculated based on each thruster's exit aperture area, be it a nozzle, accelerating grid, exit orifice, or cathode dimension. These areas ranged from more than 8.0 cm^2 for the micro ion thruster down to roughly 0.002 mm^2 for colloids. Estimated thrust and specific impulses were not available in some cases.

An ammonia-fueled micro-resistojet is currently under development at Busek Co. Inc., which is expected to achieve thrust levels of 5 to 12 mN with specific impulses as high as 210 s. The expansion nozzle is 150 mm in diameter with a 23:1 area ratio. Ammonia offers a vapor pressure of 0.85 MPa at ambient temperature, and is convectively heated to 1100 ^{o}C within coaxial platinum tubes. The ammonia micro-resistojet is expected to have a 25 W power output level (Robin et al., 2008).

Table 1. Appraisal of micropropulsion devices and relevent characterisitics.

Thruster Type	Research Group	Propellant	Time Scale	Initial Plume Size (m^2)	Estimated Thrust	Estimated I_{sp}	Misc. Thruster Dimensions	Reference
Colloid (CMNT)	Busek/ MIT, TDA/ CU-Boulder	Tributyl Phosphate	Continuous	$2.0x10^{-9}$	0.1 - 1 μN	> 275 s*	~ 300 nA Operating Current	Randolph et al., 2006;
Field Emission	ARCS	Indium	160 s	$1.4x10^{-5}$	< 55 μN	> 4000 s	2 mA Input Current, < 20 W Input Power	Ziemer, 2003; Genovese et al., 2003
Field Emission	Busek	Mo, BN, CNT	Continuous	$1.3x10^{-4}$	Not Available	Not Available	1 mA Output Current	Busek Co. Inc. Press Release, 2007; Deline et al., 2004
Hollow Cathode	NASA GRC	Xenon	Continuous	$8.0x10^{-6}$	Not Available	> 1500 s	1-25 W Input Power	Patterson et al., 2001
Micro Ion	NASA JPL	Xenon	Continuous	$8.6x10^{-4}$	93 mN	3100 s	60-600 mA Discharge Current	Wirz et al., 2001; Wirz, 2005
Micro-resistojet	Busek	Ammonia, Methanol	Continuous	$1.8x10^{-8}$	5 - 12 mN	150 - 210 s	10 - 15 W Input Power	Hruby, 2004; Robin et al., 2008
Micro-resistojet (FMMR)	AFRL/ USC	Argon, N_2, Water	~ 60 s	$7.9x10^{-9}$	129 μN	79 s	100 sccm Flowrate, MEMS Fabricated	Lee et al., 2007; Ketsdever, et al., 1998
RF Ion	Busek	Xenon	Continuous	$7.0x10^{-4}$	< 1.6 mN	500 - 3000 s	38 W Beam Power	Hohmann, 2004; Tsay, 2006
Solid Coaxial μPPT	Busek	Teflon	~ 10 μs	$2.0x10^{-5}$	80 μN-s (Impulse Bit)	827 s	< 2 J Discharge Energy	Busek Co. Inc. Press Release, 2007
Water-fed μPPT	JHU/APL	Water	< 10 μs	$6.4x10^{-7}$	1.1 μN-s (Impulse Bit)	< 4,300 s at 10 J	< 30 J Discharge Energy, MEMS Fabricated	Simon & Land, 2003

* Meets ST7 I_{sp} Mission Requirement

Researchers at the University of California in conjunction with the Air Force Research Laboratory (AFRL) are developing and testing a MEMS-fabricated free molecule micro-resistojet (FMMR) which offers slightly more specific impulse over a cold gas micronozzle also being considered for attitude control systems (ACS) on microsatellites. The FMMR uses nitrogen or water at a mass flow rate of 100 sccm heated by a wall temperature of 575 K and is ejected through 13 μm by 100 mm slots. The FMMR has applications to an upcoming Texas A&M nanosatellite mission with a confirmed specific impulse of 65 s and nominal thrust of 1.2 mN. Carbon dioxide, argon, and helium were also considered as candidate propellants, with water vapor yielding a thrust level as high as 1.7 mN (Lee et al., 2007). Variation of propellant molecular weight, nozzle expansion angle, wall temperature, and thin film heater width and their impact on specific impulse were theoretically investigated and compared with direct simulation

monte-carlo (DSMC) results to provide initial optimal FMMR dimensions. FMMR scaling was also investigated for Argon based on Knudsen number analysis and yielded small impulse bit capability for a reduction of stagnation pressures without a significant sacrifice in specific impulse (Ketsdever, et al., 1998). Utilizing water vapor would meet the mission thrust requirements with only 87 mg of stored propellant. Power consumption was observed to be 3.2 W during steady-state operation and 5 W during transient operation (Lee et al., 2007). Another FMMR being developed at the AFRL also utilizes water as a propellant, and is designed with 100 μm slot widths such that the stagnation pressure of the FMMR closely matches the vapor pressure of ice (195 Pa), producing a thrust per unit slot length of ~ 10 mN/m (Wong et al., 2000).

The California Institute of Technology in conjunction with the NASA Jet Propulsion Laboratory has done extensive modeling and testing of a 3 cm diameter micro ion thruster. Effectively a scaled version of the xenon ion propulsion system (XIPS) providing the primary propulsion for Deep Space 1 launched in 1998, the micro ion thruster uses xenon as a propellant and provides a continuous 93 mN of thrust at a specific impulse of 3100 s. The discharge current range is only 60 to 600 mA s (Wirz et al., 2001). Several design types have been performance tested, yielding an optimal length to diameter aspect ratio of 1.0 with a three-ring configuration of ion optics. Propellant efficiency was measured to be as high as 87% (Wirz, 2005).

The Massachusetts Institute of Technology and Busek. Co. Inc. are currently designing a radio frequency (RF) ion thruster offering less than 1.6 mN of thrust with a continuous 38 Watts of beam power. Specific impulse is expected as high as 5000 s. The RF ion thruster has no need for an internal cathode, as all ionization is achieved through the RF discharge ionizer (Hohmann, 2004). The coupling efficiency has been confirmed at more than 80%, however, the beam is

space-charge limited. Research is currently underway to determine optimal operating frequency, which currently ranges from 1.41 MHz to 1.84 MHz, and utilization efficiency as power losses across the RF system can be as high as 80% as well. This thruster also requires a neutralizer power of an additional 10 W (Tsay, 2006).

Research at Busek Co. Inc. and Worcester Polytechnic Institute is also underway to develop and test a coaxial micro pulsed plasma thruster (μPPT). This thruster has a total diameter of no more than 0.5 cm and is fueled by solid Teflon® separating the anode and inner cathode. The coaxial μPPT has a specific impulse as high as 827 s at discharge energies of less than 2 J per pulse. The most notable property of this thruster is its capability to consistently deliver an impulse bit as low as 80 μN-s. In fact, the US Air Force Academy's FalconSat-3 mission is currently deploying a 3-axis version of the coaxial μPPT aboard four clusters for ACS. These thrusters, under the acronym MPACS (micro propulsion attitude control system), also offer an observed efficiency of 16%, a specific thrust of 48 μN/W and only use 19.7 μg of propellant per pulse. (Busek Co. Inc. Press Release, 2007).

Another coaxial μPPT has been successfully tested by researchers at the Air Force Research Laboratory (AFRL) which has a specific impulse of several hundred seconds and has a thrust to power ratio of roughly 7 μN/W (Gulczinski et al., 2000). Radial electrode gaps ranged between 625 μm and 1100 μm and were driven by 2.0 μF capacitors at 0.8-1.0 kV resulting in a capacitor energy of up to 1.0 J. While this thruster offers a significant reduction in the thruster package's overall dry mass, substantial late term ablation is required to clean the propellant surface to ensure reliable performance (Simon & Land, 2003). Refined diagnostic methods aimed at characterizing the thruster discharge and plume characteristics would aid in the minimization of the impulse bit and the increased consistency of thruster performance.

The Johns Hopkins University Applied Physics Laboratory (JHU/APL) has designed and fabricated a prototype Micro-Liquid Pulsed Plasma Thruster (MiLiPulT) which utilizes distilled and degassed water as a propellant (Simon et al., 2006). The thruster has dimensions of 2.55 cm wide by 2.55 cm high by 0.82 cm deep excluding the external circuitry, water reservoir, and connections. The sustain capacitance has a maximum of 700 V DC and the trigger has a maximum range of 7.0 kV. The water reservoir has a capacity of roughly 2.3 cc although nominally the water supply is kept at a maximum of 0.5 cc per operational cycle (~500 shots). Microelectromechanical systems (MEMS) fabrication techniques were applied to produce a planar geometry Teflon-fed μPPT design with small electrode gaps. These methods allowed for the entire thruster to be built layer by layer on either an alumina or a G10 printed circuit board (PCB) substrate. Alternating layers of copper and Teflon were deposited with a relatively high degree of precision, allowing for very controlled electrode and propellant tolerances over entire batches of thrusters. Copper traces on the top substrate layer allow for the mounting of the sustain capacitor, while all other electronics are remotely positioned for testing purposes. The MiLiPulT itself has a dry weight of 13.5 g without its power electronics and consists of three electrodes: a common electrode (-), a sustain electrode (+), and a trigger electrode (+). The sustain capacitor is mounted directly on the substrate surface to minimize inductance in the main discharge circuit. Thrust stand measurements of the MiLiPulT have yielded an estimated impulse bit range of approximately 0.1 to 0.5 μN-s. Inherent EMI noise and capacitor-induced vibration associated with a PPT capacitive discharge makes microthrust stand measurements cumbersome, and ultimately a thorough plume characterization becomes necessary (Emhoff, 2007). Additionally, these microthrust stand measurements were hindered by electrical noise, and the application of Langmuir probe diagnostics were recommended for further testing of the

MiLiPulT (Simon & Land, 2003). Nevertheless, this work further established MEMS fabrication as an ideal means of mass-producing micropropulsion devices with the added capability to adjust thruster dimensions relatively easily.

Performance optimization of the MiLiPulT device could be accomplished through the application of both modeling and experimental diagnostics to investigate plume behavior (Awadallah et al., 2005). The unsteady nature of the PPT plume also does not lend itself well to time-averaged diagnostic methods, such as that of the Single Langmuir Probe (SLP). Full characterization of the thruster plume will therefore require more implicit and time-resolved techniques, including the application of electron energy and density diagnostics such as the Triple Langmuir Probe (TLP) and the Retarding Potential Analyzer (RPA).

1.2 Pulsed Plasma Thrusters

The Pulsed Plasma Thruster (PPT) is a proven and reliable electrostatic thruster concept which has been implemented on many satellite packages including three Navy NOVA spacecraft, the aforementioned EO-1 spacecraft, and several other missions (Myers & Arrington, 1996). Additional PPT flight applications also included the Lincoln Experimental Satellite (LES) missions 6, 7, 8, and 9 (Sicotte, 1970, Dolbec, 1970, & Thomassen, 1973), particularly for station-keeping and station-changing thrust provisions. MightySat II was designed to utilize a PPT to perform an orbit raising maneuver from an initial 215 nautical mile altitude (space-shuttle deployment) to more than 250 nautical miles (Markusic & Spores, 1997). This extensive in-flight experience has indicated minimal adverse effects of PPT plumes on the spacecraft. However, future missions will require a more complete assessment of possible plume/spacecraft interactions. Of particular concern is potential backflow of charged propellant to sensitive

surfaces and instrumentation (Partridge & Gatsonis, 2003). Thorough characterization and modeling of the PPT plume will aid satellite designers in the eventual reduction of these harmful effects. Most PPTs consist of a main capacitor and parallel plate electrode geometry (cathode and anode). During each pulse, a capacitive discharge is applied to the cathode, causing an arc discharge across the propellant. Thrust is generated as a result of the Lorentz forces intrinsic on the partially ionized propellant (Gatsonis et al., 2004b). Thruster efficiency η can then be defined as the ratio of thrust energy to capacitor energy given by

$$\eta = \frac{u_{\text{exhaust}} \int T dt}{2E_{\text{cap}}} \tag{1.3}$$

where u_{exhaust} is the exhaust velocity, T is the thrust, and E_{cap} is the stored capacitor energy (Simon & Land, 2003). PPT propellant types include solid, gas-fed, and liquid-fed. Efforts are also underway to miniaturize the PPT to provide consistent thruster efficiency at a fraction of the mass. These efforts include producing breadboard fabricated and micro electrical mechanical systems (MEMS) fabricated PPT designs, in both parallel and coaxial electrode orientations.

1.2.1 Solid Teflon Pulsed Plasma Thrusters

The rectangular geometry solid Teflon or PTFE (polytetrafluoroethylene) PPT typically consists of a Teflon bar approximately 1” by 1” in cross section and roughly 5-6” in length (Dolbec, 1970). A schematic of the solid Teflon PPT is shown in Figure 1, but the ionization and acceleration processes are virtually similar for nearly all PPT design types. A negator spring is the Teflon-fed thruster’s only moving part, allowing for minimal system integration problems. The arc discharge across the electrodes (i.e. along the propellant face) ablates and ionizes the Teflon propellant, which has been previously modeled in a three-stage ablation process

incorporating an eventual two-phase (crystalline solid and amorphous gel) treatment of the Teflon fuel bar (Stechmann, 2006).

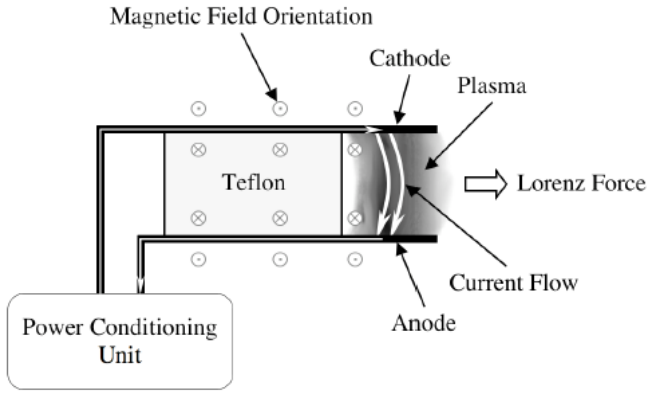

Figure 1. Schematic of a rectangular geometry solid Teflon-fed PPT (Stechmann, 2006).

Significant performance-hindering inefficiencies of the solid Teflon PPT include macro-particulate emission, late-time evaporation, and other propellant impurities (Markusic & Spores, 1997). The inefficient transfer of energy stored within the capacitor to actual ionization and acceleration processes also been known to contribute to decreased performance.

1.2.2 Liquid-fed Pulsed Plasma Thrusters

The implementation of liquid propellants allows for but does not require the elimination of valve-based propellant delivery systems which require synchronizing propellant delivery with thruster firing. A passive approach can instead be applied which relies on the diffusion of the liquid propellant through a porous filtering material. A first order approximation of the propellant mass flow rate is given by Darcy's law as

$$\dot{m} = \rho K A \frac{dp}{dl} \tag{1.4}$$

where ρ is the density of the propellant, K is the permeability, A is the flow area, and $\frac{dp}{dl}$ is the pressure gradient across the length of the diffusive material (Scharlemann & York, 2003). Since continuous flow is not desired, some sort of gating will eventually be required, such as a voltage-induced flow through the porous material.

Water is perhaps the most attractive option for PPT propellant since it is nontoxic and reduces plume contamination. Numerical simulations indicate an improved thrust to power ratio over other propellants. For eventual manned or unmanned deep space missions, water can be shared with other spacecraft systems and possible In-Situ-Resource-Utilization (ISRU) missions could make use of water's relative abundance in space. Researchers at the Ohio State University were able to perform direct comparisons between the performance of water and Teflon by designing and testing a 30 J PPT which was able to utilize both propellants interchangeably. The peak discharge current in the case of water was smaller on average by more than 40%, with a slightly longer period (Scharlemann & York, 2003).

Dual Langmuir probe testing at 2.54 cm from the thruster surface yielded a higher peak probe current in the case of water propellant by more than 700%, indicating a higher degree of ionization. This is believed to be due partially to the lesser amount of material supplied to the discharge in the water case. More energy is utilized in the Teflon case in the vaporization, decomposition, and ablation processes. However, the signal strength in the case of water decreased much more rapidly at further distances and Teflon propellant produced longer signals overall. While a quartz tube pressure probe indicated higher pressure impact signals in the case of Teflon, a more efficient acceleration process was observed for the water case. Specifically, peak velocities of 127 km/s and 46 km/s were calculated from the pressure probe signals for water and Teflon, respectively. The difference was mainly attributed to lower plasma densities

for water as well as to the higher average mol weight for Teflon of 31 g/mol versus only 6 g/mol for water (Scharlemann & York, 2003). Overall, this work established water as a viable pulsed thruster propellant, with relatively high thruster efficiency and high specific impulse.

Further comparison of water to Teflon propellant performance was conducted on the interchangeable PPT at NASA Glenn Research Center using a microthrust stand. Thruster performance characteristics for both water and Teflon modes are listed in Table 2. Time of flight measurements of the PPT were correlated with the torsional microthrust stand results and yielded a close fit, further validating the impact pressure measurements of both plumes. Impulse bit was calculated using the impact pressure measurements from previously collected data, integrated over both time, t, and cross-sectional area, A_{cs}, of the plume, and is given by

$$I_{\mathrm{bit}} = C \iint p_{\mathrm{impact}} dt dA_{\mathrm{cs}} . \tag{1.5}$$

The constant C represents loss mechanisms including thermal losses and shock effects present during momentum transfer from the plasma to the probe. Based on a total cross-sectional area of 150 cm^2 and previous impulse bit measurements which were calibrated using a shock tube, the loss mechanism constant was found to be $C \approx 10.2$ for both propellants. Specific impulse was then estimated using

$$I_{sp} = \frac{I_{\mathrm{bit}}}{\overline{m}_{\mathrm{loss}} g} \tag{1.6}$$

where $\overline{m}_{\mathrm{loss}}$ is the average amount of mass lost per thruster firing and g is the gravitational constant (Scharlemann & York, 2003).

Table 2. PPT performance characteristics for both Teflon and Water modes over discharge energies (adapted from Scharlemann & York, 2003).

Discharge energy [J]	Impulse Bit, Pressure probe [μN-s]		Mass bit [μN/discharge]		Specific impulse [s]		Efficiency [%]	
---	Teflon	Water	Teflon	Water	Teflon	Water	Teflon	Water
10	124	47	11.9	~1.1	1,060	4,355	6.5	10.0
20	281	90	27.5	~1.1	1,040	8,350	7.2	18.0
30	440	128	35.3	~1.1	1,270	11,860	9.1	24.8

Observed carbonization of the Teflon ablation surface accounts for the low mass bit in the 10 J case, but otherwise the Teflon mode results agree with similar thruster performances reported for the LES 8/9 and NOVA PPTs (Scharlemann & York, 2003). Although these results are considered preliminary and are based on relatively volatile loss mechanism estimations and impact pressure results, they clearly validate water as a viable propellant for mission profiles requiring both low mass bits and high specific impulses.

1.2.3 Previous Pulsed Plasma Thruster Diagnostic Methods

Spectroscopic emission measurements were performed on the solid Teflon XPPT-1 in order to determine the constituent species, electron temperature, and exhaust velocity within the plume. Results were limited to emission measurements from 3500 to 7500 Angstroms for a discharge energy from 15 to 45 J. A spectrometer employing two different diffraction gratings (1200 g/mm and 2400 g/mm) and an electrically cooled charge-coupled device (CCD) camera yielded a wavelength resolution of 0.13 Angstroms. A series of external optics and periscopes allowed for the rotation of the imaging plane and viewing of both the front and side of the thruster simultaneously. Species observed included F, F^+, C^+, C^{++}, and C_2, although C and other species having weak lines in the monitored wave number range were expected to exist. Average carbon ion particle speed was calculated from observed PPT emissions to be 9.6 ±5.5 km/s.

Time of flight (TOF) plasma streaming speed as calculated from experimentally observed Doppler shifts ranged from 8.1 km/s to 15.1 km/s. Resolution of the plasma temperature measurements was compromised by the manner in which the emission images were spatially integrated. Since the incident light to the CCD camera contained numerous layers of light from indeterminate layers of the temperature-variant plasma, the reported electron temperature of 1.4 eV could not be associated with an accurate channel distance (Markusic & Spores, 1997). This work provided a baseline for more advanced investigations into the PPT plume, such as constituent species analysis using RPAs and laser induced fluorescence (LIF) investigations into plume energy partitioning.

Researchers at the Computational Gas and Plasma Dynamics Laboratory (CGPL) of Worcester Polytechnic Institute performed rigorous TLP and QLP testing of a solid-Teflon fed PPT at the NASA Glenn Research Center to determine time-resolved profiles for electron number density, electron temperature, and ion speed ratio. Plume characterization involved a complete 2D polar sweep at various thruster discharge energies of 5, 20, and 40 J (Eckman et al., 2001). A current mode theory of operation was developed and validated to eliminate noise inherent with the traditional voltage-mode Langmuir probe operation. Due to a lack of available oscilloscope channels, current measurements were limited to measuring the current differences between probe lines and extracting the individual currents under the assumption that the currents were being measured accurately and summed to zero. Data extraction followed two regimes of TLP probe current theory, a thin sheath approximation and a transitional methodology, which account for the absorption of both ions and electrons when the biasing potentials between the probe wires are known (Gatsonis et al., 2004a). Results indicated number densities on the order

of 10^{18} to 10^{21} m^{-3} and electron temperatures of more than 12 eV. Incorporation of a cross probe yielded time-resolved ion speed ratio measurements as high as 7.0 (Gatsonis et al., 2004b).

The University of Washington continued investigations of Teflon-fed PPT plume constituent species concentrations through the application of a gridded 2" aperture diameter RPA in the wake of the DawgStar PPT. TOF measurements were also performed by mounting the RPA at 3.68 m from the thruster face. The inherent limitations of the RPA prevented the TOF measurements to be classified as a fully capable TOF mass spectrometer. Namely, the RPA only sets a lower bound on the class of ions it allows through to the collection plate. When factoring in the complexities of a multispecies plasma and the EMI problems common to PPTs, the RPA energy measurements in this case provided limited accuracy regarding the ion species concentrations and other macroscopic ion properties (Burton et al., 2002). The following year, experimental improvements made by the same group yielded complete I-V curve data for several thruster power settings at various plume angles. The RPA, in this case termed the gridded energy analyzer or GEA, provided detailed mass characterization and plasma temperatures reduced from normalized collector current profiles. Although the GEA contained grids which were 50% transparent and spaced only 18 μm apart, space charge limitations most likely persisted between the ERE and the IRE, obliging the normalization of the current profiles and preventing the extraction of plasma density. Results indicated small but significant concentrations of C^{++}, F^{++}, C^{+++} and F^{+++} ions with ion temperatures of $T_i \geq 6.0\ \mathrm{eV}$. The integrated distribution function was then compared against the experimentally obtained I-V curve once again to serve as an indicator of fit quality (Shumlak et al., 2003). Despite the arbitrary collector plate currents, this work effectively demonstrated the necessary theoretical

adjustments and reduction techniques associated with multispecies plasma parameter and concentration extraction.

1.2.4 Pulsed Plasma Thruster Noise and Electromagnetic Emissions

Radiated electromagnetic interference (EMI) or radio frequency interference (RFI) is another primary concern for PPT integration into space missions. Antenna array testing of PPT noise at ultra-high frequencies (UHF) was performed on the solid Teflon LES-6 station-keeping prototype thruster to determine any potential radio frequency (rf) coupling with the spacecraft antenna system. Since an anechoic chamber large enough to house the satellite with both the thruster and antenna system in flight orientation was not available, a ferrite 366 Ω/sq absorber material was used to line the vacuum chamber to minimize ringing and other resonance effects. Free-space waves were absorbed by placing a short circuit one wavelength behind the absorber material. The experimental bandwidth threshold was 100 kHz. Monopole antennas located both inside and outside the chamber indicated minimal RF coupling. Noise amplitude was found to be independent of antenna location. Measurement results yielded a center frequency of 300 MHz for the first 2-3 μs with a peak power range of -139 to -149 dBmW/Hz (Sicotte, 1970).

RFI testing continued during the development of the solid Teflon LES-7 PPT, which was used for both station-keeping and station-changing. Although the PPT noise of the LES-6 was determined to negligibly interfere with spacecraft communications and other electronics, the LES-7 PPT was ten times more powerful over its LES-6 counterpart. An X-band horn antenna yielded noise pulses with a 1.0 μs duration and a peak power of 4.5 dbm at 100 MHz bandwidth centered at 8 GHz. Thruster noise varied 5-10 db per shot, possibly suggesting PPT thrust output varies considerably with each discharge. Similar absorption shielding detailed in the LES-6

experiment was in place, yet the RFI results indicated that the noise was directional and was observed to taper off in the horizontal plane as the thruster angle off centerline was increased (Dolbec, 1970).

Attempts to quantify the radiation intensity and spectral distribution of the solid Teflon PPTs designed for the LES-8 and -9 were made in 1973. Radiated power measurements were taken in the 0.2-20.0 GHz range using 3 cavity-backed spiral antennas, 2 horn antennas, and a crossed dipole antenna with a broadband hybrid coupler. Results indicated a power density of 6-60 mW into the 1 GHz band for the first 0.5-1.0 μs after thruster firing (Thomassen, 1973). Prior studies had indicated 28 mW in the 1 GHz band and 4.5 dbm in the 100 MHz band (Dolbec, 1970). Negligible noise was found in the 1-8 GHz bandwidth, with an average shot spectral density of 6.2 dbm at 100 MHz. The radiation was originally assumed to originate from random collisions along the arc discharge resulting from particle acceleration. However, theoretical modeling yielded collision times associated with 10^{16}-10^{18} Hz (Thomassen, 1973). Plasma instabilities partially explain the aforementioned spectral intensities, but would be nearly impossible to calculate accurately. Additional noise could be attributed to capacitor discharge and conducted common-mode EMI noise. EMI and electrostatic pickup due to inadequate shielding led to problems with several logic circuits and an optical sensor. This interference, in addition to thruster thermal cycling problems, ultimately led to the replacement of the PPTs with cold gas ammonia thrusters for LES-8 and -9 (Sovey et al., 1987).

Significant PPT-related EMI suppression was accomplished by Fairchild Industries, Inc. and the Air Force Rocket Propulsion Laboratory in 1977. The shield effectiveness of an aluminum Faraday cage structural thruster frame was tested across a broad range of frequencies against the control of the unshielded thruster. The millipound thrust PPT used for these

experiments had a peak discharge of 47 kA, a 21-23 mN-s impulse bit, and was able to be operated in air at atmosphere. Shield effectiveness was defined as

$$\mathrm{SE}_{\mathrm{dB}} = 10 \log_{10} \frac{\mathrm{IPD}}{\mathrm{TPD}} \tag{1.7}$$

where IPD is the incident power density at the measuring point without the shield in place and TPD is the transmitted power density at the measuring point with the shield in place. The thruster shield incorporated both gasketless metal covers with closely spaced screws and knitted metal gaskets where necessary. Bypass capacitors were placed in several small holes in the thruster enclosure to provide additional noise attenuation for frequencies less than 100 MHz. A combination of rod, biconal, conical log spiral, and loop antennas, in addition to spectrum and interference analyzers allowed for the monitoring of 0.015 to 10,000 MHz. Results showed a 20 db shield effectiveness at 0.01 MHz increasing logarithmically to 1000 db at 100 MHz as measured 1 cm from the thruster face. As expected, decreasing the thruster shielding thickness slightly decreased the shielding effectiveness, which obliges the concept of shielding density as given by

$$\mathrm{SD} = \mathrm{SE}_{\mathrm{dB}} \;\; W / A \tag{1.8}$$

where W / A is the weight per unit area of metal having a certain barrier thickness t. This allowed for the calculation of the required barrier thicknesses of other shielding materials (i.e. copper) to produce the same shielding effectiveness. Other shielding improvements included interrupting the igniter plug lead used as the electrical trigger with a removable loop of triaxial cable. A step-down transformer was placed in line with the ignition pulse prior to the external test equipment which reduced the high-voltage ignition pulse to provide a reproducible but significantly less noisy oscilloscope trigger input signal (Begun & Guman, 1977).

A thorough appraisal of observed EMI effects on electric propulsion systems was performed in 1987, indicating that the four LES-6 PPTs had operated for more than 8600 hours over 5 years with no observed EMI effects on spacecraft subsystems, communication, and telemetry. The fore and aft PPTs on the NOVA-1 spacecraft, which had each experienced over one million pulses over five months of flight time, also had no observed EMI effects on the spacecraft. Bell jar testing of the Japanese engineering test satellite IV (ETS IV) PPT yielded a very narrow noise pulse, significant only in the 100 to 120 MHz range. Effects on the spacecraft's command signals and instruments were negligible. The 1981 ballistic test flight of China's MDT 2A spacecraft employed five Teflon PPTs, and had no observed effects on spacecraft subsystems. Transmission signal interactions with the plumes of electric propulsion systems were also identified. Namely, RF signal reflection, attenuation, and phase shifting could occur due to the plume. RF signal-plume interactions could also include generated noise in both amplitude and phase. At frequencies above 500 MHz, free electrons are the major contributor to these interactions, due to their relatively lighter weight and ability to absorb more incident energy as compared to ions. Absorption of the transmitted signal typically occurs if the plasma electron frequency is greater than the RF frequency. However, beam spreading and scattering (diffraction and refraction, respectively) caused by the plume can still lead to RF attenuation and phase shifting. Contributing RFI/EMI sources in an ablative PPT were observed to include the ignitor discharge, the main discharge, the exhaust plasma, and the wire harnesses (Sovey et al., 1987). A thruster's power processing unit (PPU) has also been known to produce to EMI common-mode noise.

The EO-1 mission also employs a solid Teflon propelled PPT with a specific impulse of 650-1400 s and relatively small impulse bits of 90-680 μN-s (Benson et al., 1999). Although the

thruster maintains a low power level of 12-70 W, EMI noise during capacitor discharge has been demonstrated be as high as 160 dBm/MHz for frequencies lower than 1.0 MHz. These levels are nearly twice the EO-1 component limits, particularly for the Advance Land Imager (ALI) control electronics and the Focal Plane Assembly (FPA) electronics. Semi-conductor devices, in addition to 200 angstrom thick silicon-dioxide capacitors and small semi-conductor junctions within these control electronics and instrumentation are highly susceptible to both over-voltage damage and electro-static discharge (ESD). Bell jar testing of the EO-1 PPT with various shielding elements provided EMI radiated noise reductions to below component limits for all frequencies except $4.0\ \mathrm{MHz} \leq f \leq 12.5\ \mathrm{MHz}$ (Zakrzwski et al., 2001). Further shielding improvements also allow for improved diagnostic capabilities during thruster development and performance optimization.

1.3 Langmuir Probe Design Variations and Attributes

A Single Langmuir Probe (SLP) is perhaps one of the simplest plasma diagnostic devices and has been commonly used to characterize a broad range of steady and unsteady plasmas. A SLP consists of an exposed conductive cylindrical probe tip (typically tungsten) ideally perpendicular to the mean plasma flow to provide information regarding the time-averaged electron number density, electron temperature, and floating potential. An I-V sweep is obtained by varying the potential of the probe and measuring the resultant currents, which provides a means to extract the average electron number density and electron temperature (Peterson & Talbot, 1970). The SLP voltage sweep can therefore only provide a time-averaged value for electron number density and electron temperature (Chen, 2003). For unsteady plasmas, these data can be misleading. Attempts to mitigate this lack of resolution have yielded four distinct

approaches. The first method simply involves performing the I-V sweep as fast as possible, which would yield an unacceptable temporal resolution of ~1s from most commercially available high-end sourcemeters. This technique also introduces inaccuracies stemming from transient effects of the fast sweep and possible delays between the true bias voltage and the data collection. A second method involves a periodic bias voltage waveform, such as a sine wave to resolve the resultant current waveform across the transition region. This method has been proven to have a resolution of ~1 ms (Siefring et al., 1998). A possible but unverified third method requires a fixed bias voltage with the current waveform being monitored by an oscilloscope or other electrometer with a high sampling rate. This process is repeated for several bias voltage values in the transition region to generate multiple current traces, making electron number density and electron temperature extraction somewhat more difficult.

The fourth and perhaps the most reliable method is the implementation of a triple Langmuir probe (TLP) consisting of three exposed conductive wires parallel to the average plasma flow direction. This diagnostic can provide time-resolved measurements of electron temperature, electron number density, and plasma space potential. A schematic of a TLP with its potential biases is shown in Figure 2. Bias voltages are applied between probe wires 1 and 2 as well as probe wires 1 and 3. These biases allow for the monitoring of the current pulses between each probe wire and the plasma itself. Time-resolved electron number density and electron temperature can then be extracted using the relevant TLP current-mode theory of operation and the appropriate numerical solver algorithms. A more detailed discussion of the TLP current-mode theory of operation is presented in Chapter 2. A TLP designed for small-scale plasma plumes has a limited range as a result of decreased current signals and will require noise filtration techniques and signal amplification in order to fully capture the plume's behavior.

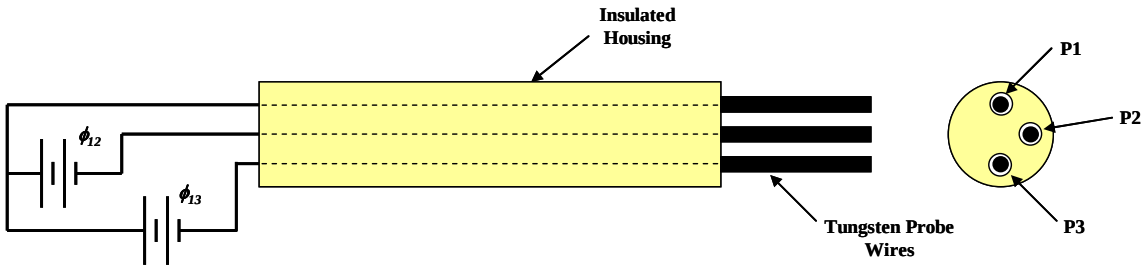

Figure 2. TLP components and basic bias circuit schematic.

Quadruple Langmuir Probes (QLPs) make use of a cross probe in addition to the standard TLP parallel probes. The cross probe lies perpendicular to the flow of plasma, with a unique bias potential. Examining the current through the cross probe provides the ability to extract the time-resolved ion speed ratio in addition to time-resolved electron number density and electron temperature (Kanal, 1964). However, QLPs are not applicable to small-scale plasmas since the cross probe would need to be larger than the plume area for all relevant distances from the source.

1.4 Retarding Potential Analyzer Design Variations and Attributes

Retarding potential analyzers employ a series of variably biased electrodes to selectively filter incident plasma flux, allowing only high-energy ions and neutrals access to a collector plate. A schematic of the RPA electrodes is shown in Figure 3. Typically the first electrode is kept floating to provide the incident plasma with a germane interface. The floating electrode (FE) also allows for the average plasma or space potential to be monitored. The second electrode, the Electron Retarding Electrode (ERE), is biased negatively so as to repel all of the incident electrons. The third electrode is biased positively to repel low energy ions and is typically denoted as the Ion Retarding Electrode (IRE). The IRE positive bias is varied

throughout an experiment from zero bias up to the limit where all ions, including the high energy tail of the ion velocity distribution, are repelled away (Kelley, 1989). This process produces an I-V curve which can then be analyzed to determine several critical macroscopic plume properties, including ion number density, ion temperature, ion drift velocity, and constituent species concentrations (Shumlak et al., 2003).

Based on the thickness of the electrodes, the values of the electron retarding potential and ion retarding potential, and the plasma properties present in the electrode series, potential 'cupping' may occur normal to the plasma flow, resulting in an effective ion retarding potential lower than actual bias. To minimize this phenomenon, a second IRE is sometimes placed adjacent to the first IRE to ensure that the desired ion retarding potential is present in the electrode series. Lastly, a Secondary Electron Suppression Electrode (SESE) is placed in the electrode series and is biased negatively (usually equal to the electron retarding potential) to repel any secondary electrons which may have been emitted throughout the electrode series (Partridge & Gatsonis, 2003).

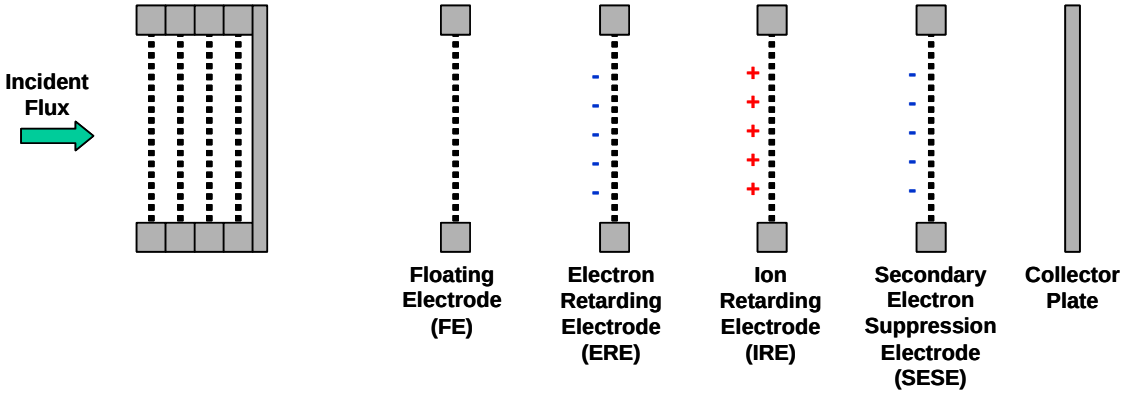

Figure 3. Schematic of the classical RPA electrode series (Partridge & Gatsonis, 2003).

The electrodes are typically isolated from each other via some insulating material such as Nylon, Delrin®, or Teflon. The collector plate is located a relatively small distance from the

SESE and is typically made of molybdenum because of its high work function so as to minimize secondary electron emission. Collector plate current is then closely monitored at various ion retarding potential settings to populate the I-V curve. Other RPA attributes could include a wake flux electrode series on the aft end of the RPA to reduce RAM pressure buildup (Marrese et al., 1997), or a flux limiting apparatus such as a microchannel plate (MCP) to reduce the incident plasma flux (Hutchinson, 2002).

At present there are two basic RPA electrode design types: traditional gridded and single-orifice. Gridded RPAs are typically used for relatively low plasma densities ($n_i \leq 1\text{x}10^{18}\ \text{m}^{-3}$) or where the plasma flux is generally low enough to the point where the plasma within the ERE and the IRE would not be space charge limited (i.e. the plasma would not be dense enough to detract or otherwise significantly effect the bias profile within this region). Single orifice, or single channel RPAs, consist of solid electrodes with a single aligned bore through each electrode. In relatively highly dense plasmas ($n_i \leq 1\text{x}10^{18}\ \text{m}^{-3}$), single orifice RPAs have been applied to curb the effects of space charge limitation by ensuring that plasma flux is kept below a certain threshold (Marrese et al., 1997). This limit manifests itself as a set of design constraints based on a simple one dimensional analysis by Hutchinson (2002) between two electrodes expressed as

$$\frac{x}{\lambda_D} = 1.02\left(\frac{qV}{T_e}\right)^{3/4} \tag{1.9}$$

where x is the distance between the electrodes and V is the potential difference between the electrodes (Hutchinson, 2002). Since V must be equal to a few times the electron temperature, it follows that the sheath thickness is $\sim 4\lambda_D$. Thus the electrode orifice diameters must be less than or equal to 2 Debye lengths while the electrode spacing must be less than or equal to 4

Debye lengths (Marrese et al., 1997). These constraints are particularly important in the region between the ERE and the first IRE, where electrons and ions are both incident and being repelled (i.e. where space charge limitations would most likely exist). Factoring in the priority for distinguishable collector plate current signal strength, the ideal single-orifice RPA becomes optimized as the electrode orifice diameter approaches 2 Debye lengths. Likewise, the electrode spacing is obliged to be as small as possible before Paschen breakdown or substrate breakdown becomes a significant possibility (Partridge & Gatsonis, 2005). Ideally, RPA dimensions are chosen based on an anticipated operational envelope defined by electron temperature and electron number density ranges.

Orifice alignment across the electrode series induces a significant fabrication problem when the anticipated Debye lengths are on the order of $\lambda_D \sim 10^2\ \mu\mathrm{m}$ or lower. The aforementioned MCP or other flux-limiting device serves to reduce the incident plasma flux and relax the Debye-length constraints on the electrode dimensions. Previous RPA applications, the current manufacturability limit, and the trend by which this limit is relaxed due to controlled incident plasma flux limitation are illustrated in Figure 4. This increased RPA applicability was calculated based on the transparency calculations of a low-transparency MCP in a theoretical test case scenario (Partridge & Gatsonis, 2005). Note that the graph assumes $T_e = 10\ \mathrm{eV}$ and thus represents only a single slice of the overall 3D operational envelope (i.e. RPA electrode diameters would decrease for increasing temperatures and vice-versa.). Further flux limitation beyond that of a MCP with <0.30% transparency in this case would yield a collector plate current signal to be immeasurably low.

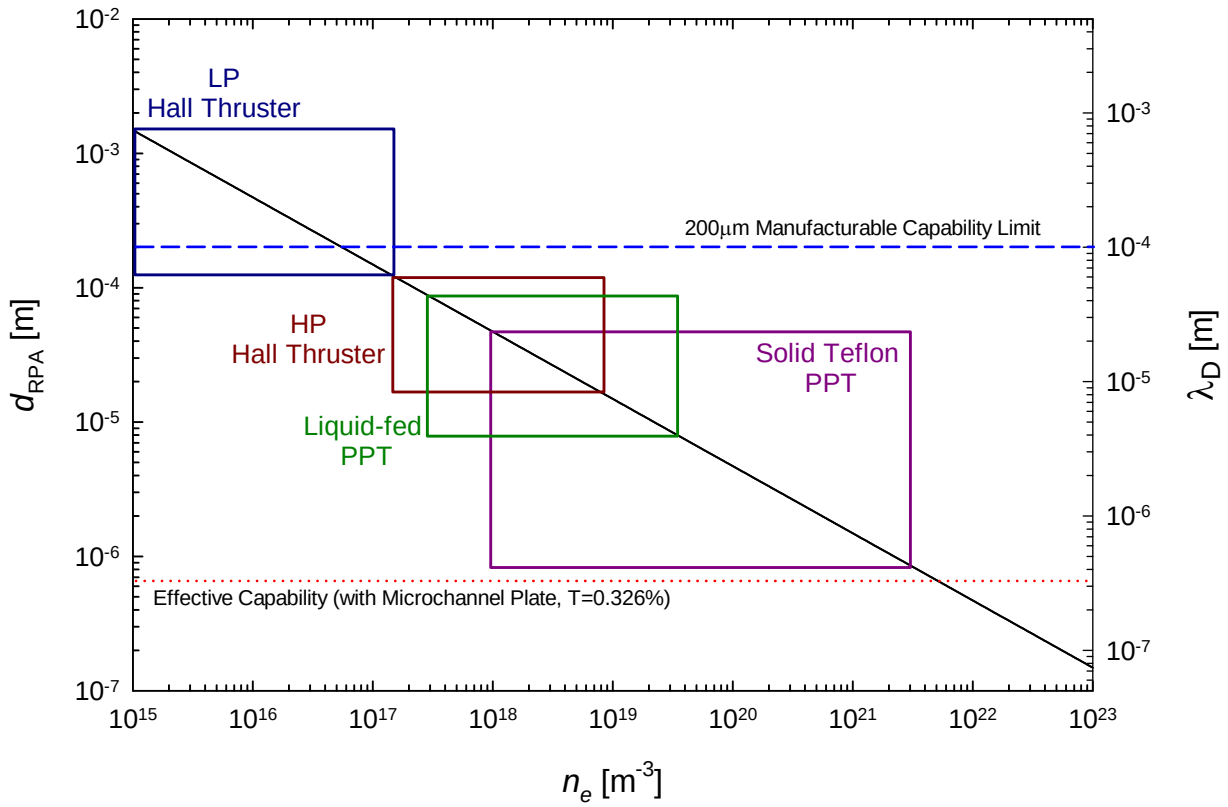

Figure 4. RPA applications, manufacturability limitations, and increased range as a result of flux limitation.

Further RPA theory, including basic current collection theory, geometric flux limitations, voltage effect considerations, and the Maxwellian distribution assumption, as well as their relevance to small-scale plasmas and MiLiPulT plume characterization specifically are addressed in Chapter 2.

1.5 Research Objectives and Research Approach

The first goal entails the development of a current-mode TLP design that is suitable for small-scale, high-density, unsteady, noisy, plasma plumes and represents a significant improvement over the original design of Gatsonis et al. (2004a; 2004b). The objectives and approaches are as follows:

- Review and, where necessary, derive all relevant plasma kinetic, electromagnetic, and diagnostic theories pertaining to the design and implementation of TLPs towards the characterization of small-scale, high-density, unsteady, noisy, plasma plumes.
    - Develop an analytical model for the plume divergence of a small-scale plasma as well as the spatial resolutions of the TLPs and QLPs.
    - Review and calculate the collision frequencies and mean free paths for relevant collisions within a multispecies plasma based on the anticipated operational envelopes of typical micropropulsion devices, including Debye lengths, collision rates, mean free paths, Knudsen numbers, tip effects, and sheath effects relevant to basic TLP design and operation.
    - Expand upon the existing current-mode TLP theory of operation to include current-mode regimes for probe radius to Debye length ratios of $r_p / \lambda_D < 5$, where the orbital motion limited (OML) and Allen-Boyd-Reynolds (ABR) models would apply.
    - Improve upon existing TLP data reduction algorithms by including the OML regime. Self-consistently monitor the resultant probe radius to Debye length ratios and update the error analyses as necessary.
- Design, build, and optimize a TLP bias circuit for use in noisy (EMI) plumes characterization experiments which provides an increased range and sensitivity over that of a basic TLP bias circuit:
    - Apply operational amplifiers in both differential input amplifier configurations and voltage follower modes to properly amplify the TLP current signals such that the applicable range of the TLP is increased.

- Determine the ideal amplification ratios and subsequent resistance values within the instrumentation amplifiers to minimize both normal-mode noise and operational amplifier saturation. Calibrate the TLP bias circuit for given instrumentation amplifier resistor values such that the true overall amplification factor of each channel is well-known.
- Employ several RFI/EMI noise attenuation techniques to prevent operational amplifier saturation. These techniques include but are not limited to RC filtration, signal averaging, faraday cage isolation, common-mode noise shielding, digital oscilloscope resolution enhancement, and trigger pulse RF choking, transformation, & isolation. Ensure the accuracy of the TLP bias circuit and instrumentation amplifiers by monitoring the magnitudes and polarities of the three current waveforms and confirming that the current sum is close to the zero.

- Validate the new TLP bias circuit and modified current collection theory by experimentally implementing the TLP in the plume of the MiLiPulT and conducting the appropriate data reduction analyses:
  - Optimize the resistance values in the TLP bias circuit for use in the MiLiPulT plume.
  - Perform a 1D sweep of the MiLiPulT plume using the basic TLP bias circuit and the TLP operational amplifier TLP bias circuit. Demonstrate the increased range, if any, for the operational amplifier TLP bias circuit.
  - Further ensure the accuracy of the TLP bias circuit by monitoring the current difference ratio such that it maintains a value between 0 and 1 for a majority of

the pulse (with the exception of current inversions and other asymptotic behavior).

- Reduce the TLP obtained measurements of the 1D plume sweep into time-resolved electron parameter behavior including $T_e(t)$, $n_e(t)$, $\lambda_D(t)$, and $\phi_{s1}(t)$. Demonstrate the increased sensitivity, if any, for the operational amplifier TLP bias circuit.

The second goal entails the development of two distinct collimating RPA designs in the form of a single collimating channel and a low-transparency microchannel plate (MCP) suitable for small-scale, high-density, unsteady, noisy, plasma plumes. The objectives and approaches are as follows:

- Perform a comprehensive review of existing RPA collector plate current collection theories for both gridded RPAs and single-orifice RPAs and derive the necessary modifications to extend these models towards the collimating designs.
    - Review and calculate relevant parameters for a multispecies plasma based on the anticipated operational envelopes of typical micropropulsion devices, including Debye lengths, space charge effects, and sheath effects relevant to basic TLP design and operation.
    - Review the classical RPA current collection theory as it pertains to a traditional gridded RPA. Review and modify the geometric flux limitation theory and the current collection theory for a single-channel constant voltage RPA.
    - Derive the RPA current collection theory as it applies to a gridded, collimating design. List the inherent design constraints of such a design.

- Implement the updated collimating RPA current collection theory in an ion parameter extraction methodology developed in MATLAB.

- Design and build the baseline gridded RPA as well as the two collimating RPAs optimized for the expected operational envelope of the MiLiPulT plume. Provide a comparative analysis amongst the three design types by experimentally implementing the RPAs to characterize the MiLiPulT plume.
  - Design and build a gridded μRPA with a removable collimating nozzle optimized for the anticipated operating plasma parameter envelope of the MiLiPulT plume.
  - Design and build a removable low-transparency MCP supplement to the gridded μRPA optimized for the anticipated operating plasma parameter envelope of the MiLiPulT plume.
  - Develop a method of precise alignment for the MCP with grids of the μRPA to comprise the multi-channel μRPA (MC-μRPA) design configuration.
  - Where applicable, apply operational amplifiers in the aforementioned instrumentation amplifier configurations and EMI filtration techniques to adequately amplify and resolve unsteady I-V curves inherent to the MiLiPulT plume.
  - Collect unsteady I-V-t curve measurements of the MiLiPulT plume using all three RPA design configurations (i.e. the gridded RPA, the collimating μRPA, and the MC-μRPA).
  - Perform ion parameter extraction using the maximum collector plate current values of the unsteady I-V-t curve data to validate the accuracies of each of the

two μRPA designs using the gridded RPA results as a baseline. Obtain T_i, n_i, $\mathbf{c}_i$, and α profiles for all three designs across the various reduction techniques.

- Derive the subsequent experimental and numerical errors associated with the RPA I-V curve extracted ion parameters based on the relevant current collection theory cases and least square analyses.

The presentation of this research is structured as follows: The second chapter outlines the theory necessary to fully encapsulate the relevant physical processes inherent to an unsteady diverging small-scale plasma plume. The resultant influence on the design constraints and applicability of several types of energy diagnostics is also discussed. TLP theory of operation is listed for several relevant conditions, as well as RPA current collection theory for several pre-existing and relatively new design types. The third chapter details the experimental work performed to optimize a TLP bias circuit in order to increase both the range and sensitivity of a TLP in the plume of the MiLiPulT plume. Noise filtration techniques and improvements to the Newton-Raphson solver and data reduction program are also discussed. Results are analyzed for a 1D plume sweep using various TLP bias circuit configurations. The fourth chapter demonstrates the validation of the collimating RPA designs by comparing measurements from the MiLiPulT plume calibrated against a gridded RPA. Time-resolved ion parameter extraction methods for all three designs are also presented. Chapter 5 contains conclusions as well as recommendations for future testing and development of TLPs and RPAs towards the MiLiPulT plume specifically as well as other small-scale plumes in the more general sense.

Chapter 2: Diagnostic Theory for Unsteady Small-Scale Plasmas

The theory contained in this chapter is intended to provide a thorough analysis of the physics that govern plasma particle motion, collisions, ionization, and other various macroscopic properties. The physical processes by which some electric propulsion systems operate are not yet fully accounted for, while in other cases they are still not completely understood (Koizumi et al., 2007; Laframboise and Sonmor, 1993). The following empirical formulae and analytical models depict not only the discharge, acceleration, and collisional transport mechanisms present within these devices, but they also comprise the foundation of accurate diagnostic design and the appropriate post-processing data analyses. In fact, probe design constraints are predicated on the anticipated range of properties to be measured as well as on the relevant assumption methodologies (i.e. when it is necessary to assume one theoretical regime over another). To extend this theory more generally to all propulsion applications, calculations of all collision parameters are repeated and listed for the following six monatomic ion species: hydrogen, carbon, oxygen, fluorine, argon, and xenon. Hydrogen and oxygen are relevant because the MiLiPulT uses distilled, degassed water as a propellant. Calculations are repeated for carbon and fluorine as Teflon is used in many rectangular and coaxial PPTs. Similarly, argon and xenon are used in many ion thrusters, Hall thrusters, and other electromagnetic and electrothermal applications (Wirz, 2005).

This chapter begins with a description of the various components of multispecies plasma and their basic properties contained in Section 2.1. A treatment of particle motion is subsequently presented in Section 2.2 which defines the essence of charged particle acceleration in the presence of electric and magnetic fields, as well as several significant velocity definitions and reference frames. The distribution function, velocity space, and the Maxwellian assumption

are also discussed. Section 2.3 details all of the pertinent collision types and provides definitions and calculations of collision frequencies and mean free paths for each type based on a considerably broad range of plasma parameters. Section 2.4 contains a tabulation of Knudsen numbers based on the results of Section 2.3 and an assumed probe radius or other characteristic length for demonstration purposes. A discussion of single Langmuir probe (SLP) theory is outlined in Section 2.5. A thorough description of various triple Langmuir probe (TLP) current collection theories is provided in Section 2.6, in addition to the data extraction methods typically applied to TLP measurements. Small-scale plume divergence angle considerations are discussed in Section 2.7 along with a brief discussion of quadruple Langmuir probe (QLP) theory. Section 2.8 contains retarding potential analyzer (RPA) current collection theory for several design types as well as their applicable post-processing methods.

2.1 Plasma Components

An appraisal of the basic plasma parameters relevant to this research and the species most often present in EP thruster plumes will allow for the later analyses of collisional transport, probe theory development, and data reduction methods. The plasma considered here may consist of multiple species denoted by the subscript s and include neutrals, ions, and electrons. Charged and uncharged macroparticles are not considered. Perhaps one of the most fundamental properties relevant to the eventual determination of source efficiency and thrust capability is the total plasma number density, having units of particles per unit volume, and is given by the sum of each individual charged species number density as

$$n = \sum n_s \ . \tag{2.1}$$

The density of the entire mixture is also a function of each species mass, given by a weighted sum defined by Chapman & Cowling (1939) as

$$\rho = \sum_s \rho_s = \sum_s n_s m_s \tag{2.2}$$

The ionization fraction for a given species s is given by the ratio of ions to neutrals as

$$X_s = \frac{n_{i,s}}{n_{i,s} + n_{n,s}}. \tag{2.3}$$

Values for the mass to charge ratios for the six ion species considered ranged over charge number (degree of ionization) were calculated using mass information from Bird (1994) and are shown in Table 3.

Table 3. Mass to charge ratios for ionic elements of EP source propellants (units of kg/C).

	Hydrogen	**Carbon**	**Oxygen**	**Flourine**	**Argon**	**Xenon**
Singly Charged Ion	$1.04\text{x}10^{-8}$	$1.24\text{x}10^{-7}$	$1.66\text{x}10^{-7}$	$1.97\text{x}10^{-7}$	$4.14\text{x}10^{-7}$	$1.36\text{x}10^{-6}$
Doubly Charged Ion	$5.22\text{x}10^{-8}$	$6.22\text{x}10^{-8}$	$8.29\text{x}10^{-8}$	$9.85\text{x}10^{-8}$	$2.07\text{x}10^{-7}$	$6.80\text{x}10^{-7}$
Triply Charged Ion	$3.48\text{x}10^{-8}$	$4.15\text{x}10^{-8}$	$5.53\text{x}10^{-8}$	$6.56\text{x}10^{-8}$	$1.38\text{x}10^{-7}$	$4.54\text{x}10^{-7}$

Neutrals considered in the case of the MiLiPulT include H, O, and H_2O and are assumed to decompose in the following reaction:

$$x_1\mathrm{H_2O} \rightarrow x_2\mathrm{H} + x_3\mathrm{H}^+ + x_4\mathrm{O} + x_5\mathrm{O}^+ + x_6\mathrm{OH} + x_7\mathrm{H_2} + x_8\mathrm{O_2} \tag{2.4}$$

where $x_1,\ x_2,\ x_3,\ \mathrm{etc...}$ are unknown stoichiometric coefficients, which are of course application specific. Water could also decompose into ionized molecules such as OH^-, which would detract from the accuracy of the experimental results since these species concentrations are assumed negligible. Additional doubly charged ions, triply charged ions, and perhaps negatively charged ions may also exist for either or any ion species, but for the purposes of simplicity, all ions are assumed to have a single positive charge within the scope of this research. Previous TLP data extraction and modeling have assumed an evenly distributed ionization based on the number of

species (i.e. 50% each for a two species plasma) or based on the composition of the unused propellant (Gatsonis et al., 2004). However, the true ionization fractions are more likely also a function of the excitation properties of the species, most notably their first ionization potentials. Similarly, Teflon is assumed to decompose in the following manner:

$$x_6\mathrm{C_2F_4} \rightarrow x_7\mathrm{C}+x_8\mathrm{C}^+ + x_9\mathrm{F}+x_{10}\mathrm{F}^+ + x_{11}\mathrm{C_2} + x_{12}\mathrm{F_2} + x_{13}\mathrm{CF} \tag{2.5}$$

where $x_6,\ x_7,\ x_8,\ \mathrm{etc...}$ are again unknown stoichiometric coefficients. Doubly and triply charged ion species may also exist. Centerline species concentrations of Teflon within the DawgSTAR miniPPT yielded 40% of C^+, 31% a combination of C^{++} and F^{+++}, 12% C^{+++}, 12% F^+, and 5% F^{++}. Off center plume angle RPA analysis yielded concentrations of C_2, CF, and F_2 singly charged ions as high as 6% (Shumlak, 2003). Argon and xenon neutrals and ions are considered monatomic for the purposes of these studies.

2.2 Particle Motion

The total velocity for a particle of species s is denoted by $\mathbf{c}_s(\mathbf{r},t)$, relative to a given reference frame. The mean velocity of species s relative to that same reference frame, $\mathbf{c}_{0s}(\mathbf{r},t)$, is defined by

$$\mathbf{c}_{0s}(\mathbf{r},t) = \frac{\sum \mathbf{c}_s(\mathbf{r},t)}{n_s(\mathbf{r},t)d\mathbf{r}}. \tag{2.6}$$

From Chapman and Cowling (1939), the introduction of a mean velocity allows for the definition of a peculiar or unique velocity $\mathbf{C}_s(\mathbf{r},t)$ for a particle in species s, such that

$$\mathbf{c}_s(\mathbf{r},t) = \mathbf{c}_{0s}(\mathbf{r},t) + \mathbf{C}_s(\mathbf{r},t). \tag{2.7}$$

The dependence of velocity on space and time is considered a given and the notation is often dropped, more commonly yielding the velocities shown in the vector diagram of Figure 5.

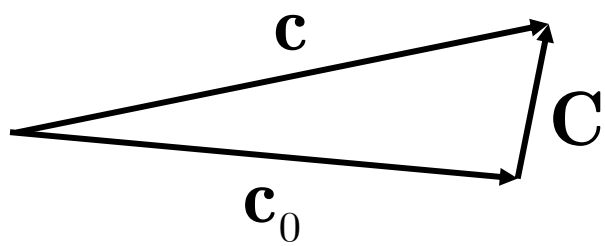

Figure 5. Total velocity, drift (mean) velocity, and thermal (unique) velocity vector diagram.

While the total number of particles in a system is defined as N, the class of particles having respective velocity components between $\mathbf{c}$ and $\mathbf{c} + d\mathbf{c}$ is defined as dN. For each species s, the number of particles dN_s within the velocity element $\mathbf{c} + d\mathbf{c}$ can be classified by the generic velocity distribution function $f_s(\mathbf{c}(\mathbf{r}, t))$, such that

$$dN_s = N_s f_s(\mathbf{c}(\mathbf{r}, t)) d\mathbf{c}. \tag{2.8}$$

More commonly referred to as f_s, the value of the velocity distribution function is always a positive number between zero and one. The species subscript can be dropped when describing velocities as they relate to a species distribution function (i.e. $f_s(\mathbf{c}_s(\mathbf{r}, t)) d\mathbf{c} = f_s(\mathbf{c}(\mathbf{r}, t)) d\mathbf{c}$). Number densities dn_s and n_s can replace dN_s and dN_s respectively, since the unit volume of velocity space remains the same in both cases (Bird, 1994). Subsequently, normalization provides

$$\frac{dn_s}{n_s} = f_s(\mathbf{c}(\mathbf{r}, t)) d\mathbf{c}. \tag{2.9}$$

Species distribution functions will be governed by the species Boltzmann equation. Since $\nabla_c \cdot \mathbf{F}_s = 0$, the Boltzmann equation for each species becomes

$$\frac{\partial}{\partial t}(n_s f_s) + \mathbf{c} \cdot \nabla n_s f_s + \frac{\mathbf{F}_s}{m_s} \cdot n_s \nabla_c f_s = \sum_r \mathbb{C}_{sr} \tag{2.10}$$

for species $s = n,\ i,\ i^{++}, \text{and}\ e$ (Mitchner & Kruger, 1973). Plasma species are often assumed to have a Maxwellian distribution of energy and velocity, which correspond to the Gaussian bell curves of Figure 6 for either an equilibrium or drifting species, and is defined by Bird (1994) as

$$f_s = \frac{\beta^3}{\pi^{3/2}} \exp(-\beta^2 C_s^2) \ \text{ where } \beta = \left(\frac{m_s}{2kT}\right)^{1/2}. \tag{2.11}$$

For the purposes of this research all plasmas generated by a small-scale source are assumed to be of a Maxwellian distribution and electrostatic (no applied magnetic fields except for the acceleration mechanisms are assumed to be present in the source). Should the distribution not be Maxwellian in nature, additional current collection theory would then need to be developed.

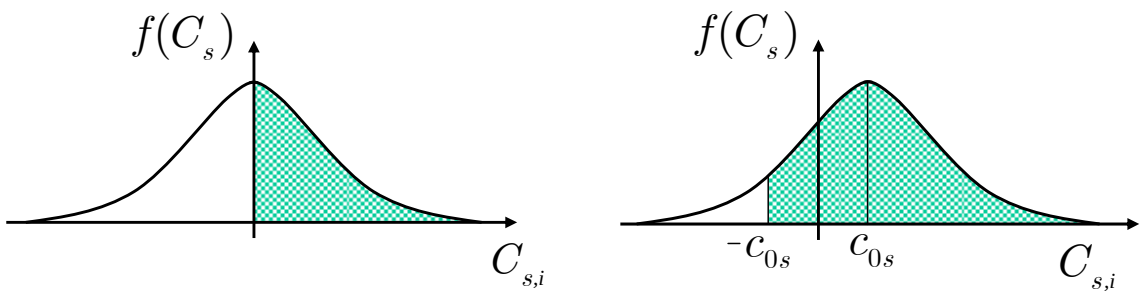

Figure 6. Distribution functions for a Maxwellian equilibrium species (left) and a drifting Maxwellian species (right).

The shaded portions of these distribution function plots are representative of the particles which would pass through a surface element having a unit normal vector parallel and opposite to the drift velocity. Should the drift velocity be zero (i.e. a stationary equilibrium gas), the shaded portion would represent the net flux through that surface element. For a non-zero drift velocity, the flux through the surface element would encompass all particles having a peculiar velocity greater than the negative value of the drift velocity. Beyond this minimum limit, the total velocity of these particles would then be negative and moving away from the surface element.

The mean thermal speed for ions of species s is defined as

$$c_{i,s} = \sqrt{\frac{8kT_{i,s}}{\pi M_{i,s}}} \tag{2.12}$$

where $M_{i,s}$ is the molecular mass of the ion. Equivalently, the electron mean thermal speed is given by

$$c_e = \sqrt{\frac{8kT_e}{\pi M_e}}\,. \tag{2.13}$$

Ion sound velocity for species s is a function of both the electron and relevant ion temperature and is defined as

$$C_s = \sqrt{\frac{\gamma_s Zk(T_e + T_{i,s})}{M_{i,s}}}\,, \tag{2.14}$$

where γ_s is the specific heat ratio of the species and Z is the charge degree of ionization (i.e. 1 for singly-charged ions, 2 for doubly-charged, etc…).

This review of plasma theory would be incomplete without an assessment of Maxwell's equations, which will of course govern the electromagnetic fields and properties of the plasma plume. They are defined in rationalized MKS units as

$$\nabla \cdot \mathbf{D} = \rho_c\,, \tag{2.15}$$

$$\nabla \cdot \mathbf{B} = 0\,, \tag{2.16}$$

$$\nabla \times \mathbf{E} = -\frac{\partial \mathbf{B}}{\partial t}\,, \tag{2.17}$$

$$\nabla \times \mathbf{H} = \mathbf{j} + \frac{\partial \mathbf{D}}{\partial t}\,, \tag{2.18}$$

where $\mathbf{D}$ is the electric displacement, $\mathbf{B}$ is the magnetic induction, $\mathbf{E}$ is the electric intensity, $\mathbf{H}$ is the magnetic intensity, ρ_c is the charge density, and $\mathbf{j}$ is the current density (Mitchner & Kruger, 1973). The constitutive relations for a partially ionized gas are

$$\mathbf{D} = \varepsilon_0 \mathbf{E} \tag{2.19}$$

and

$$\mathbf{B} = \mu_0 \mathbf{H} . \tag{2.20}$$

From Mithcner & Kruger (1973), the Lorentz force is given in MKS units as

$$\mathbf{F} = q[\mathbf{E} + \mathbf{c} \times \mathbf{B}] . \tag{2.21}$$

Lastly, to ensure conservation of charge,

$$\nabla \cdot \mathbf{j} + \frac{\delta \rho_c}{\delta t} = 0 . \tag{2.22}$$

To obtain an expression for the particle number flux based on a given distribution, it is first necessary to define the flux of an undefined quantity Q through a surface element with a unit normal vector $\hat{n} = \hat{\mathrm{x}}$. Assuming that the flux is in the negative $\hat{n}$ direction, has a number density n and a total velocity vector $\mathbf{c}$ $\{u, v, w\}$, the fluxal quantity is defined as $n\overline{Qu}$. One can then define the generic fluxal quantity using the following integral of the distribution function f as

$$n\overline{Qu} = n \int_{-\infty}^{\infty} \int_{-\infty}^{\infty} \int_{0}^{\infty} Quf_s dudvdw . \tag{2.23}$$

Expanding the integral, setting the fluxal quantity $Q = 1$, and also assuming that $\mathbf{c}$ lies entirely within the x-y plane, the inward normal particle flux is defined by

$$\dot{N}_s = \frac{n_s \beta^3}{\pi^{3/2}} \int_{-\infty}^{\infty} \exp(-\beta^2 W_s^2) dw_s \int_{-\infty}^{\infty} \exp(-\beta^2 V_s^2) dv_s \int_{0}^{\infty} u_s \exp(-\beta^2 U_s^2) du_s . \tag{2.24}$$

Integration over particular ranges of peculiar velocity components $\{U, V, W\}$ for various sets of conditions is discussed in Section 2.8.1 resulting in expressions correspond to classical RPA

current collection theory. Other definitions of Q have also been applied to yield expressions for momentum flux and energy flux (Chapman & Cowling, 1939).

2.3 Plasma Collisions and Relevant Collisional Parameters

The Coulomb logarithm accounts for the interaction potential between charged particle binary collisions and is equal to the natural logarithm of the Lambda parameter. While inaccurate for small values, the Coulomb logarithm is independent of relative particle velocity (Ordonez & Molina, 1994). The lambda parameter is present in nearly all expressions of charged particle collision frequency, and has several definitions in literature which yield slightly different values. Species dependent definitions of the Coulomb logarithm can be found in the NRL Plasma Formulary (2004), which typically diverge at electron or ion temperatures greater than 10,000 K. For the purposes of this research, the lambda parameter will be defined for all species by

$$\Lambda = \Lambda_{ee} = \Lambda_{ie} = \Lambda_{ii} = 12400000\left(\frac{T_e^{\,3}}{n_e}\right)^{\frac{1}{2}}. \tag{2.25}$$

Table 4 contains a corresponding chart of the expected Debye lengths for this range of electron parameters as calculated from (1.2).

Table 4. Debye length values (in meters) various electron temperatures and number densities.

		n_e (m^{-3})		
		1.00E+16	**1.00E+18**	**1.00E+20**
T_e (eV, K)	**4.0, 46416.0**	1.487E-04	1.487E-05	1.487E-06
	8.0, 92832.0	2.102E-04	2.102E-05	2.102E-06
	12.0, 139248.0	2.575E-04	2.575E-05	2.575E-06

λ_D (m)

Debye length for the electron parameter envelope ranges from more than 250 μm down to roughly 1 μm. From Section 1.5, recall that RPA design constraints are predicated on the

expected Debye lengths of the plasma to be characterized. With a range of more than two orders of magnitude, RPA design optimization can be arduous without more well-defined expectations of the plume properties.

The collision cross section for momentum transfer collisions is independent of mass as long as $Z = 1$. From Mitchner & Kruger (1973), and assuming that $T_i \approx T_e$,

$$\bar{Q}_{ei} = \bar{Q}_{ee} = 6\pi \bar{b}_0^2 \ln \Lambda \tag{2.26}$$

where

$$\bar{b}_0 = \frac{Zq^2}{12\pi\varepsilon_0 kT}. \tag{2.27}$$

The Coulomb collision frequency for an electron-electron Coulomb collision is given as

$$\nu_{ee} = \frac{16\sqrt{\pi}}{3} n_e \left(4k\frac{T_e}{M_e}\right)^{-\frac{3}{2}} \left(\frac{q^2}{4\pi\varepsilon_0 \frac{M_e}{2}}\right)^2 \ln(\Lambda). \tag{2.28}$$

Since the lambda parameter is proportional to the natural logarithm of the collision frequency, and since it typically ranges on the order of ~10^4 to 10^6 for relevant plasma parameters, the term $\ln(\Lambda)$ can be approximated by $\ln(\Lambda) \approx 10$. However, a more rigorous calculation of the lambda parameter for the anticipated plasma property ranges yields the values shown in Table 5.

Table 5. Lambda parameter values for various electron temperatures and number densities.

		n_e (m^{-3})		
		1.00E+16	**1.00E+18**	**1.00E+20**
T_e (eV, K)	**4.0, 46416.0**	1.240E+06	1.240E+05	1.240E+04
	8.0, 92832.0	3.507E+06	3.507E+05	3.507E+04
	12.0, 139248.0	6.443E+06	6.443E+05	6.443E+04

The mean free path, or the average distance between particle collisions, is expressed for electron-electron Coulomb collisions in terms of the electron thermal speed and the collision frequency as

$$\lambda_{ee} = \frac{c_e}{\nu_{ee}}. \tag{2.29}$$

The collision frequency for ion-electron Coulomb collisions is given as

$$\nu_{i1e} = \frac{16\sqrt{\pi}}{3} n_i \left(2k \left(\frac{T_i}{M_i} + \frac{T_e}{M_e} \right) \right)^{-\frac{3}{2}} \left(\frac{q^2}{4\pi\varepsilon_0 \frac{M_i M_e}{M_i + M_e}} \right)^2 \ln(\Lambda). \tag{2.30}$$

The notation of the subscript '1' indicates species type 1. The mean free path for ion-electron Coulomb collisions then becomes

$$\lambda_{i1e} = \frac{c_{i1e}}{\nu_{i1e}}. \tag{2.31}$$

The Coulomb collision frequency for a same species ion-ion collision is given as

$$\nu_{i1i1} = \frac{16\sqrt{\pi}}{3} n_{i1} \left(\frac{4kT_{i1}}{M_{i1}} \right)^{-\frac{3}{2}} \left(\frac{q^2}{4\pi\varepsilon_0 \frac{M_{i1} M_{i1}}{M_{i1} + M_{i1}}} \right)^2 \ln(\Lambda) \tag{2.32}$$

with a corresponding mean free path of

$$\lambda_{i1i1} = \frac{c_{i1}}{\nu_{i1i1}}. \tag{2.33}$$

Commas between particle type and particle species have been dropped for conciseness. The species number notation becomes necessary when defining the ion-ion Coulomb collision frequency between ions of different species 1 and 2 as

$$\nu_{i2i1} = \frac{16\sqrt{\pi}}{3} n_{i2} \left(2k \left(\frac{T_{i2}}{M_{i2}} + \frac{T_{i1}}{M_{i1}} \right) \right)^{-\frac{3}{2}} \left(\frac{q^2}{4\pi\varepsilon_0 \frac{M_{i2} M_{i1}}{M_{i2} + M_{i1}}} \right)^2 \ln(\Lambda). \tag{2.34}$$

The corresponding mean free path is then based on the average of the two ion thermal speeds as

$$\lambda_{i2i1} = \frac{c_{i21}}{\nu_{i2i1}}, \tag{2.35}$$

where c_{i21} is the average of c_{i1} and c_{i2}. Coulomb collision frequencies are plotted for a broad range of ion and electron number densities for electron-electron, ion-electron, and same species ion-ion collision types in Figure 7. The corresponding mean free paths are plotted in Figure 8, assuming a characteristic length of 75 μm. For the purposes of simplicity these graphs assume quasineutrality and $T_i = T_e$. To demonstrate the collisional parameter's dependence on temperature, traces corresponding to both $T_i = T_e = 1.0\ \mathrm{eV}$ and $T_i = T_e = 10.0\ \mathrm{eV}$ are displayed. While ion-electron and same-species ion-ion collision frequencies and mean free paths ranged over species are not identical, the variance is minimal and their treatment in these plots is generalized (Yin, 1999).

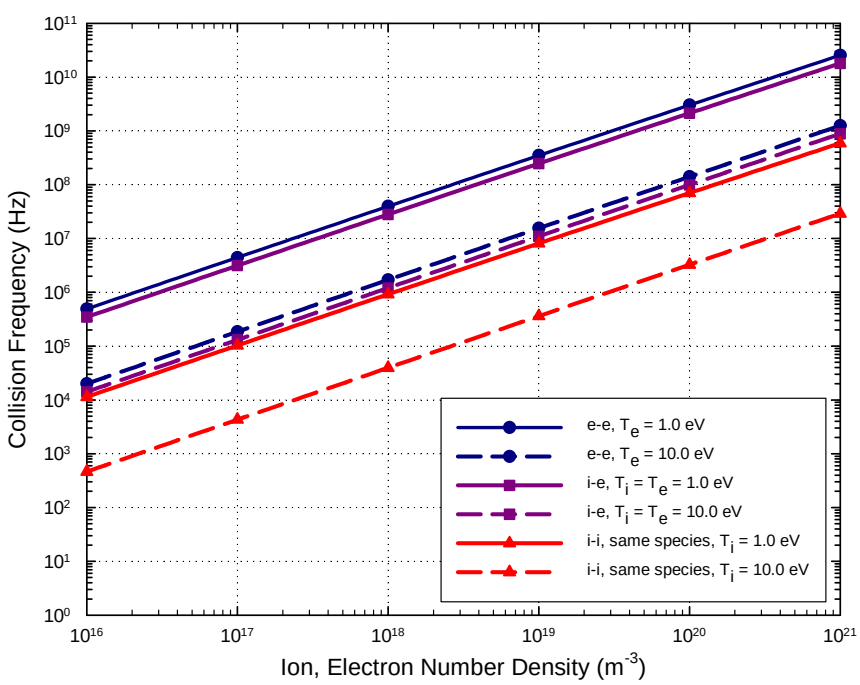

Figure 7. Coulomb collision frequencies for various electron and ion temperatures and number densities.

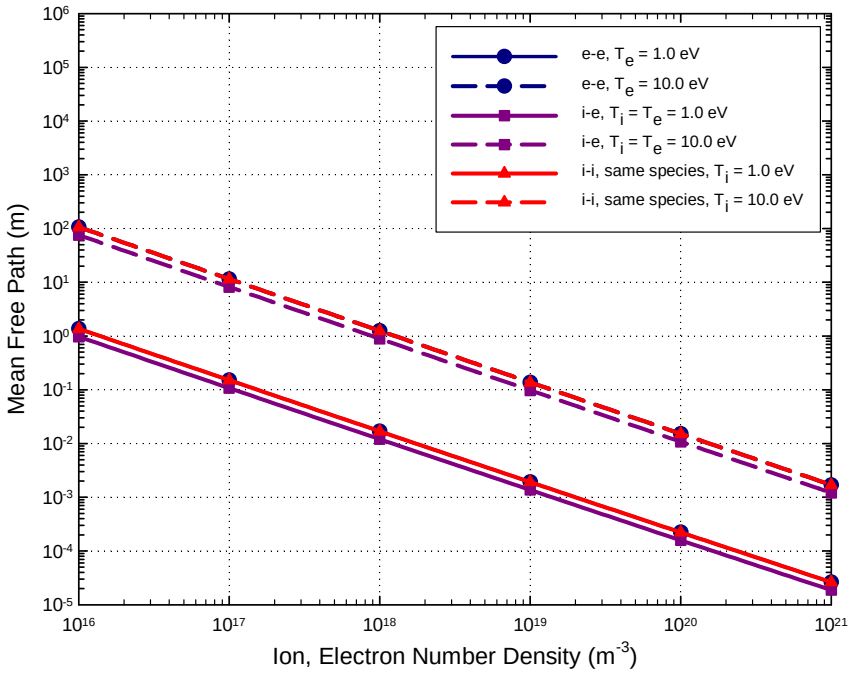

Figure 8. Coulomb collision frequencies for various electron and ion temperatures and number densities.

While collision frequencies for Coulomb collisions are heavily dependent on species collision type, mean free path variance among even the ion-ion to electron-electron Coulomb collision types is within an order of magnitude.

Coulomb collision frequencies for different species ion-ion collisions are considerably different from their same-species equivalents (Demars & Schunk, 1979). Figure 9 displays a comparison of two common interspecies ion-ion collision types (H^+-O^+ and C^+-F^+) common to EP thruster plumes. These collision frequencies are compared to the collision frequencies for same species ion-ion Coulomb collisions.

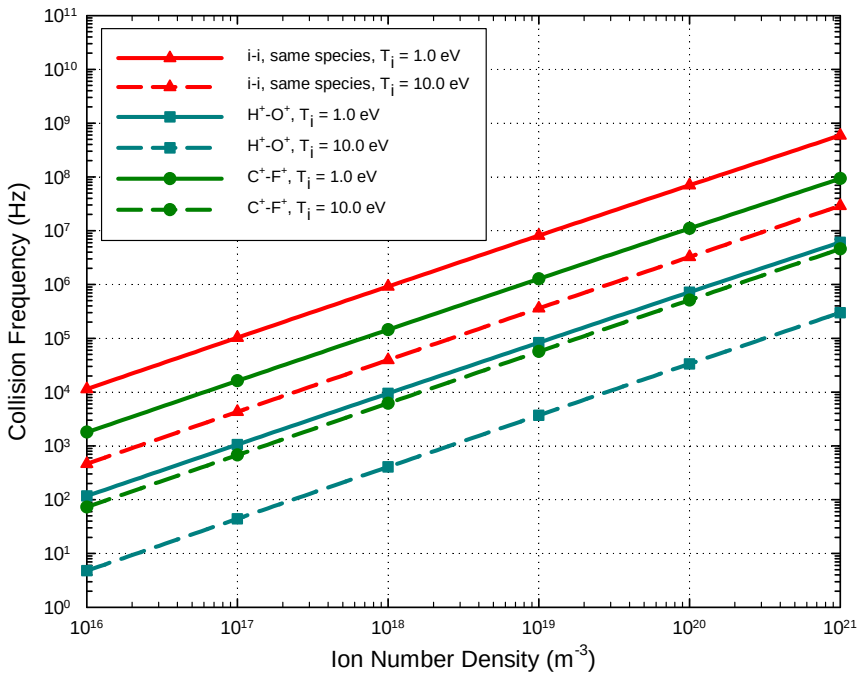

Figure 9. Collision frequency comparison for same species ion-ion and common interspecies ion-ion Coulomb collisions for various ion temperatures and number densities.

The corresponding mean free paths for these collision types are plotted in Figure 10. As was the case for Figure 9, interspecies ions are assumed to have identical temperatures and number densities for simplicity. Interspecies ion collisions have a slightly elevated mean free path compared to same species collisions, which makes sense since their collision cross sections are slightly lower.

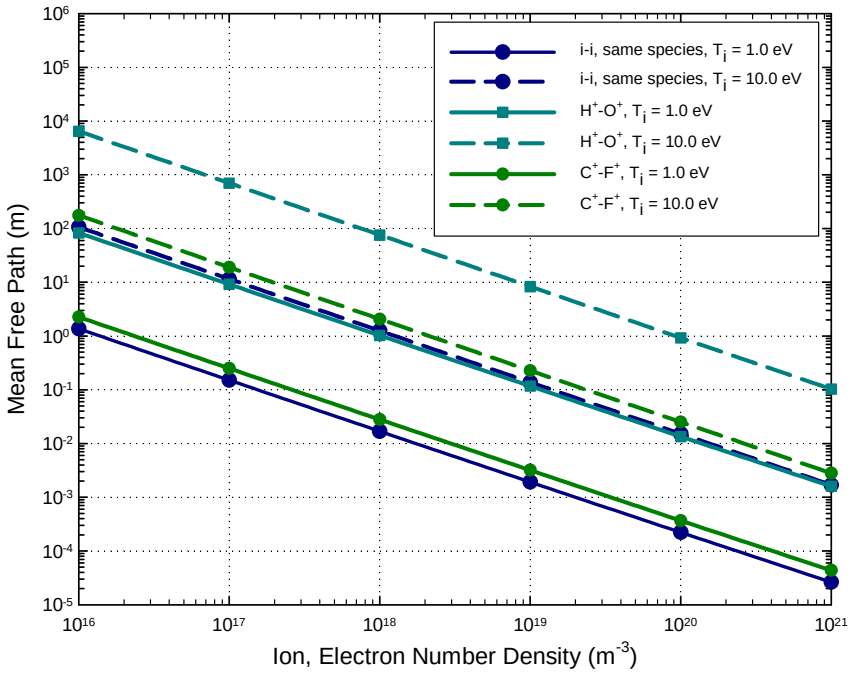

Figure 10. Mean free path comparison for same species ion-ion and common interspecies ion-ion Coulomb collisions for various ion temperatures and number densities.

To once again illustrate the minimal variance of species type on ion-electron Coulomb and ion-ion Coulomb collisions, the mean free paths for the six ion species considered in this research for micropropulsion applications are plotted in Figure 11. Again, minimal variation is observed over species mass from Hydrogen up to Xenon.

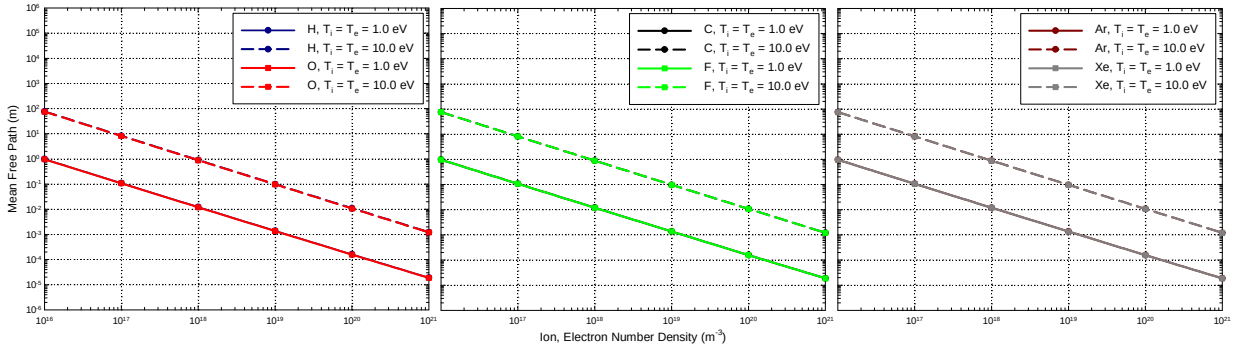

Figure 11. Ion-electron Coulomb collision mean free paths for several propellant species.

These calculated mean free paths of the Coulombic force collisions can then be used towards a Knudsen number analysis to yield optimal Langmuir probe dimensions. For the case of a Langmuir probe, the Knudsen number definition from (1.1) can be rewritten as

$$Kn_{s_1,s_2} = \frac{\lambda_{s_1,s_2}}{r_p}. \tag{2.36}$$

where the probe radius r_p is the characteristic length. Ideally, for the TLP current collection theories described later in this chapter to be valid, the plasma should be considered collisionless within the presheath and sheath regions of the exposed cylindrical probe. The probe radius is therefore constrained to be as small as possible to ensure a sufficiently collisionless regime with $Kn_{s_1,s_2} \gg 1$ (i.e. where the mean free path between collisions is many orders of magnitude greater than the probe radius). Optimizing TLP probe dimensions is then a balance of ensuring large enough exposed probe area such that a measurable current signal is obtained.

Ion-neutral same species charge exchange (CEX) collision frequencies and mean free paths were also investigated to ensure that the plasma could be considered collisionless on the spatial scales expected of TLP exposed probe wires. For these estimates, the plasma was assumed 1% ionized. It was also necessary to define a relative particle velocity range for c_{ni}. For these studies, a relative velocity range of 1.0 km/s to 10.0 km/s was assumed. The collision frequency for charge exchange ion neutral collisions is given as

$$\nu_{in}^{cex} = \frac{4}{3}\sigma_{cex} n_n \sqrt{\frac{8k}{\pi M_r}\left(T_i + T_n\right)}, \tag{2.37}$$

where σ_{cex} is the charge exchange collision cross section and M_r is the reduced mass defined as

$$M_r = \frac{M_i M_n}{M_i + M_n}. \tag{2.38}$$

The charge exchange collision cross section is defined as

$$\sigma_{cex} = (k_1 \ln c_{ni} + k_2)^2 \cdot 10^{-20} \text{ m}^2 ,$$

where k_1 and k_2 are species-dependent coefficients (Yin, 1999). For hydrogen, $k_1 = -1.2522$ and $k_2 = 8.3343$. For oxygen, $k_1 = -2.6797$ and $k_2 = 17.771$ (Barakat & Schunk, 1981). These values, for a given velocity, yield charge exchange collision cross sections comparable with those tabulated in Sakabe & Yasukazu (1991). Table 6 and Table 7 show the collision frequencies for same species ion-neutral charge exchange collisions ranged over relative particle velocities of 1.0 km/s and 10.0 km/s for hydrogen and oxygen, respectively. For the calculation of these collision frequencies, it was necessary to assume a neutral temperature of 600 K. An additional degree or range of calculation could also include ranging the neutral temperature.

Table 6. Ion-neutral CEX collision frequencies (in Hz) for hydrogen.

Assuming c_{ni} = 1.0 km/s:

		n_n (m^{-3})			
		1.00E+18	**1.00E+19**	**1.00E+20**	
T_i (eV, K)	**1.0, 11604.0**	1.382E+04	1.382E+03	1.382E+02	ν_{in}^{cex} (Hz)
	10.0, 116040.0	4.273E+04	4.273E+03	4.273E+02	

Assuming c_{ni} = 10.0 km/s:

		n_n (m^{-3})			
		1.00E+18	**1.00E+19**	**1.00E+20**	
T_i (eV, K)	**1.0, 11604.0**	1.004E+04	1.004E+03	1.004E+02	ν_{in}^{cex} (Hz)
	10.0, 116040.0	3.104E+04	3.104E+03	3.104E+02	

Table 7. Ion-neutral CEX collision frequencies (in Hz) for oxygen.

Assuming c_{ni} = 1.0 km/s:

		n_n (m^{-3})		
		1.00E+18	**1.00E+19**	**1.00E+20**
T_i (eV, K)	**1.0, 11604.0**	7.346E+03	7.346E+02	7.346E+01
	10.0, 116040.0	2.271E+04	2.271E+03	2.271E+02

ν_{in}^{cex} (Hz)

Assuming c_{ni} = 10.0 km/s:

		n_n (m^{-3})		
		1.00E+18	**1.00E+19**	**1.00E+20**
T_i (eV, K)	**1.0, 11604.0**	5.323E+03	5.323E+02	5.323E+01
	10.0, 116040.0	1.646E+04	1.646E+03	1.646E+02

ν_{in}^{cex} (Hz)

Table 8 and Table 9 show the corresponding mean free paths for same species ion-neutral CEX collisions of hydrogen and oxygen, respectively. These values were calculated using the particle relative drift velocity as opposed to the mean thermal velocities and sound velocities for the Coulomb collision mean free paths. For a majority of the ranges presented, the mean free paths are significantly larger than the spatial scales of TLP exposed probe wires, indicating that the collisionless assumption for TLP current collection is valid. For higher temperatures, low relative drifts, and high neutral densities, these mean free paths are on the order of TLP exposed probe wire distances. However, at the corresponding ion densities resultant from an assumed 1% ionization, the sheath diameters under these conditions would be relatively small.

Table 8. Ion-neutral CEX mean free paths (in meters) for hydrogen.

Assuming c_{ni} = 1.0 km/s:

T_i (eV, K)	n_n (m^{-3}) 1.00E+18	1.00E+19	1.00E+20
1.0, 11604.0	7.235E-02	7.235E-03	7.235E-04
10.0, 116040.0	2.340E-02	2.340E-03	2.340E-04

λ_{in}^{cex} (m)

Assuming c_{ni} = 10.0 km/s:

T_i (eV, K)	n_n (m^{-3}) 1.00E+18	1.00E+19	1.00E+20
1.0, 11604.0	9.960E-01	9.960E-02	9.960E-03
10.0, 116040.0	3.222E-01	3.222E-02	3.222E-03

λ_{in}^{cex} (m)

Table 9. Ion-neutral CEX mean free paths (in meters) for oxygen.

Assuming c_{ni} = 1.0 km/s:

T_i (eV, K)	n_n (m^{-3}) 1.00E+18	1.00E+19	1.00E+20
1.0, 11604.0	1.361E-01	1.361E-02	1.361E-03
10.0, 116040.0	4.403E-02	4.403E-03	4.403E-04

λ_{in}^{cex} (m)

Assuming c_{ni} = 10.0 km/s:

T_i (eV, K)	n_n (m^{-3}) 1.00E+18	1.00E+19	1.00E+20
1.0, 11604.0	1.879E+00	1.879E-01	1.879E-02
10.0, 116040.0	6.077E-01	6.077E-02	6.077E-03

λ_{in}^{cex} (m)

Ion-neutral interspecies CEX collisions for that of water neutrals (O^+-H_2O and H^+-H_2O CEX collisions) as well as other interspecies CEX collisions (O^+-H and H^+-O) were not calculated due to a lack of available cross section coefficient data. These interspecies ion-neutral CEX collisions would occur with comparable frequency in the case of oxygen-hydrogen interactions. In the case of water neutral collisions, the neutral temperature would more than likely be less than that of the monatomic neutral temperatures, and therefore the collisions would occur with

comparable or lesser frequency. The relative particle drift would most likely be less in this case, contributing to a lower collision frequency between ions and water neutrals.

Other collisions types occurring within the plasma include but are not limited to ion-neutral same species elastic collisions, ion-neutral interspecies elastic collisions, electron-neutral collisions, neutral-neutral same species elastic collisions, neutral-neutral interspecies elastic collisions, single ionization collisions, double ionization collisions, double ion ionization collisions, excitation collisions, and recombination collisions. Analysis of these collisions yielded lower collision frequencies (and larger mean free paths). As they are not the most frequent collisions (Barakat & Schunk, 1980), they can be excluded from the probe sizing Knudsen number analysis.

2.4 Single Langmuir Probe Theory

Single Langmuir Probes (SLPs) operate by exposing a thin conductive wire of known length and radius at a variable potential to a plasma. By varying the probe voltage and measuring the current through the wire, an I-V curve can be extracted. A typical SLP I-V curve can be seen in Figure 12. If the voltage is sufficiently low, the probe wire will attract only ions, and the ion saturation current $I_{i,sat}$ is detected. Conversely, at higher voltages the probe will collect only electrons, and the electron saturation current $I_{e,sat}$ is detected. Of particular interest is the I-V curve behavior between the two saturation currents, known as the transition region. An I-V curve of relatively high quality will have a noticeable 'knee' at the intersection of the transition region and electron saturation region, indicating the space potential. There are also other circumstances when the curve could be of high quality (strong signal) but with a less pronounced knee, particularly when the plasma is in the presence of a strong enough magnetic

field such that the probe radius becomes larger than the Larmor radius. In this case, the electron saturation current is limited to roughly 10 to 20 times the ion saturation current (Chen, 2003). The floating potential is defined where the net current is equal to zero. While Langmuir probes are invasive, they offer a simple, consistent technique to obtain electron number density, electron temperature, and ion number density in the presence of sheath expansion (Chen, 2003).

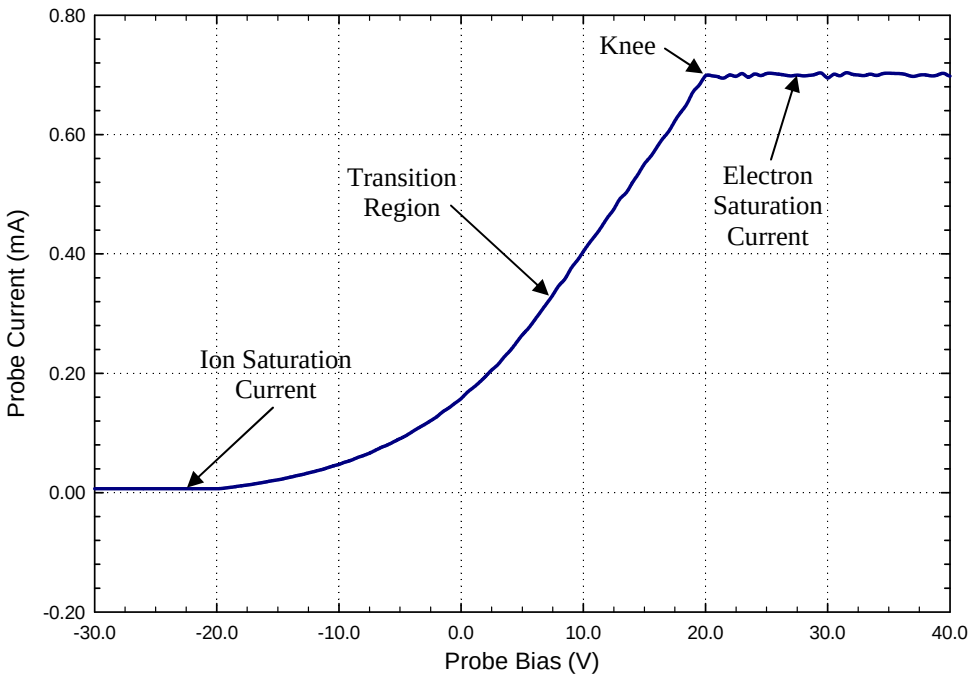

Figure 12. Typical SLP I-V curve for a drifting Maxwellian plasma.

Extensive theory exists on the analysis of I-V curves, including several methods of plasma parameter extraction. Most commonly, if the plasma is assumed to have a Maxwellian energy distribution, the slope of the I-V curve within the transition region will be equal to the inverse of the electron temperature (in electron volts) as given by

$$m = 1/T_{eV}\,. \tag{2.39}$$

Additionally, once the ion saturation current is subtracted from the entire I-V curve, the electron number density can be obtained from the expression for the electron saturation given by

$$I_{es} = qn_e A\left(\frac{kT_e}{2\pi m}\right)^{1/2} \tag{2.40}$$

where A is the exposed area of the probe (Chen, 2003).

Unfortunately, SLPs do not offer a time-resolved profile for electron parameters since the temporal resolution is limited by the time it takes to perform the sweep (~1 ms to more than 1 s at best). From Section 1.4, an alternative SLP technique for characterization of unsteady plasmas exists in fixing the probe potential and measuring the time-resolved probe current, and repeating this process for enough probe potentials along the transition region, ion saturation region, and electron saturation region to obtain an I-V curve. The data analysis for this method is somewhat cumbersome, marking an additional need for a more robust method. The addition of a second, third, and in some cases a fourth exposed probe wire with known potential biases between them offers such a method. Monitoring the currents between these probe wires allows for time-resolved measurements with the added advantage of a manageable data reduction technique. Another benefit of double Langmuir probes (DLPs) or other multiple probes over SLPs is that since the electrodes and biasing voltages comprise a completely closed and isolated circuit, there is no net charge drain from the plasma (Chung et al., 1974). This research focuses more on the implementation of and theory of operation for triple Langmuir probes (TLPs) so that a complete system of equations can be solved to yield values of the three relevant plasma plume unknowns: electron temperature, electron number density, and space potential.

2.5 Triple Langmuir Probe Theory

The current collection theory for TLP operation is heavily dependent on the assumptions made regarding sheath formation around the probe wires which is a function of the expected electron number densities and temperatures to be encountered. It is therefore necessary to

provide bounds for both of these properties, yielding an expected operational envelope on the $n_e - T_e$ plane. From equation (1.2), the envelope would also be bounded by a minimum and maximum Debye length, as shown in Figure 13. The probe diameters and exposed probe lengths are then chosen based on these bounds in addition to Knudsen number analyses and other considerations to be discussed in this section (Gatsonis et al., 2004).

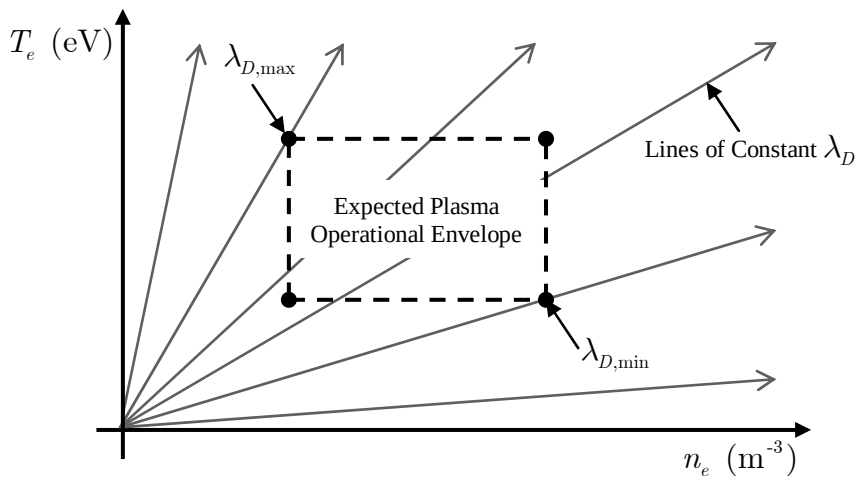

Figure 13. Electron number density vs. temperature plot illustrating the plasma operational envelope bounded by both minimum and maximum expected Debye Length.

The TLP current-mode theory of operation assumes that no two sheaths will overlap. Consequently, the interprobe spacing must be larger than one sheath diameter. These dimensions are illustrated in a front view diagram of the TLP wires shown in Figure 14.

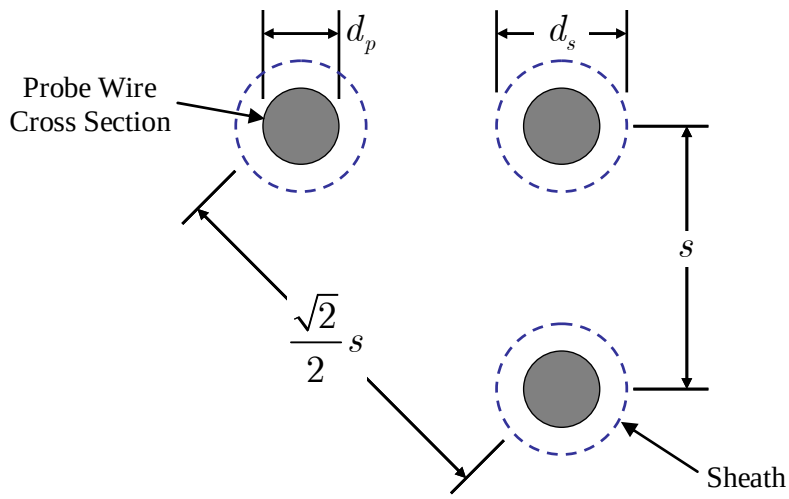

Figure 14. Sheath diameter and probe spacing of a TLP (front view).

Further assumptions include that the probe wires are aligned with the direction of the drifting plasma flow (alignment angle $\varphi = 0$) and that the exposed probe areas are equal: $A_1 = A_2 = A_3 = A_\parallel$. This area is a function of the exposed parallel probe length $L_\parallel$ and the probe radius r_p as

$$A_\parallel = 2\pi r_p L_\parallel + \pi r_p^2 . \tag{2.41}$$

From Section 2.2, all plasma species are assumed to have a Maxwellian velocity distribution.

2.5.1 Current-mode vs. Voltage-mode Operation

Voltage-mode operation of a TLP or QLP requires biasing voltages applied between probe wires 1 and 3 while probe wire 2 is allowed to float electrically in the plasma. The resultant potential difference between probe wires 1 and 2, $\phi_{12}(t)$, and the collected current of $I_3(t)$ are then monitored to extract $n_e(t)$ and $T_e(t)$. This method has been applied to arcjets and gasdynamic PPTs, but is not favorable in the presence of RF plasmas as measurement of ϕ_{12} is susceptible to EMI noise (Gatsonis et al., 2004).

Current-mode operation requires applying a fixed, known ϕ_{12} and ϕ_{13} such that $\phi_{12} \neq \phi_{13}$. The three currents $I_1(t)$, $I_2(t)$, and $I_3(t)$ are measured and allow for the analysis of $n_e(t)$ and $T_e(t)$ and the difference between the space potential and the potential of probe wire 1, known as ϕ_{s1}. Voltage diagrams of both voltage-mode and current-mode are shown in Figure 15.

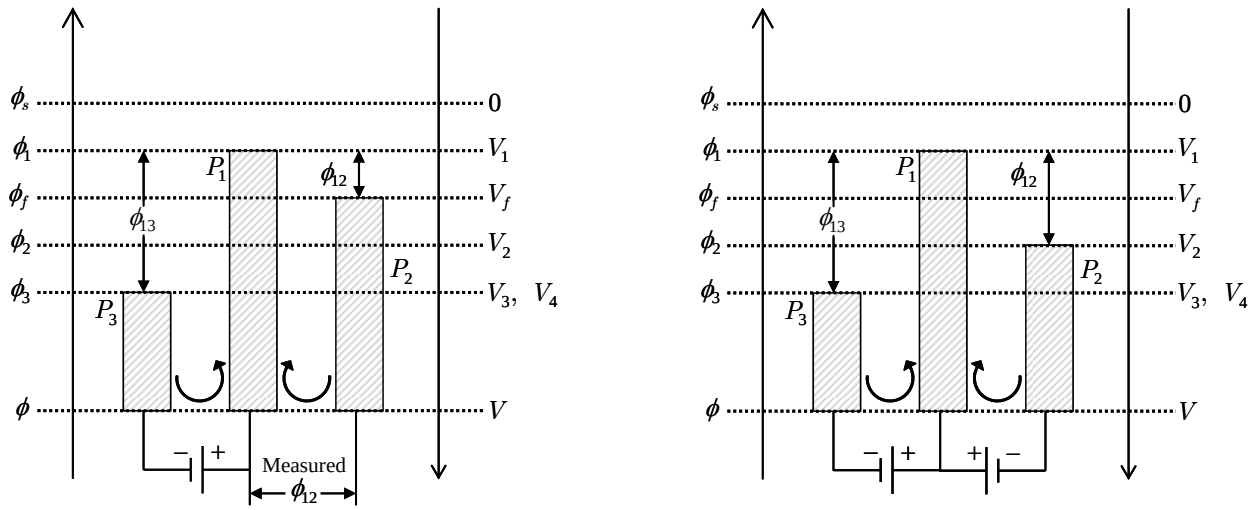

Figure 15. TLP voltage-mode operation (left) and current-mode operation (right).

There are several other assumptions inherent to TLP current-mode operation. First, bias potentials ϕ_{12} and ϕ_{13} are assumed to be less than the space potential ϕ_s. It is assumed that the plasma is quasineutral outside of the probe sheaths and the distribution function is a drifting Maxwellian (Lam, 1965). Other assumptions include $T_i \approx T_e$ and that all ions are of single, positive charge ($Z_i = 1$).

The thin sheath regime applies for $r_p / \lambda_D > 100$ and the current collected on each probe is given by Chen & Sekiguchi, (1965) as:

$$I_1 = A_{\|} J_{e0} \exp\left(-\frac{q\phi_{s1}}{kT_e}\right) - A_{\|} q n_e \sqrt{\frac{kT_e}{M_i}} \exp\left(-\frac{1}{2}\right), \tag{2.42}$$

$$I_2 = A_{\parallel} J_{e0} \exp\left(-\frac{q(\phi_{s1} + \phi_{12})}{kT_e}\right) - A_{\parallel} q n_e \sqrt{\frac{kT_e}{M_i}} \exp\left(-\frac{1}{2}\right), \tag{2.43}$$

$$\text{and } I_3 = A_{\parallel} J_{e0} \exp\left(-\frac{q(\phi_{s1} + \phi_{13})}{kT_e}\right) - A_{\parallel} q n_e \sqrt{\frac{kT_e}{M_i}} \exp\left(-\frac{1}{2}\right), \tag{2.44}$$

where

$$J_{e0} = q n_e (kT_e / 2\pi M_e)^{\frac{1}{2}}. \tag{2.45}$$

The transitional regime, as developed by Laframboise in 1966, applies when $5 < r_p / \lambda_D < 100$ and is given by Laframboise (1966) as:

$$I_1 = A_{\parallel} J_{e0} \exp\left(-\frac{q\phi_{s1}}{kT_e}\right) - A_{\parallel} J_{i0} \exp\left(\beta + \frac{q\phi_{s1}}{kT_e}\right)^{\alpha}, \tag{2.46}$$

$$I_2 = A_{\parallel} J_{e0} \exp\left(-\frac{q(\phi_{s1} + \phi_{12})}{kT_e}\right) - A_{\parallel} J_{i0} \exp\left(\beta + \frac{q(\phi_{s1} + \phi_{12})}{kT_e}\right)^{\alpha}, \tag{2.47}$$

$$\text{and } I_3 = A_{\parallel} J_{e0} \exp\left(-\frac{q(\phi_{s1} + \phi_{13})}{kT_e}\right) - A_{\parallel} J_{i0} \exp\left(\beta + \frac{q(\phi_{s1} + \phi_{13})}{kT_e}\right)^{\alpha}, \tag{2.48}$$

where

$$J_{i0} = q n_i (kT_e / 2\pi M_i)^{\frac{1}{2}}, \tag{2.49}$$

$$\alpha = 2.9 / [\ln(r_p / \lambda_D) + 2.3] + 0.07 (T_i / Z_i T_i)^{0.75} - 0.34, \tag{2.50}$$

$$\text{and } \beta = 1.5 + (T_i / Z_i T_i) \left\{ 0.85 + 0.135 [\ln(r_p / \lambda_D)^3 \right\}. \tag{2.51}$$

Expressions for the parameters α and β were obtained via an algebraic curve fitting to experimental data first obtained by Laframboise for an aligned single electrostatic probe and

consequently extended to double and triple Langmuir probes (Peterson and Talbot, 1970). In either case, the solution of the three unknowns n_e, T_e, and ϕ_{s1} is typically performed numerically for each timestep using a Newton-Raphson solver as outlined in Chapter 3.

The tip effect, or end effect, parameter is given by

$$t_p = \frac{L_\parallel}{\lambda_D} \frac{\sqrt{kT_e/M_i}}{u_i}. \tag{2.52}$$

For $t_p \gg 1$, the end effect becomes negligible (Chung et al., 1974). A tip effect parameter greater than 10 is typically considered acceptable, placing a bound on the minimum exposed parallel probe length.

2.5.2 The Orbital Motion Limited Regime

Orbital motion limited (OML) theory considers the current collection of cylindrical probes at a positive probe bias ϕ_{probe} based on the orbital motion of electrons assuming the probe's space charge sheath region is infinitely large. In other words, the OML theory assumes the limit $\frac{r_p}{\lambda_D} \to 0$ is approached (Chung et al., 1974). Electron absorption by the probe is based on whether the particle's distance of closest approach p_{approach} is less than the probe radius r_p as shown in Figure 16. The impact parameter represents the orthogonal distance between the probe center and the particle's velocity vector at an infinite distance from the probe.

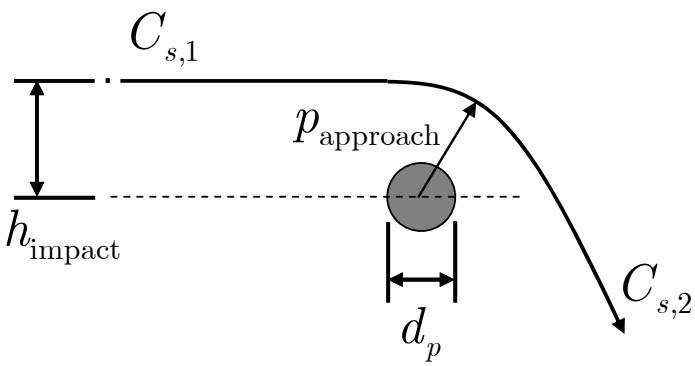

Figure 16. Orbital motion and relevant dimension definitions of a charged particle attracted to an electrically biased cylindrical probe.

For an electron incident to the probe with velocity $C_{s,1}$ such that it exactly grazes the probe surface with velocity $C_{s,p}$, conservation of angular momentum yields the following expression containing the impact parameter:

$$M_e C_{s,1} h_{\text{impact}} = M_e C_{s,p} r_p \,. \tag{2.53}$$

For a grazing electron with initial energy of $q\phi_{\text{initial}}$ the impact parameter is then defined by

$$h_{\text{impact}} = r_p \sqrt{1 + \frac{\phi_{\text{probe}}}{\phi_{\text{initial}}}} \,. \tag{2.54}$$

A two-dimensional analysis of a Maxwellian distribution in conjunction with (2.54) performed by Allen (1992) yields the electron current incident on the cylindrical probe as

$$I_e = 2\pi n_e r_p L_{\parallel} q \left(\frac{kT_e}{2\pi M_e} \right)^{1/2} \left(\frac{2}{\sqrt{\pi}} \left(\frac{q\phi_{\text{probe}}}{kT_e} \right)^{1/2} + \exp\left(\frac{q\phi_{\text{probe}}}{kT_e} \right) erfc \left(\frac{q\phi_{\text{probe}}}{kT_e} \right)^{1/2} \right). \tag{2.55}$$

For values of $\frac{q\phi_{\text{probe}}}{kT_e} \geq 2$, the collected electron current expression simplifies to

$$I_e = 4\sqrt{\pi} n_e r_p L_{\parallel} q \left(\frac{kT_e}{2\pi M_e} \right)^{1/2} \left(1 + \frac{q\phi_{\text{probe}}}{kT_e} \right)^{1/2} . \tag{2.56}$$

Under this approximation for the case of a TLP, the application of the probe bias voltages ϕ_{12} and ϕ_{13} in relation to the space potential ϕ_s and the addition of the collected ion current terms yield the following system of equations:

$$I_1 = 4\sqrt{\pi} r_p L_{\parallel} q \left(n_e \left(\frac{kT_e}{2\pi M_e} \right)^{1/2} \left(1 + \frac{q\phi_{\mathrm{s1}}}{kT_e} \right)^{1/2} - n_i \left(\frac{kT_i}{2\pi M_i} \right)^{1/2} \left(1 - \frac{q\phi_{\mathrm{s1}}}{kT_i} \right)^{1/2} \right), \tag{2.57}$$

$$I_2 = 4\sqrt{\pi} r_p L_{\parallel} q \left(n_e \left(\frac{kT_e}{2\pi M_e} \right)^{1/2} \left(1 + \frac{q(\phi_{\mathrm{s1}} + \phi_{12})}{kT_e} \right)^{1/2} - n_i \left(\frac{kT_i}{2\pi M_i} \right)^{1/2} \left(1 - \frac{q(\phi_{\mathrm{s1}} + \phi_{12})}{kT_i} \right)^{1/2} \right), \tag{2.58}$$

and

$$I_3 = 4\sqrt{\pi} r_p L_{\parallel} q \left(n_e \left(\frac{kT_e}{2\pi M_e} \right)^{1/2} \left(1 + \frac{q(\phi_{\mathrm{s1}} + \phi_{13})}{kT_e} \right)^{1/2} - n_i \left(\frac{kT_i}{2\pi M_i} \right)^{1/2} \left(1 - \frac{q(\phi_{\mathrm{s1}} + \phi_{13})}{kT_i} \right)^{1/2} \right). \tag{2.59}$$

This system can be solved for the three unknowns using numerical methods as done for the thin sheath and transitional regimes. However, the OML theory is not applicable for relatively dense plasmas. For dense plasmas, the implicit OML assumption that at least some particles of all velocity classes are incident to the probe surface is no longer valid. Specifically, this assumption (and consequently the entire OML theory) is only valid for

$$r_p / \lambda_D < \sqrt{-\frac{kT_i}{q\phi_{\mathrm{probe}}}}\,. \tag{2.60}$$

Beyond this limit an absorption radius effectively replaces the probe radius which varies as a function of velocity class (Allen, 1992). For relatively low values of r_p / λ_D (less than 5) under the aforementioned limit, OML theory offers an effective model for the collected TLP currents and electron parameters.

2.5.3 Allen-Boyd-Reynolds (ABR) Theory of TLP Operation

An additional model for particle collection by a cylindrical probe involves a more detailed analysis of the radial motion of particles incident to the probe and was originally developed by Allen, Boyd, and Reynolds (hence the designation ABR theory). ABR theory assumes that all particles initially have zero velocity at an infinite distance away from the probe. Based on the assumption that angular momentum is conserved, the ion or electron motion must be entirely radial (i.e. there is no orbital motion). ABR theory would then also have to assume that $T_{i,e} = 0$ at infinity (Evans et al., 2001).

Chen (1965) provides a solution to the Poisson equation as it relates to ABR theory in cylindrical coordinates assuming that the probe is centered at $r = 0$. With the definition of a normalized radius based on Debye length given as $\xi = \frac{r}{\lambda_D}$ and the term $\eta = -\frac{q\phi}{kT_e}$, the cylindrical probe ABR equation becomes (for ions):

$$\frac{\partial}{\partial \xi}\left(\xi \frac{\partial \eta}{\partial \xi}\right) = \frac{qI}{2\pi k T_e}\sqrt{\frac{M_i}{2\varepsilon_0 n_i \eta}} - \xi \exp(-\eta). \tag{2.61}$$

Integration of this equation can be performed over all radii. Since the number density is not yet known, multiple $n_i - \eta$ must be generated and compared to arrive at an appropriate solution (Chen, 1965). Unlike the previous three TLP current collection regimes, implementation of the cylindrical ABR equation in a TLP current-mode operation is somewhat more arduous. As such, it will not be considered as a viable option for TLP data reduction.

Neither OML nor ABR theory assumes collisions occur within the presheath region (OML doesn't even assume a presheath region exists.) and therefore they would not account for the reduction in particle flux due to particles colliding and exchanging momentum and energy such that their new trajectories cause them not to impinge on the probe (Evans et al., 2001). It is

therefore necessary to adjust for the changes in angular momentum for collisions based on a Maxwellian distribution and the appropriate collision rates.

A model for the absorption of an assumed monoenergetic species of plasma has also been developed by Bernstein & Rabinowitz extending from cylindrical probe collection theory from Laframboise, and has been appropriately denoted as BRL theory. Like the OML regime, BRL theory assumes conservation of angular momentum. As a result of the monoenergetic assumption, BRL theory consistently overestimates plasma number densities (Evans et al., 2001). The implementation of BRL theory towards electron parameter reduction will therefore not be used for the purposes of this research.

2.5.4 TLP Macroscopic Electron Parameter Data Extraction

As previously mentioned in Section 2.5.1, electron parameter extraction is performed by solving for the three unknowns $n_e(t)$, $T_e(t)$, and $\phi_{s1}(t)$ given experimentally obtained probe currents $I_1(t)$, $I_2(t)$, and $I_3(t)$ for a given time t. The solution can often be obtained using a Newton-Raphson solver based on an initial set of guesses. In the case of the thin sheath regime, the system of current collection equations is often rearranged to form the following two equations:

$$n_e = \frac{\dfrac{I_3 - I_2 \exp\left(-\dfrac{q}{kT_e}(\phi_{13} - \phi_{12})\right)}{\exp\left(-\dfrac{q}{kT_e}(\phi_{13} - \phi_{12})\right) - 1}}{A \exp\left(-\dfrac{1}{2}\right) q \sqrt{\dfrac{kT_e}{M_i}}}, \text{ and} \tag{2.62}$$

$$I^* = \frac{I_1 - I_2}{I_1 - I_3} = \frac{1 - \exp\left(-\frac{q}{kT_e}\phi_{12}\right)}{1 - \exp\left(-\frac{q}{kT_e}\phi_{13}\right)}. \tag{2.63}$$

This provides a computationally inexpensive way to solve for n_e and T_e and showcases the significance of the current ratio I^* (Gatsonis et al., 2004a).

To provide a self-consistent solution, it is also necessary to output the resulting r_p / λ_D values as a check method to ensure the TLP theory supplied an applicable set of plasma parameters. For program troubleshooting and trend analysis, solutions using all three TLP current collection regimes can be calculated and compared, along with their respective r_p / λ_D outputs. This method is also useful in determining which theory is applicable for most of the pulse.

2.5.5 TLP Macroscopic Electron Parameter Error Analysis

An uncertainty analysis of the experimental factors of TLP plume characterization is more than warranted by the dependence of all TLP theories of operation on numerous parameters and assumptions. It is therefore imperative to quantify the influence of both experimental and computational uncertainty associated with each parameter when eventually comparing the results obtained through each of the three TLP regimes (thin sheath, transitional, and OML). The applicability of each regime would subsequently be determined not only by the assumptions made a priori, but also by uncertainty mitigation. In other words, substantial uncertainties could yield the possibility that other TLP theories might also be applicable for a given data point. Formulation of expressions for the absolute uncertainties of the electron parameter unknowns

first requires listing the variables involved in each of the three systems of equations for TLP current collection. Following Gatsonis et al. (2004a),

$$I_1 = f_1(T_e, n_e, \phi_{s1}, r_p, L_\parallel, M_i), \tag{2.64}$$

$$I_2 = f_2(T_e, n_e, \phi_{s1}, r_p, L_\parallel, M_i, \phi_{12}), \tag{2.65}$$

$$\text{and } I_3 = f_3(T_e, n_e, \phi_{s1}, r_p, L_\parallel, M_i, \phi_{13}). \tag{2.66}$$

Full differentiation of equations (2.64), (2.65), and (2.66) yields the following non-linear system:

$$\frac{\partial f_1}{\partial T_e}\Delta T_e + \frac{\partial f_1}{\partial n_e}\Delta n_e + \frac{\partial f_1}{\partial \phi_{s1}}\Delta \phi_{s1} = -\begin{pmatrix} \frac{\partial f_1}{\partial M_i}\Delta M_i + \frac{\partial f_1}{\partial L_\parallel}\Delta L_\parallel \\ + \frac{\partial f_1}{\partial r_p}\Delta r_p \end{pmatrix} + \Delta I_1, \tag{2.67}$$

$$\frac{\partial f_2}{\partial T_e}\Delta T_e + \frac{\partial f_2}{\partial n_e}\Delta n_e + \frac{\partial f_2}{\partial \phi_{s1}}\Delta \phi_{s1} = -\begin{pmatrix} \frac{\partial f_2}{\partial M_i}\Delta M_i + \frac{\partial f_2}{\partial L_\parallel}\Delta L_\parallel \\ + \frac{\partial f_2}{\partial r_p}\Delta r_p + \frac{\partial f_2}{\partial \phi_{12}}\Delta \phi_{12} \end{pmatrix} + \Delta I_2, \tag{2.68}$$

$$\text{and } \frac{\partial f_3}{\partial T_e}\Delta T_e + \frac{\partial f_3}{\partial n_e}\Delta n_e + \frac{\partial f_3}{\partial \phi_{s1}}\Delta \phi_{s1} = -\begin{pmatrix} \frac{\partial f_3}{\partial M_i}\Delta M_i + \frac{\partial f_3}{\partial L_\parallel}\Delta L_\parallel \\ + \frac{\partial f_3}{\partial r_p}\Delta r_p + \frac{\partial f_3}{\partial \phi_{13}}\Delta \phi_{13} \end{pmatrix} + \Delta I_3. \tag{2.69}$$

The above differential equations have been arranged in such a manner so as to separate the unknown sensitivity coefficients on the left from the known uncertainty coefficients on the right (Gatsonis et al., 2004a). Numerically solving equations (2.67), (2.68), and (2.69) will produce values for ΔT_e, Δn_e, and $\Delta \phi_{s1}$ at each timestep. Further discussion of the uncertainty coefficients is contained in Chapter 3.

2.6 Quadruple Langmuir Probe Theory and Divergence Angle Considerations

Quadruple Langmuir probes (QLPs) make use of an additional cross-probe inserted perpendicular to the plasma flow direction and provide a time-resolved measurement of the ion speed ratio $S_i(t)$ in addition to the ion parameters obtained with the traditional TLP. The ion speed ratio is defined as the ratio of the ion mean (drift) speed $u_i(t)$ in the direction of plasma flow to the most probable thermal ion speed $C_{m,i}(t)$ as

$$S_i(t) = \frac{u_i(t)}{C_{m,i}(t)} \tag{2.70}$$

where

$$C_{m,i}(t) = \sqrt{\frac{2kT_i}{M_i}}\,. \tag{2.71}$$

Thus with information regarding the time-resolved ion temperature, one could also extract the time-resolved ion drift velocity (Kanal, 1964). As with the parallel probe wires, a bias voltage is applied between the cross probe and the parallel probe wire designated as probe wire 1. Unlike ϕ_{12} and ϕ_{13}, which cannot be equal, the unique orientation of the cross probe allows for either $\phi_{14} = \phi_{13}$ or $\phi_{14} = \phi_{12}$ for ease of implementation (Gatsonis et al., 2004). Note that it is not recommended to use the same exact voltage source (typically a common household battery) to provide the identical bias, but rather the *same type* of voltage source (i.e. two 9-V batteries each separately providing ϕ_{13} and ϕ_{14}). The current collection theory for a QLP manifests itself as an additional equation for the collected current of the cross probe denoted as I_4 and is given by Kanal (1964) as

$$I_4 = A_\perp J_{e0} \exp\left(-\frac{q(\phi_{s1} + \phi_{14})}{kT_e}\right) - A_\perp n_e q \left(\frac{kT_e}{2\pi m_e}\right)^{\frac{1}{2}} \frac{2}{\sqrt{\pi}} \exp(-S_i^2) \sum_{n=0}^{\infty} \left[\frac{S_i^n}{n!}\right] \Gamma\left(n + \frac{3}{2}\right) \tag{2.72}$$

Where the cross probe area is defined as

$$A_{\perp} = 2\pi r_p L_{\perp} + \pi r_p^2 \tag{2.73}$$

and the gamma function is defined as

$$\Gamma(x) = \int_0^{\infty} u^{x-1} e^{-u} du \,. \tag{2.74}$$

The cross probe current equation applies to both the transitional regime and the thin sheath regime of TLP operation. The ion speed ratio can either be solved for simultaneously with the other three unknowns (n_e, T_e, and ϕ_{s1}), or solved for after the TLP analysis has been performed using the secant method.

An analysis of plume divergence and its influence on ion number density dispersal and cross probe signal strength is required to determine the applicability of QLPs towards the characterization of small-scale plasma plumes. Figure 17 contains a diagram of a simplified arbitrary plume with relevant dimensions defined.

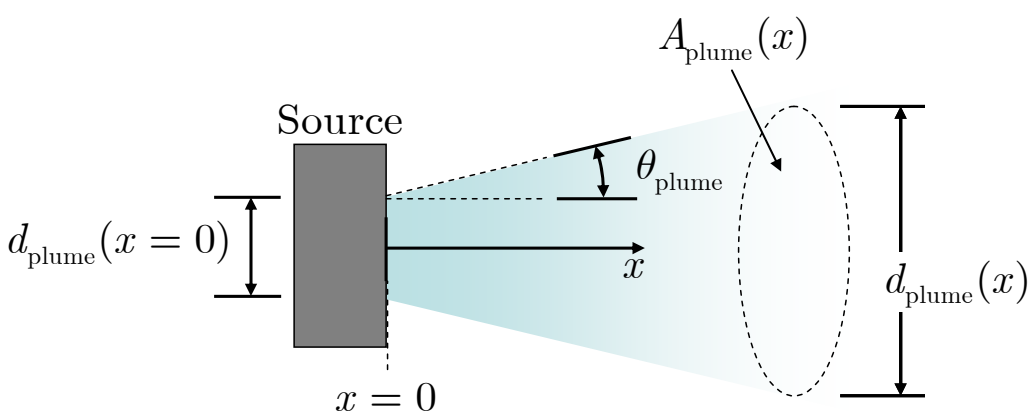

Figure 17. Small-scale plume divergence angle considerations.

This first order plume divergence study assumes most if not all plasma particles stay within the plume volume bounded by a given divergence angle θ_{plume}, which would certainly not be the

case in an actual plume. This approximation is made so that the diameter of the plume at a distance x from the thruster face can be defined as

$$d_{\text{plume}}(x) = d_{\text{plume}}(x=0) + 2x\cos(\theta_{\text{plume}}) \tag{2.75}$$

where $d_{\text{plume}}(x=0)$ is the initial plume diameter at the source exit plane. The plume area at a distance x from the thruster face can then be defined as

$$A_{\text{plume}}(x) = \pi\left(\frac{d_{\text{plume}}(x=0)}{2} + x\cos(\theta_{\text{plume}})\right)^2. \tag{2.76}$$

A first order approximation for the plume's ion or electron number density dispersal as a function of x can be made by taking the ratio of plume area at x to the plume area at the source exit plane as given by

$$\frac{n_{i,e}(x)}{n_{i,e}(x=0)} = \frac{A_{\text{plume}}(x)}{A_{\text{plume}}(x=0)} = \frac{\left(\frac{d_{\text{plume}}(x=0)}{2} + x\cos(\theta_{\text{plume}})\right)^2}{\left(\frac{d_{\text{plume}}(x=0)}{2}\right)^2}. \tag{2.77}$$

For plasmas with particularly small initial area with large divergence angles, the number density would clearly decrease rapidly as distance from the source is increased. Conversely, plumes with small initial area and relatively small divergence angles would maintain their number densities at greater distances from the source, but the overall plume size would not sufficiently increase, making spatial resolution an important factor when determining a diagnostic device's viability.

The spatial resolutions of Langmuir probes play an important role in determining their precision and applicability. Resolution is often defined as being inversely proportional to the instrument size, or in this case, the exposed probe wires. The largest distance between sheaths generated around separate probe tips in a particular direction represents the sample spacing, or

delta, of the instrument. A decrease in the probe delta would result in an increase in resolution. The ratio of a plasma diagnostic device's spatial resolution delta to the overall plasma plume size determines the applicability of the instrument.

Assuming that the QLP cross probe wire makes a perfect right angle with respect to the probe shielding, the deltas in the parallel plasma flow direction are the sum of the exposed parallel probe length and one sheath thickness, as given by

$$\delta_{\parallel,QLP} \approx \delta_{\parallel,TLP} = L_{\parallel} + \frac{(d_s - d_p)}{2}. \tag{2.78}$$

In reality, the cross probe wire can be difficult to bend at exactly a right angle. Therefore, the parallel QLP delta is usually slightly bigger than its TLP counterpart. Figure 18 shows TLP and QLP exposed probe tips as viewed from the plasma source (front view) in order to demonstrate their respective spatial resolution deltas in the direction perpendicular to the plasma flow.

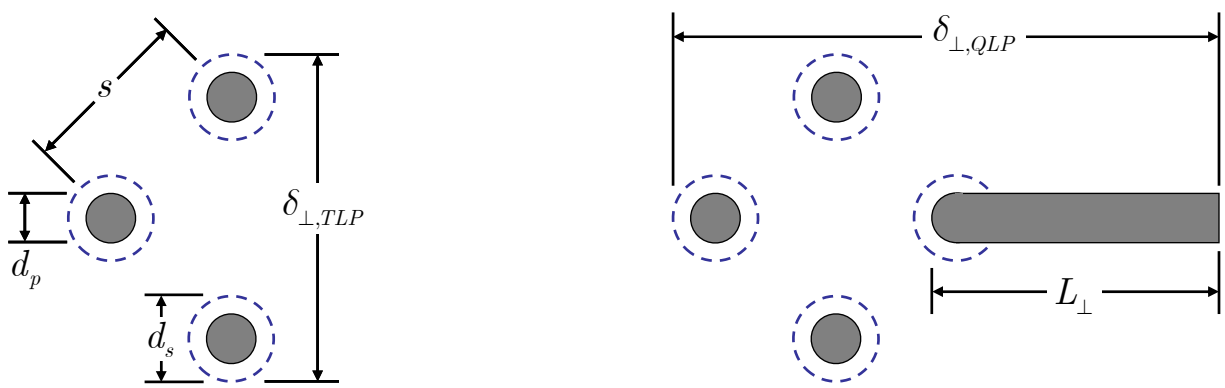

Figure 18. Spatial resolution deltas for the TLP (left) and QLP (right).

The perpendicular spatial resolution delta for a TLP is then given by

$$\delta_{\perp,TLP} = \frac{\sqrt{2}}{2} s L_{\parallel} + d_s. \tag{2.79}$$

The equivalent delta for a QLP would be a function of the perpendicular exposed cross probe length $L_{\perp}$ and is defined as

$$\delta_{\perp,QLP} = \frac{\sqrt{2}}{2} s + L_{\perp} + \frac{(d_s - d_p)}{2}. \tag{2.80}$$

For the QLP cross probe to collect a measurable current, often $L_{\perp} \geq L_{\parallel}$. This can result in a particularly large perpendicular QLP delta and a significant decrease in the overall spatial resolution of the instrument. From Figure 17, QLPs would clearly not be applicable towards small-scale plasmas with relatively small divergence angles and small initial plume areas (< 5 mm), as the QLP's spatial resolution would be insufficient. For a 2° plume divergence angle and a 1.0 mm initial plume diameter, a QLP with a cross probe length would not be applicable for probe-source distances of 11.4 cm. Additionally, relatively larger plume divergence angles would disperse the plasma such that the cross probe would collect a non-uniform current across its axis, introducing considerable measurement error. For example, a 45° plume divergence angle and a 1.0 mm initial plume diameter, a 5.0 mm long cross probe would only be contained in the plume for a probe-source distance greater than 3.2 mm, but at that point, the spatial resolution would still be on the order of the plume size. It is logical to conclude that QLPs are not applicable to small-scale plumes unless the initial plasma plume area at the source exit is significantly larger than the QLP perpendicular delta.

2.7 Retarding Potential Analyzer Current Collection Theory

Retarding potential analyzers (RPAs) are another useful diagnostic which allow for the extraction of macroscopic ion properties. From Section 1.5, RPAs employ a series of biased grids (electrodes) which filter out all electrons and low energy ions, allowing only ions with a certain minimum energy access to a collector plate (Partridge, 2006). The grid electric potential profile for a typical gridded or single-orifice RPA in a steady state plasma plume is illustrated in Figure 19. By varying the IRE potential and recording the current flowing to the collector plate

to counteract the impinging high-energy ions, one can generate an I-V curve, a direct demonstration of the ion energy distribution. Previous research with gridded energy analyzers has also included the maximization of IRE potential to repel all ions and the placement of a particle collector at the exit of the electrode series to measure the neutral particle flux (King & Gallimore, 1996). The slope, local maxima, and zero-voltage current value are indicative of the ion speed ratio, temperature, ion number density, and species concentrations (Kelley, 1989). In order to extract these parameters, it is first necessary to account for these relationships in a self-consistent and robust RPA set of current collection theories.

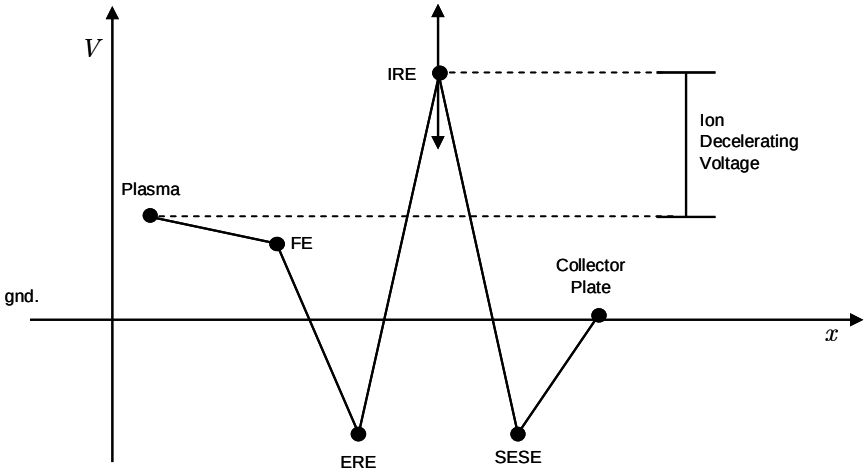

Figure 19. Potential profile for a traditional RPA with one ion retarding electrode in a steady plasma plume.

From Figure 19, obtaining an accurate assessment of the ion decelerating voltage would require a separate measurement of the plasma potential. As a best possible estimate, one may assume the measurement floating electrode potential approximates the plasma potential, but this would lead to significant uncertainty in the current collection theory error analyses, especially for small ion retarding electrode voltages.

RPAs have been established as a viable ion energy diagnostic both on the ground in vacuum chamber experimentation as well as aboard satellite and space shuttle diagnostic

packages. In situ RPAs aboard satellites have been used extensively to characterize relatively low density plasmas in the ionosphere. The sixth Orbiting Geophysical Observatory (OGO-6) mission employed a planar RPA to study the ion number density of multiple ion species within the magnetosphere (Hanson et al., 1973). A later iteration of the same planar RPA design was aboard the Atmosphere Explorer to yield ion mean velocity and temperature distributions (Heelis & Hanson, 1998). Shuttle missions STS-60 and STS-69 performed the Charging Hazards and Wake Studies (CHAWS) experiments, which contained a planar RPA with both a ram side electrode series and a wake series. The CHAWS experiments characterized the ion species present in low Earth orbit (LEO). Results were compared to 3-D hybrid Particle in Cell (PIC) simulations and preexisting LEO ion data to produce ion number density and temperature ranges as well as accurate values of LEO floating potentials (Giffin, 1996).

The one-dimensional analysis by Hutchinson (2002) previously defined in Section 1.5 demonstrates that space charge limitations occur between electrodes when the electrode spacing is more than four Debye lengths or when the grid or electrode entrance diameters exceed two Debye lengths. These limitations would most likely manifest between the ERE and the IRE where number density of both species are highest, thus contributing to the true ion decelerating voltage.

A more detailed investigation of space charge limitations involves an analysis of the longitudinal electric field of an energy analyzer as governed by the one dimensional Poisson's equation given as

$$\frac{\partial E_x}{\partial x} = qZ_i n_i \,. \tag{2.81}$$

Both the momentum equation and charge conservation equation are also required, given in SI units as

$$M_i c_i \frac{\partial u_i}{\partial x} = qZ_i E_x \tag{2.82}$$

$$\text{and } qZ_i c_i n_i = \text{constant}. \tag{2.83}$$

The combination of these equations yields

$$\frac{\partial^2 \phi}{\partial x^2} = -\frac{qZ_i n_i c_i}{\sqrt{c_i^2 - \frac{2Z_i q\phi}{M_i}}}, \tag{2.84}$$

where ϕ is the applied potential. A modified Debye shield length can then be written as

$$\lambda_0 = \sqrt{\frac{M_i c_i}{2n_i q^2 Z_i^2}}. \tag{2.85}$$

Integration of (2.84) and application of several boundary conditions based on an axial potential gradient from the spacing between grids L_{grid} ($\phi = 0$ at $x = 0$ and $\phi = \frac{M_i c_i^2}{2qZ_i}$ at $x = L$) yields the requirement of

$$L_{\text{grid}} < \frac{2}{3}\lambda_0$$

for the avoidance of significant space charges between electrodes (Green 1970). In essence, RPAs are susceptible to space charge limitations when the allowed beam diameter limited by the RPA entrance area is much greater than the electrode thicknesses and spacings.

As a direct result of these Debye length constraints, plasmas with ion number densities of $n_i \geq 5.0\text{x}10^{18}\ \text{m}^{-3}$ required using a novel single-orifice RPA design (Marrese et al., 1997). With each electrode consisting of a single small orifice, these Debye length constraints can be met, at the risk of low signal strength and the introduction of alignment problems. The single orifice RPA has the added benefit of increasing the spatial resolution by decreasing the entrance area diameter. For extremely high density plasmas ($n_i \approx 1.0\text{x}10^{20}\ \text{m}^{-3}$ or greater), the

aforementioned Debye length constraints oblige dimensions unrealistic of current manufacturing capabilities corresponding to $\lambda_D \approx 100\ \mu\mathrm{m}$. Electrical discharge machining (EDM) could be used to produce orifice diameters down to ~ 50 μm, except that consistently producing electrodes with orifice location precision within a tolerance of a few microns would not be feasible. One could assemble the electrodes with the insulating spacers between them, and EDM the channel, but the energy required to EDM through electrodes, which are typically made of molybdenum for its high work function to minimize secondary electron emission and maximize incident ion neutralization, is much greater than the energy it takes to melt insulating materials (typically Delrin, Teflon, or Nylon, as glass or silica is too brittle). Microelectromechanical systems (MEMS) fabrication of an RPA aperture is possible and has been investigated, but would be an extremely expensive alternative (Partridge, 2006). This method would entail deposition of alternating layers of conductive and insulating material on a substrate, save for the aperture channel area.

Hutchinson suggests that the reduction of ion number density can be achieved via the application of low transparency entrance slits or grids (2002). Microchannel plates (MCPs) are one example of these entrance slits, and are manufactured using laser machining, capable of channel diameters to less than 1 μm through thicknesses greater than 100 μm. Ideally, the desired reduction in flux is achieved by limiting the entrance surface area using a relatively thin orifice. Transparency would then be easily defined as the ratio of open entrance area to blocked area. Since no orifice is truly infinitely thin, a more realistic form of flux reduction is achieved by collimating the plasma using a longer channel, where the diameter to length ratio (aspect ratio) is closer to zero. The channel wall would neutralize nearly all ions which make contact with it, most of which are colliding with the walls because they are non-directional. That is, their

peculiar velocity is on the order of or greater than the species drift velocity, or perhaps they entered the channel close to a wall, and despite being mostly directional, the aggregate effect of a small peculiar velocity vector towards that wall resulted in relatively dominant neutralization. Regardless, the ion distribution which exits a long cylindrical channel is almost purely directional. This research assumes the RPA electrode series channel or grid series are aligned with the drift velocity vector (if not, a collimating tube would produce severe flux limitations).

Collimation occurs within single-orifice RPAs because the electrode spacing produces a non-zero channel length. Likewise, collimation occurs in MCPs. Previous theoretical investigation of these single-channel RPAs and their respective current collection theories was limited by the assumption that the exit plasma distribution remained Maxwellian in nature (Partridge 2006). Further considerations of cylindrical channel flux limitations, collimation, and the impact to ion energy distributions are discussed in Section 2.8.4.

2.7.1 Classical Retarding Potential Analyzer Current Collection Theory

To quantify the ion flux impingent upon an RPA collector plate resulting from a drifting Maxwellian plasma in the presence of an applied ion decelerating potential, it is first necessary to study the constituent effects of each of these assumptions. Starting with a stationary gas species or plasma with no applied potential, consider the flux through a surface element having unit normal vector $\hat{n}$. The number flux through that surface element is determined by integrating the distribution function of that species for all particles with a positive velocity in the $-\hat{n}$ direction (i.e. all particles in the green shaded portion of Figure 6.). After integration of (2.24), the resultant number flux for a stationary Maxwellian gas or plasma with no applied potential is then given by

$$\dot{N}_s = \frac{n_s}{2\beta\pi^{1/2}} = \frac{n_s c_s}{4}, \tag{2.86}$$

where c_s is the average thermal speed or standard deviation from zero of the species distribution and β is the inverse of the most probable velocity (Bird, 1994). This quantity is defined in Section 2.2. Next consider a stationary Maxwellian plasma in the presence of an applied potential ϕ_{eff}. This potential corresponds to an equivalent energy E_{eff}, which in turn corresponds to an equivalent particle velocity v_{eff} should the species mass be known. Once again modifying and integrating (2.24) as demonstrated by Partridge (2006), the particle number flux for a stationary plasma influenced by an applied potential becomes

$$\dot{N}_s = \frac{n_s \exp\left(-V^2\right)}{2\beta\pi^{1/2}}, \tag{2.87}$$

where $V = \beta v_{eff}$.

To account for the number flux of a drifting Maxwellian gas or plasma with no applied potential it is necessary to define the total velocity vector components used in the fluxal integration as a function of both the peculiar velocity components and the mean (drift) velocity components $\{u_0, v_0, w_0\}$. Assuming that the drift velocity vector lies entirely within the x-y plane and is at some angle θ with respect to $\hat{n}$, this yields total velocity components of

$$\begin{aligned} x&: \quad \mathrm{u} = U + u_0 = U + c_0 \cos\theta \\ y&: \quad \mathrm{v} = V + v_0 = V + c_0 \sin\theta \\ z&: \quad \mathrm{w} = W, \end{aligned} \tag{2.88}$$

which can then be used to integrate (2.24) for a given species s. The number flux for a drifting, Maxwellian gas or plasma with no applied potential becomes

$$\dot{N}_s = \frac{n_s}{2\sqrt{\pi}}\left[\frac{\exp(-\beta^2 c_{0s}^2)}{\beta} + c_{0s}\sqrt{\pi}\{1 + erf(\beta c_{0s})\}\right]. \tag{2.89}$$

The combined cases of a drifting Maxwellian plasma and an applied potential yields the final case, the number flux of which is derived as

$$\dot{N}_s = \frac{n_s}{2\pi^{1/2}}\left[\frac{\exp(-\beta^2(v_{eff}-c_{0s})^2)}{\beta} + c_{0s}\sqrt{\pi}\{1-\mathrm{erf}(\beta(v_{eff}-c_{0s}))\}\right]. \tag{2.90}$$

Multiplying (2.90) by the physical collector plate surface area and ion charge q (assuming all ions are positively, singly charged), the incident RPA collector plate current is defined as

$$I_{cp} = q\dot{N}_s A = \frac{qn_s A}{2\pi^{1/2}}\left[\frac{\exp(-\beta^2(v_{eff}-c_{0s})^2)}{\beta} + c_{0s}\sqrt{\pi}\{1-\mathrm{erf}(\beta(v_{eff}-c_{0s}))\}\right]. \tag{2.91}$$

For a multispecies plasma, the total collector plate current is given by a sum of the individual collector plate currents of each species, weighted by species concentration α_s as

$$I_{cp} = \sum_{s=1}^{n} q\dot{N}_s A = \sum_{s=1}^{n} \frac{q\alpha_s n_s A}{2\pi^{1/2}}\left[\frac{\exp(-\beta^2(v_{eff}-c_{0s})^2)}{\beta} + c_{0s}\sqrt{\pi}\{1-\mathrm{erf}(\beta(v_{eff}-c_{0s}))\}\right]. \tag{2.92}$$

The above expression is known as the classical gridded RPA current collection theory (Kelley, 1989). Note that these number fluxes could have also been derived in spherical coordinates, or any coordinate system for that matter, and have been proven to yield the same result (Partridge, 2006). Expressing these results in spherical coordinates aids in the eventual integration of these cases when also considering geometric flux limitations due to a collimating cylindrical channel, as seen in the next section.

The energy distribution can then be extracted from the slope of the I-V curve as stated by Burton et al. (2002) as

$$f(\phi_{eff}) = \frac{M_i}{Aq^2}\left(-\frac{dI_{cp}}{d\phi_{eff}}\right). \tag{2.93}$$

For the equivalent energy distribution, the effective ion decelerating voltage is converted to the equivalent energy defined as

$$E_{eff} = q\phi_{eff} = \frac{M_i v_{eff}^2}{2}, \tag{2.94}$$

which yields

$$f(E_{eff}) = \frac{M_i}{Aq}\left(-\frac{dI_{cp}}{dv_{eff}}\right). \tag{2.95}$$

Such that the derivative of the collector plate current can be calculated with respect to the equivalent velocity v_{eff} corresponding to the ion decelerating potential (Burton et al., 2002). Normalization of the ion energy distribution is often performed when comparing experimentally obtained energy distributions (Marrese et al., 1997).

2.7.2 Geometric Flux Limitations

The process of dividing each velocity by the most probable ion speed yields the velocity ratios illustrated in Figure 20 and is necessary to alleviate complications when integrating the number flux expressions in spherical coordinates (Partridge 2006).

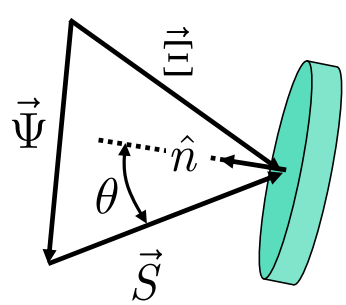

$$\vec{\Xi} = \vec{\Psi} + \vec{S}$$
$$\vec{\Xi} = \beta \mathbf{c}_s$$
$$\vec{\Psi} = \beta \mathbf{C}_s$$
$$\vec{S} = \beta \mathbf{c}_{0s}$$

Figure 20. Surface element velocity vector diagram and velocity ratio definitions.

For a single species gas or plasma with speed ratio S flowing through a right cylindrical channel of diameter d and length L, the number flux can be divided into two separate sub-species: Those which travel through the channel without making a collision with the channel wall and those which make their first collision with the channel wall between a normalized axial distance

measured from the entrance X and $X + dX$ (Patterson, 1971). These subspecies are denoted as N_{cc} and N_{cr}, respectively, and are illustrated in Figure 21. The diameter to length aspect ratio D is defined as

$$D = \frac{d}{L} \ . \tag{2.96}$$

Aspect ratios approaching $D \to \infty$ represent infinitely thin orifices while aspect ratios approaching zero represent long, directional tubes. Clearly N_{cc} will dominate for thin orifices while N_{cr} will dominate for directional collimators.

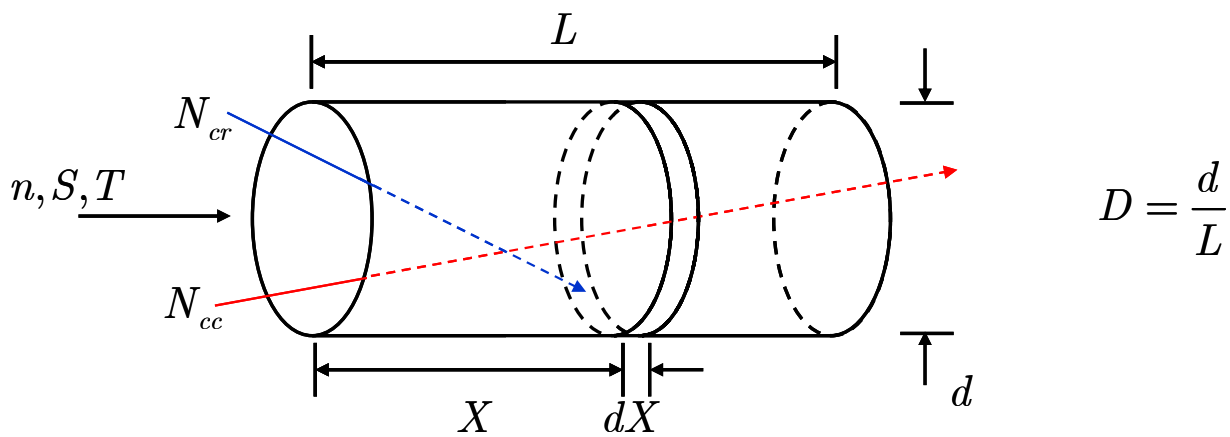

Figure 21. Cylindrical channel flux species classification.

The total number flux is then a function of the two subspecies, which are in turn functions of S, D, and X as given by

$$\dot{N} = N_{cc}(S,D) + \int_0^1 N_{cr}(S,X) w(X,D) dX \tag{2.97}$$

where $w(X,D)$ is the Clausing probability function and determines the rates at which particles are either absorbed or redistributed amongst the velocity classes (Clausing, 1932). Since an ion

making contact with a conductive channel wall will most likely be neutralized or otherwise absorbed, one can assume $w(X,D) \to 0$ leaving only the uninhibited number flux of

$$\dot{N} = N_{cc}(S,D). \tag{2.98}$$

For a neutral gas or a plasma not in the presence of an applied potential, the uninhibited flux is derived by Patterson (1971) for a Maxwellian plasma by integrating the distribution function over the angles required to ensure a particle would reach the channel exit for a given entrance point, and then integrating over the entire entrance area. Specifically, the fluxal quantity $\frac{nS}{\beta\pi^{3/2}}\exp\left[-\left(\Xi^2 - 2S\Xi\cos\varphi + S^2\right)\right]\Xi^3 d\Xi \sin\varphi\cos\varphi d\varphi d\theta dA$ must be integrated over all of the full range of normalized total speeds ($0 \le \Xi \le \infty$), the inlet area, and the outlet area. Based on an $\{x,y,z\}$ coordinate system, the angles of integration are defined in and , where the outlet area integration is performed using the bounds $0 \le \varphi \le \varphi_1$ and $0 \le \theta \le 2\pi$. It then becomes necessary to define an alternative two dimensional coordinate system $\{y',z'\}$ which is rotated from the absolute system by the angle θ. With the definitions of $dA = dy'dz'$ and $z' + \tau_1 = \sqrt{r^2 - y'^2} = a$, integration over z' with constant y' is performed from $-a \le z' \le a$, $0 \le \tau_1 \le 2a$, and $0 \le \varphi_1 \le \tan^{-1} 2a/L$ since $dz' = d\tau_1 = -L\sec^2\varphi_1 d\varphi_1$.

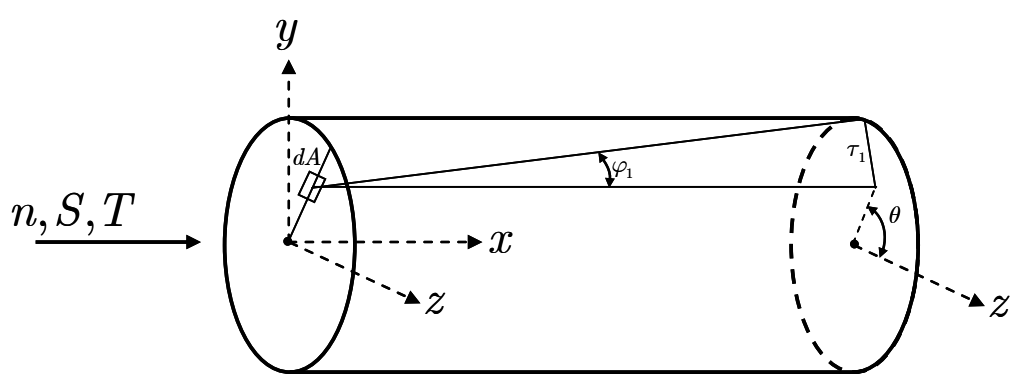

Figure 22. Exit flux integration angle definitions for a cylindrical channel (adapted from Patterson, 1971).

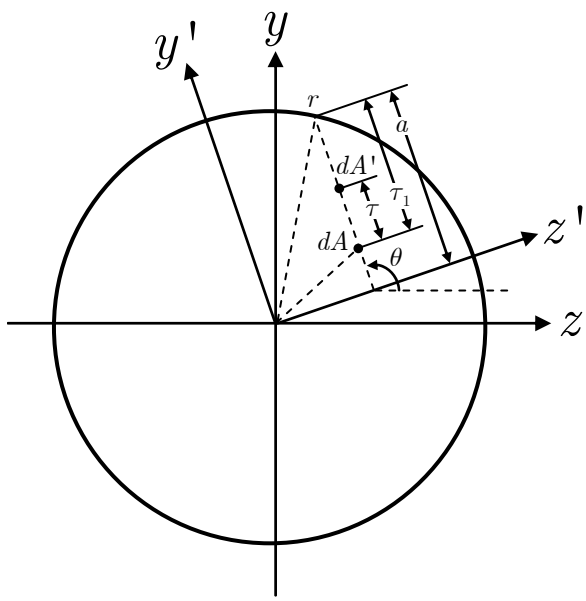

Figure 23. Integration bounds defined on a superimposed entrance and exit plane of a cylindrical channel (adapted from Patterson, 1971).

Integration over y' is then performed over the normalized parameter $Y = y'/r$ over $-r \le y' \le r$ with the substitution $dy' = rdY$. This results in the expression

$$N_{cc}(S,D) = \frac{nC_m}{2\sqrt{\pi}} 2rL \int_0^1 dY \int_0^{\tan^{-1} D\sqrt{1-Y^2}} \frac{d\varphi_1}{\cos^2\varphi_1} \Big\{ \exp(-S^2)\sin^2\varphi_1 + S\sqrt{\pi}(1+\mathrm{erf}S) - \big[S\sqrt{\pi}1 + erf(S\cos\varphi_1)\big]\cos^3\varphi_1 \exp(-S^2\sin^2\varphi_1) d\varphi_1 \Big\} . \tag{2.99}$$

Only the first and second terms of the integrand can be integrated analytically. The resultant expression becomes

$$N_{cc}(S,D) = \frac{nC_m}{2\sqrt{\pi}} \pi r^2 \left[\chi(S) - \Psi(D)\exp(-S^2) - \frac{4S}{\sqrt{\pi}} \eta(S,D) \right] \tag{2.100}$$

where

$$\chi(S) = \exp(-S^2) + S\sqrt{\pi}(1 + erf(S)), \tag{2.101}$$

$$\Psi(D) = \frac{2}{D^2}\left(\sqrt{1+D^2} - 1\right), \tag{2.102}$$

and $\eta(S,D) = \frac{1}{D}\int_0^1 dY \int_0^{\tan^{-1} D\sqrt{1-Y^2}} [1 + erf(S\cos\varphi)]\cos\varphi \exp(-S^2 \sin^2\varphi) d\varphi$. (2.103)

An additional method was also established using beamlet integration, the numerical results of which are identical to those of Patterson for a given test case (Hughes & de Leeuw, 1965). For an ion species influenced by an applied potential, it is necessary to reintegrate the number flux to account for the updated integrand and bounds of integration. The expression with rearranged bounds which facilitate complete integration is given by:

$$N_{cc} = \frac{n_s}{\beta\pi^{3/2}} \int_0^1 \int_0^{\arctan\left(D\sqrt{1-Y^2}\right)} \int_0^{\zeta} \int_{Veff/\cos\theta}^{\infty} \Xi^3 \cos\theta \exp(-(\Xi^2 + S^2 - 2\left|\vec{\Xi}\right|\left|\vec{S}\right|\cos\theta)) \sin\theta d\Xi d\theta d\zeta dY ,$$

(2.104)

where Y and ζ are bounds of integration based on entrance location and uninhibited exit angle definitions by Patterson (1971). Integration of all but the final bound yields

$$N_{cc} = \frac{2nrl}{\sqrt{\pi}\beta} \int_{0}^{\arctan(D)} \left(\frac{\tan(\phi)}{2\mathrm{D}} \sqrt{D^2 - \tan^2(\phi)} - \tan(\phi)\sqrt{D^2 - \tan^2(\phi)} \right)$$

$$\tan(\phi)\exp\left(\frac{-V^2 - 2S^2\cos^2(\phi) + S^2\cos^4(\phi)}{\cos^2(\phi)} \right)$$

$$\left[\begin{array}{l} \cos^2(\phi)\exp(2VS + S^2 - S^2\cos^2(\phi)) \\ +S\cos^2(\phi)\exp(2VS + S^2 - S^2\cos^2(\phi)) \\ +V^2\exp(2VS + S^2 - S^2\cos^2(\phi)) \\ +S^2\cos^4(\phi)\exp(2VS + S^2 - S^2\cos^2(\phi)) \\ +\frac{3}{2}\sqrt{\pi}S\cos^3(\phi)\exp\left(\frac{V^2 + S^2\cos^2(\phi)}{\cos^2(\phi)} \right) \\ +S^3\sqrt{\pi}\cos^5(\phi)\exp\left(\frac{V^2 + S^2\cos^2(\phi)}{\cos^2(\phi)} \right) \\ -S^3\sqrt{\pi}\cos^5(\phi)\exp\left(\frac{V^2 + S^2\cos^2(\phi)}{\cos^2(\phi)} \right) erf\left(\frac{V - S\cos^2(\phi)}{\cos(\phi)} \right) \\ -\frac{3}{2}\sqrt{\pi}S\cos^3(\phi)\exp\left(\frac{V^2 + S^2\cos^2(\phi)}{\cos^2(\phi)} \right) erf\left(\frac{V - S\cos^2(\phi)}{\cos(\phi)} \right) \end{array} \right] d\phi. \tag{2.105}$$

The quantities of $erf\left(\frac{V - S\cos^2(\phi)}{\cos(\phi)} \right)$ in the last two terms cannot be integrated analytically by standard math solvers and therefore the entire expression must be numerically integrated for specific values of ion speed ratio S, voltage ratio $V = V_{eff}$, and aspect ratio D (Partridge, 2006). This expression is known as the Maxwellian ion number flux for a collimating cylindrical channel with an applied voltage. It is most applicable to the SC-μRPA design type, which consists of a series of electrodes, each of which has a small single orifice drilled through it and aligned with the other electrodes. In effect, collimation and retardation of the ions is performed simultaneously.

2.7.3 Single- and Multi-channel Retarding Potential Analyzer Current Collection Theory

The two distinct, collimating RPA design types developed for this research attempt to avoid space charge limitations by decreasing the ion number density within the grid series using two types of collimators. The resultant collimating RPAs have a set of relaxed Debye length constraints within the grid series. One design employs a single collimator and has been termed the single-channel RPA (SC-RPA), while the other design makes use of a microchannel plate consisting of multiple collimators and has been termed the multi-channel RPA (MC-RPA). The schematics of these designs are illustrated in Figure 24. Also note that when the collimators are of sufficiently small diameter, the design is termed a multi-channel μRPA or MC-μRPA.

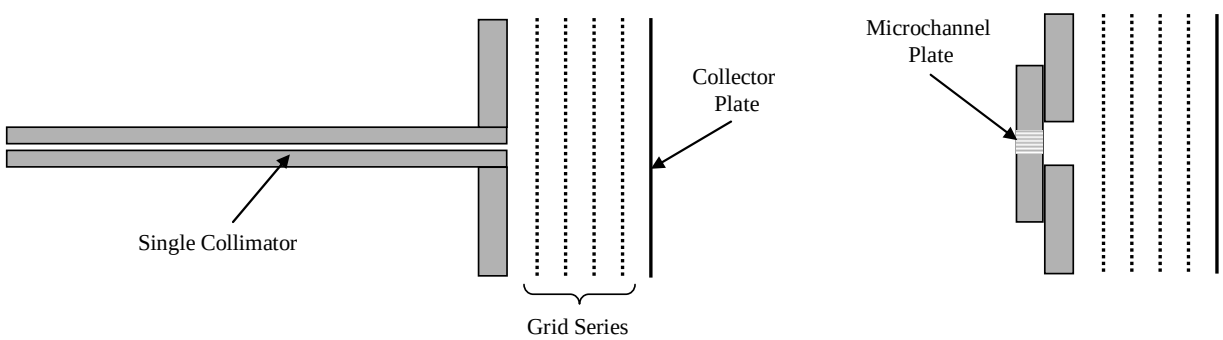

Figure 24. Schematic of the single-channel RPA design (left) and the multi-channel μRPA design (right).

With the definition of the collimating number flux from (2.105), the fraction of ions exiting a given collimator is simply defined as the ratio of the number of ions that exit the channel to the number of ions that entered the channel. This quantity is termed the collimating transmission fraction χ_{C} as

$$\chi_{\mathrm{C}}(S,D) = \frac{N_{cc}(S,D)}{N_{cc}(S,\infty)}. \tag{2.106}$$

Note that χ_{C} is not only dependent upon the collimator geometry but also upon the ion drift velocity, the macroscopic ion temperature, and the assumed ion Maxwellian distribution

function. It is therefore not possible to define a universal collimator transmission fraction for a given geometry *without also knowing* the ion speed ratio. Subsequently, different classes of ion velocities will respond differently to the collimation. For a given aspect ratio, high energy particles will be affected minimally, while more of the low energy particles will be absorbed, as shown in Figure 25. The effects of plasma expansion within the collimator are assumed negligible over the distance of the collimators, although some expansion may occur due to charge separation effects in the assumed collisionless plasma. Charge separation would cause the ions to expand away from each other, but this effect would be somewhat reduced by the presence of electrons in the collimator. Thermal expansion due to a plasma emanating from a point source and flowing into a low-pressure vessel presents only minimal adverse effects as compared to the adiabatic flow assumed for the baseline channel flux model (Engeln et al., 2002). The electric field of an ion front would also be only slightly greater than the nominal field, resulting in free plasma expansion which would only slightly increase ion collimation throughout the channel (Mora, 2003). Since it is hypothetically possible for ions in a small but positive velocity class to still make it through a channel uninhibited (i.e. compared to the particle's axial velocity component, its two other velocity components happen to be negligible and/or the ion enters at the center of the entrance orifice), the collimating transmission fraction approaches zero for low velocities but never reaches it until negative velocity classes are considered. Although, since Figure 25 is plotted in terms of total unique velocity and not total axial velocity, it is technically possible for a particle to have a net negative velocity but also traverse the channel uninhibited. This would occur for relatively shallow channels ($D \rightarrow 0$) if and only if the net velocity components of the particle summed to be negative, but the axial velocity component was positive and large enough such that the particle still made it through

without absorption. For simplicity it is assumed that all particles with negative unique velocity are absorbed.

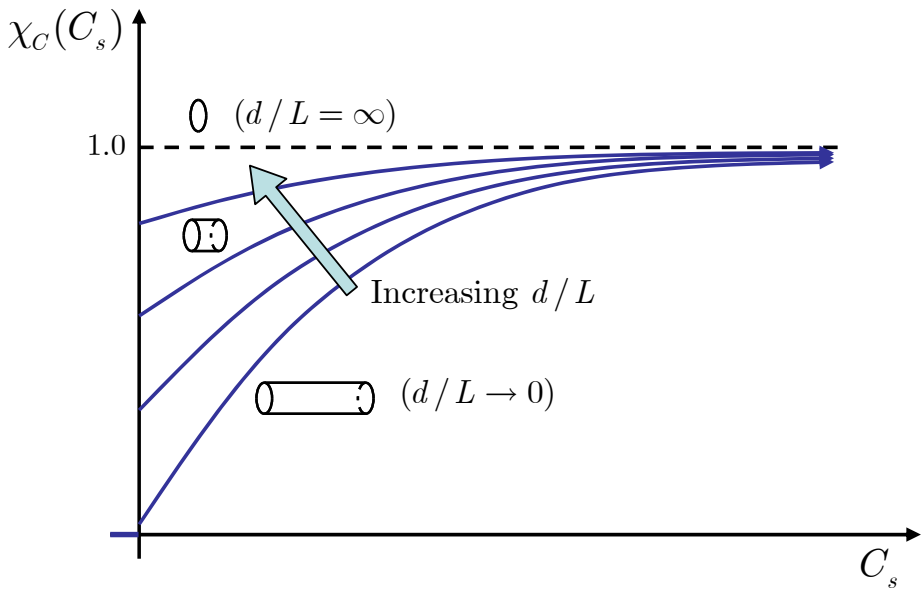

Figure 25. Collimating transmission fraction as a function of velocity class.

Conversely, the collimating transmission fraction asymptotically approaches 1.0 at the high energy tail of the distribution but never reaches it, because despite the directionality of the high energy ions, the case can be made that at least one of them has a comparable velocity component towards a given azimuthal section of the channel wall. Should the ion enter the channel near this section of the wall it may be absorbed, contributing to a transmission fraction decrease. The physical presence of these ions is statistically minimal (as is the contribution of the extreme low energy ions). A quantitative analysis of collimating transmission fraction as a function of ion speed ratio and various channel geometries is depicted in Figure 26. This analysis assumed a Maxwellian ion species with zero channel wall potential and that the collimator was aligned with the plasma flow (i.e. $\alpha = 0^{\circ}$).

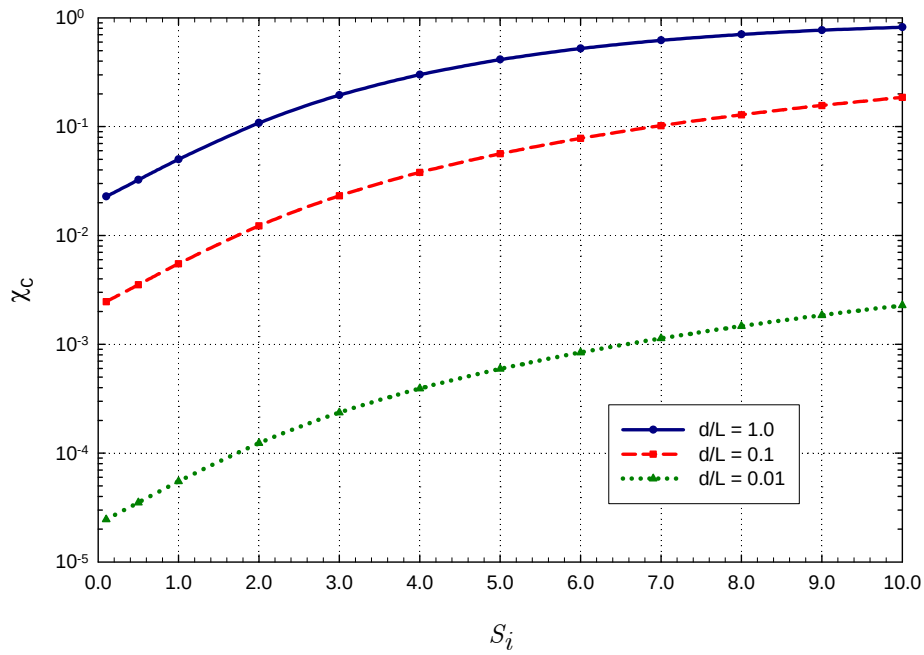

Figure 26. Collimator transmission fraction as a function of speed ratio and collimator geometry.

In the case of relatively low speed ratios, collimation can clearly provide a severe reduction in exit number flux as evidenced by transmission fraction values of $\chi_C \sim 10^{-5}$ for channel diameter to length ratios approaching 100. A positive channel wall potential would further reduce the ion number flux at the exit. The angle between the collimator's axial vector and the average plasma flow α also has a significant influence on the collimator transmission fraction (Maynard, 1996). Figure 27 shows the calculated transmission fractions for a cylindrical channel with diameter to length ratio of 0.1. For a given alignment angle and channel geometry, there exists a speed ratio at which the transmission fraction is maximized. As an example, transmission fraction is maximized for a channel with diameter to length ratio of 0.1 and an alignment angle of $\alpha = 10^{\circ}$ when the speed ratio is approximately $S_i \approx 6.0$ as evidenced in Figure 27. Below this speed ratio, the particles tend to be absorbed because their thermal velocities are comparable to the mean species velocity and the channel geometry is such that they would be absorbed anyways regardless of channel angle. Passing above this speed ratio, the

combination of the non-zero alignment angle and the overall drift velocity being considerably greater than the individual ions' peculiar velocities causes more and more ions to travel directly towards one side of the channel wall and be absorbed.

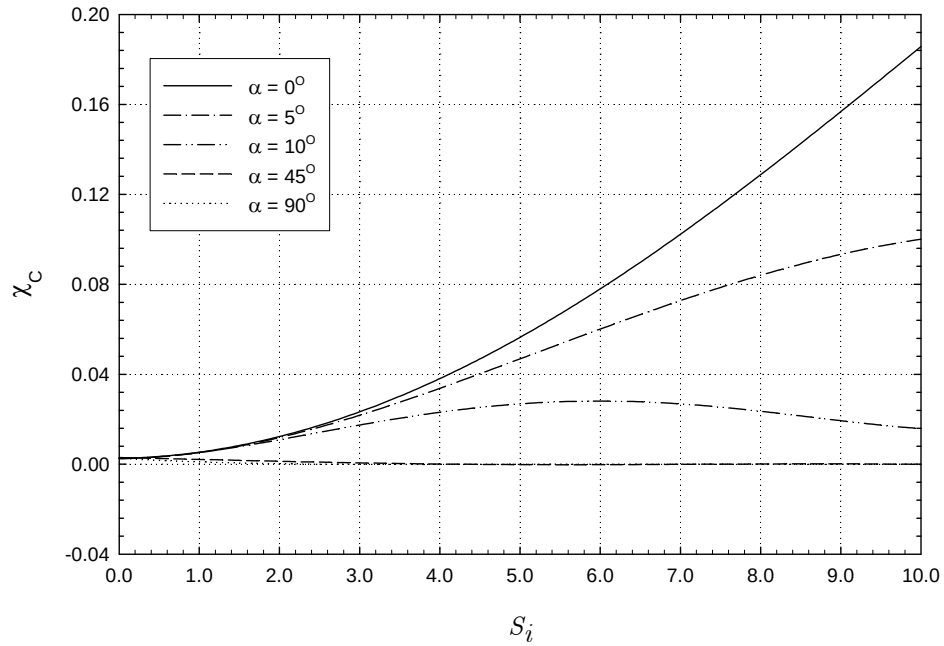

Figure 27. Collimator transmission fraction as a function of speed ratio and collimator-plasma flow alignment angle (assumes d/L = 0.1).

The nonlinearity in the transmission fraction for collimating tubes clearly suggests that the resulting distribution of ions exiting a collimator is no longer Maxwellian. This assumption is discussed in the next section and has serious implications towards the ability to reliably extract macroscopic ion properties from collimating RPA data. Single-orifice RPA current collection theory operated on the somewhat-valid assumption that the electrode series provided both the collimating and ion repelling in a self-consistent manner. The only inaccuracy resulted from the fact that the collimator was not at a uniform applied potential (Partridge, 2005). Previous MC-RPA current collection theory development defined the MCP transmission fraction as

$$\chi_{\mathrm{MCP}}(S,D) = \mathrm{N}_{\mathrm{MCP}} \frac{N_{cc}(S,D_{\mathrm{MCP}})}{N_{cc}(S,\infty)}, \tag{2.107}$$

where N_{MCP} is the number of channels. An approximation of the collimating current collection theory assumes that the exiting microchannel ion flux is still Maxwellian as it enters the grid series, allowing for the combination of the classical RPA current collection theory with the MCP transmission fraction as:

$$I_{cp} = \chi_{\mathrm{MCP}} qAN_i = \chi_{\mathrm{MCP}} \frac{qAn}{2\pi^{3/2}} \left[\frac{\exp(-\beta^2 (v_{eff} - c_0)^2)}{\beta} + v_{dr}\sqrt{\pi}\{1 - \mathrm{erf}(\beta(v_{eff} - c_0))\} \right]. \quad (2.108)$$

This assumption is known as the separation approximation, since one is essentially decoupling the flux limitations which are so clearly dependent on one another. The separation approximation could also be extended to the general collimating case as:

$$I_{cp} = \chi_{\mathrm{C}} qAN_i = \chi_{\mathrm{C}} \frac{qAn}{2\pi^{3/2}} \left[\frac{\exp(-\beta^2 (v_{eff} - c_0)^2)}{\beta} + v_{dr}\sqrt{\pi}\{1 - \mathrm{erf}(\beta(v_{eff} - c_0))\} \right]. \quad (2.109)$$

The accuracy of the separation approximation increases as the channel aspect ratio also increases. Recall that it also requires a value for the ion speed ratio and numerical integration to determine the transmission fraction.

The flux limitation effect of the grid series is assumed to be cumulative based on an allowable entrance area fraction and manifests itself within the RPA area considered. Collimation effects through each grid are assumed to be negligible.

2.7.4 Collimating Retarding Potential Analyzer Current Collection Theory

The most crucial assumption to classical RPA current collection theory is that the distribution of plasma incident to the electrode series is of a Maxwellian distribution. Unfortunately, collimation of the plasma prior to the electrode series will most certainly produce a non-Maxwellian plasma, as illustrated in Figure 28. Most of the high energy particles will make it through the channel, while the fraction of particle transmission per velocity class will

non-linearly decrease as velocity class is decreased. Particles having a negative velocity would not make it through the channel. These distribution plots assume collisionless plasma, but even with the presence of collisions redistribution of the collimated particles towards a more Maxwellian distribution would still be negligible. For channels approaching a thin orifice aspect ratio (diameter to length ratios approaching zero) or for particle distributions with a relatively small mean axial velocity component, the total velocity vector minimum could also be negative.

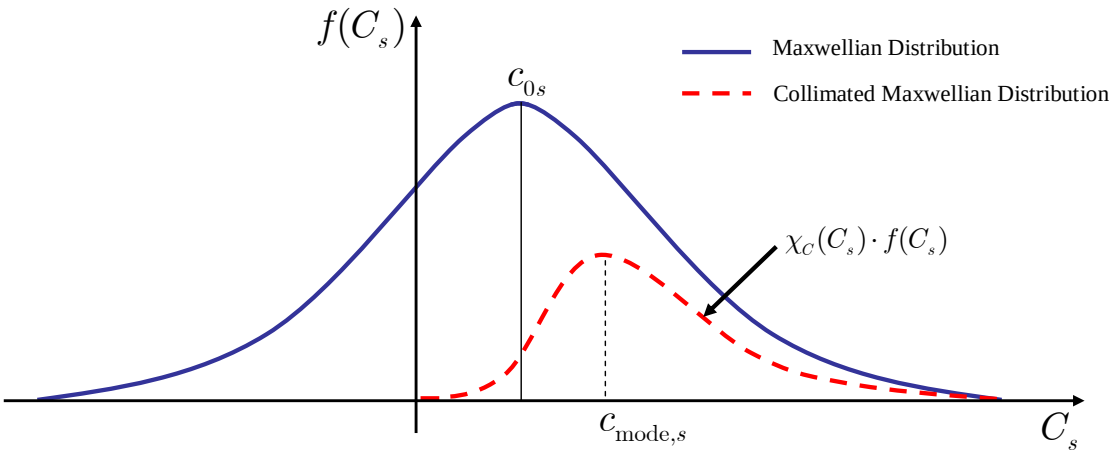

Figure 28. Maxwellian distribution function of particles and its collimated counterpart.

Again, the two distribution functions approximate each other at the high energy tail because most of those particles traverse the channel without being absorbed by the channel wall. Like the Maxwellian distribution, the collimated Maxwellian distribution of particles is unimodal, except that the new mode velocity $\mathbf{c}_{\mathrm{mode}}, s$ is no longer equal to the drift velocity. The distribution is no longer symmetric about c_{0s}, and depending on speed ratio, applied potential, and aspect ratio of the channel this collimation could severely impact the accuracy of any data extraction methods operating under the assumption that the incident plasma to the electrode series is still Maxwellian in nature. Additionally, the change to a plasma species collimation distribution would be even more drastic if an electrical potential were applied to the cylindrical channel wall.

A non-Maxwellian ion species generated by a collimating-gridded RPA hybrid would have drastic implications to the resulting I-V curves. Particularly, low effective ion retarding potentials corresponding to ion velocities less than the minimum collimating distribution velocity would have little to no effect on the collector plate current. Save for slowing down the rest of the particles so that slightly more of them would impinge on the grid material, the collector plate current would remain constant with increasing ion retarding potential as in the figure below. For the general case with a given channel geometry, a collimated Maxwellian distribution would generate a mostly horizontal I-V curve, as shown in Figure 29. Should a positive potential be applied to the collimator channel wall (i.e. the collimator is no longer left floating, or if the RPA has a single channel electrode series), the collector plate current would reach the zero at a lower effective ion retarding potential. This is because the biased channel wall would cause the ions to decelerate, thus increasing the amount of collimation and reducing the overall collector plate current. A purposefully segmented, or biased, channel wall could also then be used to further repel either electrons or ions as needed. However, the current collection theory for a segmented channel is relatively cumbersome (Partridge, 2005). Direct Simulation/ Monte Carlo (DSMC) modeling of the channel flow could also provide insight into the behavior and sensitivities of ion distributions within both unsegmented and segmented channels, and would serve to validate the aforementioned theories.

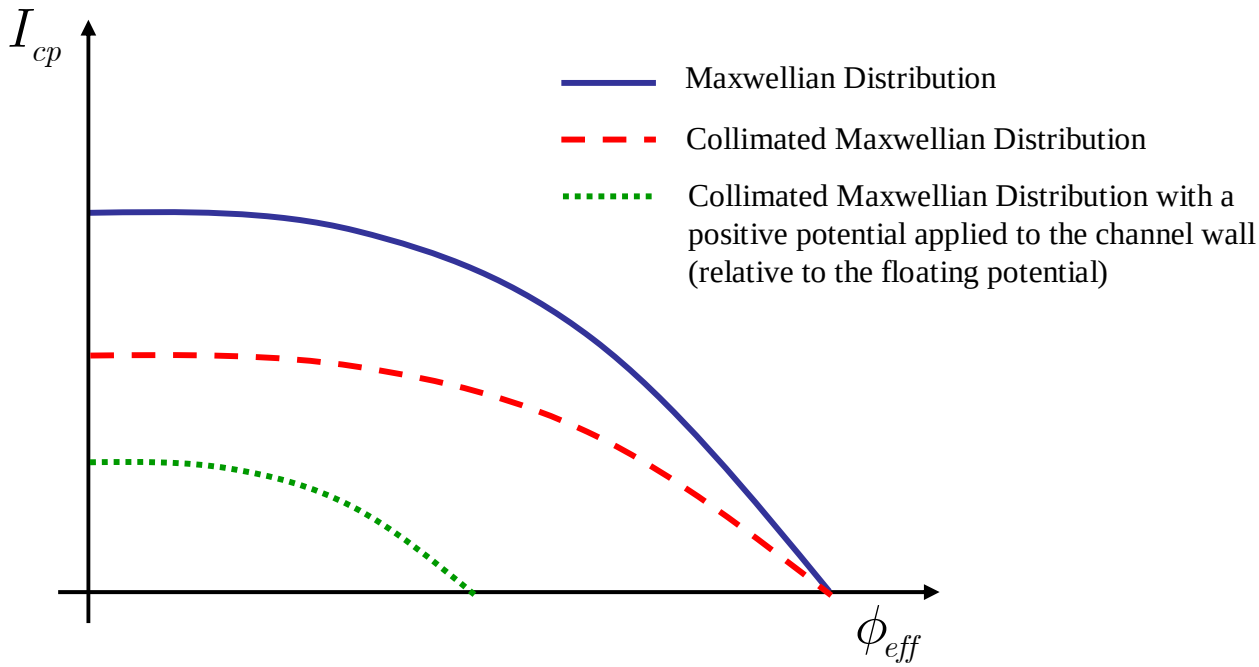

Figure 29. I-V curve trends for a Maxwellian distribution and its collimated equivalent.

The zero voltage value of the "horizontal" portion of the collimated RPA collector plate current would also be significantly less than the zero voltage value of its Maxwellian equivalent. Applying standard ion parameter extraction methods (IPEM) such as the nonlinear least-square method (NLSM) would result in significant error (Partridge, 2006). For example, since the zero voltage value of the collector plate current is directly proportional to ion number density, NLSM using the classical RPA current collection theory with an assumed speed ratio would yield a severely underestimated ion number density. Development of an IPEM suitable for collimating RPAs is discussed in Section 2.8.5.

2.7.5 Treatment of I-V Curves Generated from Unsteady Plasmas

Extension of traditional I-V curve data collection for steady sources for application to unsteady plumes requires the repeated measurement of time-resolved collector plate current traces for each ion retarding potential. This process results in the population of a 3D surface plot of I-V-t curve data, as shown in Figure 18. Typically each time-resolved current trace for a given effective ion retarding potential is an average of five to ten individual thruster firings. This minimizes shot to shot variances in both current magnitude and time and allows for smoother data reduction, the details of which are discussed in the next section. Analyzing every point on the 3D I-V-t surface tends to be rather cumbersome. Assuming a unimodal pulse for each I-V-t trace, a commonly applied simplification method involves taking the maximum current of each I-t trace to generate a standard maximum I-V curve (Shumlak et al., 2003). However, inconsistencies arise when the maximum of each trace does not occur at the same time. One could also take the maximum current value of the entire I-V-t surface plot, and use the time at which it occurs to produce a time-consistent I-V curve.

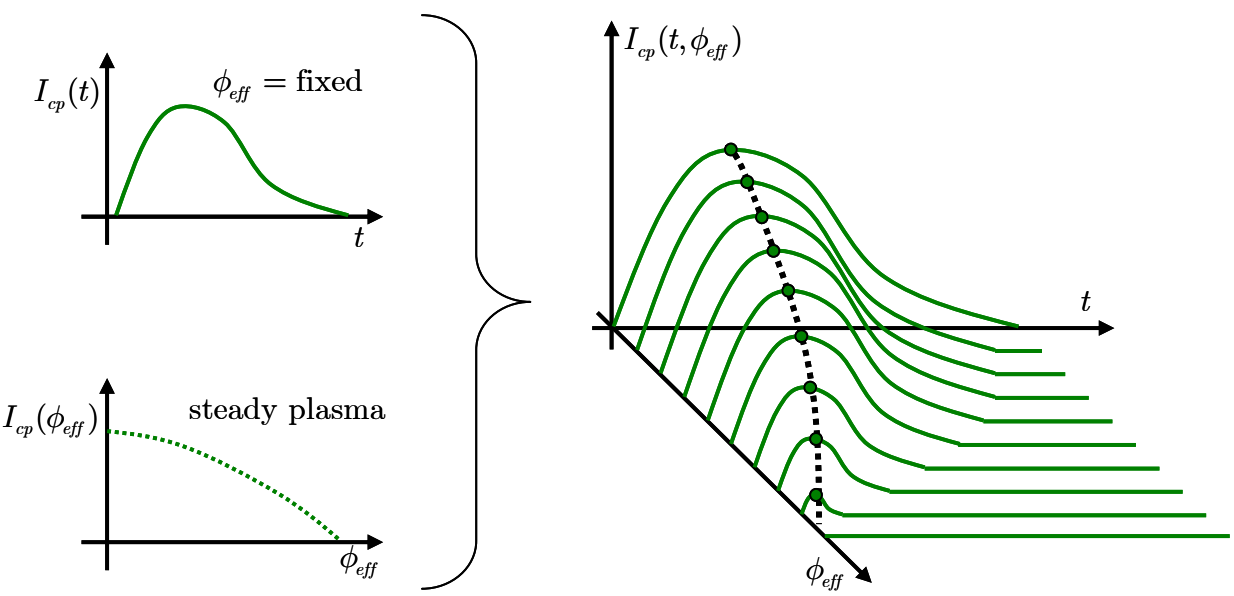

Figure 30. Surface plot representation of an unsteady series of I-V curves.

The observed change in floating potential of unsteady plasmas also has a significant effect on the resultant I-V-t surface plot. Recall from Figure 19 that the effective ion retarding potential is equal to the difference between the applied ion retarding potential and the measured plasma potential (i.e. the ion decelerating voltage). The ability of the IRE to effectively repel ions is measured as the floating potential approaches the ion retarding potential, as shown in Figure 31. Positive shifts in floating potential would bend the I-t curves towards the negative V direction. Additionally, ϕ_{IRE} may have a transient component as a result of EMI noise or space charge-limiting occurring at the IRE itself. Although the measured floating electrode potential is the best approximation for the plasma space potential, the assumption that the measured floating electrode potential approximates the actual plasma space potential becomes less valid for large ion temperatures or large speed ratios. Therefore, particular emphasis on the I-V curve data at large applied ion retarding electrode potentials becomes necessary.

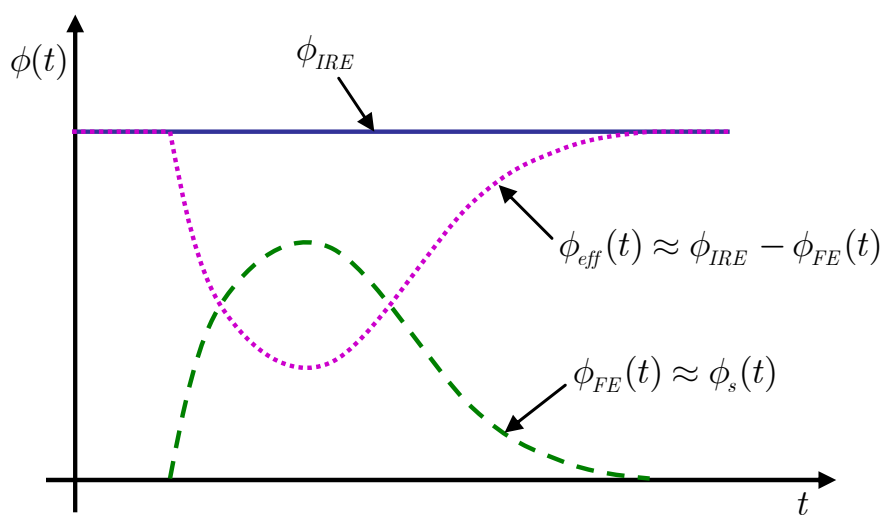

Figure 31. Effective retarding potential as a result of an unsteady floating or space potential.

Reduction of I-V-t data after the subtraction of floating potential can often yield misleading results, as the floating potential may even be greater than the IRE voltage. Previous RPA characterization of an unsteady plume kept maximum I-V plots as a function of ion retarding

potential to avoid these complications (Shumlak et al., 2003). Sweeping at higher IRE potentials ensures that an adequate range of effective potentials are reached. RPA measurements are usually validated by finding the minimum IRE potential which produces a negligible signal anyways, so the problem of ensuring a large enough potential range is often avoided. This process ensures that the IRE potential is correctly applied and that all electronics are functioning properly.

2.7.6 RPA Macroscopic Ion Parameter Extraction from I-V Curve Data

The relative simplicity of the classical RPA current collection theory allows for the extraction of ion density, temperature, drift velocity, and species concentrations via an iterative nonlinear least squares (NLSA) method. These parameters are calculated for each individual species' distribution function (Shumlak et al, 2003). As for the specific case of the classic RPA current collection theory, the general function $f(x;\lambda_1,...\lambda_n)$ becomes $I_{cp}(v_{eff};n,c_0,\beta)$ where

$$\beta = \sqrt{\frac{M_i}{2kT_i}}\,. \tag{2.110}$$

Typically, since the inverse of the most probable ion velocity $C_{m,i}$ is a function of the ion temperature T_i, β is considered as the third λ parameter until convergence for simplicity. The $\mathbf{A}$ matrix is of the form

$$\mathbf{A} = \begin{bmatrix} \left.\frac{\partial I_{cp}}{\partial n}\right|_{v_{eff,1},\lambda} & \left.\frac{\partial I_{cp}}{\partial c_0}\right|_{v_{eff,1},\lambda} & \left.\frac{\partial I_{cp}}{\partial \beta}\right|_{v_{eff,1},\lambda} \\ \vdots & \vdots & \vdots \\ \left.\frac{\partial I_{cp}}{\partial n}\right|_{v_{eff,m},\lambda} & \left.\frac{\partial I_{cp}}{\partial c_0}\right|_{v_{eff,m},\lambda} & \left.\frac{\partial I_{cp}}{\partial \beta}\right|_{v_{eff,m},\lambda} \end{bmatrix}, \tag{2.111}$$

where Gaussian elimination is performed on the matrix equation

$$\mathbf{A}^{\mathrm{T}} d\vec{x} = (\mathbf{A}^{\mathrm{T}}\mathbf{A}) d\vec{\lambda}\,. \tag{2.112}$$

Solving for $d\vec{\lambda}$ and applying it to the λ parameters allows for calculation of the next $d\vec{x}$, as outlined in more detail by Partridge (2006). This process is repeated until a specified minimum acceptable value for either $d\vec{\lambda}$ or $d\vec{x}$ is reached (Bevington, 1969). This process is looped until the sum of the least squares residuals R^2 reaches a desired convergence value, defined as

$$R^2 = d\vec{x} \cdot d\vec{x}\,. \tag{2.113}$$

A robust method for estimating the ion number density is based on the number flux analysis for a drifting Maxwellian plasma through an unbiased surface element. In this case, the drift velocity, grid entrance area, and collector plate current at a negligible effective ion retarding potential must be known, yielding

$$n_i = \frac{I_{cp}(\phi_{eff} = 0)}{qAc_0}\,. \tag{2.114}$$

Similarly, in the case of collimation,

$$n_i = \frac{I_{cp}(\phi_{eff} = 0)}{qA\chi_C c_0}\,. \tag{2.115}$$

It should be noted that the grid entrance area already accounts for the transparency of the overall grid series.

Previous methods developed for single-channel μRPAs involved the implementation of fuzzy logic rules to create a convergence program. Known as the ion parameter extraction method (IPEM) program for SC-μRPAs, it is effectively an elaborate I-V curve generation and comparison program. This process was necessitated by the fact that the SC-μRPA current collection theory of (2.105) must be integrated numerically. The 'reversal' of this current collection theory must therefore involve an iterative guess and check system or a set of look-up

tables. The IPEM program starts with initial guesses for the ion parameters, generates an I-V curve based on that information, compares it to a polyfit of the experimentally obtained I-V curve data, and makes educated revisions for the next iteration's ion parameters based on several inherent properties for I-V curves (i.e. increasing number density increases overall signal magnitude, increasing temperature increases the curves resistance to ion retarding potential, etc…). Figure 32 demonstrates the convergence of the IPEM program. While IPEM can be rather time-consuming, especially for I-V-t curve data, these methods offer an accurate and consistent convergence, and requires only a few points on the I-V curve to do so.

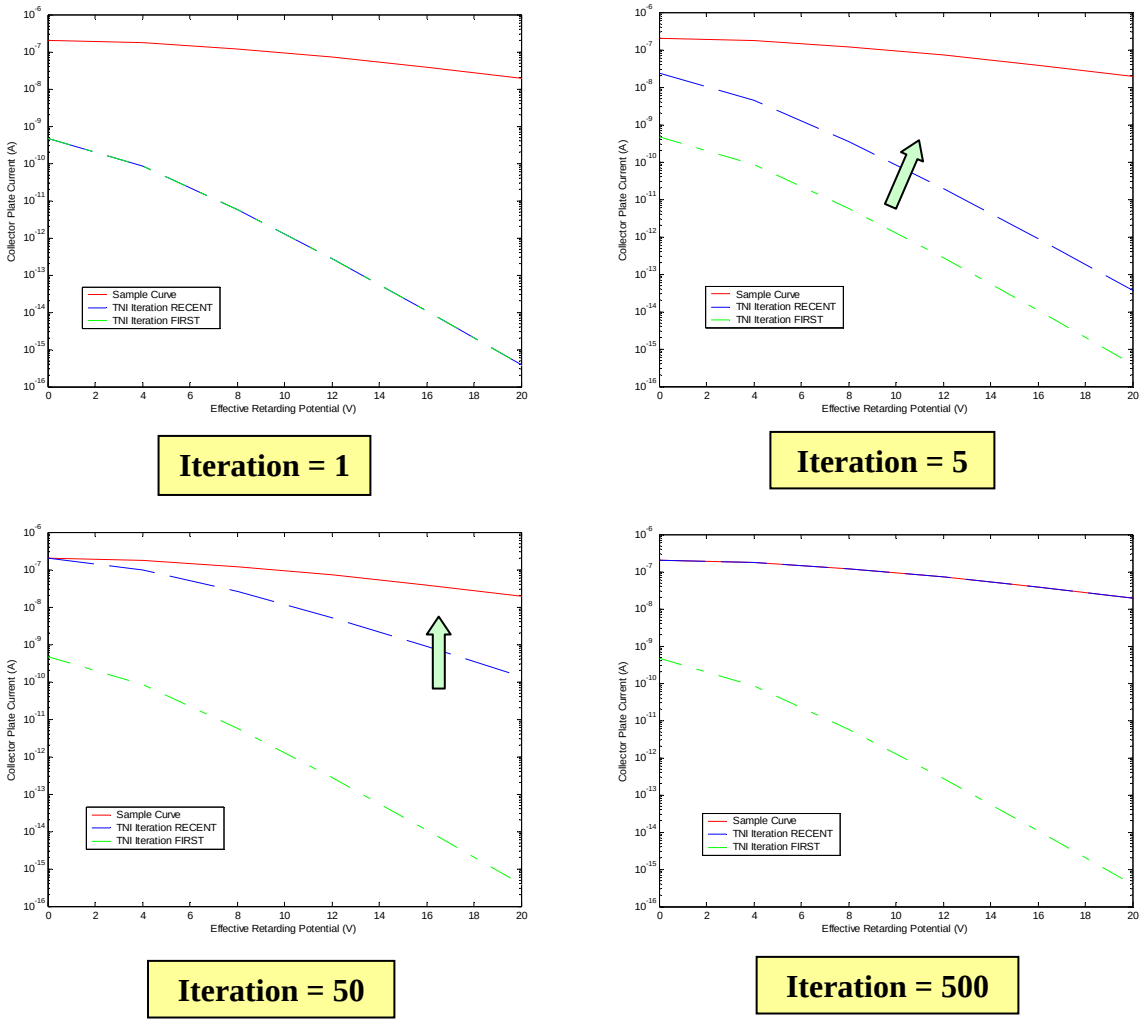

Figure 32. Standard IPEM iterations based on fuzzy logic rules for I-V curve convergence.

The uniqueness of a given set of ion temperature, ion number density, and ion speed ratio for a given I-V curve is guaranteed since each of these three ion parameters are uniquely proportional to the collector plate current. In other words, none of the three parameters appear as a ratio, such that multiple value pairings would produce identical I-V curves. This uniqueness was demonstrated when performing the IPEM convergence and monitoring the fuzzy logic dictated changes in ion parameter values at each iteration.

In substitution of the IPEM program, one could assume that the collimation and retardation effects are independent of each other, at the cost of significant error in cases where the collimating channel(s) is/are long and thin. This is known as the separation approximation. The separation approximation assumes that all of the flux limitations due to cylindrical channel wall neutralization, grid absorption, and grid repelling produce an independent transmission fraction. This method had previously been applied to the hypothetical mutlichannel RPA design containing a single-orifice electrode series (Partridge, 2006). In other words, the transmission fraction for the collimator is assumed based on an initial guess of the ion speed ratio. The overall grid transmission fraction is also calculated. Finally, the flux limitation resultant of the effective ion retarding potential analyzer is calculated based on an assumed Maxwellian plasma. The error in this approximation would become negligible for infinitely thin orifices, but is significant at any realistic values of the diameter to length ratio as shown in Figure 33. Standard IPEM based on the separation approximation for the SC-RPA and the MC-μRPA would only yield estimates of macroscopic ion properties accurate to within an order of magnitude at best.

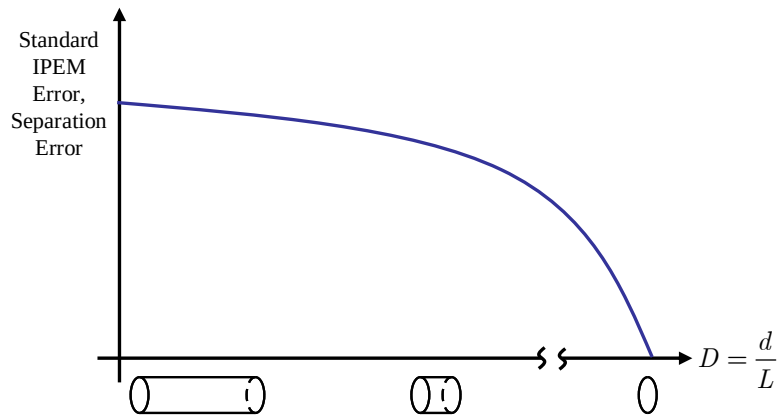

Figure 33. Hypothetical error trend of standard IPEM based on the separation approximation.

Instead, a modified IPEM program would offer the best error mitigation at the cost of computational time. This IPEM program would need to fully account for collimated Maxwellian distributions experiencing an applied effective ion retarding potential. Chronologically, the Maxwellian distribution of ions enters the collimator (or collimators) which are at a floating potential ϕ_{FE}. This process directionalizes the ion beam, producing a new non-Maxwellian distribution of ions entering the grid series. Next, the effective ion retarding potential repels away any ions with an axial velocity less than the velocity v_{eff} corresponding to ϕ_{eff}. Figure 34 depicts the resultant collected current as originating in the area bounded by the collimated Maxwellian distribution curve and by the line $C_s = v_{eff}$.

The updated IPEM program therefore calculates a modified collimated Maxwellian distribution curve based on the channel geometry, floating potential, and assumed ion speed ratio and average temperature. Next the program calculates the area under the distribution curve bounded by the effective ion retarding potential. This process is repeated for a specified range of ϕ_{eff}, and the resultant I-V curve is compared to the experimentally obtained I-V curve. Based on a set of fuzzy logic rules not unlike those of the previous IPEM program, updated estimates for the ion speed ratio, ion temperature, ion number density, and species concentrations (where

applicable) are chosen and used for the next iteration. This process is repeated until convergence to within a specified error is achieved. The IPEM program then outputs the final estimates for the ion parameters as well as the calculated error. Virtually the only additional step as compared to the previous IPEM program involves the calculation of the new distribution at each timestep.

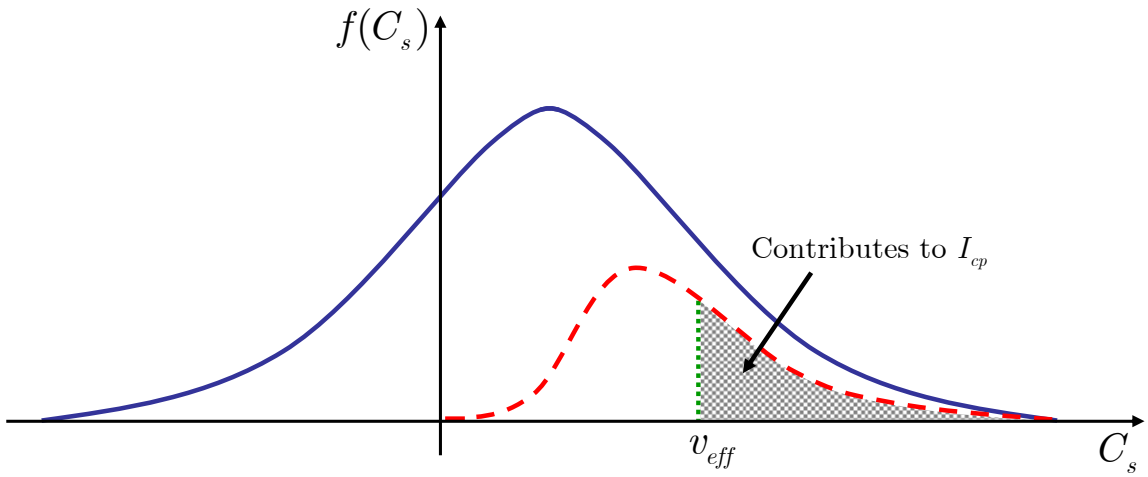

Figure 34. Collimated Maxwellian contribution to collector plate current as bounded by the effective ion retarding potential.

Since the assumption that the measured floating grid potential approximates the true plasma potential most likely results in an overestimation of the effective ion decelerating voltage, the actual contribution to collector plate current is most likely underestimated. In reality, the bounding line of v_{eff} is much closer to the origin and therefore more flux reaches the collector plate.

Chapter 3: Development and Implementation of a Triple Langmuir Probe for Small-Scale, Noisy, Unsteady Plasma Plumes

This chapter outlines the TLP plume characterization experiments performed on the MiLiPulT, beginning with a discussion of the experimental setup and procedures in Section 3.1, including equipment, circuitry, and bell jar feedthrough details. Section 3.2 involves the TLP design process used for the expected operating envelope of the MiLiPulT plume, including the unique operational amplifier modifications to the basic TLP bias circuit necessary to produce measurable current signals. Section 3.3 details the EMI/RFI noise elimination techniques applied to prevent op-amp saturation and to increase the TLP signal to noise ratios. The process of plasma parameter extraction from the collected TLP data is demonstrated in Section 3.4. Results are validated and discussed in Section 3.5.

3.1 Experimental Setup and Data Acquisition

An example of the MiLiPulT device used in these experiments is shown in Figure 35. The thruster electronics and integrated power supply were housed in a separate shielded Faraday cage outside of the Bell Jar.

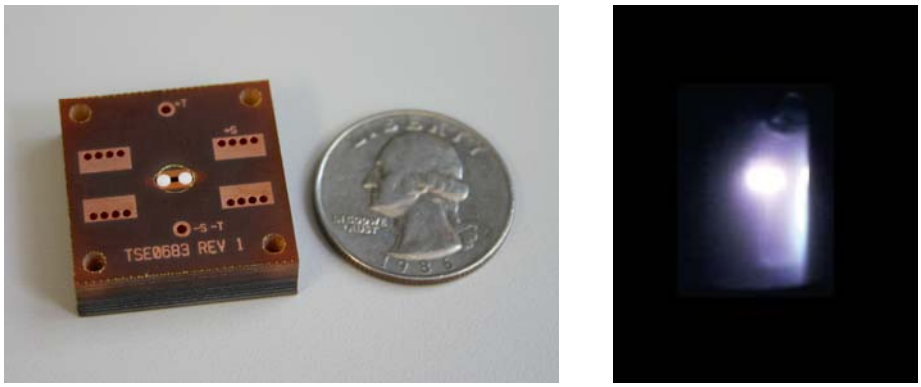

Figure 35. An example MiLiPulT device (left; courtesy of D. Simon) and the MiLiPulT plume (right; Simon & Deal, 2007).

The TLP was mounted on a linear traverse with a range of more than 14 cm from the thruster face, while the MiLiPulT was mounted on a rotational stage. Both stages are controlled using stepper motors, providing the capability to perform a highly accurate 2D polar sweep. The indexer circuit was always powered before the communication software was executed to prevent communication errors. To prevent overheating, the stepper motors were powered off when not in use (heat dissipation within the bell jar while under vacuum was minimal). The TLP, MiLiPulT, linear traverse, and rotational stage are shown in Figure 36. Positional error was minimized by the relatively high accuracy of the stepper motors. Specifically, since the linear traverse probe origin was always calibrated by positioning the probe directly against the MiLiPulT, the uncertainty in the distance was limited to the step size of the linear traverse motor given in the form of steps per revolution (100). The distance traveled per revolution was then divided by the steps per revolution (2.0 mm) to produce a resultant uncertainty (±20.0 μm). However, it was also assumed that when sending commands to the indexer, perhaps the motor might overshoot its target distance by roughly 100 to 1,000 steps (even though they are specifically designed to stop precisely after a specified number of steps), resulting in an overestimated uncertainty of (±40.0 μm). Similarly, the rotational stage has an uncertainty of $\pm 0.36^{o}$ as a result of a 1,000 step per revolution specification. Overall, the positional uncertainties of the rotational and linear translation stages are negligible compared to the uncertainties associated with other probe parameters.

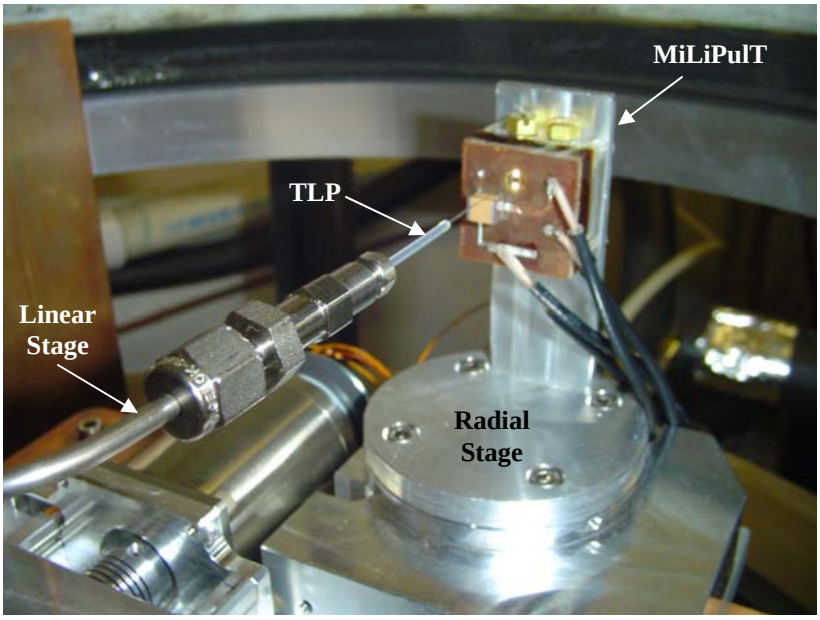

Figure 36. TLP and MiLiPulT mounted on linear and radial translation stages (respectively).

Rotational, translational, and vertical alignment could be further ensured through the application of precision optical alignment. Centerline references can be achieved even at relatively large probe-thruster distances, rather than relying on the standard method of positioning the probe at the thruster face origin and assuming the alignment is maintained as the probe is backed away from the thruster. An offset centerline, or baseline, would have to be established to provide a reference point for the optical tooling providing the alignment. This reference point could be located at the edge of the bell jar. Multiple reference points may be necessary to provide a three dimensional triangulation of the probe position. Alignment would then be made using a laser tracking tool capable of extremely high precision measurements. In addition to position, the instrument level, azimuthal alignment, and axial rotation angle (i.e. pitch, yaw, and roll) could also be calibrated. These methods might prove to be not entirely feasible for a bell jar translation table, since much of the accuracy is already achieved with the

implementation of the stepper motors. Additionally, the alignment equipment may not be vacuum rated, and would have to removed with each pump-down.

A diagram of the MiLiPulT integrated power supply and external circuitry is illustrated in Figure 37. The thruster firing rate was kept below the recommended 0.7 Hz. Roughly one in ten firings resulted in a misfire. In the event of a misfire, the sustain capacitance would not decay and no plasma discharge was observed. The sustain capacitance discharge profile is typically an exponentially decreasing curve. Misfires were not included in the data averaging.

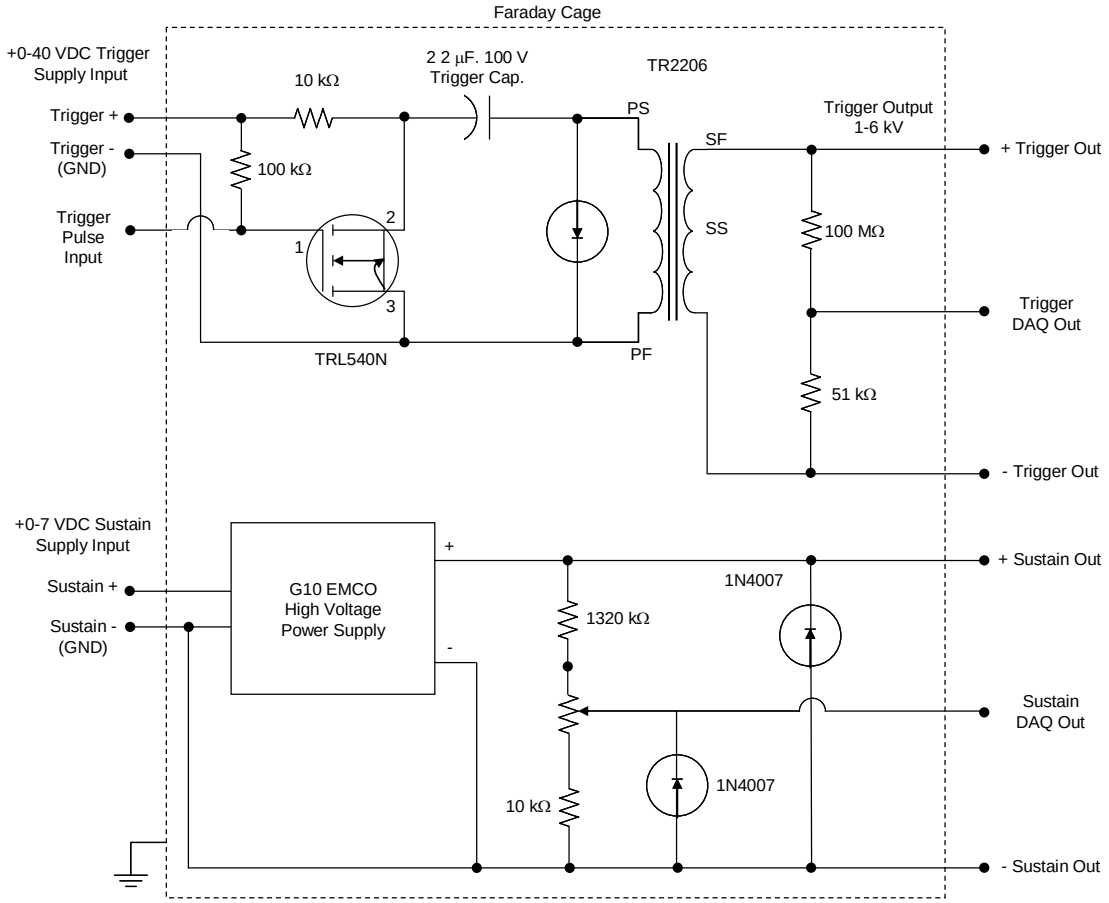

Figure 37. MiLiPulT integrated power supply electronics schematic (adapted from Simon et al., 2006).

A wiring schematic showing the electrodes of the MiLiPulT is illustrated in Figure 38. To reduce magnetic inductance within the thruster, the trigger and sustain wires were soldered directly to the thruster face, along with the sustain capacitor.

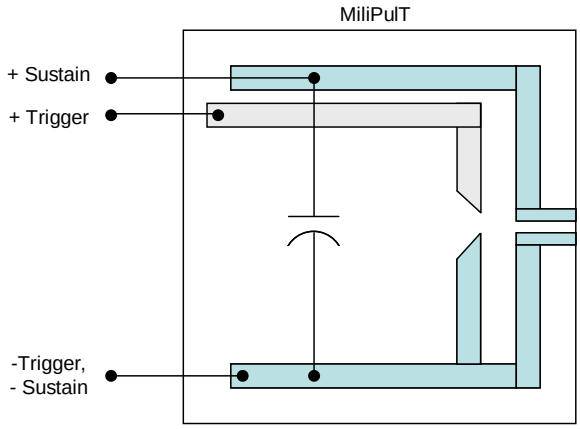

Figure 38. MiLiPulT electrode wiring schematic (adapted from Simon, et al., 2006).

The entire experimental setup of the TLP characterization of the MiLiPulT is illustrated in Figure 39. Several Faraday cages were employed in the TLP experiments to minimize the propagation of EMI noise. Specifically, the bell jar, integrated power supply, TLP bias circuit, and oscilloscope were each separately housed in a Faraday cage. The combination of a Sargent-Welch 1397 roughing pump, a TurboVac 316 turbopump, and an LN2 cold trap provided bell jar vacuum pressures as low as 10^{-5} Torr during consistent thruster operation. A diagram of the bell jar system and its operating procedures are shown in Appendix C.

The inductances in the trigger impulse circuit are the result of RF chokes designed to minimize the RF common mode noise present as a result of the capacitive discharge inherent to the MiLiPulT. Further noise elimination techniques are discussed in Section 3.3. It was found that the addition of the inductances did not change the characteristics of the thruster discharge (trigger and sustain) profiles.

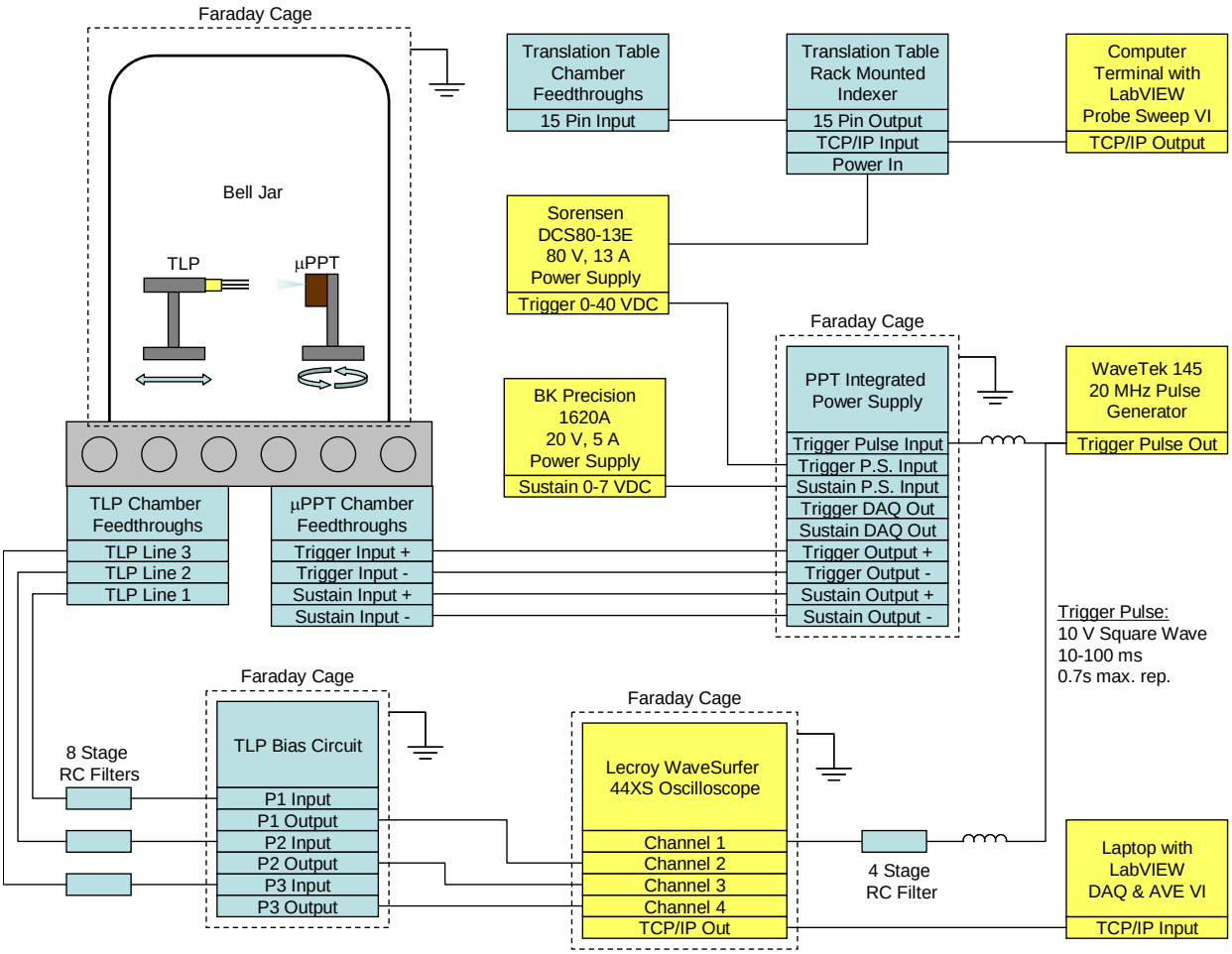

Figure 39. Experimental setup of the JHU/APL MiLiPulT plume characterization using a TLP methodology.

The trigger and sustain data acquisition (DAQ) outputs of the integrated power supply were monitored initially during setup, but were later capped off because they produced too much ground noise when channeled through the oscilloscope. Using the trigger input pulse as the oscilloscope trigger proved to be the most effective and consistent method in appropriating the desired time interval and identifying the precise moment of thruster firing. Ultimately the modifications to the trigger pulse lines can be as drastic as possible to provide minimal oscilloscope ground disturbance as long as those modifications are still germane to the integrated power supply trigger pulse input.

3.2 TLP Design and Bias Circuit Optimization

TLP sizing and collisional parameters for relevant MiLiPulT plasma conditions are shown in Table 10. Among other TLP design constraints, the probe radius to Debye length ratio must be kept large enough to assume either a thin-sheath approximation or the transitional regime. Additionally, sheath diameters have been calculated to ensure inter-probe spacing is much greater than one sheath diameter. The expected operational envelope of the MiLiPulT plasma was based on both electron number density and electron temperature. The intentionally underestimated expected electron number density was ranged from $1.0\text{x}10^{16}\ \text{m}^{-3}$ to more than $1.0\text{x}10^{18}\ \text{m}^{-3}$. It becomes necessary to err lower than truly expected for the lower bound such that the eventual TLP dimensions will produce an acceptable r_p / λ_D ratio. Similarly, if the upper bound electron number density is underestimated, the collected currents and the r_p / λ_D ratio would simply be greater. Electron temperature was assumed to range from 4 to 12 eV. While there will more than likely be many lower temperature electrons, it is necessary to overestimate the electron temperature because of converse reasoning mentioned above for the electron density. The following calculations also assumed that $\phi_{13} = 9.50\ \text{V}$.

Table 10. TLP sizing parameters for expected plasma conditions.

Probe Parameter	Charged Parameter			
	$n_{e,i} = 10^{16}$ m^{-3} $T_e = 4$ eV $T_i = 1$ eV	$n_{e,i} = 10^{16}$ m^{-3} $T_e = 12$ eV $T_i = 1$ eV	$n_{e,i} = 10^{18}$ m^{-3} $T_e = 4$ eV $T_i = 1$ eV	$n_{e,i} = 10^{18}$ m^{-3} $T_e = 12$ eV $T_i = 1$ eV
Kn_{H^+,H^+}	361.5	361.5	4.4	4.4
Kn_{O^+,O^+}	361.5	361.5	4.4	4.4
Kn_{O^+,H^+}	21,996.7	21,996.7	267.9	267.9
Kn_{e,H^+}	4,133.8	21,477.2	50.3	261.5
Kn_{e,O^+}	4,101.7	21,312.8	49.9	259.5
$Kn_{e,e}$	57,841.1	461,518.3	704.3	5,484.5
$\lambda_{e,H^+} / \lambda_D$	3.08E+03	9.23E+03	3.75E+02	1.12E+03
d_s (m)	7.13E-05	5.42E-05	7.13E-06	5.42E-06
R_p / λ_D	0.74	0.43	7.45	4.30
t_p	75.21	43.42	752.09	434.22

Based on these parameters, the TLP used in the investigation of MiLiPulT plasma parameters was designed to have probe radii of $r_p = 37.5\ \mu\mathrm{m}$ and exposed probe lengths of $L_p = 5\ \mathrm{mm}$. A magnified image of the exposed TLP probe wires is shown in Figure 40. At these probe diameters, perfect alignment with the plasma flow direction was difficult to achieve. Continuity was frequently checked amongst the probe wires to ensure they were not in contact with each other.

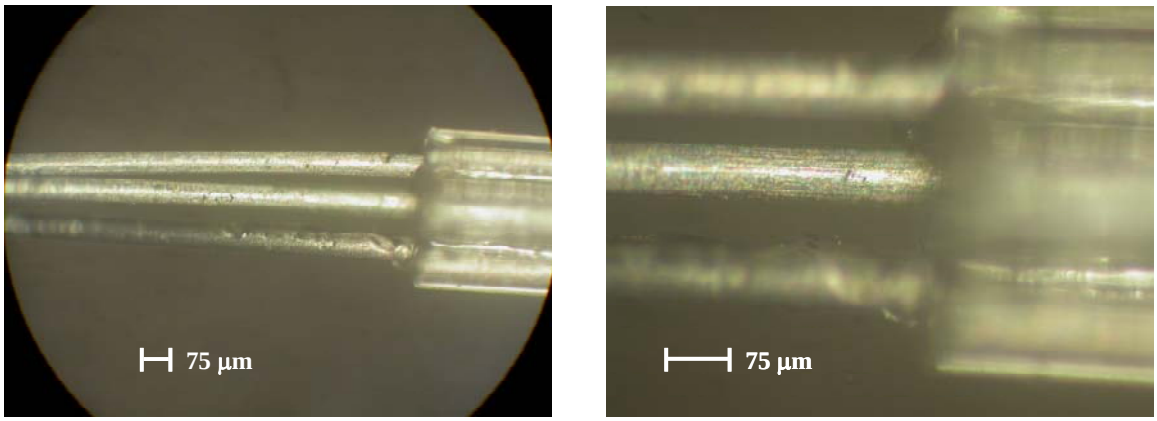

Figure 40. Microscopic images of the TLP exposed tungsten probe wires (courtesy of L. Byrne).

Based on prior SLP measurements and TLP dimensions, the TLP bias circuit was designed for expected probe currents on the order of 10^{-4}-10^{-6} A. All three TLP currents were originally measured using three Lecroy APD300 20 MHz differential probes across three individual measurement resistors of approximately 100 Ω, as shown in Figure 41. The measurement resistances were chosen such that it would provide a readable voltage signal while also not contributing a significant voltage drop, and thus minimally detracting from either ϕ_{12} or ϕ_{13}. Precise values of each measurement resistor were recorded and used during data reduction. Ammeters, Pearson coils, inductive current probes, and other current transformers were avoided due to noise, size, and functionality constraints. Unfortunately, due to the 2 mV vertical resolution of the oscilloscope, the bias circuit with differential voltage probe measurement could not discern TLP current signals at probe distances $d_{\mathrm{TLP}} \geq 10\ \mathrm{cm}$ from the MiLiPulT thruster exit plane. Further signal amplification was paramount, yet the measurement resistance could not be increased at the risk of bias voltage error.

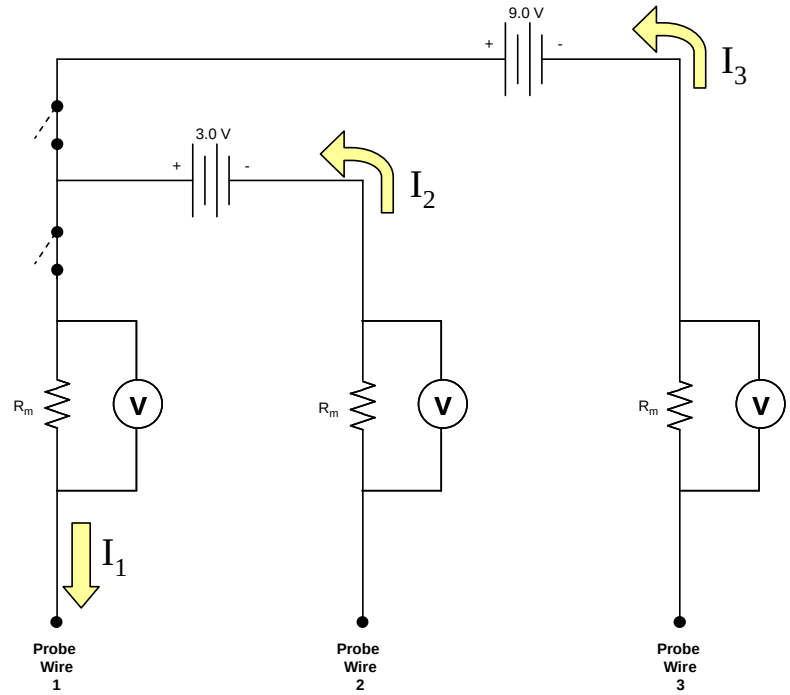

Figure 41. Basic TLP bias circuit employing measurement resistors and differential voltage probes.

To accomplish the required signal gain, three JFET LT1793 operational amplifiers were used in three differential input amplifier configurations as illustrated in Figure 42 to both increase and accurately measure the voltage drop across each of the 100 Ω resistors (Burr-Brown Research Corporation, 1963). Assuming that $R_1 = R_2$ and $R_3 = R_4$, the amplification ratio H_0 is then given as

$$H_0 = \frac{R_3}{R_1}. \tag{3.1}$$

The 100 Ω resistors in serial with the probe wires were low enough in resistance to not detract from the overall biasing voltages while providing a 100x amplification through the measurement of voltage (rather than current).

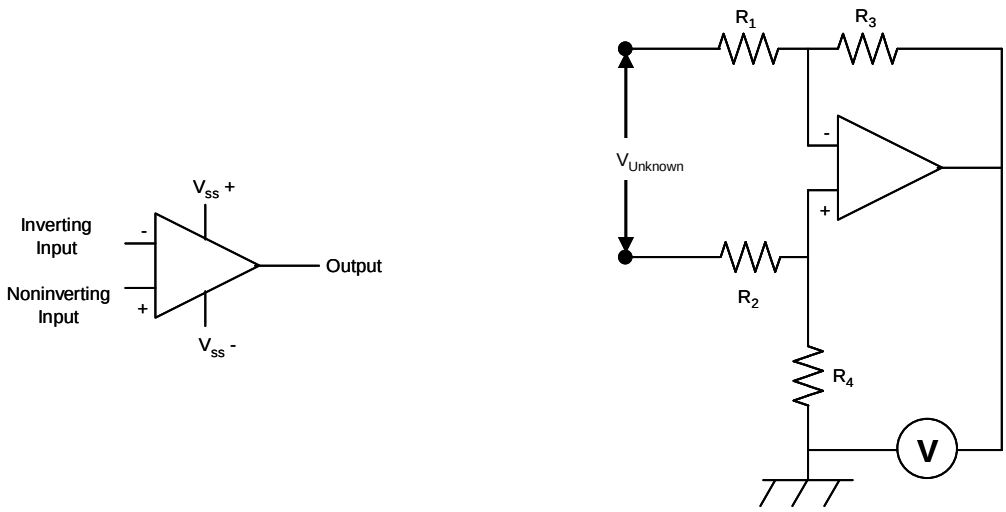

Figure 42. Operational amplifier electronic schematic symbol with dual rail power supplies (left) and differential input amplifier schematic (right, dual rails not shown per convention).

Roughly 25 Ω total resistance was observed between any two probe wires, when connected. R_3 and R_4 were set to 100 kΩ to prevent bleeding of current through the differential input amplifier circuits to ground. R_1 and R_2 were set to 10 kΩ for each op-amp to provide an additional 10x amplification of the voltage measurements. Each differential input amplifier conveniently output the amplified voltage drop with respect to ground. This also allowed the shielding of the coaxial measurement lines to be grounded for safety.

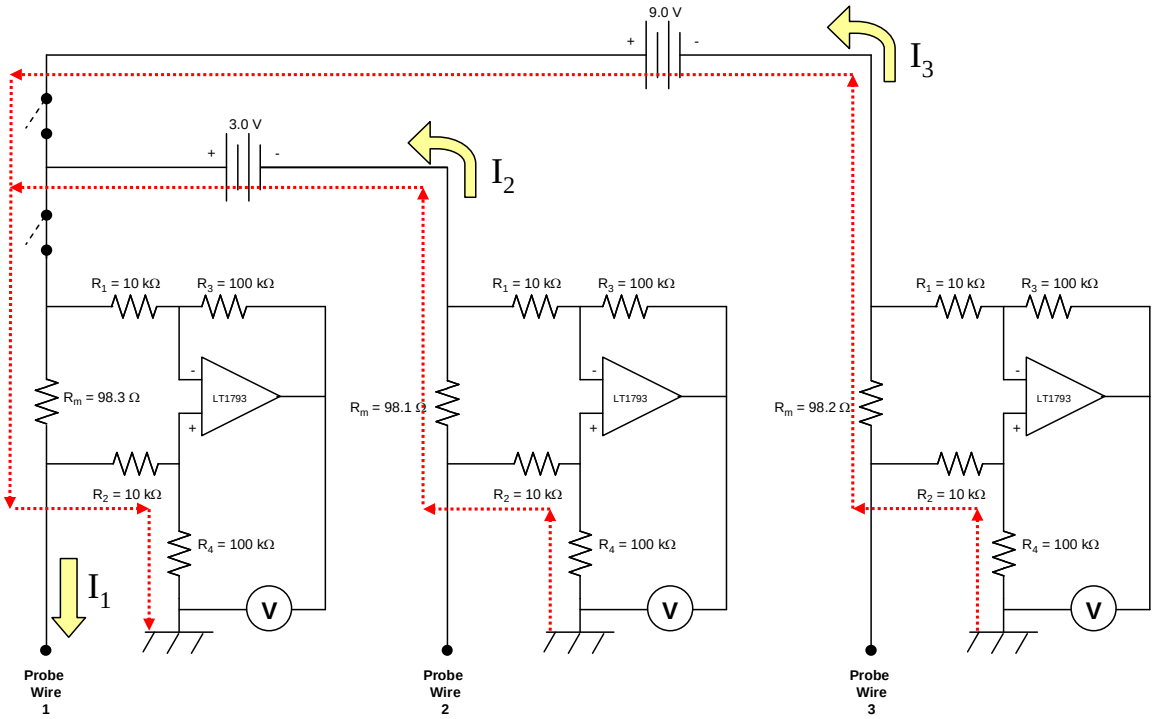

Figure 43. Leakage current paths in a TLP bias circuit with differential input amplifers.

Even with larger values for R_3 and R_4, leakage current was observed following a path from facility ground at one measurement module to that of another. This resulted in observed errors of 20% when three probe lines were simultaneously used. Leakage currents were eliminated by placing two voltage followers prior to each differential input amplifier. Voltage followers, as shown schematically in Figure 44, output the same voltage present at their non-inverting input with respect to ground, but prevent current from flowing in either direction. Diodes were avoided for noise and functionality considerations.

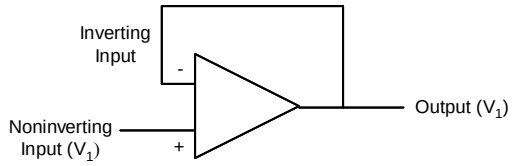

Figure 44. Operational Amplifier in a voltage follower configuration (dual rails not shown per convention).

However, since the offsets of the operational amplifiers used in each pair of voltage followers would be amplified differently, and since it would be cumbersome to measure their individual

offsets independently by a recursive measurement module, a dual JFET NTE858M operational amplifier was used. The offsets for each pair of voltage followers were then much more closely matched. Switches were incorporated for diagnostic purposes and so that the bias circuit could be used for either a TLP or a QLP. The final MiLiPulT-optimized TLP bias circuit is shown schematically in Figure 45 while the actual circuit is shown in Figure 46. Rather than soldering each resistor to a PCB, the circuit was built into a breadboard due to the high degree of design revision during the optimization process. Probe wire 3 was wired to facility ground through a 29.9 kΩ resistor to prevent the entire TLP bias circuit from floating. This allowed a reference point for the measurement modules and eliminated drift observed when the circuit was left floating. Values of the ground resistor were varied, but did not produce any observable difference until the ground resistance dropped below 1 kΩ. This result was confirmed by simulating the entire TLP bias circuit in PSPICE.

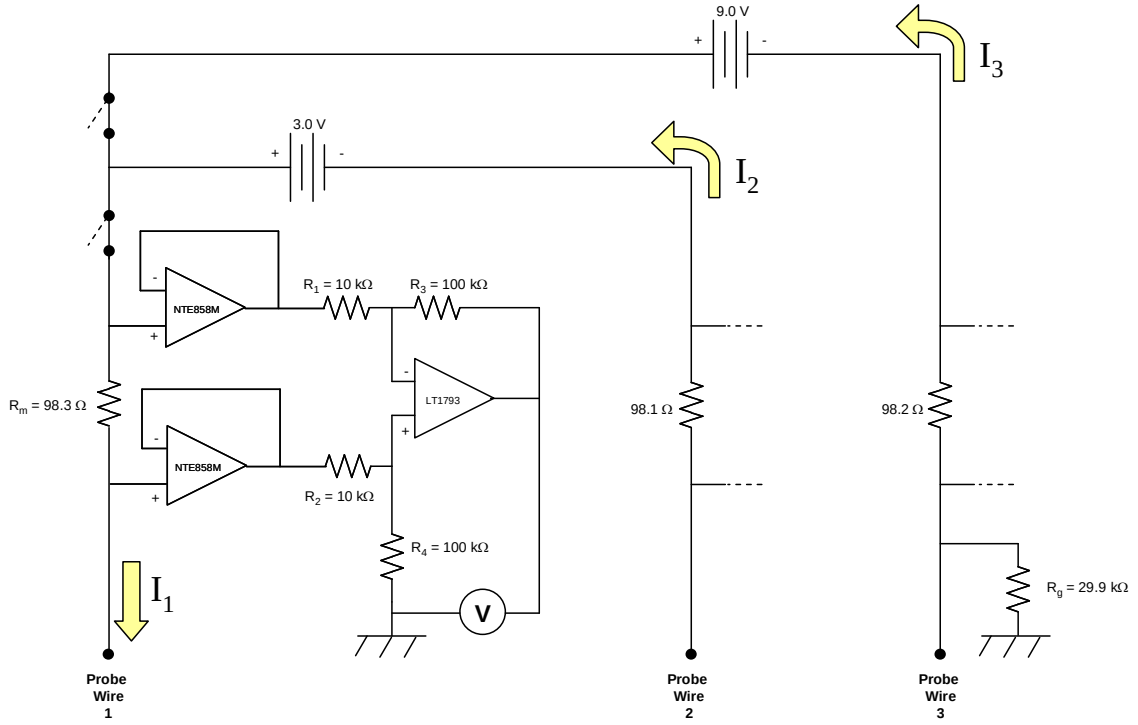

Figure 45. Optimized TLP bias circuit with differential input amplifiers and voltage followers.

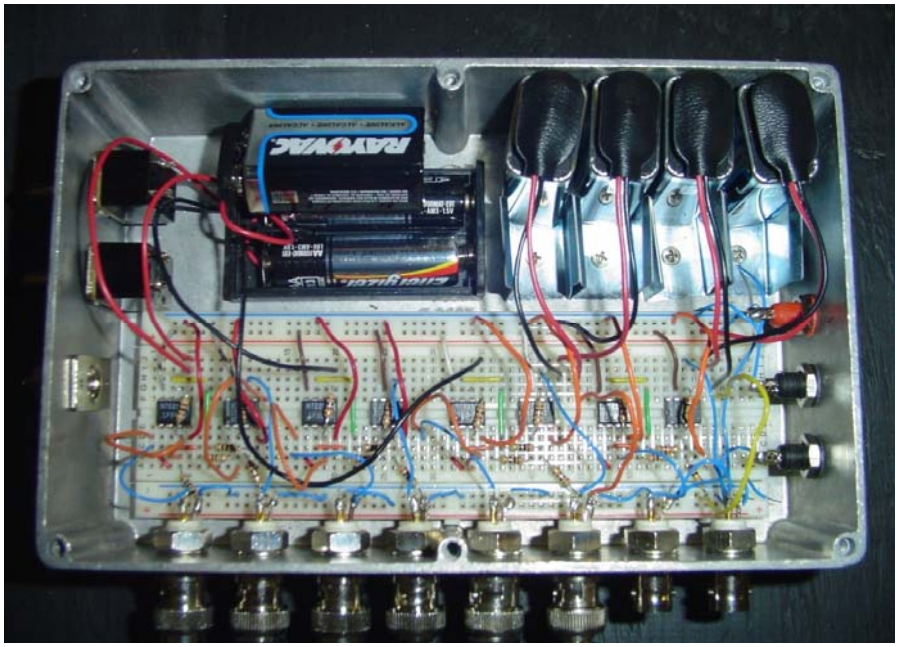

Figure 46. TLP bias circuit (with QLP channel unused).

All anticipated power levels were within the rated maximum of 25 W for all resistors used. SLP measurements indicated a consistent plasma potential greater than roughly 30.0 V. Accordingly, the values of ϕ_{12} and ϕ_{13} were chosen so as not to exceed the plasma potential for the initial portion of the pulse, while still providing significant and unique bias between probe wires. All probes were coupled to the scope with direct current 1 MΩ (DC1MΩ) impedance. Applying Kirchoff's rule around the closed switches,

$$I_1 = I_2 + I_3 . \tag{3.2}$$

The summation of all three currents at various thruster settings during operation was closely monitored, in addition to the TLP characteristic current ratio I^* from Chen (1971). Current values not producing a ratio of $0 < I^* < 1$ yield difficulty in the Newton-Raphson solver, producing complex values of T_e depending on the initial guess. Monitoring the current ratios as well as the current summations provided a valuable diagnostic for gauging the accuracy of the TLP bias circuit throughout its development.

While the intended amplification factor for each probe line was set at $H_0 = 10.0$, each probe line's true amplification factor depended on variances of the resistors within the differential amplifier, as well as the offsets and characteristics of all three operational amplifiers in each measurement module. The output of each module was tested at various voltages using both a square wave and an AC signal at frequencies ranging from 0.01 kHz to 300 MHz to calculate the true amplification factor H_0^* for each probe line. Calibration charts for each of the three instrumentation amplifier sections at the true signal frequency of 1 MHz are shown in Table 11. With slew rate defined as the maximum change in signal over time, a slew rate of less than 13.0 V/μs was observed above 70 kHz, which corresponds to the specified slew rates of the NTE858M operational amplifiers. The conversion from measured voltage V_m to true current is then simply given by

$$I = \frac{V_m}{R_m H_0^*}. \tag{3.3}$$

The dual voltage supplies for all operational amplifiers were provided by two 9 V batteries wired in series. Significant noise was observed during operation, but was eliminated by housing the dual voltage supplies inside the Faraday cage encompassing the bias circuit. Additional noise filtration techniques are discussed below.

Table 11. TLP bias circuit amplification ratio calibration results.

Node	V_{Setting} (V)	V_{Input} (V)		I_{Actual} (μA)	V_{Measured} (mV)		H_0^*
---	---	Min	Max	---	Min	Max	---
P1	0.60	-0.64	0.64	21.3	-24	17	**9.78**
	0.80	-0.93	0.93	31.0	-32	25	**9.35**
	1.00	-1.22	1.22	40.7	-40	35	**9.38**
	1.20	-1.47	1.50	49.5	-48	43	**9.35**
	1.40	-1.76	1.79	59.2	-56	51	**9.20**
	1.60	-2.05	2.08	68.8	-64	58	**9.01**
	1.80	-2.30	2.34	77.3	-72	67	**9.14**
	2.00	-2.62	2.62	87.3	-82	75	**9.14**
	2.20	-2.88	2.88	96.0	-90	84	**9.22**
P2	0.60	-0.64	0.64	21.3	-5	38	**10.27**
	0.80	-0.93	0.93	31.0	-13	46	**9.70**
	1.00	-1.22	1.22	40.7	-21	54	**9.40**
	1.20	-1.47	1.50	49.5	-29	62	**9.37**
	1.40	-1.76	1.79	59.2	-37	70	**9.22**
	1.60	-2.05	2.08	68.8	-47	79	**9.33**
	1.80	-2.34	2.34	78.0	-53	88	**9.21**
	2.00	-2.62	2.62	87.3	-62	95	**9.16**
	2.20	-2.88	2.88	96.0	-71	104	**9.29**
P3	0.60	-0.64	0.64	21.3	-30	15	**10.73**
	0.80	-0.93	0.93	31.0	-40	24	**10.50**
	1.00	-1.22	1.22	40.7	-49	35	**10.51**
	1.20	-1.48	1.50	49.7	-59	44	**10.55**
	1.40	-1.76	1.79	59.2	-68	53	**10.40**
	1.60	-2.05	2.08	68.8	-78	63	**10.42**
	1.80	-2.34	2.34	78.0	-86	71	**10.24**
	2.00	-2.62	2.62	87.3	-95	82	**10.31**
	2.20	-2.88	2.88	96.0	-105	92	**10.44**

The total amplification factors need to also account for the measurement resistor of each channel. These values are listed in Table 12. The total amplification factors are simply the measurement resistance (but dimensionless due to Ohms law) multiplied by the true amplification factor H_0^*. The average true amplification factors were taken as the averages from each set of nine values for each channel, respectively. These overall amplification factors are roughly 1000, which corresponds to the projected requirements for current sensing during TLP operation.

Table 12. Total amplification factors after accounting for the measurement resistors of each channel.

Node	R_m (Ω)	$\langle H_0^* \rangle$	Overall Amplification
P1	98.3	9.29	**912.8**
P2	98.1	9.44	**926.0**
P3	98.3	10.45	**1027.6**

An example of a saturated TLP current signal as a result of either an improper amplification ratio or the presence of EMI noise is shown in Figure 47. The combined effects of both a saturated and overly filtered current signal were observed to yield misleading results. The false TLP current signal would consist of a clean (low noise), unipolar pulse lasting several microseconds with a maximum value below the operational amplifier saturation voltage. This was due to the slew rate of the operational amplifiers when saturated, in combination with the digital scope filtering. The saturated voltage amplitude would be reduced by a factor of roughly one half. Changing the resistances within the instrumentational amplifier configurations to reduce the noise would also reduce the true current signal, therefore necessitating EMI noise elimination prior to passing the signals through the amplifiers. This noise reduction was carefully achieved using passive filtering, the corner frequencies and number of stages of which were properly calculated to provide the minimal signal frequency attenuation. Details of the applied noise elimination techniques are presented in the next section.

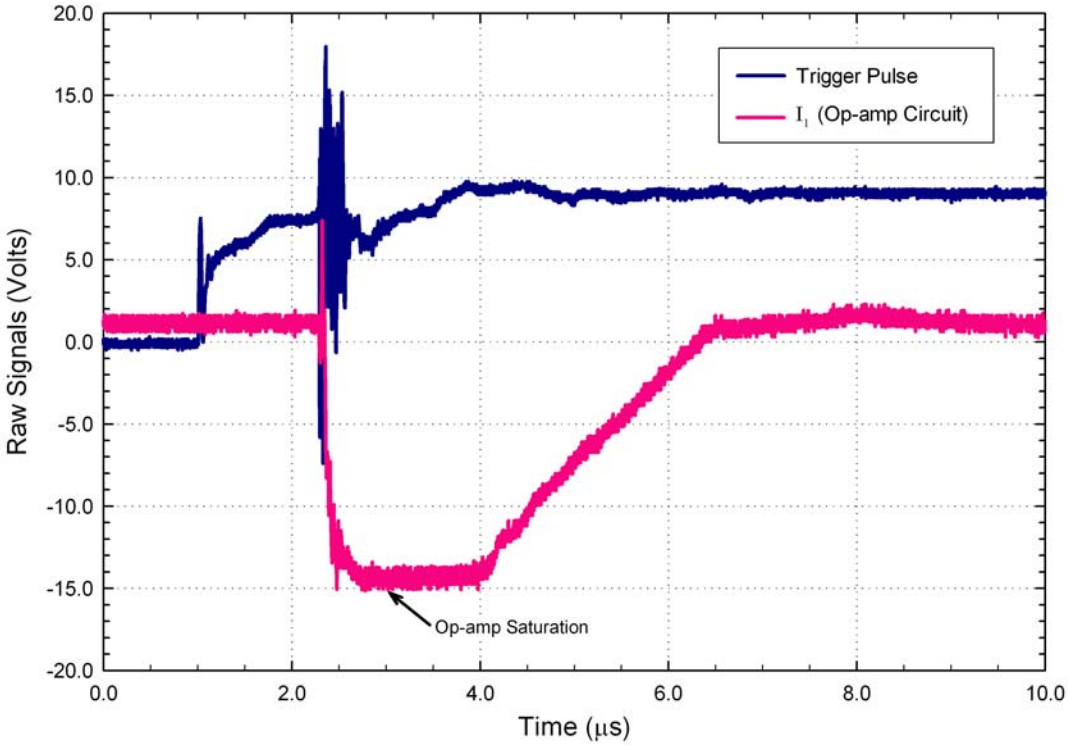

Figure 47. An example of operational amplifier saturation while measuring TLP current with EMI noise.

A data acquisition and averaging virtual instrument (entitled PPT_DAQAVE.vi) was developed in LabVIEW specifically for MiLiPulT experimentation in order to communicate with the Lecroy WaveSurfer 44Xs oscilloscope, to download TLP and RPA probe traces, and to perform summed signal averaging on all four channels to smooth out leftover noise that had not yet been eliminated. The front panel and block diagram of the PPT_DAQAVE.vi are illustrated in Appendix A. The virtual instrument consists of a three frame sequence structure. The first frame initializes several local variables for later use, including arrays for signal storage. In the second frame, a while loop contains a nested two frame sequence structure; the first of which uses Lecroy sub-vi's to communicate with the oscilloscope and download trace information after a trigger event. The waveforms for all four channels are then converted to a cluster, unbundled, converted to dynamic data, extracted to XY pairs, and tabulated in an appending array. In the

second nested frame, the user is then prompted on whether or not to use the traces in the summed average. The averaged traces are then calculated and displayed. Upon collecting a sufficient number of traces, the third frame outputs the averaged four-channel time-indexed data to a text file.

3.3 EMI Noise Identification and Filtration

In order to determine and eventually filter out the conducted EMI noise frequencies inherent to the MiLiPulT trigger, a discrete Fourier transform (DFT) of raw TLP current signals was performed using a fast Fourier transform (FFT) algorithm in MATLAB. A sample of the raw TLP signal has a sampling frequency of 1 GHz and is shown in Figure 48. A visual inspection of the waveform in Figure 48 indicates a wavelength associated with the noise of approximately 50 ns, which corresponds to a noise frequency of approximately 20 MHz. A 16,384-point FFT of the sample data yields a more exact fundamental noise frequency of 15.99 MHz. Another peak exists at approximately 1.95 MHz, which is the actual TLP current signal. The resultant power spectral density (having units of Watts/Hz) as a function of frequency is plotted in Figure 49 for the sample TLP waveform. The FFT and power spectral density calculations were repeated for 10 TLP current traces each for $I_1 - I_2$ and $I_1 - I_3$ signals. The results are listed in Table 13 and indicate an averaged noise frequency of 17.6 MHz. It should also be noted that an additional noise peak was observed in the $I_1 - I_3$ signals at approximately 30 MHz, but this value is well above the corner frequency range for the low pass RC filters.

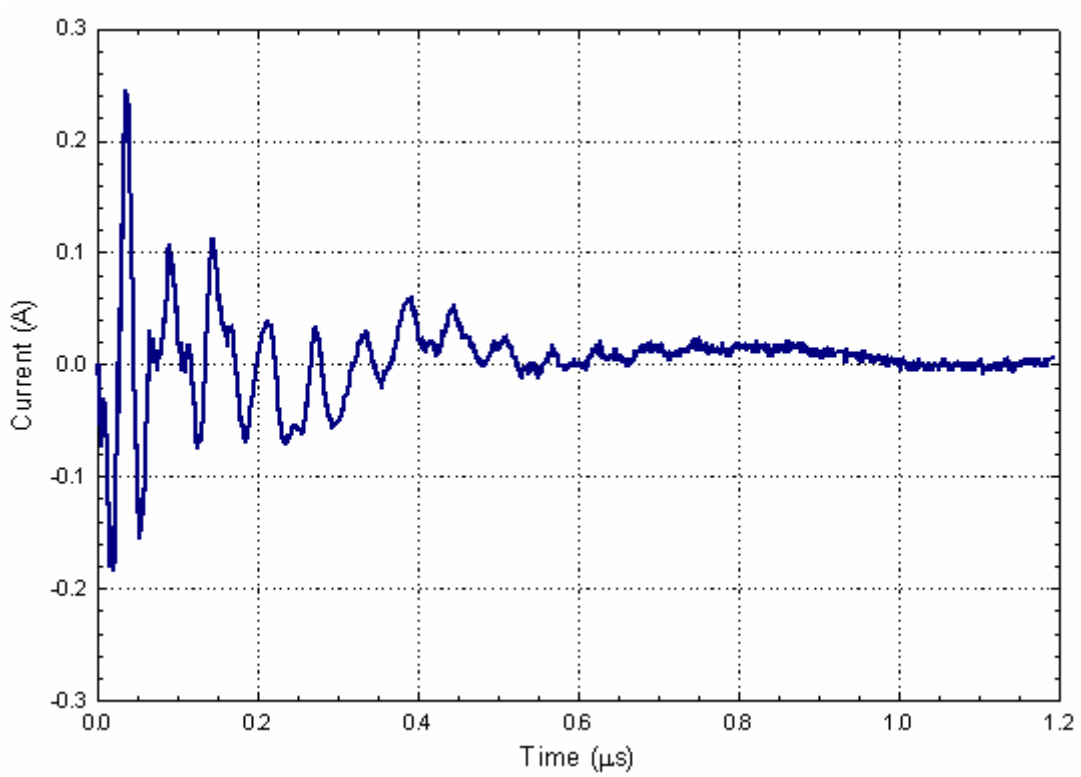

Figure 48. Raw TLP current waveform used for DFT analysis.

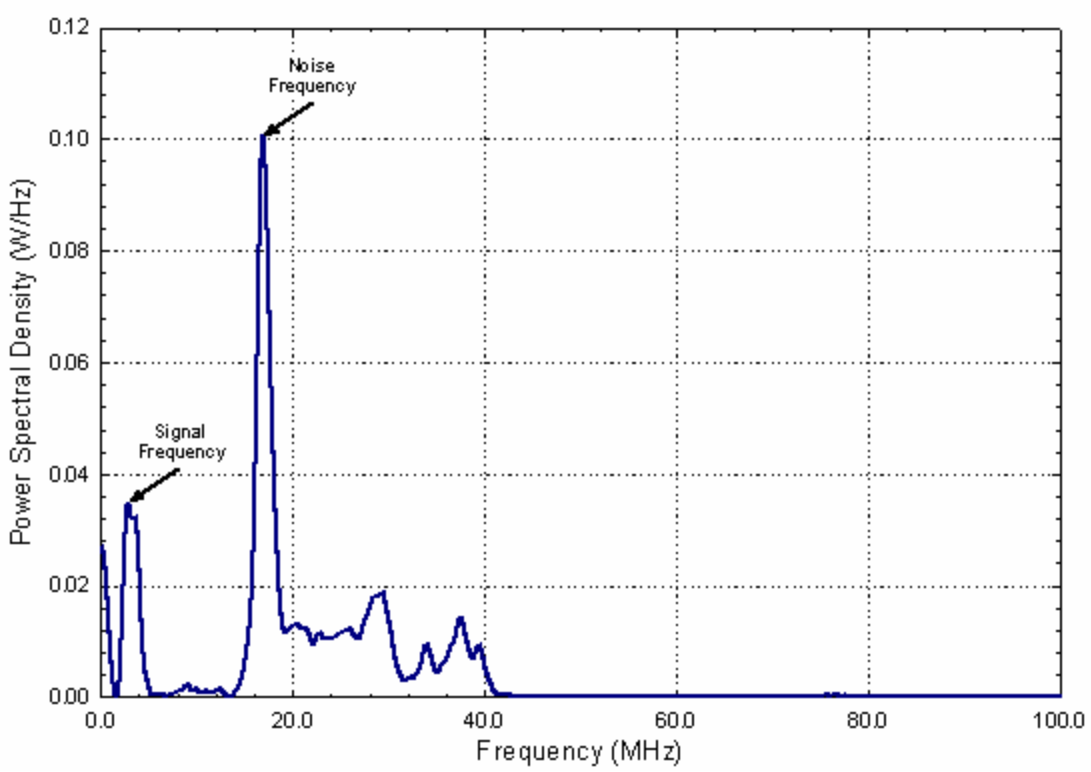

Figure 49. DFT analysis of raw TLP current waveform.

With the fundamental noise frequency identified, passive filtering can be applied to provide a clean signal prior to passing the TLP current signals through the operational amplifiers. Recalling that a low signal to noise ratio (particularly less than 1.0) will cause the operational amplifiers in a voltage differencer configuration to saturate at any useful amplification ratio, the noise must be filtered out a priori, as opposed to relying solely on thruster shot averaging in LabVIEW.

Table 13. Fundamental frequencies and power spectral densities for TLP noise and true current signals.

		Noise		True TLP Signal	
TLP Signal	**Trace Number**	**Fundamental Frequency (MHz)**	**Power Spectral Density (W/Hz)**	**Fundamental Frequency (MHz)**	**Power Spectral Density (W/Hz)**
$I_1 - I_2$	1	18.3	3.508E-03	3.78	1.490E-03
	2	16.1	1.763E-01	1.40	2.283E-01
	3	16.0	1.543E-01	1.46	1.064E-01
	4	16.1	1.822E-01	2.99	1.248E-01
	5	16.2	1.962E-01	2.50	1.669E-01
	6	16.0	3.205E-01	1.95	3.488E-01
	7	16.2	3.555E-01	1.83	2.951E-01
	8	16.1	3.126E-01	2.56	2.834E-01
	9	19.8	2.121E-01	3.60	4.207E-01
	10	20.0	1.141E-01	3.17	1.007E-01
$I_1 - I_3$	11	17.0	3.591E-01	1.46	5.456E-02
	12	17.0	4.294E-01	2.62	9.271E-02
	13	17.0	6.269E-01	1.65	8.598E-02
	14	17.2	8.174E-01	1.53	1.074E-01
	15	17.0	1.185E+00	3.72	1.573E-01
	16	17.1	1.032E+00	1.40	1.515E-01
	17	17.0	1.205E+00	3.66	1.586E-01
	18	20.6	2.014E+00	1.40	9.349E-02
	19	20.6	6.730E-01	1.46	4.188E-02
	20	20.5	4.016E-01	1.53	2.738E-02
	Average	**17.6**	**5.385E-01**	**2.29**	**1.524E-01**

An ideal low pass RC filter has a corner frequency defined as

$$f_{co} = \frac{1}{2\pi RC} \tag{3.4}$$

where R is the value of the resistor as measured in Ohms and C is the value of capacitance as measured in Farads.

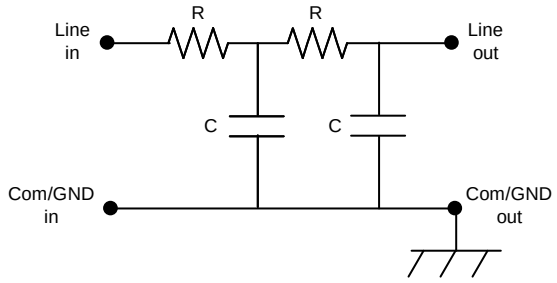

Figure 50. Electrical schematic of a passive 2 stage RC low-pass filter.

In an ideal RC filter, the corner frequency acts as a cutoff frequency, fully attenuating higher frequencies. A non-ideal RC filter has a tapered attenuation curve as it approaches the corner frequency, as shown in Figure 51. An optimal corner frequency of a non-ideal passive RC filter will attenuate the noise as much as possible while leaving the true signal intact.

With the fundamental noise frequency identified, passive filtering can be applied to provide a clean signal prior to passing the TLP current signals through the operational amplifiers. The attenuation characteristics of RC filters consisting of a various number of stages for a single corner frequency of 401 MHz were tested and are shown in Figure 52. A significant amplification of ~200 MHz noise was observed for filters with few stages. Increasing the number of stages decreases the effect of this phenomenon. Eight stage RC low-pass filters produce nearly complete attenuation at 200 MHz. A simple adjustment of the corner frequency is then required to maximize attenuation at the noise frequency while maintaining minimal attenuation at the signal frequency, as shown in Figure 53.

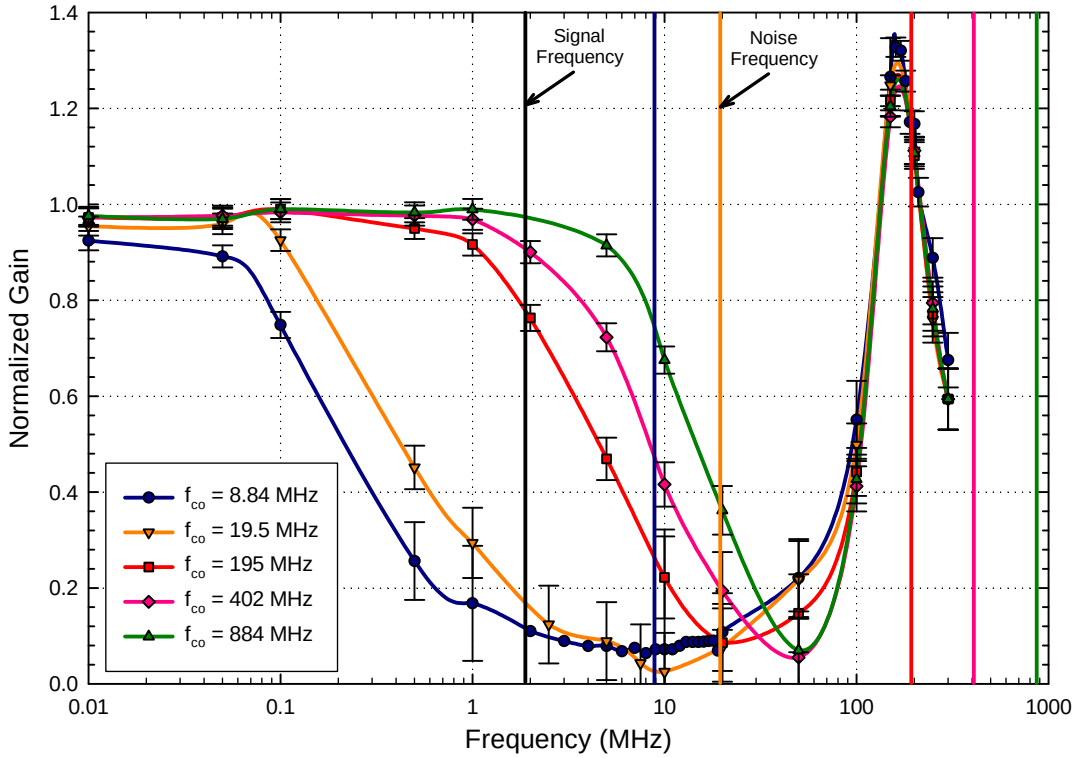

Figure 51. Attenuation profiles for 2 stage RC low-pass filters at various corner frequencies.

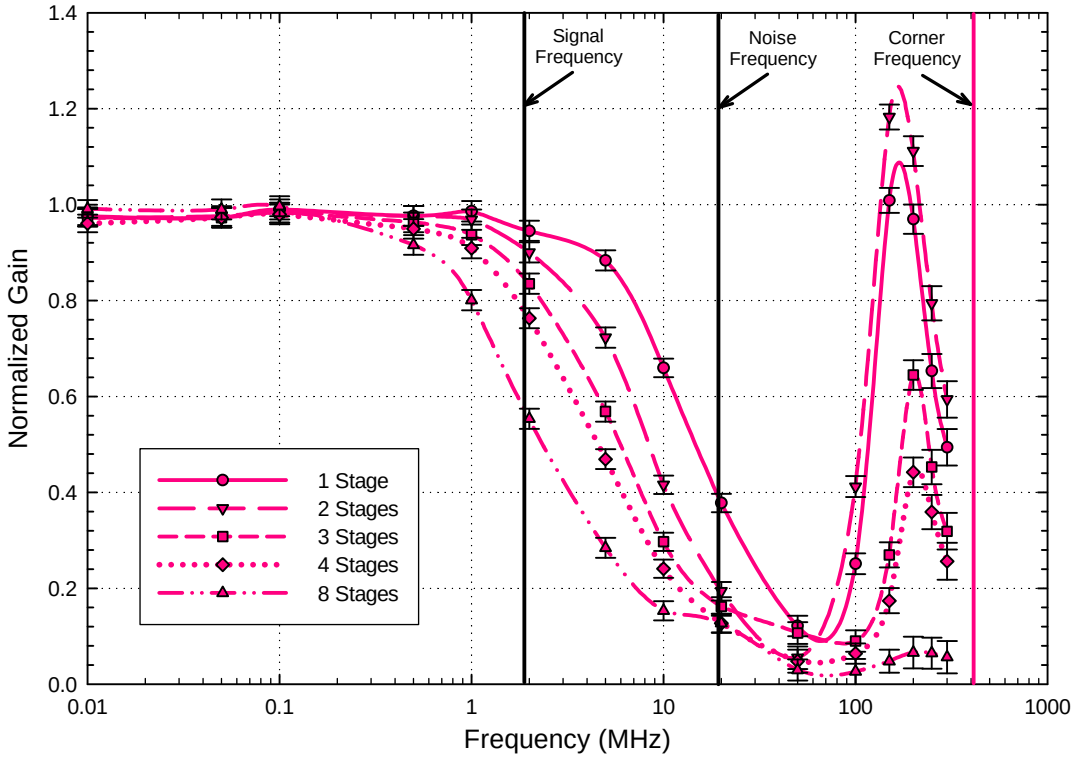

Figure 52. Attenuation profiles for various stages of RC low-pass filters (f_{co} = 402 MHz).

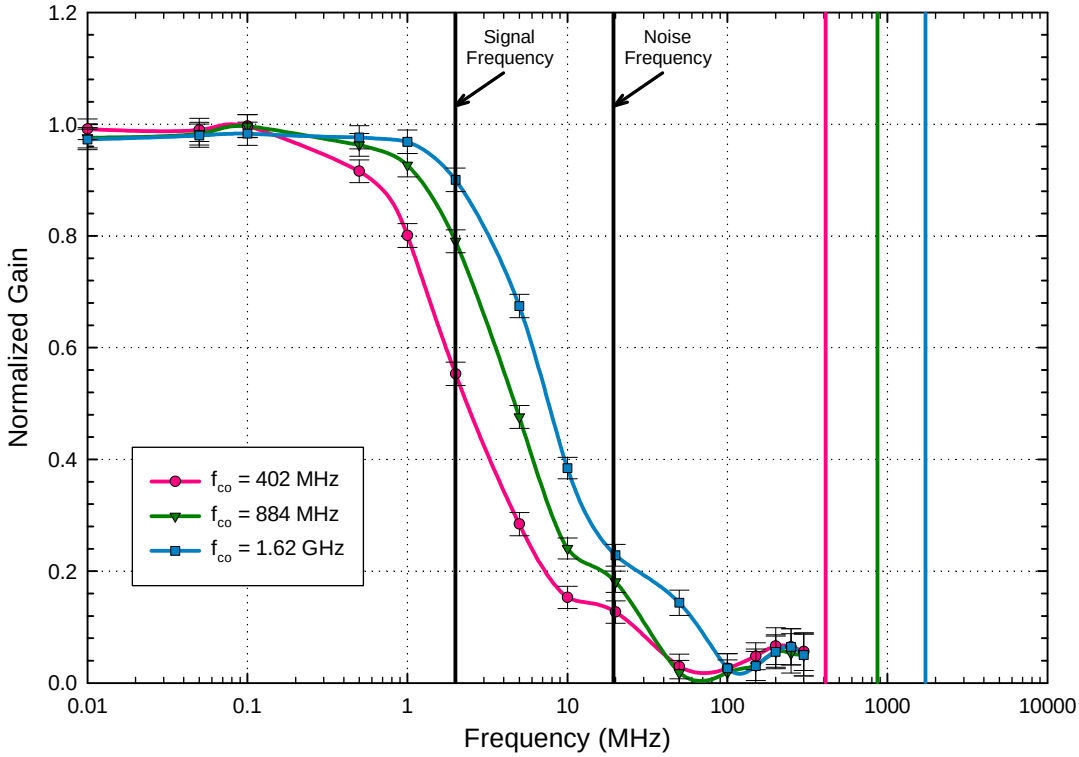

Figure 53. Attenuation profiles for 8 stage RC low-pass filters at various corner frequencies.

The attenuation profiles of Figure 53 indicate an optimal 8 stage RC low-pass filter with a corner frequency of 1.62 GHz, which provides a less than 10% reduction in the highest anticipated true signal frequency, while attenuating the most prominent noise frequency by more than 75%. While the enhanced resolution (Eres) settings on the oscilloscope alone would provide a more ideal low pass filtering, it would simply be filtering a saturated op-amp signal. Oscilloscope filtration would not provide the necessary noise attenuation prior to passing signals through the differential input amplifiers and voltage followers in the TLP bias circuit. The attenuation profiles of the Lecroy WaveSurfer 44Xs Eres settings for a horizontal resolution of either 500 ns or 1 μs per division are shown in Figure 54. These profiles are representative of a -3 dB attenuation at the frequencies corresponding to horizontal resolutions of 500 ns and 1.0 μs per division as listed in Table 14.

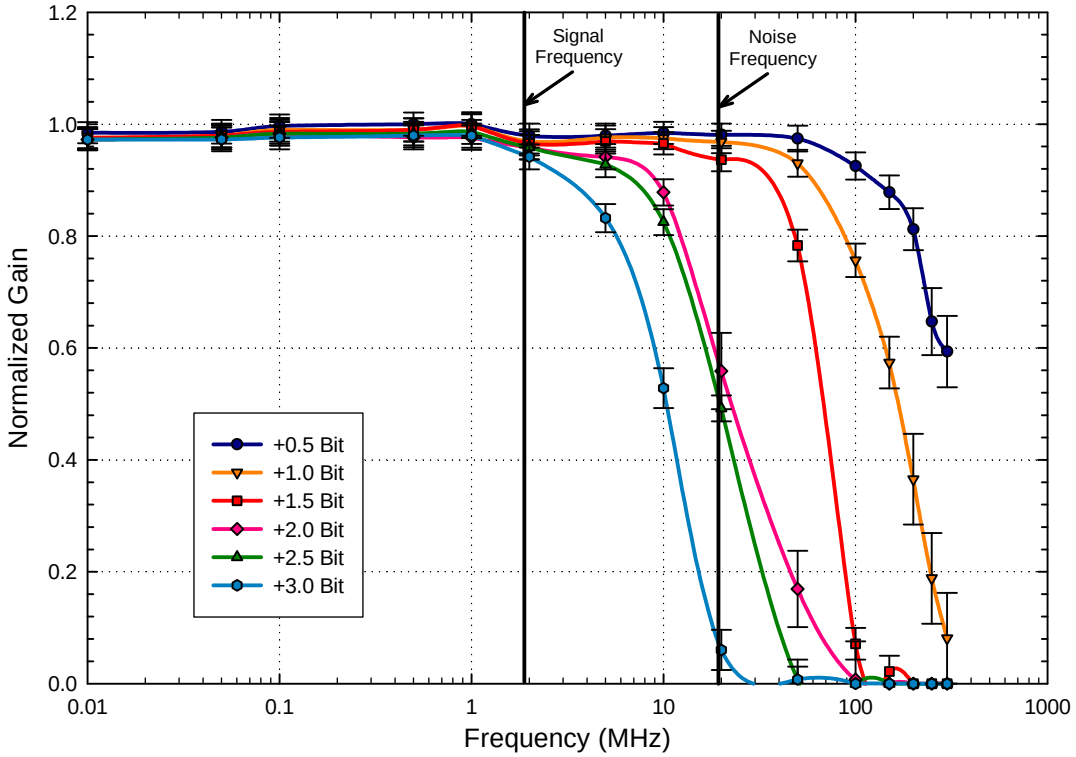

Figure 54. Attenuation profiles for LeCroy WaveSurfer 44XS oscilloscope Enhanced resolution (Eres) digital filtering at horizontal resolutions of 500 ns and 1 μs per division.

It should be noted that these filtering frequencies change drastically (as well as the filtering characteristics) as a function of the horizontal resolution setting. For example, at an Eres filtering of + 3.0 bits at 200 ns per division, the frequency corresponding to a -3 dB attenuation increases to 20.0 MHz and would provide significantly less filtering (equivalent to ~ 2.25 bits). At 2.0 μs per division, the -3 dB attenuation frequency decreases to 4.0 MHz and would provide an overly filtered signal, significantly attenuating the true signal frequency of ~2.0 MHz.

Table 14. Frequencies corresponding to a -3 dB attenuation for oscilloscope Eres settings corresponding to 500 ns and 1 μs per division horizontal resolutions only.

Eres Setting	Frequency at -3 dB Attenuation (MHz)
+ 0.5 Bit	250.0
+ 1.0 Bit	120.5
+ 1.5 Bit	60.5
+ 2.0 Bit	29.0
+ 2.5 Bit	14.5
+ 3.0 Bit	8.0

In order to reduce the observed EMI noise inherent to the MiLiPulT, the unprotected oscilloscope ground was monitored during thruster firing, as shown in Figure 55. Oscilloscope ground shows a variance of over 12 V in the first μs, which tapers off relatively slowly with time. Since the fluctuations were also observed to be present in the ground plane, the noise was most likely common-mode noise, and could have been contributing to measurement error as well as operational amplifier saturation. These ground plane fluctuations were minimized by performing several isolation improvements, which included shielding the oscilloscope and TLP electronics in a Faraday cage, shielding the bell jar in a separate Faraday cage, moving power supplies for the trigger pulse generator away from the oscilloscope, powering (and subsequently grounding) the oscilloscope using a different circuit, moving cables away from the bell jar, and most importantly positioning the trigger pulse cable used to trigger the oscilloscope directly away from the thruster electronics. These isolation improvements decreased the common-mode noise by roughly a factor of ten, as also shown in Figure 55. Since the oscilloscope and TLP bias circuit were at this point shielded by a Faraday cage, any remaining noise was therefore considered to most likely be conducted common-mode noise from the shielding of the trigger pulse cable.

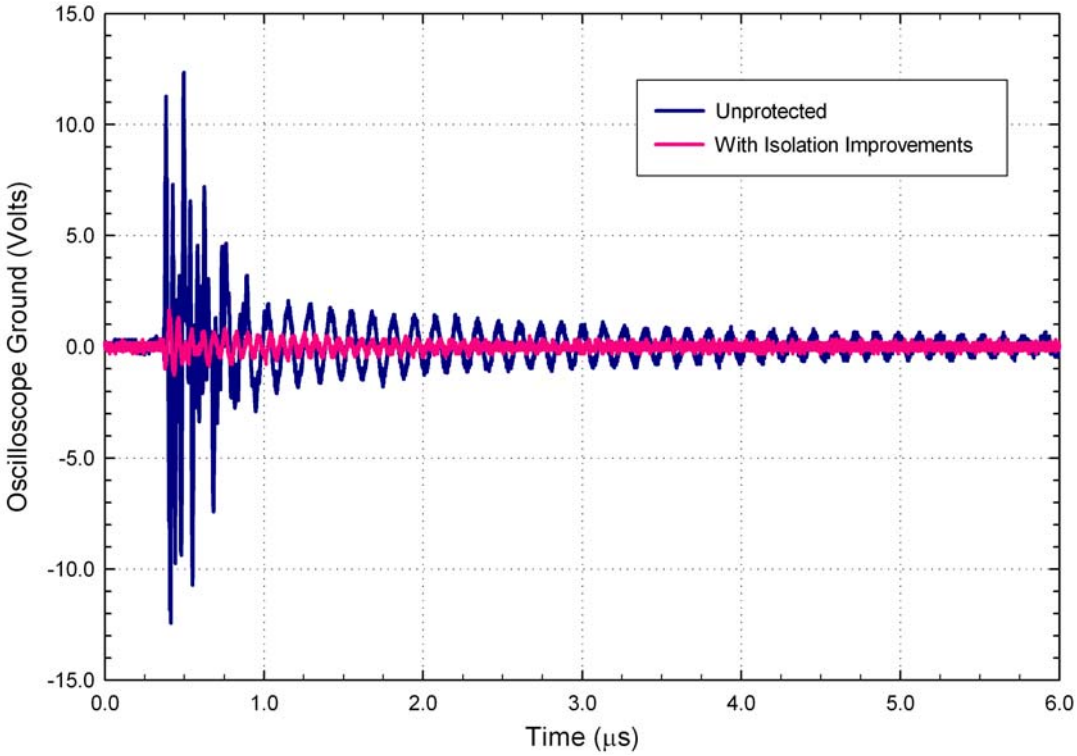

Figure 55. Common-mode noise present in oscilloscope ground before and after isolation improvements.

The combination of a priori RC low-pass filtering with the aforementioned isolation improvements reduced the common-mode noise such that the operational amplifiers in the TLP bias circuit would no longer saturate.

To further diagnose the source of the common mode noise present in the trigger pulse input (i.e. whether the noise emanated from the integrated power supply or the thruster itself), a Faraday cage was installed directly around the thruster. This Faraday cage consisted of a small 2”x2”x3” box constructed from adhesive copper tape and was grounded to the rotational stage of the translation table. A 1.0 cm diameter hole was cut at the location of the thruster orifice and aligned at 0.8 cm from the thruster face, as shown in Figure 56. The inside of the copper box was lined with Kapton® tape to ensure that the capacitor or electrodes would not arc with the Faraday cage. It was assumed that the plume divergence angle was small enough so that the 1 cm hole in the cage was not significantly absorbing the plasma or otherwise impeding/affecting

the plume. An exposed wire also was placed behind the box and channeled to the oscilloscope to contrast the noise present both behind and in front of the thruster.

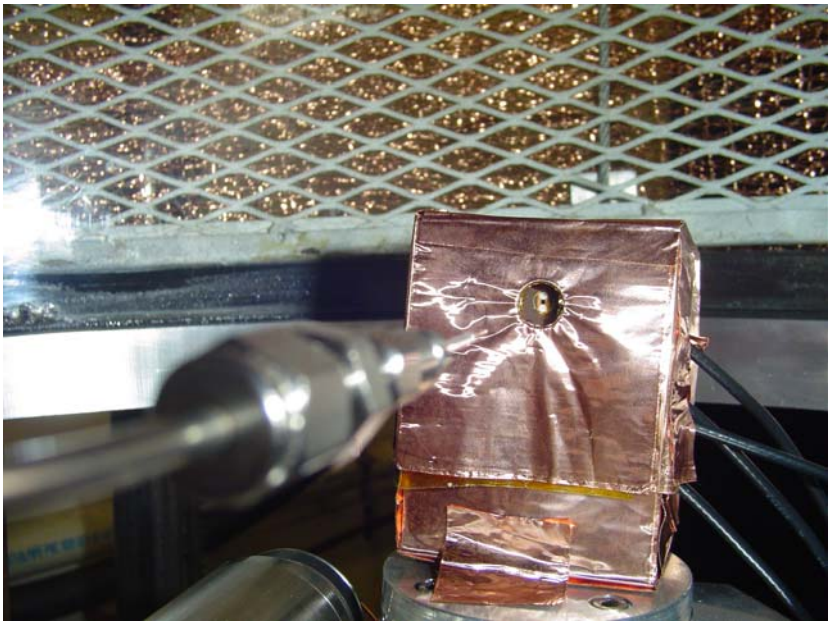

Figure 56. Copper shield housing for the MiLiPulT used for noise source diagnosis.

Comparisons between noise signals collected from the TLP and the aft wire both with and without the copper box yielded minimal differences, confirming that a majority of the noise present in the system was common-mode noise present in both the chassis ground and the instrument input signals resulting from the integrated power supply. To reject most of this noise, several RF chokes and RC filters were placed about the trigger pulse input line, the integrated power supply and output lines were further shielded, and the trigger pulse input line was placed such that it was perpendicular from the power supply circuitry (i.e. less of the wire was close to the power supply). These modifications significantly mitigated the common mode noise and the copper box about the thruster was removed.

3.4 Extraction of Plasma Parameters

A modified Newton-Raphson solver written in FORTRAN was used to reduce the three current signals to values of T_e, n_e, and ϕ_{s1} at each timestep (Press et al., 1992). Based on an initial guess, the program first iterated over the thin sheath regime equations for I_1, I_2, I_3, and their derivatives. The program then applied the same Newton-Raphson algorithm to solve the transitional regime equations for I_1, I_2, I_3. Their resultant r_p / λ_D values were also calculated and output at each timestep. Error and uncertainty analyses as outlined by Gatsonis, et al. (2004a) were applied.

This process was repeated using the OML theory. A comparison of the resultant r_p / λ_D for each timestep allowed for the determination of the applicability of each theory throughout the pulse. The values of $\phi_{12} = 3.241\ \mathrm{V}$ and $\phi_{13} = 9.514\ \mathrm{V}$ were measured before and after testing. Due to the relatively low currents being observed, the bias voltages did not change by more than 1 mV throughout TLP testing. $0 < I^* < 1$ was consistently observed over a majority of every pulse.

3.5 Results and Discussion

An example of the raw oscilloscope data for the TLP characterization experiments is shown in Figure 57. These traces correspond to a single thruster firing, with the TLP probe tip distance from the thruster fixed at 2.0 cm. No digital filtering was applied, but each channel necessitated an 8 stage RC filter with a corner frequency of 1.62 GHz. Since all three TLP currents were measured via the voltage drop across a resistor in the same direction, the polarity of the I_1 signal must be reversed before post-processing.

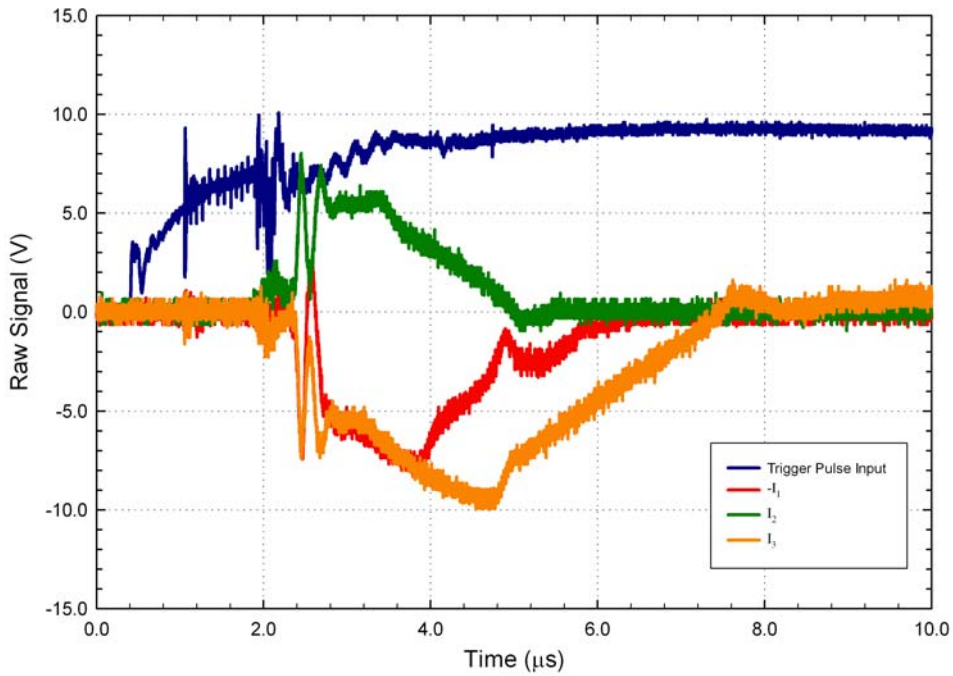

Figure 57. Raw TLP oscilloscope data, d = 2.0 cm, 40 V trigger input, single shot, no Eres.

The combination of a priori 8 stage RC low pass filtration, enhanced resolution (Eres) digital filtration on the oscilloscope, and shot averaging using LabVIEW produces a clear, clean set of TLP voltage drop signals across the measurement resistors. These traces are converted to raw currents using (3.3) by factoring out the amplification ratio to produce the true current levels shown in Figure 58. This profile is for a trigger input setting of 40.0 V at a TLP distance of 2.0 cm from the thruster orifice, averaged over 10 thruster firings with an Eres value of +3.0 bits (-3db @ 8.0 MHz). The peak current reaches ~15.0 mA in this case, which is a considerably high current for a TLP with such a small probe diameter. The current sum is also plotted and is relatively close to zero, with variance roughly an order of magnitude smaller than the actual TLP signals. The current ratio is between 0 and 1 for a majority of the pulse as shown in Figure 59. This plot also contains the normalized probe wire 1 current to show that the asymptotic current ratio behavior exists only within the noise section of the pulse.

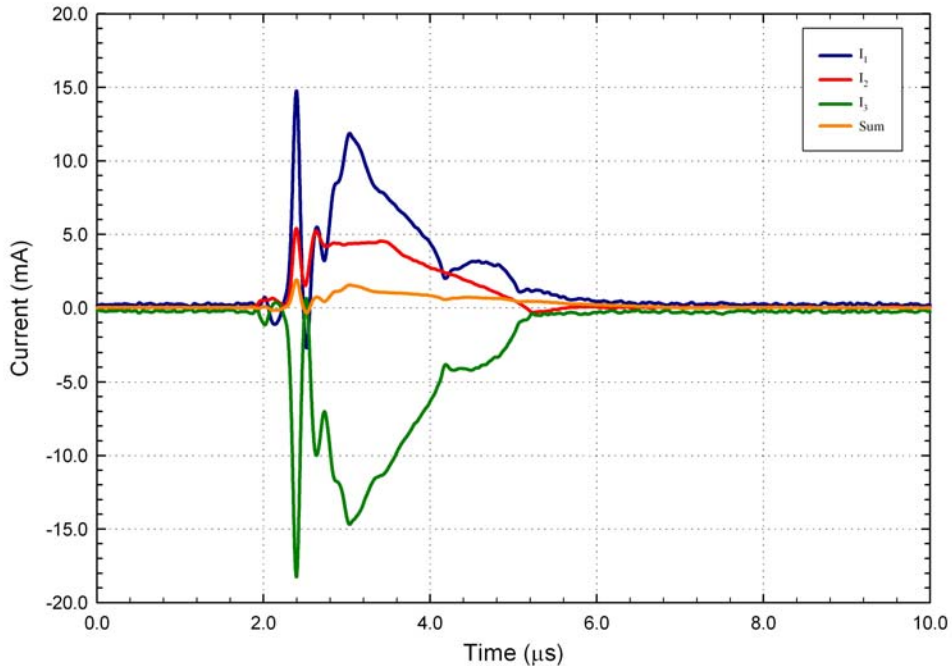

Figure 58. Converted TLP currents and sum, d = 2.0 cm, Eres = +3.0 bits, 10 shot average.

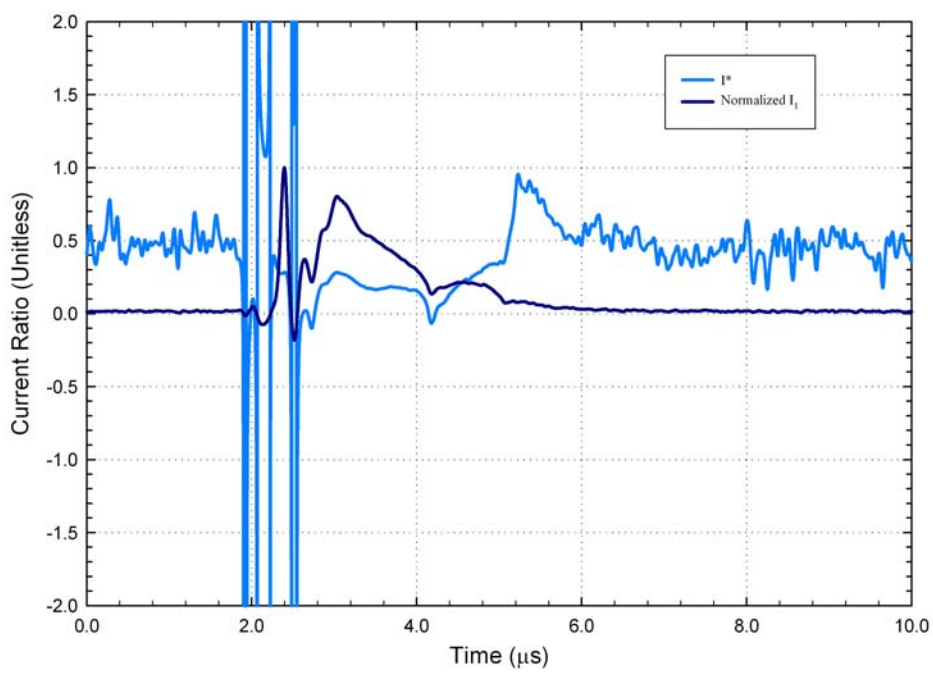

Figure 59. TLP current ratio for the 10 shot averaged pulse at d = 2.0 cm, Eres = + 3.0 Bits.

TLP measurements were collected and 10-shot averaged at three centerline locations of 2.0 cm, 6.0 cm, and 10.0 cm from the thruster face. Rotating the thruster only a few degrees in either direction caused a sharp decrease in observed probe current, indicating a relatively small divergence angle. While a complete thruster setting sweep is recommended in future characterization experiments, the thruster was kept at a trigger input voltage of 40.0 V while the sustain input voltage was kept at 6.0 V. These were the upper limits of the thruster trigger and sustain input voltage ranges, and since previous experimentation had caused the thruster's performance to degrade, any values less than these would prevent the thruster from firing. The TLP data was then passed through the FORTRAN Newton-Raphson solver outlined in Section 3.4, and TLP reduced traces of the electron temperature and electron number density were obtained for both the transitional and OML regimes. At no point was the observed r_p / λ_D high enough to allow for the thin sheath approximation. A sample of these data is illustrated in Figure 60. The TLP currents decrease as thruster distance is increased as expected. The currents at a probe distance of 6.0 cm indicate a current inversion as of approximately 7.0 μs, which has been seen in previous TLP measurements. Current spikes lasting approximately 0.1 μs exist at the beginning of the 2.0 cm and 10.0 cm cases, which only slightly correspond to the noise portion of the discharge. It is possible that these spikes are partially representative of a high energy species of ions (i.e. the high velocity hydrogen ions). Thruster discharge technically occurs for these traces at 2.0 μs, yielded signal lengths of approximately 4.0 μs in the 2.0 cm and 6.0 cm cases, and 3.0 μs in the 10 cm case. A list of the uncertainty values relevant to the TLP characterization experiments are contained in Table 15. Probe length and probe radius uncertainties were limited by the accuracy of the dial caliper used in measuring the dimensions. Measurement resistance uncertainty was a function of the resistors rated variance of ±5%. The

uncertainty in amplification ratio was taken to be a function of the calibration error, as well as the variance in resistors throughout the differential input amplifiers. Bias voltage uncertainty was limited by the accuracy of the voltmeter used to measure the drain in potential throughout the experiments. Additional uncertainties in the probe wire alignment angles and the oscilloscope resolution could have also contributed to overall error, but since these variables are not readily quantified in the TLP theory of operation, the inclusion of these uncertainties in the error analysis was not feasible.

Table 15. Uncertainty values of the TLP MiLiPulT characterization experiments.

Δr_p	2.54x10^{-5} m
$\Delta L_{\parallel}$	2.54x10^{-5} m
ΔM_i	7.227x10^{-27} kg
ΔR_m	4.915 Ohms
ΔH_0^*	0.231
$\Delta \phi_{12}$	0.0354 V
$\Delta \phi_{13}$	0.0956 V

It was observed that the calculated measurement error for the electron temperature profiles was most influenced by the uncertainties in probe current while the electron number density profiles were mostly affected by the uncertainties in bias voltages.

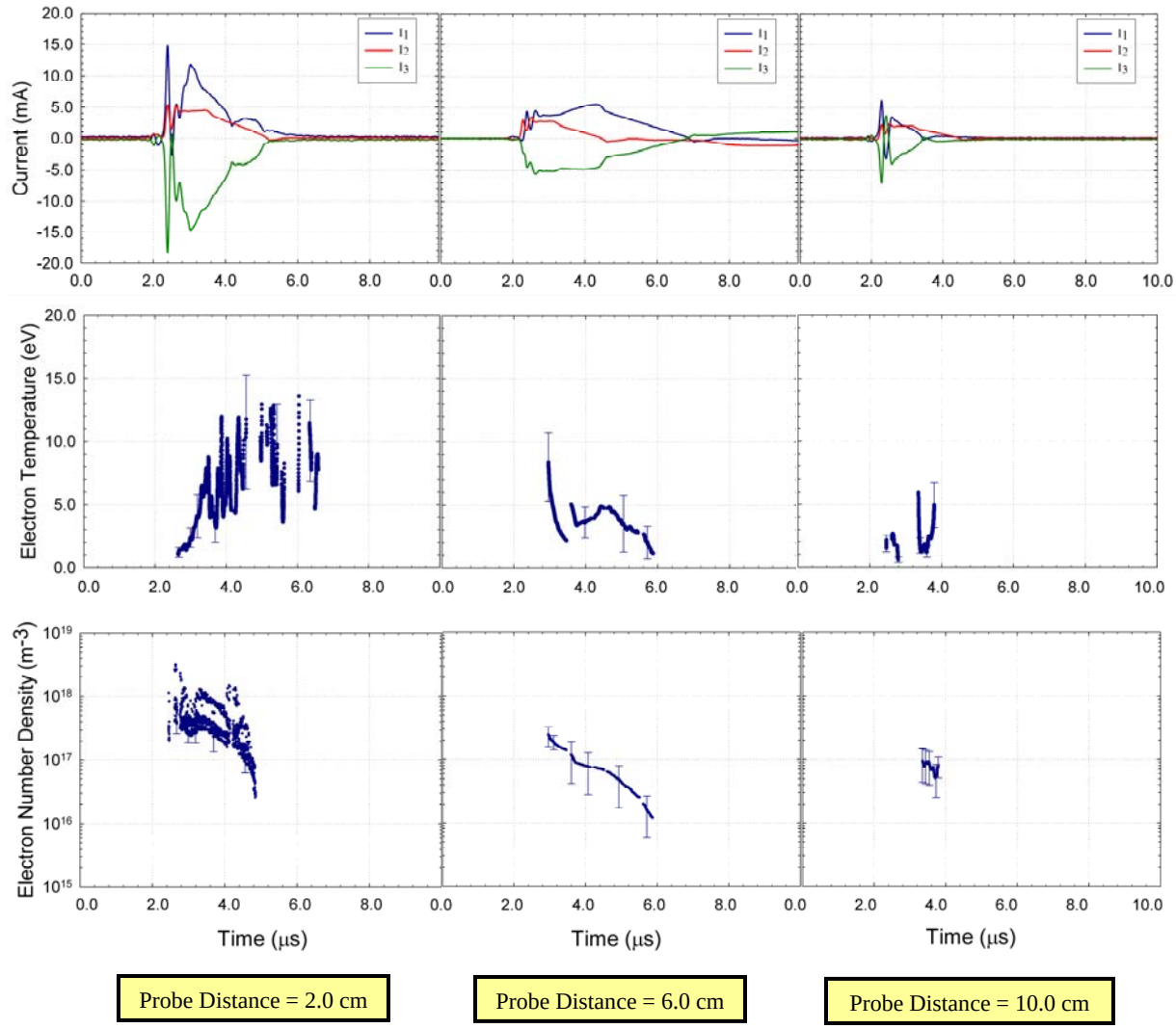

Figure 60. Reduced time-resolved electron temperature profiles and electron number density profiles, with their corresponding TLP currents.

Results indicate a peak electron temperature of 13.59 eV at 2.0 cm from the thruster face. What appear to be nearly vertical spikes in the electron temperature profiles for the 2.0 cm case are most likely a function of the sensitivity of this calculation on the current ratio. The extraction program was not able to reduce the data corresponding to the current spikes observed at the beginning of the pulses for the 2.0 cm and 10.0 cm case, as the current ratio in this region was greater than 1.0. Electron number density for the 2.0 cm case is also relatively volatile, with a peak of 3.18×10^{18} m^{-3} occurring at 0.3 ms after thruster discharge initiation. Probe radius to

Debye length ratios indicate that both the transitional and OML theories were applicable to the 2.0 cm data, as a peak r_p / λ_D value of 5.48 was observed. The 2.0 cm plots show the transitional regime reduced data where applicable, but part of the pulse was also reduced using the OML algorithm. The 6.0 cm and 10.0 cm cases show a much more continuous trend for both the electron number density and electron temperature profiles. This is attributed to the shape of the current signals as well as the fact that the OML regime was used for the entire data reduction, as neither method yielded $r_p / \lambda_D > 5.0$. Peak electron number density and temperature results, including the peak r_p / λ_D values are listed in Table 20. Note that the peak r_p / λ_D for each case does not correspond the Debye length constituted by the peak electron number density and temperature values. This is because the location of the peak electron temperature was not the same as the location of the peak electron number density. Additionally, since plume density displays an approximate exponential dependence on distance, these data indicate a conical plume shape with a small but significant plume divergence angle.

Table 16. Reduced electron properties for each TLP location.

TLP Distance to Source	Applicable Theory	Peak Electron Number Density (m^{-3})	Peak Electron Temperature (eV)	Peak r_p / λ_D
2.0 cm ± 0.07 mm	Transitional/ OML	3.18×10^{18} m^{-3}	13.59 eV	5.48
6.0 cm ± 0.07 mm	OML	2.43×10^{17} m^{-3}	8.37 eV	2.11
10.0 cm ± 0.07 mm	OML	9.54×10^{16} m^{-3}	5.97 eV	1.37

Through the development and optimization of the TLP bias circuit improvements, the applied noise elimination and signal amplification techniques, and the post-processing of experimentally obtained TLP measurements, this research clearly demonstrates the applicability of a current-mode TLP towards the characterization of small-scale, unsteady, noisy plasmas.

Chapter 4: Development and Implementation of Retarding Potential Analyzers for Small-Scale, Noisy, Unsteady Plasma Plumes

This chapter details the development and testing of two new Retarding Potential Analyzer (RPA) design types which incorporate cylindrical collimating channels to reduce the incident number flux throughout the electrode series. This number flux reduction relaxes the Debye length restrictions on the grid dimensions and minimizes the presence of space charge limiting effects on the accuracy of the effective ion retarding potentials. The single-channel RPA (SC-RPA) design incorporates a long thin needle in front of the floating grid which presents the plume with a significantly reduced cross-sectional area. The multichannel μRPA (MC-μRPA) uses a low transparency microchannel plate (MCP) consisting of an array of highly directional channels to more drastically reduce the electrode series flux. Both design types are validated by performing a comparative analysis against a traditional gridded RPA. The MiLiPulT plume is used as a means to demonstrate these new energy analyzer designs in a small-scale, noisy, unsteady plasma. Unsteady collector plate current measurements were taken at the thruster plume centerline for each of the three design types. Three new methods of extracting the macroscopic ion properties from the collected I-V-t curve data are also presented.

Section 4.1 details the experimental setup of the RPA experiments, as well as the RPA designs themselves. Section 4.2 contains the collected gridded RPA I-V-t curve data for the MiLiPulT plume. Section 4.3 contains the SC-RPA I-V-t curve data. Amplification methods for the MC-μRPA data collection process are described in Section 4.4, along with the corresponding I-V-t measurements for the MC-μRPA. Several methods of ion parameter extraction (data reduction methods) are presented in Section 4.5, in addition to the resultant parameters for each method, the computational error, and a discussion on the validity of these methods.

4.1 Collimating RPA Design and Experimental Setup

Since all three RPA design types would make use of a series of grids, it was advantageous to keep the design modular. A gridded RPA was designed with a removable front guard ring such that the collimating needle and the MCP could be easily installed for the SC-RPA and MC-μRPA configurations. Table 17 contains a complete list of the relevant dimensions and transmission parameters for each of the three RPA designs. The outer housing of the RPA was 2.54 cm in diameter, 3.00 cm in length, and made from an aluminum tube with an inner diameter of 2.22 cm. Figure 61 shows the basic RPA design, complete with grid and collector plate leads. The front guard ring was also made of aluminum and was 0.50 cm in thickness with an entrance hole diameter of 3.81 mm. The rear guard ring was made of Teflon, to ensure that the shielding was left floating in the plasma. The mount consisted of a brass 3/8" Swagelok male to male fitting for easy installation on the linear translation stage. The leads were color coded to avoid wiring mistakes when installing the RPA on the linear translation stage. Set screws were used to keep the front and back guard rings in place. All copper wire leads were housed in insulating tubing, and were soldered to D-pin connectors for easy installation and removal. The RPA was designed so that the collector plate wire and insulation tube were fed through the brass Swagelok mount and through the stainless steel tube of the translation stage such that a majority of the wire was electrically shielded. The other four grid wires exit the rear guard ring at 90° increments. A Teflon inner housing contains the grid series, the collector plate, and the insulating spacers. Set screws were used in the inner housing to clamp the grid and collector plate wires and prevent any tension on the leads outside of the RPA from breaking the solder joints to the grids. The grid, insulating spacers, and the collector plate all had diameters of 7.7 mm. The collector plate was cut from 100 μm thick molybdenum.

Table 17. Dimensions and transmission properties for all three RPA design types.

		RPA Design Type		
Parameter	**Nomenclature**	**Gridded RPA**	**SC-RPA**	**MC-mRPA**
Inlet Diameter	d	3.81 mm ± 0.07 mm	406 mm ± 5 μm	2 mm* ± 1 μm
Inlet Area	A	$1.14\text{x}10^{-5}$ m^2	$1.29\text{x}10^{-7}$ m^2	$2.01\text{x}10^{-10}$ m^2
Collimator Length	L	N/A	0.0508 m ± 0.07 mm	100 mm ± 5 μm
Diameter to Length Aspect Ratio	$D = d / L$	N/A	0.008	0.020
Frontal Cross-sectional Area to Incident Plasma	A_{cs}	$5.07\text{x}10^{-4}$ m^2 (2.54 cm O.D.)	$3.97\text{x}10^{-7}$ m^2 (711 μm O.D.)	$5.07\text{x}10^{-4}$ m^2 (2.54 cm O.D.)
Grid Thickness	t_{grid}	100 μm	100 μm	100 μm
Grid Wire Thickness	$t_{\text{grid,wire}}$	50 μm	50 μm	50 μm
Grid Wire Gap	$d_{\text{grid},\perp}$	650 μm	650 μm	650 μm
Hypotenuse Grid Wire Gap	$\left(\sqrt{2}/2\right) d_{\text{grid},\perp}$	919 μm	919 μm	919 μm
Grid Transmission Fraction[§]	χ_{grid}	0.75	0.75	0.75
Grid Series Transmission Fraction	$\chi_{\text{grid,total}}$	0.32	0.32	0.32
Grid Spacing	L_{grid}	1.52 mm	1.52 mm	1.52 mm
Distance from Source	$L_{\text{RPA-source}}$	0.080 m ± 0.07 mm	0.080 m ± 0.07 mm	0.037 m ± 0.07 mm

* 64 MCP hole array

[§] Assumes negligible collimation

The grids used were made from brass and had a thickness of approximately 100 μm. Although not required by the current collection theory, grid alignment was still a priority when soldering and installing each grid. After final assembly, all grids were observed to be within ±10° of a universal origin. Previous implementation and troubleshooting of the RPA using

similar brass grids with a wire spacing of 400 μm and a maximum hypotenuse (corner to corner) spacing of approximately 566 μm resulted in a transparency of ~40%. With four grids at 40% transparency each, the total transparency of the gridded aperture was estimated to have a maximum of 2.5%, but was more than likely much lower if the grids were misaligned. Due to possible misalignment and the relatively low transparency, conceivably no area of the collector plate had a direct line of sight to the uninhibited plasma flow outside of the RPA. Not surprisingly, collector plate current signals were observed to be non-existent at all ion retarding potentials despite applying the operational amplifier methods developed in Chapter 3. It was concluded that there were simply no ions reaching the collector plate. The RPA was then retrofitted with new brass grids having a transparency of ~75% and a wire spacing of 650 μm, resulting in a maximum hypotenuse separation of 919 μm from one etched grid channel corner to its opposite corner. The resultant overall transmission fraction of the grid series then became 0.32. Ultimately the true grid series transparency would also be a function of grid to grid alignment as well as the speed ratio and distribution function of the (possibly collimated and non-Maxwellian) plasma flowing through it. However, for the purposes of this research the collimating effects of the grids were assumed to be negligible.

The grid thicknesses were held constant at 100 μm to ensure minimal 'cupping,' a phenomena observed during 2D electromagnetic (EM) modeling (Marrese et al., 1997) and 3D unstructured Particle in Cell (PIC) simulations (Spirkin & Gatsonis, 2003) of RPA electrodes. Cupping is the result of potential field reduction near the midpoint of a given distance, the endpoints of which are biased to a specific value. Cupping is also the result of space charge limiting in the presence of highly dense plasmas. Previous single orifice RPAs have incorporated a second IRE to minimize cupping and to ensure the center of the electrode series

orifice presented the desired ion retarding potential to the incident plasma (Marrese et al., 1997). In this case, the combination of the relatively thick grids and the collimating single channel and multi channel designs will compensate.

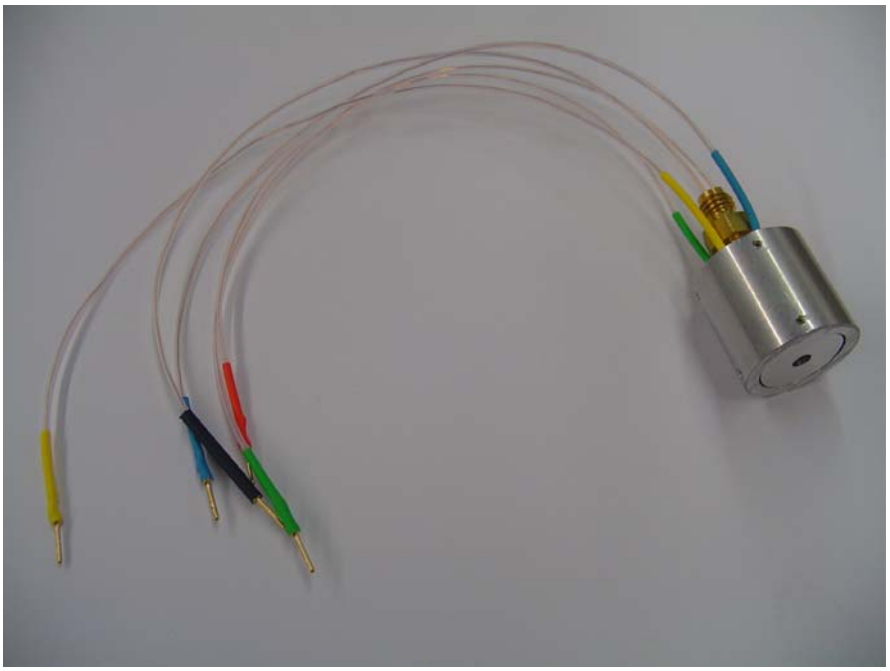

Figure 61. The gridded retarding potential analyzer (entrance aperture area = 1.14×10^{-5} m^2).

In the case of the baseline gridded RPA (no collimation) the plasma was found to be somewhat space charge limited, the observation of which would then prove the necessity of a collimating methodology to reduce the incident plasma number density. Such collimation is achieved with the SC-RPA design, which incorporates a long directional channel in front of the RPA grid series, as shown in Figure 62. The collimating needle is a 22 gauge stainless steel needle with a 1/8" NPT hub. The needle itself has an inner diameter of 406 μm and a length of 0.051 m, resulting in an overall diameter to length aspect ratio of 0.008 (i.e. the length is approximately 125 times the diameter). The length of the collimating channel obliged a minimum distance between the collector place and thruster face of 0.10 m. As such, the gridded

RPA was kept at this distance as well to provide an appropriate comparison between I-V-t curve data.

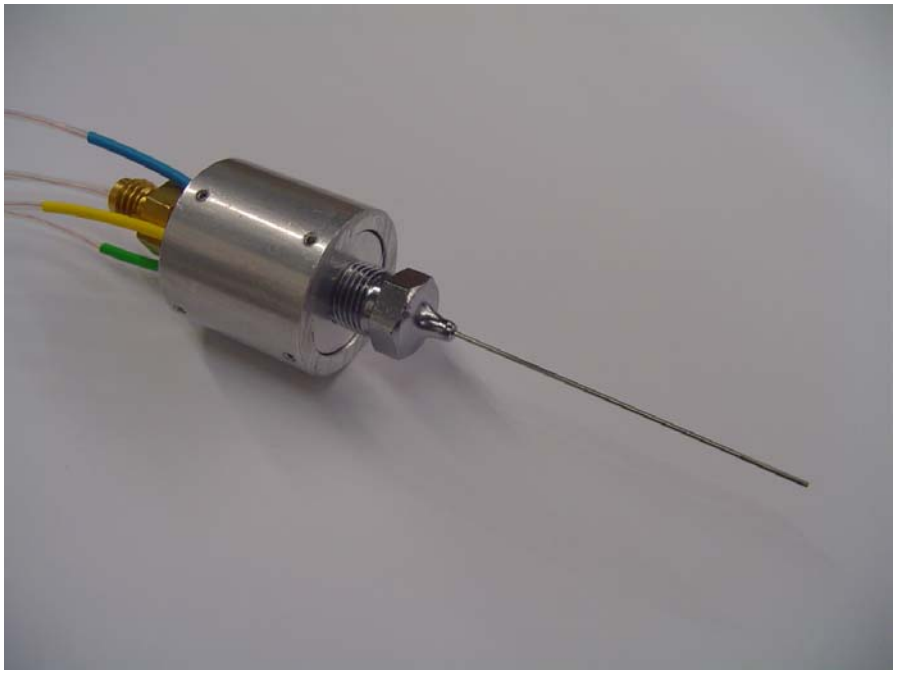

Figure 62. The collimating gridded RPA (entrance aperture area = 1.30×10^{-7} m^2).

The outer diameter of the collimating needle is 528 μm and as a result the needle presents incident plasma with an oblique area more than 1,000 times smaller than the gridded RPA. This reduction in effective frontal cross-sectional area from the reference frame of the incident plasma has the advantage of minimizing any shock effects or density gradients typically caused by a blunt stagnating surface typical of bulkier instrumentation.

A low transparency MCP consisting of sixty-four 2 μm diameter holes was incorporated into the gridded RPA design to produce the MC-μRPA. The MCP is made of 100 μm molybdenum, resulting in a channel diameter to length ratio of 0.02. The channels were formed using precision laser machining techniques, the diameters of which have a tolerance of ±1.0 μm. Although larger diameters would also be suitable for this application, the 2 μm channel

diameters were chosen because they represented the present limit of laser machining technology. This design results in less collimation over the SC-RPA needle, but the smaller channel diameters and overall entrance area ensure a lower number density within the grid series. The MCP was cut to size and spot welded onto the front guard ring surface from the gridded design with the more easily visible laser entrance side facing outward towards the thruster, as shown in Figure 63. As with all of the RPA parts, the MCP was thoroughly cleaned with acetone and isopropanol to ensure there was no extraneous material clogging the microchannels.

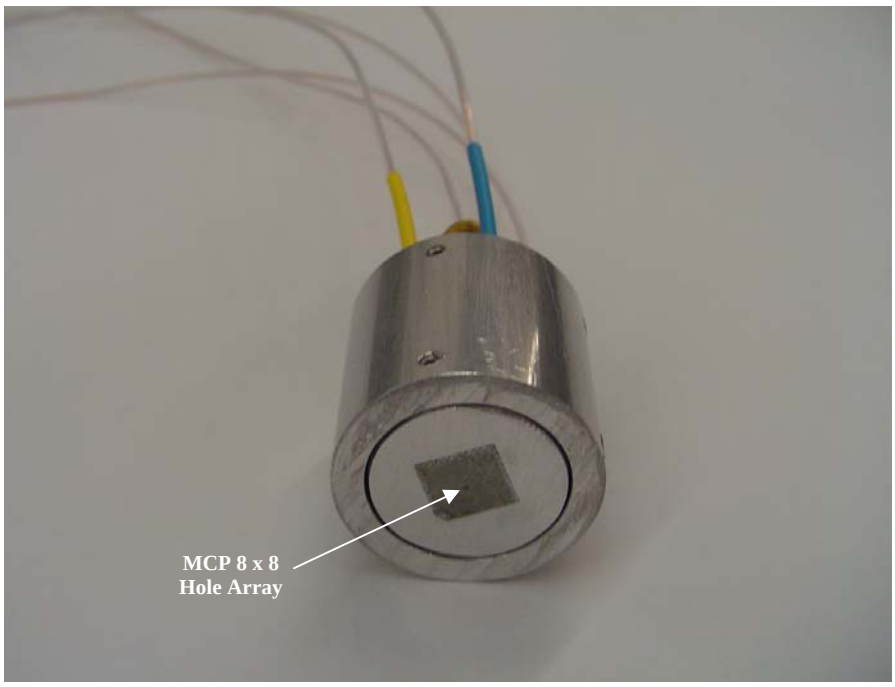

Figure 63. The gridded multi-channel μRPA (entrance aperture area = 2.01x10^{-10} m^2).

The column to column offset angle ϕ_{MCP} of the microchannels was set at 30° as viewed from left to right and the channel to channel spacing p_{MCP} along the -30° axis is 50 μm. The number of channels per unit area can then be calculated as

$$CpA = \left(2p_{MCP}2\cos\phi_{MCP}\sin\phi_{MCP}\right)^{-1}. \tag{4.1}$$

The number of channels per unit area for this MCP is 4.62×10^{-4} μm^{-2} with a geometric acceptance angle of 0.851^{o}, defined as

$$\theta_{MCP} = \pm \arctan(d/2L). \tag{4.2}$$

The corresponding aspect ratio is given by

$$AR = \pi \theta_{MCP}^2 \tag{4.3}$$

and has a value for this MCP of 6.93×10^{-4} steradians.

Figure 64 shows scanning electron microscope images taken of the MCP laser entrance and exit sides. The notch removed from the lower left corner of the MCP denotes the orientation of the 8 x 8 hole array. In other words, the notched corner corresponds to either the lower left or upper right corner of the laser entrance side of the MCP. Aside from requiring that the microchannels be aligned parallel to the plasma flux, the exact orientation of the MCP with respect to the thruster is not constrained in any other way.

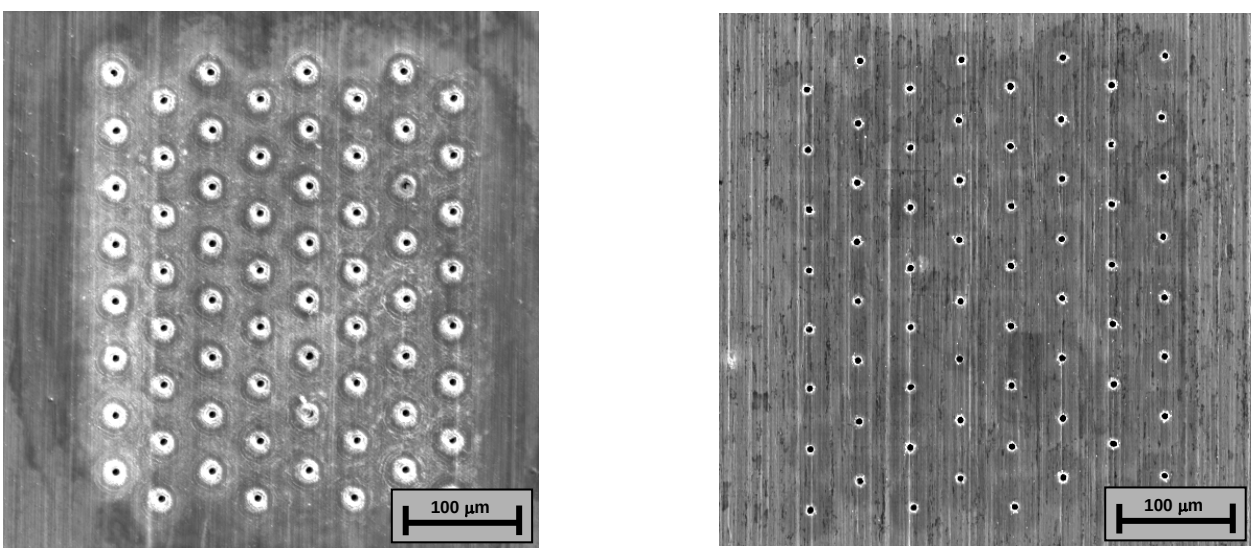

Laser Entrance Side **Laser Exit Side**

Figure 64. SEM imaging of the MCP used in the gridded MC-µRPA (channel diameter = 2 µm).

The gridded RPA was tested first. The gridded RPA configuration was installed on the linear traverse as shown in Figure 65. The entrance area of the RPA was aligned and centered with the

thruster orifice in all three dimensions. This was achieved by installing the RPA and positioning it as close as possible to the thruster face to ensure alignment in two dimensions. When backed away, the vertical placement of both the thruster orifice and center of the RPA entrance area were double checked at 6.6 cm ±0.1 cm from the translation table surface. The RPA was also checked for true level.

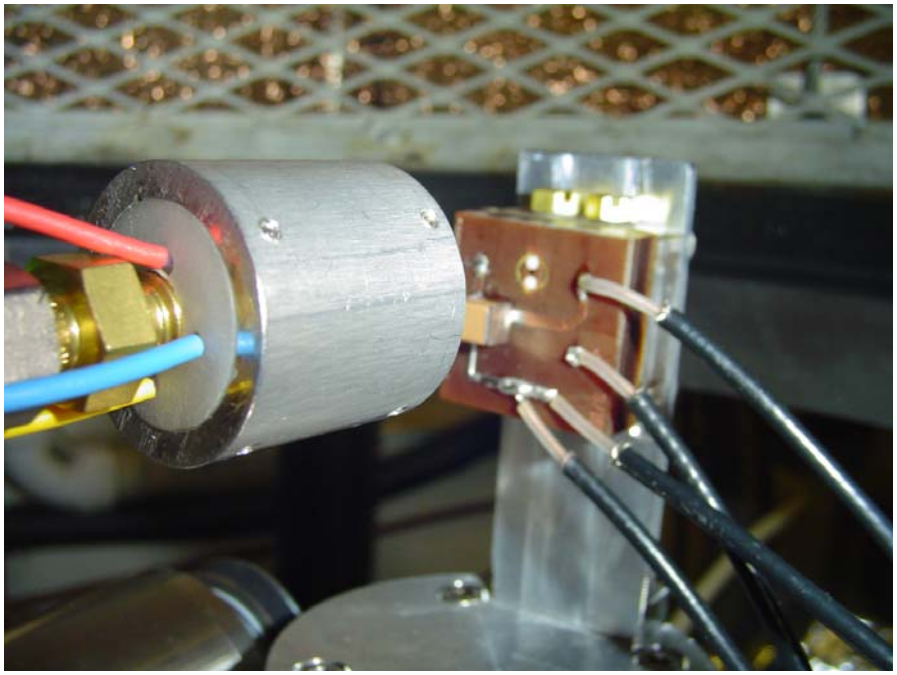

Figure 65. RPA installation in line with the MiLiPulT showing the floating shield configuration.

The RPA was not removed from the linear traverse when switching design configurations. Instead, the set screws to the front guard ring were loosened and the collimators were switched out accordingly. The alignment process, however, was repeated with each new configuration.

The distance between the gridded RPA entrance face and the MiLiPulT face was chosen as 8.0 cm such that there was sufficient space available to include the single channel needle and maintain the collector plate distance. Since the front face of the collector plate resides ~1.5 cm (within a measurable tolerance of about 2 mm) aft of the front aluminum guard ring, which has a thickness of 0.5 cm, the collector plate is considered as 0.1 m ±0.002 m away from the thruster

face in the case of the gridded RPA and SC-RPA. Since signal strength and alignment were both concerns for the highly flux limiting MC-μRPA, the probe-thruster distance was minimized to 3.7 cm.

The experimental setup is illustrated in Figure 66, most of which is identical to the TLP experimental setup. Additional power supplies were used to provide the IRE, ERE, and SESE potentials.

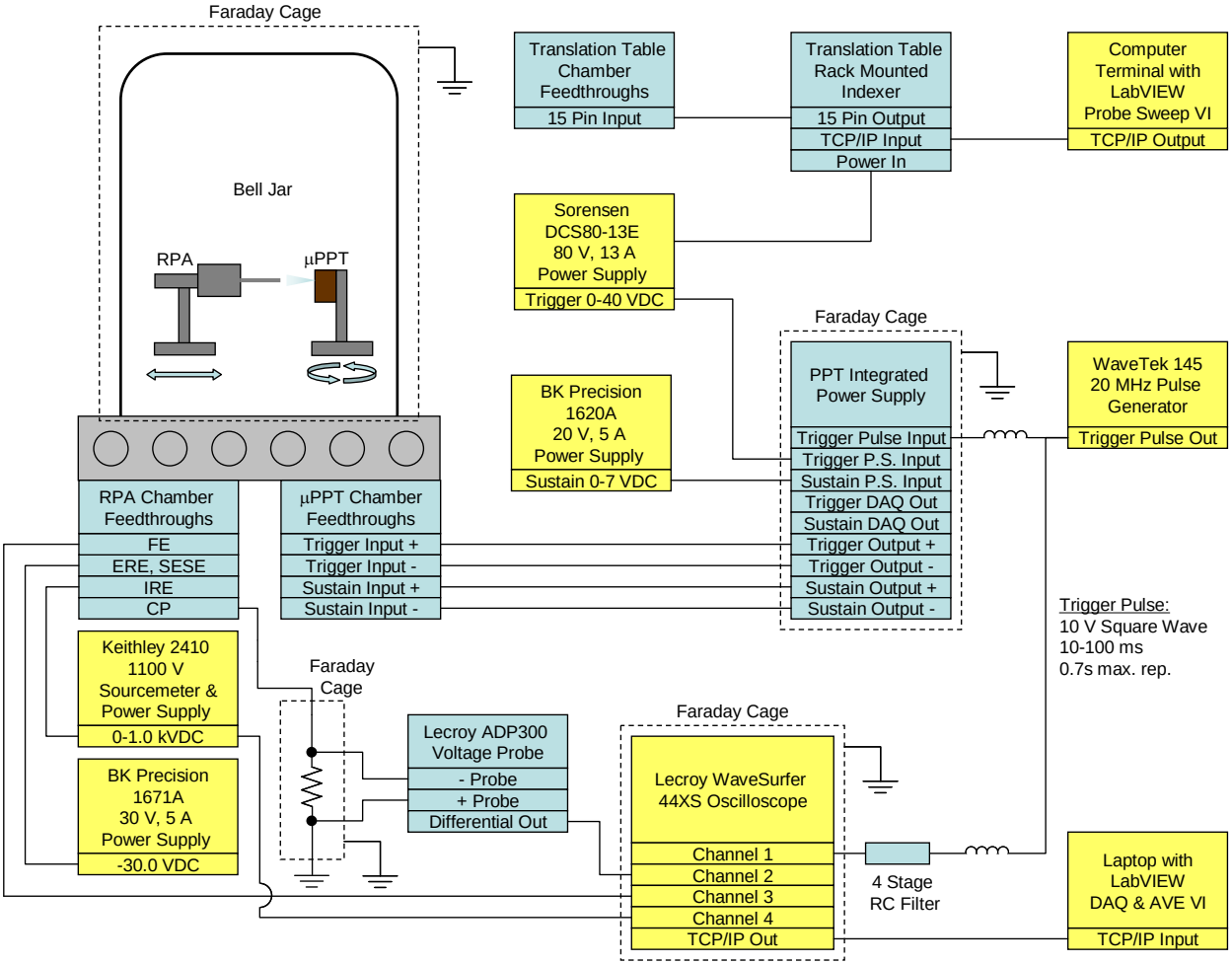

Figure 66. Experimental setup of the JHU/APL MiLiPulT plume characterization using RPA methodology.

The ERE and SESE grids were set at -30.0 V to repel nearly all electrons from the collector plate. To verify the elimination of electron current, the ERE was subjected to a 1.0 kV bias using the Keithley sourcemeter. Beyond roughly 20 V, no discernable increase in collector plate

current was observed during repeated thruster firings, indicating that the 30.0 V ERE bias would suffice.

A 100 Ω measurement resistor was placed between the collector plate and facility ground, and was protected by a Faraday cage. The voltage drop across this resistor was monitored by a Lecroy ADP300 20 MHz voltage probe. In the case of the SC-RPA, the measurement resistance was increased to 10 kΩ to provide a measurable voltage drop signal. In addition to recording the trigger pulse input signal (for oscilloscope triggering) and the collector plate current, the floating grid potential and the IRE potential were also recorded. A sample of the raw data collected for the gridded RPA is shown in Figure 67. Floating potential of the FE was observed to reach as high as 15.0 V with a shot to shot variance of ±5.0 V and an average of about 10.0 V. After the pulse, the floating potential would rapidly drop to approximately 1.0 V and then would slowly taper off to the zero after no more than 1.0 ms.

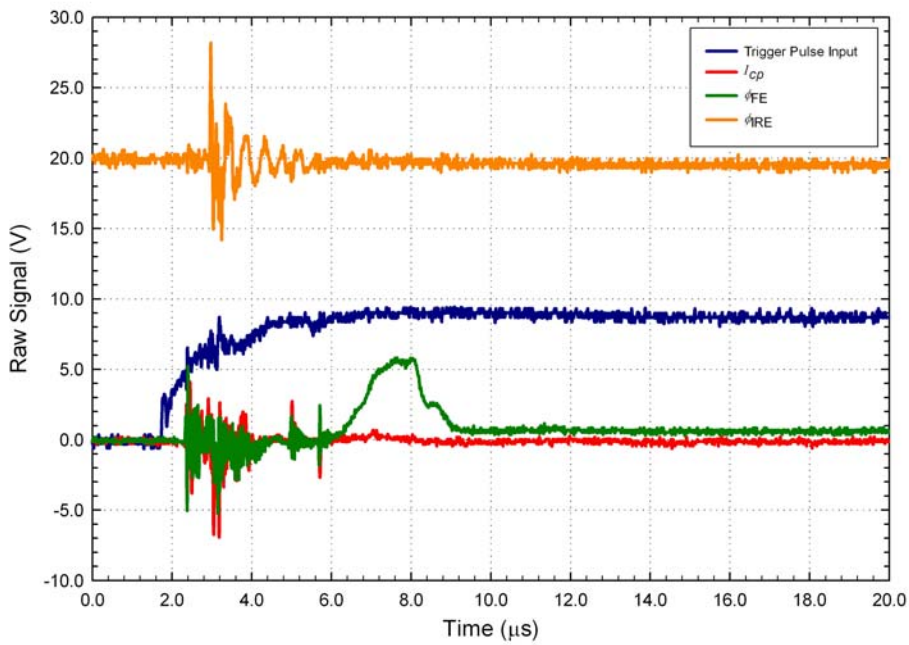

Figure 67. Example of the raw voltage signals from the gridded RPA experiments.

The leads of the Lecroy ADP300 voltage probe were reversed across the measurement resistor to confirm that the polarity of the collector plate current would also be reversed. This method provided an indication that the pulse was a true signal and not the result of common-mode or normal-mode noise. Collector plate current signals at high IRE voltages (1.0 kV) were also obtained to ensure that a negligible signal was obtained. This provided a check for proper setup, as well as to indicate the remaining signal noise. After single shot traces were validated, enhanced resolution (Eres) digital filtering set at +3.0 bits were applied. Each I-t curve represents an average of 10 thruster firings, to average out variations in both time and signal magnitude. I-V-t curve data were obtained for all three RPA designs at 5.0 V increments up to a maximum voltage where a distinct decrease in the I-V slope was observed.

4.2 Gridded Retarding Potential Analyzer Results

A surface plot representation of the MiLiPulT plasma I-V-t data collected using the gridded RPA configuration is shown in Figure 68. Peak collector plate currents occur at roughly 6.0 μs after thruster firing. The I-V curve corresponding to the peak currents at each point is not a perfectly sloping I-V curve for either a single species or multispecies plasma, but it does have an overall increasingly negative slope. The ridges at the end of the pulse vary slightly across IRE voltage, indicating that 10 thruster firings may not have been enough to provide sufficient points for a smooth average. Note that the IRE voltage axis is not the true decelerating voltage. From Chapter 2, the effective ion decelerating voltage also accounts for the unsteady floating potential. Subtracting the unsteady floating potential from each I-t curve would result in multiple points being colocated in the V-t. The aforementioned nature of the floating potential pulse obliges the adjustment of the peak currents towards the origin of the voltage axis. A plot

of the peak collector plate currents extracted from the surface plot is shown in Figure 69. Current traces for IRE potentials greater than 50.0 V were avoided because the currents were minimal under such circumstances.

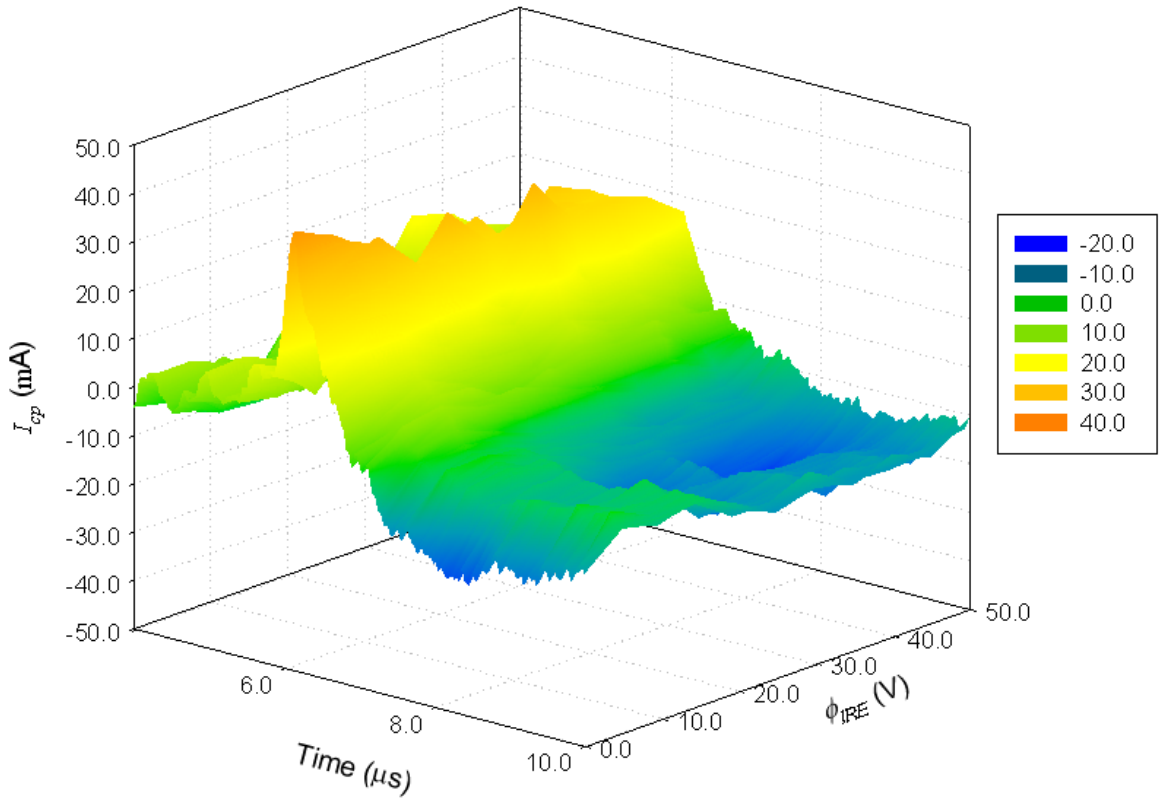

Figure 68. Surface plot representation of the gridded RPA I-V-t data.

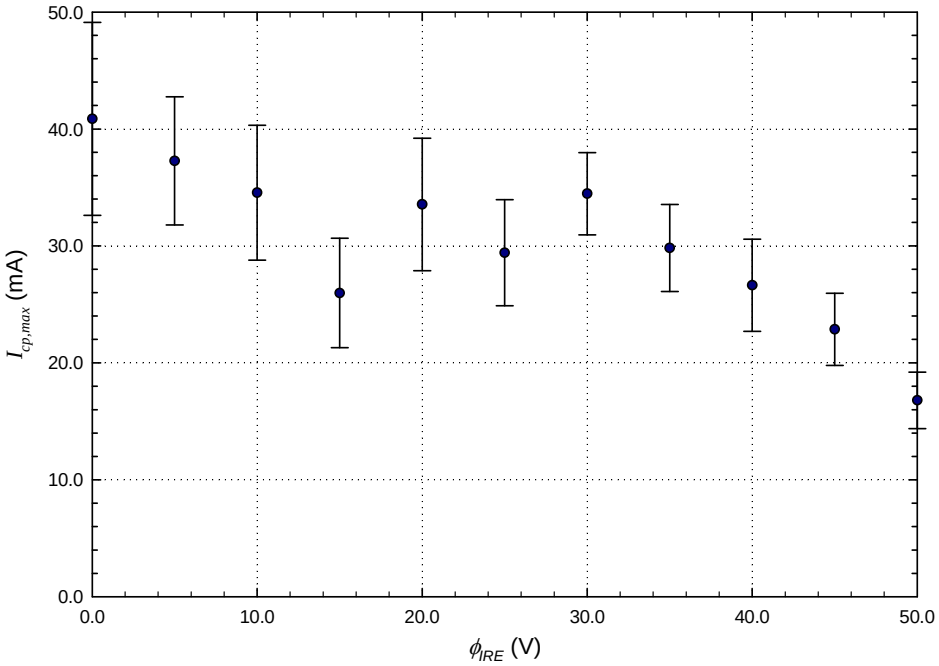

Figure 69. Maximum collector plate currents for the gridded RPA.

The error bars were calculated using a nonlinear least squares analysis involving the uncertainties associated with the measurement resistor, IRE potentials, and most significantly the floating potential and the estimated overall grid series transmission fraction (which is accounted for in the area uncertainty). Specifically, the error was calculated through a similar process as compared to the TLP uncertainty analysis. The collector plate current for the gridded RPA is first written as a function of various independent variables as

$$I_{cp,\text{Gridded RPA}} = f(T_i, n_i, c_{o,i}, A, \phi_{eff}, M_i, R_m)\,. \tag{4.4}$$

Full differentiation yields

$$\frac{\partial f}{\partial T_i}\Delta T_i + \frac{\partial f}{\partial n_i}\Delta n_i + \frac{\partial f}{\partial c_{0,i}}\Delta c_{0,i} = -\begin{pmatrix} \frac{\partial f}{\partial M_i}\Delta M_i + \frac{\partial f}{\partial A}\Delta A \\ + \frac{\partial f}{\partial \phi_{eff}}\Delta \phi_{eff} + \frac{\partial f}{\partial R_m}\Delta R_m \end{pmatrix} + \Delta I_{cp,\text{Gridded RPA}}\,. \tag{4.5}$$

However, since at this point the unknown sensitivity coefficients are not necessarily relevant (only the uncertainty in collector plate current is being plotted), the uncertainty calculation for collector plate current becomes a function of the known uncertainty coefficients given by

$$\Delta I_{cp,\text{Gridded RPA}} = \frac{\partial f}{\partial M_i}\Delta M_i + \frac{\partial f}{\partial A}\Delta A + \frac{\partial f}{\partial \phi_{eff}}\Delta \phi_{eff} + \frac{\partial f}{\partial R_m}\Delta R_m . \tag{4.6}$$

The uncertainty in effective potential manifests itself within the differentiated current collection theory equation as the corresponding uncertainty in effective velocity, which is also a function of the uncertainty in species ion mass via the relation

$$\Delta v_{eff} = \frac{2q\Delta \phi_{eff}}{\Delta M_i} . \tag{4.7}$$

It should be noted that the measurement resistance uncertainty factors into the overall current collection theory prior to dividing out the true amplification factor.

Specific values of the known uncertainty coefficients are listed in Table 18. Uncertainty in species mass is a result of the single species approximation. Uncertainty in measurement resistance is a result of the variance rating of the resistor. The area uncertainty factors in possible misalignment and the non-collimating transmission fraction of the grid series. Lastly, the uncertainty in effective potential is not only a function of the tolerance in the applied ion retarding potential which is listed in Table 18 with an asterisk, but also in the assumption that the floating potential approximates the plasma potential. As such the uncertainty in the effective potential is the dominant factor in the uncertainty analysis.

Table 18. Uncertainty values of the RPA MiLiPulT characterization experiments.

ΔA	3.652x10^{-6} μm^2
ΔM_i	7.227x10-27 kg
ΔR_m	4.915 Ohms
$\Delta \phi_{eff}$	0.001 V*

Estimates in the uncertainty of the effective potential is at least on the order of magnitude of the floating potential at its maximum (approximately 10.0 V) in addition to the differences between the floating potential and the true plasma potential. The uncertainty in the floating potential and effective retarding potential could also be assessed as horizontal error bars, although they would be the same for all points.

4.3 Collimating Retarding Potential Analyzer Results

Peak SC-RPA ion currents are on the order of tens of microamperes, as evidenced by the I-V-t surface plot representation contained in Figure 70. Again the general I-V slope trend is increasingly negative as applied IRE voltage is increased. The average time of peak current is unexpectedly longer than the gridded RPA data at roughly 7 μs. It was assumed the collimation would eliminate more of the low energy ions, providing an overall ‘faster’ ion beam.

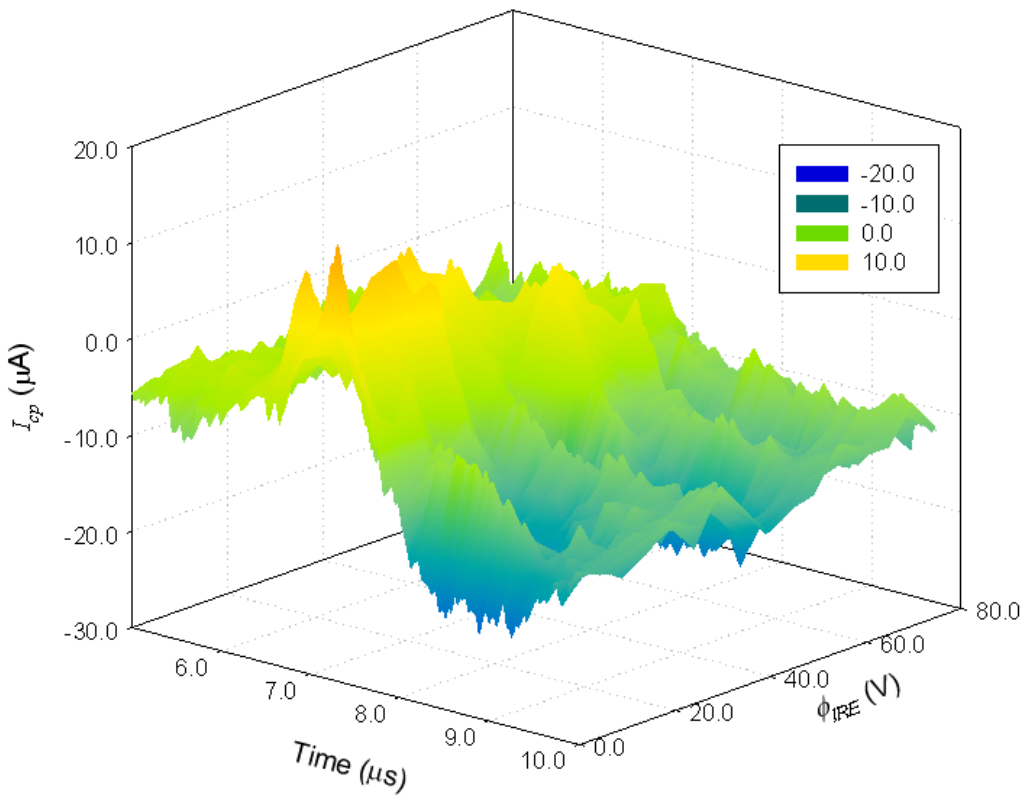

Figure 70. Surface plot representation of the SC-RPA I-V-t data.

The relatively large variance in the ridges amongst the IRE voltage values can again be attributed to insufficient thruster shot averaging. Better averaging of either 50 or 100 thruster firings per IRE voltage is recommended. Figure 71 contains a peak I-V plot of the SC-RPA data.

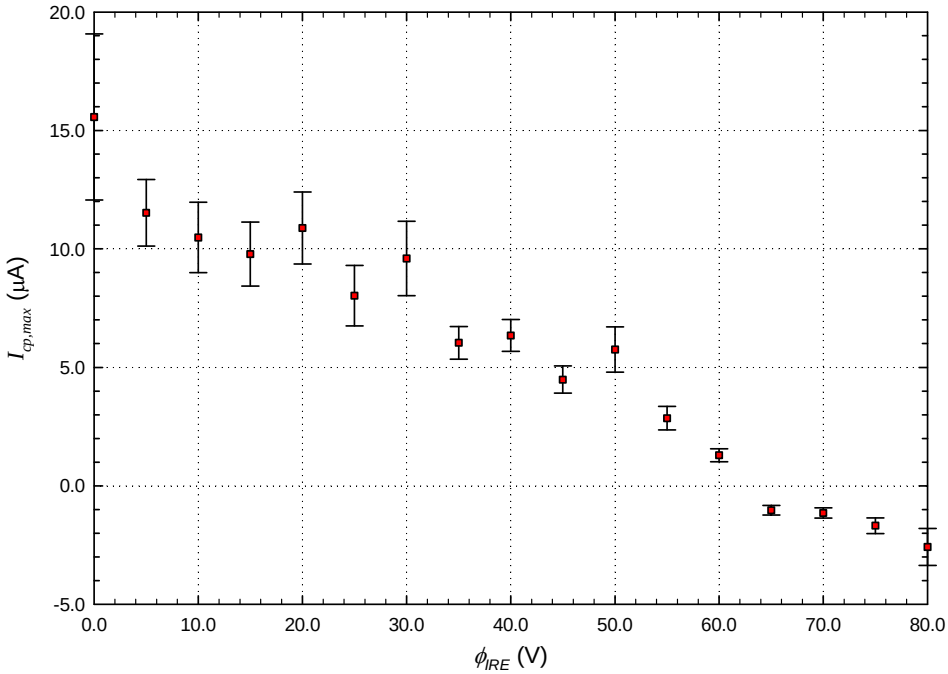

Figure 71. Maximum collector plate currents for the SC-RPA.

The vertical error bars for the collector plate were calculated using the same uncertainty analysis as outlined for the gridded RPA. It should be noted that additional uncertainty coefficients corresponding the diameter and length of the collimator should also factor in to the uncertainty analysis. However, the differentiation of the collimating current collection theory with respect to these variables becomes too cumbersome to calculate (even in the case of the separation approximation). Fortunately, from Table 17 these uncertainties are relatively small compared to the dominant uncertainty coefficients. Consequently these uncertainties are considered negligible. The negative current values for the relatively high IRE potentials could be a result of possible encroachment of electrons. At these high IRE potentials, the negative applied electric field at the ERE may be compromised by the large gradient to the positive electric field. More than likely this is just an artifact of the signal measurement calibration itself. Data beyond an IRE voltage of 60.0 V was discarded in the IPEM analysis.

4.4 Multi-channel Micro-Retarding Potential Analyzer Results

The particularly low entrance area of the MC-μRPA resulted in current signals on the order of tens of nanoamperes and required further amplification. The instrumentation amplifier from channel 1 of the TLP bias circuit was used, which had a calibrated amplification ratio of 9.29. A measurement resistance of 9.88 MΩ was applied, resulting in an overall current signal amplification of 9.18×10^7. The particularly large measurement resistance was applicable since it was assumed that the electrons flowing through the circuit to the collector plate to counteract the impingent ions had no other closed circuit path with comparable resistance. The voltage follower configurations provide the only alternate circuit path, but provide an impedance which is much greater than the measurement resistor. The resultant amplified voltage signals for the collector plate currents were monitored for operational amplifier saturation, but with the measurement and amplifier resistances chosen, no saturation was observed. This absence of saturation was confirmed both with and without Eres digital filtering applied to the channel using the Lecroy oscilloscope. Figure 72 shows an example of the converted collector plate currents both with and without Eres filtering applied. The maximum voltage of the unfiltered signal in this case was 6.36 V, which is well below the saturation voltage of approximately 18.0 V. Note that the Eres filtered trace and the unfiltered case do not correspond exactly to each other, as they were from separate thruster firings. A smooth tapering of the current signals was observed which was not present within the collected data for the previous two RPA designs. This was attributed to the slew rates inherent to the operational amplifiers. Additionally, the signals appear to initiate slightly closer to time $t = 0$ over the previous RPA I-V-t data. Peak currents occur at approximately 5.0 μs after thruster discharge initiation. This is most likely because the MC-μRPA was located less than half the distance to the MiLiPulT compared with the other

RPAs in order to maximize signal strength. This could also be attributed to the fact that the collimated ion beam consists mostly of high energy ions by the time it reaches collector plate, more so in this case as compared to the SC-RPA.

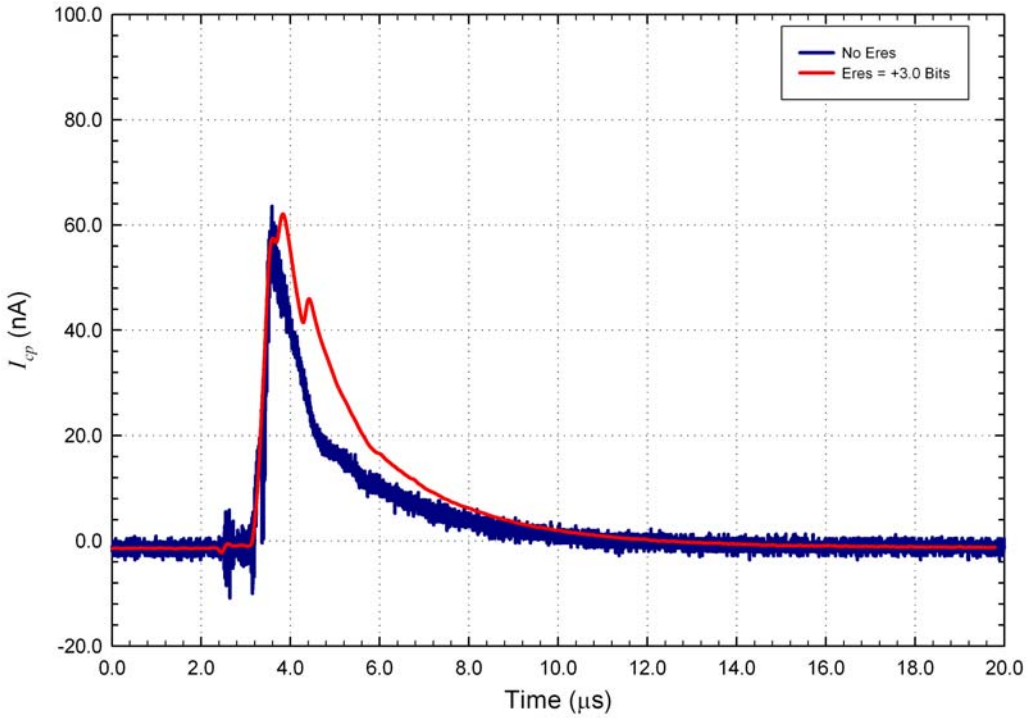

Figure 72. Comparison of MC-μRPA collector plate current traces with and without digital filtering.

It is possible that this signal is a combination of true signal and the result of over amplified noise from the capacitive discharge, but the typical MiLiPulT noise is also present before the pulse. When compared to the trigger pulse input waveform, the current signal occurs at a slightly later time than the noise, as is the case with the other RPA and TLP measurements.

A 3D surface plot representation of the I-V-t data collected using the MC-μRPA is shown in Figure 73. Maximum collector plate signal magnitude is on the order of tens of nanoamps, and decreases as IRE voltage is increased. Data were collected up to applied IRE potentials of 100 V. Peak currents are plotted against the applied IRE voltage in Figure 74. Error decreases

as applied IRE voltage is increased as a direct result of the IRE potential becoming much larger compared to the assumed and somewhat more uncertain plasma potential.

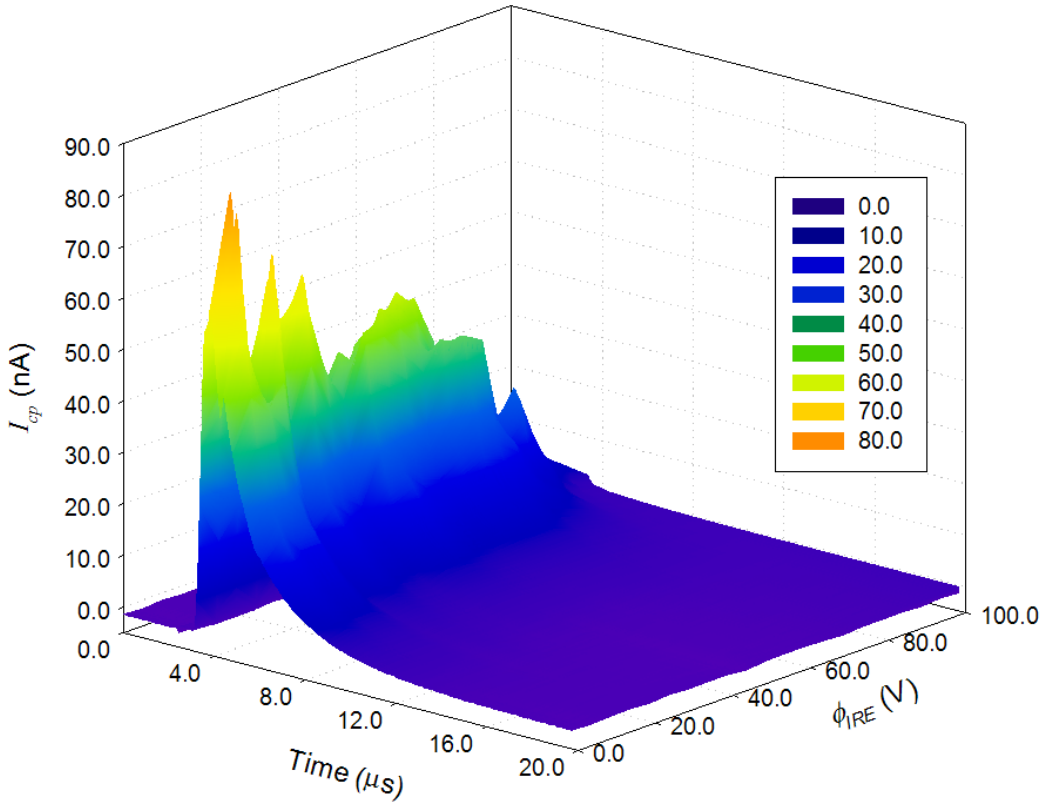

Figure 73. Surface plot representation of the MC-μRPA I-V-t data.

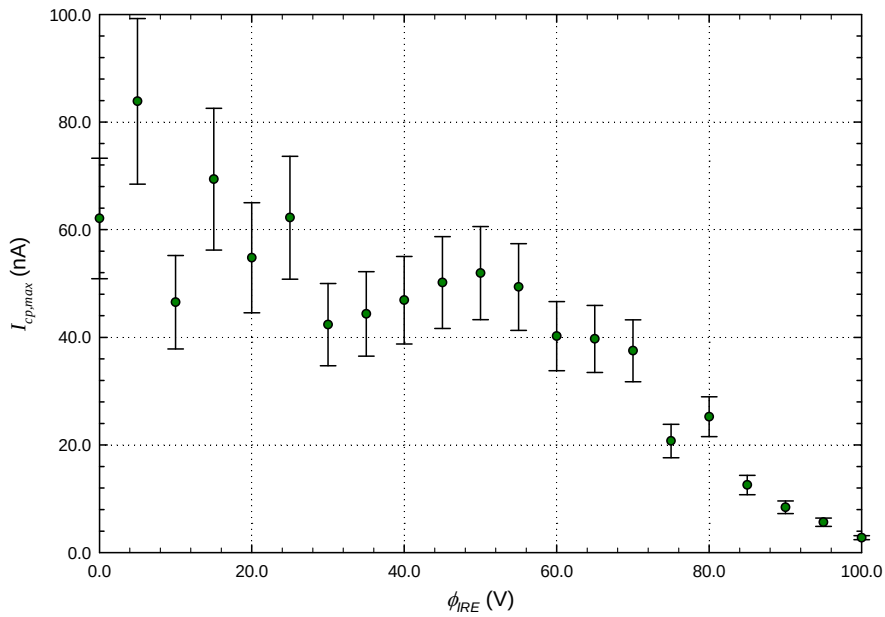

Figure 74. Maximum collector plate currents for the MC-μRPA.

Vertical error bars were calculated using a similar method to the previous two RPA uncertainty analyses. Again, the uncertainty due to the diameter to length ratio is considered negligible since these values are well known from the specifications of the laser-machined MCP as well as from direct measurement using the scanning electron microscope. Since the operational amplifier methods were applied, it becomes necessary to account for an additional uncertainty relating to the true amplification ratio of the input amplifier. From Table 15, this value was calculated as $\Delta H_0^* = 0.231$ and is applied as a directly proportional constant to the overall current, since it relates the raw voltage waveform to the true current value. The peak I-V curve vaguely indicates two ion species with the presence of an additional local maxima occuring at an applied voltage of ~50.0 V. Ideally the second ion species would manifest itself as an inflection point on the I-V curve and not an actual local maximum (Kelley, 1989). The presence of a positive slope on the I-V curve can be attributed to thruster shot averaging error.

4.5 Ion Parameter Extraction Methods, Reduced Results, and Discussion

Previous ion parameter extraction methods (IPEMs) have primarily consisted of nonlinear least squares analyses (NLSA) for both single and multispecies plasmas (Kelley, 1989; Shumlak et al, 2003). Iterative fuzzy logic methods were also demonstrated for a single species sample I-V curve generated using the current collection theory initially developed for a single-orifice RPA (Partridge, 2005). NLSA cannot be applied to any current collection theory which requires numeric integration to calculate current values from a given set of ion number density, temperature, speed ratio, and species concentrations. The reverse process of obtaining ion parameters from a set of I-V curve data points is limited by the complexity of the appropriate current collection theory. One IPEM entails the generation and storage of multiple I-V curves in the form of 'lookup tables.' The experimental curve is then compared to the set of I-V curve lookup tables to find the closest match. A more accurate and expedient process involves the iterative generation of successive I-V curves based on consistently refined estimates for the ion parameters, starting with some initial guess. If the new estimates are based on known rules for the nature of I-V curves (i.e. an increase in estimated ion number density increases the overall magnitude of the I-V curve), the generated set of curves will rapidly converge on the experimental curve. This process is foundation of the iterative fuzzy logic IPEM program, where the fuzzy logic rule set contains a generalized rule for each ion parameter. As an example, should the generated curve have a lower slope as compared to the experimental slope, the ion temperature and/or speed ratio is increased, and vice versa. Three separate IPEMs were developed in MATLAB and tested on the collected I-V-t data from the three RPAs. The individual current collection theory for each of these methods comprised a separate MATLAB

function which could then be called by a larger m-file containing the fuzzy logic iteration framework and I/O subroutines.

The RPA IPEM code is contained in Appendix D and includes all of its called functions. The RPA IPEM program assumes a a Maxwellian plasma with a known single species ion mass. For the purposes of this research, an average atomic weight of 8.505 was used assuming a 50% molar fraction between hydrogen and oxygen ions. While this approximation for mass would affect the results minimally (i.e. collisions parameters, speed ratios, and distributions are not affected significantly by changes in mass), the results could be bounded by performing ion parameter extraction using both masses of oxygen and hydrogen separately. The two masses could also be processed separately assuming each species is at half density, and then the results could be averaged. This resulted in an approximate ion mass of 1.423×10^{-26} kg. After defining physical constants, the RPA geometry, and the initial guess of ion number density, ion temperature, and ion speed ratio, the RPA IPEM program reads in the peak I-V data for a given RPA design, and applies a polyfit to obtain a smoothed I-V curve. Figure 75 shows the polyfits of the gridded RPA data for degrees of both 2 and 3. Polyfits of the SC-RPA and MC-μRPA data are shown in Figure 76 and Figure 77, respectively. For the purposes of data reduction, the polynomial degrees of the polyfits were kept at 2. Increasing the polyfit degree to 3 or above allowed for the polyfit equations to produce inflection points normally present in a multispecies I-V curves. A polyfit for the gridded RPA data with a polynomial degree of 4 produced a severe local maxima with respect to the I-V curve data. Resolution of the polyfit I-V curves being generated can also be specified.

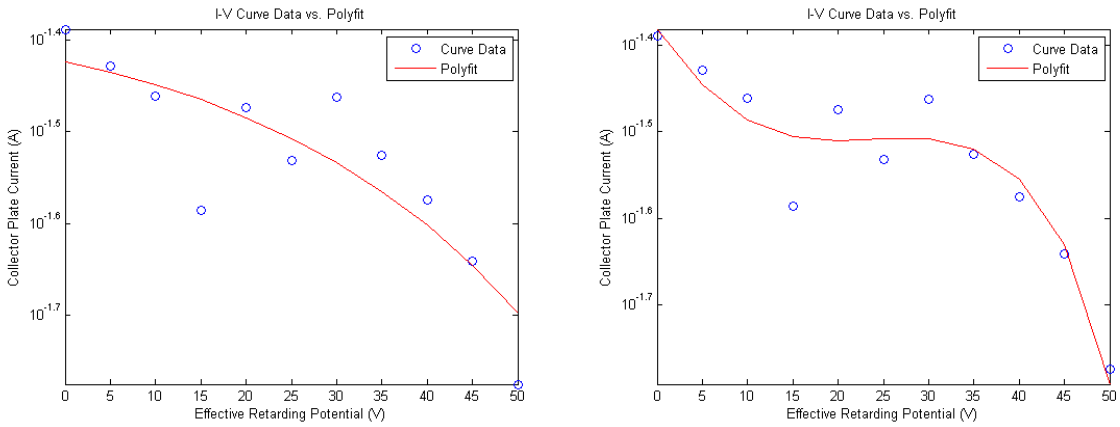

Figure 75. Polyfits of maximum gridded RPA I-V data: Polyfit degree of 2 (left) and polyfit degree of 3 indicating multispecies (right).

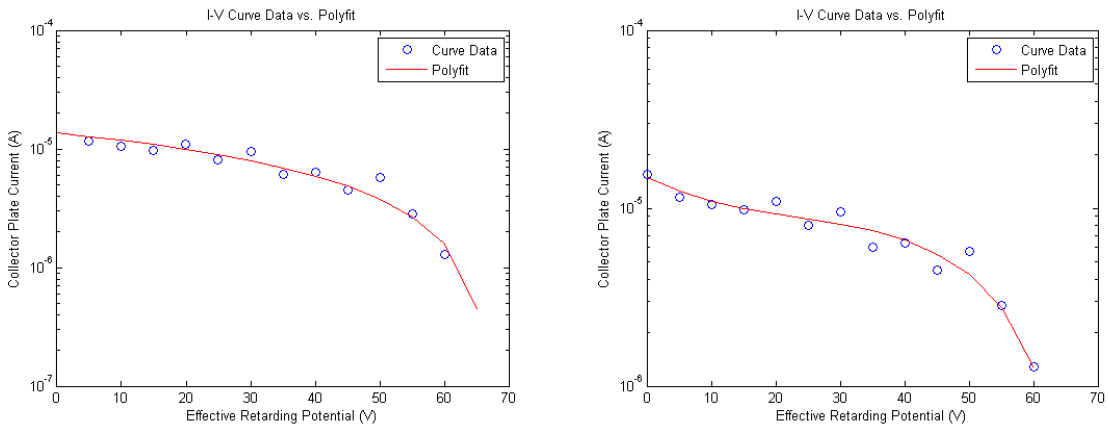

Figure 76. Polyfits of maximum SC-RPA I-V data: Polyfit degree of 2 (left) and polyfit degree of 4 indicating multispecies (right).

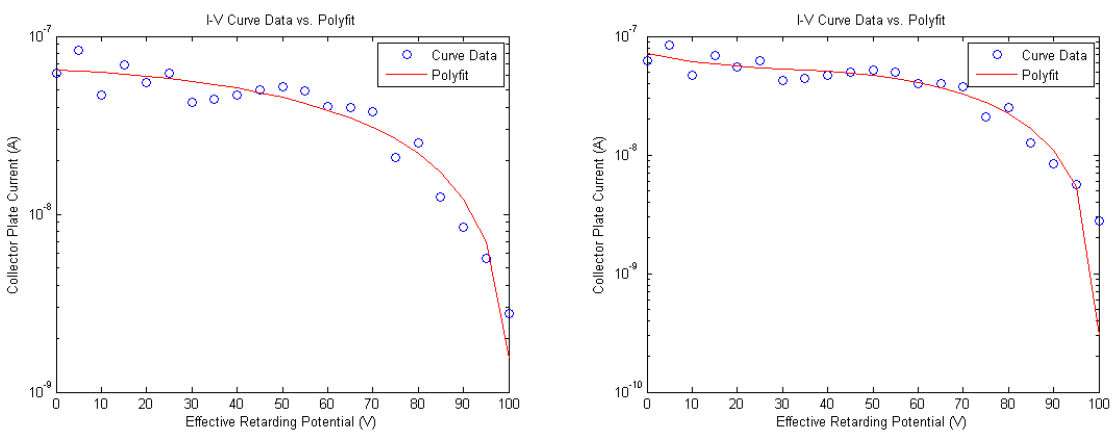

Figure 77. Polyfits of maximum MC-μRPA I-V data: Polyfit degree of 2 (left) and polyfit degree of 4 indicating multispecies (right).

The next subroutine of the IPEM program calls a specified current collection theory function to generate the I-V curve based on that iteration's macroscopic ion properties. The three individual IPEM functions developed in MATLAB were termed the classic IPEM, the separation IPEM, and the collimating IPEM. The classic IPEM method corresponds to the NLSA method for a gridded RPA in that it applies the classical current collection theory stated in Kelley (1989). This theory, demonstrated for a single species in (2.91) as the Maxwellian drifting ion flux through a surface at an applied potential. The theory accounts for both the collector plate area and the overall grid transparency and was relatively straightforward to implement in MATLAB to generate a current value based on an effective ion decelerating voltage and a given set of ion parameters. Once a curve is generated for a given iteration, the slopes and zero bias magnitudes for both the experimental curve and the generated curve are calculated and compared. The aforementioned fuzzy logic rules are applied to generate the next iteration's ion parameter estimates. This process is repeated until convergence to within a specified amount of error is reached. The error is calculated using the absolute values of the differences between the real and generated data points, normalized over the curve. The progression of the IPEM generated curves towards the experimental curve is shown in Figure 78. The experimental curve is plotted in red, while the I-V curve generated by the initial guesses is displayed in green. The blue curves indicate the decreases in slope achieved by the fuzzy logic rules for the ion speed ratio and temperature.

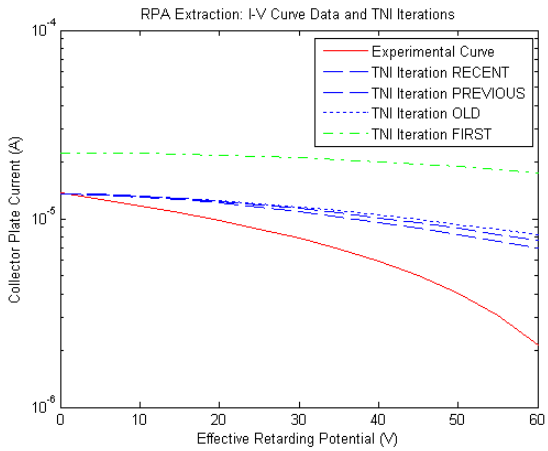

Figure 78. Example of RPA IPEM iteration towards I-V curve convergence.

The allowable change in values of the ion parameters between iterations could be specified in the IPEM m-file. Typically these parameter resolutions were set to one tenth of the initial guess value. The IPEM program would be executed and monitored until rough convergence was reached and then stopped. The program would then be restarted with the updated parameters with resolutions of one hundredth the current parameter value. Typically, the ion number density estimates would converge more rapidly than the ion speed ratio and temperature. Uniqueness of the final set of ion parameters is ensured because they are each uniquely proportional to the collector plate current. Additionally, the fuzzy-logic rules were constructed so as to avoid competing changes in ion speed ratio and temperature resulting in divergence or a trend towards poorer curve fit with different parameter values.

The separation IPEM function operates on the same iteration and convergence process as the classic IPEM function, except that it employs an alternative method of calculating the comparative I-V curves. Operating under the separation approximation explained in Chapter 2, the separation IPEM function uses (2.109) to generate I-V curves. The separation approximation is a simplification of the true flux limitations present in a collimating RPA design. Specifically, the separation approximation assumes that the ion retarding flux limitations present within the

grid series are independent of the cylindrical channel flux limitations present within the collimator. As such, any changes to the ion flux exiting the collimator are assumed to preserve the Maxwellian nature of the distribution. While this is not an accurate portrayal of the true flux limitations, it provides a simplified current collection theory. The known collimator geometry and guess for the speed ratio are used to calculate the collimating transmission fraction by (2.100) and (2.106), and is applied as being directly proportional to the collector plate current. As a small but significant contributing factor to the flux defined by (2.100), the double integral in (2.103) requires numeric integration. Math solvers were unable to either analytically or numerically integrate this function due the cosine term present within the error function term. Similar difficulties were encountered when trying to integrate the single-orifice RPA current collection theory, which were addressed through the application of nested triple numeric integration (Partridge, 2006). In a similar fashion, nested double numeric integration of (2.103) is performed in MATLAB using a composite Simpson's rule approximation of the integral using quadratic interpolation. This algorithm was validated for a test function of

$$h(x,y) = \int_0^1 \int_0^{g(y)} f(x)dxdy = \int_0^1 \int_0^{y^2} x^2 dxdy = 1/21\,. \tag{4.8}$$

In essence the outer integral is divided into small subintervals and evaluated based on Simpson's rule, in turn requiring the division and evaluation of the inner integral subintervals. A subinterval resolution of 100 x 100 would result in 10,000 subinterval calculations of the innermost integral. Careful analysis of the subinterval resolutions for the test function yielded an error of 0.67% for a subinterval resolution of 500 x 500, down to 0.08% for a subinterval resolution of 4000 x 4000. Further increase in the subinterval resolution was found to be overly computationally expensive. Since the collimator is assumed floating, the actual potential of the channel walls are assumed not to contribute ion flux limitations, thus avoiding repeated triple

numeric integration of (2.105). Once the collimating transmission fraction for a given iteration's assumed speed ratio is calculated, it is assumed invariant over all velocity classes and would theoretically effect the Maxwellian distribution equally as a proportional constant.

Subsequent to the implementation of the nested double numeric integration algorithm for calculating flux based on (2.103), further analytical integration was achieved using an approximation for the error function and various algebraic manipulations. The inner integral was first divided into two separate integrands, as shown by

$$\int_0^{\tan^{-1} D\sqrt{1-Y^2}} \text{Integrand}_1 d\varphi = \int_0^{\tan^{-1} D\sqrt{1-Y^2}} \cos\varphi \exp(-S^2 \sin^2 \varphi) d\varphi \tag{4.9}$$

and $$\int_0^{\tan^{-1} D\sqrt{1-Y^2}} \text{Integrand}_2 d\varphi = \int_0^{\tan^{-1} D\sqrt{1-Y^2}} erf(S\cos\varphi)\cos\varphi \exp(-S^2 \sin^2 \varphi) d\varphi \,. \tag{4.10}$$

Based on the definition $u = S\sin\varphi$ resulting in $\cos\varphi d\varphi = \dfrac{du}{S}$, substitution yields

$$\int_0^{\tan^{-1} D\sqrt{1-Y^2}} \text{Integrand}_1 d\varphi = \frac{1}{S}\int_0^{u_l(Y)} \exp(-u^2) d\varphi \,, \tag{4.11}$$

where $u_l(Y)$ is the upper bound function resulting from the modification of the bounds of integration and is defined as

$$u_l(Y) = \frac{SD\sqrt{1-Y^2}}{\sqrt{D^2(1-Y^2)+1}} \,. \tag{4.12}$$

With the definition of the error function given by

$$\text{erf}(x) = \frac{2}{\sqrt{\pi}}\int_0^{\infty} \exp(-\xi^2) d\xi \,, \tag{4.13}$$

the evaluation of the inner integral for the first integrand reduces to

$$\int_{0}^{\tan^{-1} D\sqrt{1-Y^2}} \text{Integrand}_1 d\varphi = \frac{\sqrt{\pi}}{2S} \operatorname{erf}(u_l(Y)) \,. \tag{4.14}$$

The second integrand requires an approximation for the error function to allow for analytical integration of the inner integral. Specifically, this approximation is given by Hastings, Jr. (1955) as

$$\operatorname{erf}(x) \approx 1 - (a_1 t + a_2 t^2 + a_3 t^3 + a_4 t^4 + a_5 t^5) \exp(-x^2) \,, \tag{4.15}$$

where

$$t = \frac{1}{1 + 0.3275911x} \,, \tag{4.16}$$

Along with the following set of defined constant coefficients:

$$\begin{aligned} a_1 &= 0.254829592, \\ a_2 &= -0.284496736, \\ a_3 &= 1.421413741, \\ a_4 &= -1.453152027, \\ \text{and } a_5 &= 1.061405429. \end{aligned} \tag{4.17}$$

This approximation is valid for $0 \le x \le \infty$ to within $\pm 1.5\text{x}10^{-7}$. In this case, $x = S\cos\varphi$, yielding

$$\int_{0}^{\tan^{-1} D\sqrt{1-Y^2}} \text{Integrand}_2 d\varphi = \int_{0}^{\tan^{-1} D\sqrt{1-Y^2}} (1 - (a_1 t + ...)) \cos\varphi \exp(-S^2 \cos^2\varphi) \exp(-S^2 \sin^2\varphi) d\varphi \,, \tag{4.18}$$

which then simplifies to

$$\int_{0}^{\tan^{-1} D\sqrt{1-Y^2}} \text{Integrand}_2 d\varphi = \int_{0}^{\tan^{-1} D\sqrt{1-Y^2}} (1 - (a_1 t + ...)) \cos\varphi \exp(-S^2) d\varphi \,. \tag{4.19}$$

The terms

$$a_n t^n = \frac{\cos\varphi}{\left(1 + 0.3275911 \cdot S\cos\varphi\right)^n} \tag{4.20}$$

are able to be analytically integrated for $n = 1,2,3,4,5$. This method still requires numeric integration of the outer integral, which was performed using the Gauss Quadrature method in MATLAB. IPEM results using this approximation versus the DNI method with 4000 x 4000 subintervals were comparable to within 0.37%, with a greatly increased computational efficiency.

The third and perhaps the most complex IPEM function contains the full collimating current collection theory. The collimating IPEM function calculates a transmission fraction distribution as a function of velocity for the known collimator geometry and the assumed speed ratio, similar to the qualitative curves shown in Figure 25. This function is then multiplied with the Maxwellian distribution generated from the set of ion parameter estimates, producing the non-Maxwellian distribution function representing the ion flux exiting the collimator and entering the electrode series. Calculation of the ion species contribution to collector plate current is then a matter of numerically integrating the new distribution function as bounded by the ion decelerating potential. This process is repeated over IRE bias voltage to produce an I-V curve to be used in the same convergence algorithm used for the previous two methods. Figure 79 shows an example of the calculated collimating transmission fraction as it is applied to a Maxwellian distribution function. A sample velocity corresponding to the effective ion decelerating voltage is also represented. The area under the non-Maxwellian collimated distribution function bounded by the effective voltage contributes to the collector plate current.

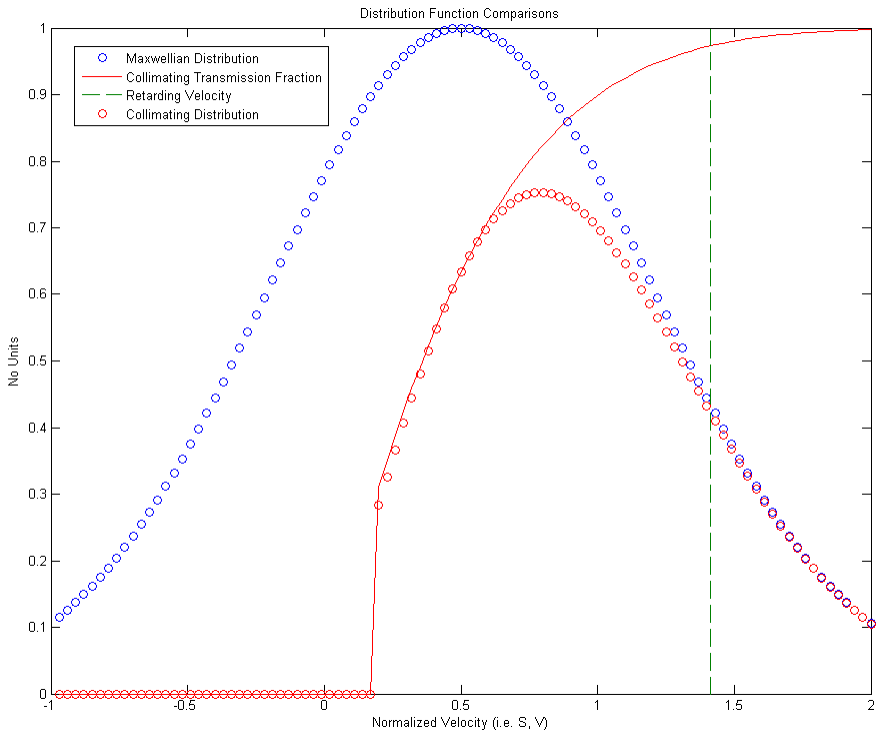

Figure 79. Collimated distribution function as a result of a Maxwellian distribution affected by the collimated transmission fraction (S_i = 0.5, D = 0.02, T_i = 1.0 eV, ϕ_{eff} = 2.0 V).

Note that for large ion retarding voltages, the two distributions approximate each other. This can be attributed to the high energy ions traveling through the collimator uninhibited. The resultant collimating transmission fraction approaches 1.0 towards the high-energy tail of these distributions. As such, the separation approximation is accurate provided that only high IRE potential data points on the I-V curve are considered in the post-processing.

All three IPEM functions were tested using the collected MiLiPulT peak I-V curve data from all three RPA designs. The extracted macroscopic ion parameters are listed in Table 19. The collimating transmission fraction for the gridded RPA as used by both the separating and collimating IPEMs was assumed to be 1.0. As such the ion parameter estimates remained unchanged over IPEMs for the gridded RPA data.

Table 19. Macroscopic ion properties for all three RPA designs as determined by all three IPEM functions.

	RPA Design Type		
Parameter & Reduction Method	**Gridded RPA**	**SC-RPA**	**MC-μRPA**
Peak Ion Number Density/ Classic IPEM	2.39×10^{18} m^{-3}	1.24×10^{17} m^{-3}	1.92×10^{17} m^{-3}
Peak Ion Number Density/ Separation IPEM	2.39×10^{18} m^{-3}	1.19×10^{18} m^{-3}	1.71×10^{17} m^{-3}
Peak Ion Number Density/ Collimating IPEM	2.39×10^{18} m^{-3}	1.18×10^{18} m^{-3}	1.68×10^{17} m^{-3}
Ion Temperature at Peak I_{cp}/ Classic IPEM	2.63 eV	2.61 eV	2.64 eV
Ion Temperature at Peak I_{cp}/ Separation IPEM	2.63 eV	2.14 eV	1.94 eV
Ion Temperature at Peak I_{cp}/ Collimating IPEM	2.63 eV	2.09 eV	1.72 eV
Ion Speed Ratio at Peak I_{cp}/ Classic IPEM	1.10	0.61	1.35
Ion Speed Ratio at Peak I_{cp}/ Separation IPEM	1.10	0.63	1.74
Ion Speed Ratio at Peak I_{cp}/ Collimating IPEM	1.10	0.54	1.59
Collimating Transmission Fraction/ Separation IPEM	N/A	0.7493	0.9925
Collimating Transmission Fraction/ Collimating IPEM	N/A	0.7280	0.9785

The larger number density as observed by the gridded RPA could be attributed to space charge limiting effects present within the grid series. The collimating IPEM typically produced lower ion number densities and temperatures over the separation IPEM, which is most likely a result of the separation approximation. Relatively low speed ratios were observed by the collimating designs over the gridded RPA, but are considered to be more accurate. The collimating transmission fractions listed for the collimating IPEM are the values taken at the velocity class

equivalent to the ion speed ratio (recall that the true transmission fraction for the collimating IPEM is a function of velocity).

The computational errors for each RPA design and each IPEM are listed in Table 20. The method of calculating these errors were previously outlined in this section, but involve the summation of the absolute values of the data point differences between the true and assumed I-V curves. Collimating RPAs yielded slightly better convergence, which is also possibly a byproduct of space charge limiting effects present in the gridded RPA design.

Table 20. Calculated computational error for the three IPEM functions.

Reduction Method	Gridded RPA	SC-RPA	MC-mRPA
Classic IPEM	19.6%	16.3%	18.4%
Separation IPEM	19.6%	4.5%	12.6%
Collimating IPEM	19.6%	5.7%	12.1%

A more complete appraisal of the true error between the extracted parameters and their actual physical values would also require the quantification of the uncertainties of the polyfit, the assumptions made in the current collection theory applied to each method, and the experimental error. The experimental error was extracted from the aforementioned uncertainty analyses for each RPA design type. The single species assumption was accounted for in the uncertainty analyses in the form of an uncertainty in the species mass. Positioning and alignment error of the RPA characterization experiments is assumed negligible due to the resolution of the stepper motor drive system. The computational fit error could be further estimated and compared with the aforementioned fit error by performing the three IPEMs bounded by the extremes of the I-V curves. Most importantly, this description of the curve-fit error does not account for the fact that the MiLiPulT exhibited significant performance variance amongst thruster firings. The variation

in I-V curve behavior can be mostly attributed to this shot to shot variance of the MiLiPulT (i.e. sections of the peak I-V curves still had positive slopes). The 10-shot averaging for each I-t curve simply could not eliminate this variance sufficiently. Consequently, it is recommended that the MiLiPulT characterization experiments be performed using data point averages of 100 or more thruster firings, as opposed to the 10 shot averaging performed for the proof of concept experiments of this research. Nevertheless, this work provided adequate proof of concept for both the SC-RPA and the MC-μRPA towards the characterization of unsteady, small-scale plumes. The fundamental principles behind iterative IPEMs were also successfully demonstrated.

Comparison between the TLP and RPA extracted macroscopic plasma properties yield somewhat correlated results. Specifically, the gridded RPA and SC-RPA data can be directly compared to the corresponding 10 cm TLP data, since the RPA-thruster distance was 8.0 cm with an additional 2.0 cm to the RPA collector plate. Electron and ion number densities at this distance are well within an order of magnitude, indicating somewhat quasineutral plasma. Electron temperature is slightly elevated relative to average ion temperature, which is to be expected. The factor of 2 increase in TLP-reduced electron temperature in relation to RPA-extracted ion temperature could also be explained by the error in ion mass calculation and the assumption of a single species plasma with an average molar ratio. The MC-μRPA extracted properties are best compared to the 6.0 cm TLP case, since the MC-μRPA was moved closer to the source (3.7 cm) to obtain a signal. This position places the collector plate roughly 5.7 cm away from the thruster exit plane. Electron and ion number densities at this distance are also comparable. Electron temperature is slightly more elevated and sustained for a longer portion of the pulse as evidenced by the TLP-reduced data, yet the average ion temperature remained

somewhat constant in the range of 1.0 and 2.0 eV at this location as compared to the data obtained using the other RPA designs. In summation, both the TLP and RPA processed measurements yield comparable results within deviations small enough to be explained by either the physical nature of the plume, the IPEM curve-fit error, and/or the RPA and TLP uncertainties.

A normalized comparison of the extracted ion energy distributions for each of the three RPA peak I-V curves is shown in Figure 80. Negative slope values were calculated according to (2.95) for each I-V curve data point of the three RPA design types and normalized against the maximum value available for each design type, respectively.

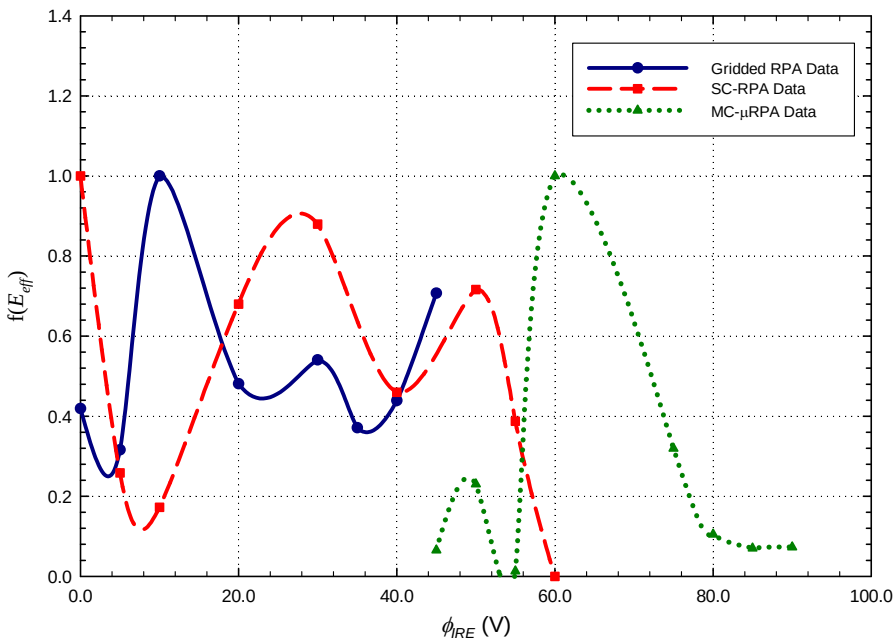

Figure 80. Normalized extracted ion energy distributions based on the negative slopes of the peak I-V curve data from each of the three RPA design types.

The gridded RPA shows a mean energy at roughly 10.0 V while the MC-μRPA shows a peak energy of slightly greater than 60.0 V. The SC-RPA shows a peak energy of approximately 25.0 V with an assumed extraneous data point at 0.0 V. If the point had not been included, the value at 25.0 V would have been the peak value and all other SC-RPA data points would have been

normalized against its value. The positive slopes existing in several sections of the peak I-V curve data resulted in negative energy values which were not considered for plotting.

Chapter 5: Conclusions and Recommendations

This chapter provides an overall appraisal of the work performed for this dissertation research and describes the conclusions drawn in regards to TLP extension towards small-scale, unsteady plasma plumes as well as to the collimating RPA design validation. Achievements related to the goals, objectives, and approaches established in Chapter 1 are reviewed and qualitatively assessed. Recommendations and future work are suggested for further MiLiPulT characterization specifically as well as general probe theory, design, and data reduction improvements. Conclusions regarding TLP implementation, bias circuit development, and EMI noise elimination are contained in Section 5.1. Recommendations for the next phase of TLP bias circuit design and further TLP implementation are presented in Section 5.2. Section 5.3 contains conclusions regarding the collimating RPA design and current collection theory in addition to the experimental validation of these designs and their accompanying ion parameter extraction methods. Section 5.4 details a list of further current collection theory development and possible improvements to the aforementioned data reduction methods.

5.1 TLP Characterization for Small-scale Unsteady Plasma Thruster Plumes

The first of two primary goals for this research involved the extension of a current-mode TLP towards the characterization of small-scale unsteady plasma plumes. To accomplish this goal, objectives necessitated the thorough review and development of the applicable TLP theory of operation, the optimization of a TLP bias circuit capable of sub-microampere current signal measurement, and the experimental implementation of a TLP in the plume of a small-scale, high-density, unsteady, noisy plasma plume complete with the corresponding data analysis techniques resulting from additional probe theory.

Achievement of the first objective was demonstrated in Chapter 2, with the addition of the orbital motion limited (OML) theory applied to the bias voltages of a current-mode TLP. Additional ABR and BRL theories of probe current collection were also addressed. Investigations into the applicability of QLPs towards small-divergence angle plumes where the probe's spatial resolution approaches and surpasses the plume size were also performed.

The second and third objectives were addressed in Chapter 3. Development, optimization, and calibration of the new TLP bias circuit provides the framework for future TLP characterization of small-scale micropropulsion devices where the current signals would be relatively weak. The implementation of operational amplifiers provided a self-consistent method of TLP signal amplification in the presence of noisy, unsteady small-scale plumes. Despite being susceptible to conductive EMI noise and consequent signal saturation, the TLP operational bias circuit can still serve as a reliable means of plume characterization with the application of several of the aforementioned filtration techniques. Characterization of the MiLiPulT plume has confirmed the reliability and accuracy of time-resolved measurements via a TLP current-mode methodology. These methods were successfully extended to small-scale, relatively high-density plasmas with a small divergence angle where the implementation of a QLP was no longer appropriate. In cases where the previously applied data reduction methods no longer applied, the data reduction methods were further supplemented by the addition of the orbital motion limited theory modified for TLP bias voltages. Several techniques for the elimination of the EMI and common-mode noise inherent to unsteady plasmas were also presented.

Analysis of the reduced MiLiPulT data confirms the TLP as a viable probe package for unsteady, small-scale plasmas. A majority of the TLP error can be attributed to misalignment of the exposed probe wire with the direction of the flow. Recalling that a primary assumption in the

TLP theory is that the parallel probes are aligned with the direction of the plasma flow such that the probe angle $\varphi = 0$, any misalignment will yield biased results. Alignment of the tungsten probe wires becomes particularly difficult at $r_p \leq 200\ \mu\mathrm{m}$ and any bends in the wires as a result of construction or installation are permanent. One of the probe wires was observed to have a ~10° angle off centerline, while the other two probe wires appeared to be directly aligned.

5.2 Recommendations for Future TLP Implementation and Bias Circuit Improvements

The passive RC filters could be replaced with current dividers for increased noise attenuation. The 2 stage low pass RC filters were originally designed for placement between the TLP bias circuit outputs and the oscilloscope, where they were to be measuring voltage signals. The passive RC filters remain applicable, provided that the resistances used are not high enough to oblige a significant voltage drop as compared to the bias voltages. However, an optimized current divider provides greater accuracy when measuring current signals, as is the case when the filters are placed in line with the TLP bias circuit inputs. The passive components and the loading effect of the current dividers must first be properly assessed. Further noise elimination could be achieved through mu-metal covering the PPT EMI shield box and the external thruster electronics to reduce radiated magnetic fields.

It is recommended that the TLP optimized bias circuit be utilized for a complete 2D polar plume and thruster setting characterization of the MiLiPulT, to discern current signals at greater distances and offset angles where traditional TLP difference and bias circuits fail. Implementation of the ABR and BRL regimes to supplement the OML regime data reduction methods is also recommended.

Optimization of the TLP bias circuit for a given plasma source can be performed by performing an iterative analysis of resistance value variation based on observed probe current signals. If access to the plasma source is not available prior to the circuit design and fabrication process, a target amplification ratio should be chosen based on the operational amplifier characteristics and an anticipated current signal. One could calculate the predicted TLP current signal ranges based on the expected operational envelope of plasma parameters to be characterized. The amplification ratio should be such that the maximum raw voltage signal after amplification is kept to within a 50% margin of the operational amplifier saturation voltage. This prevents any EMI/RFI noise from saturating the amplifiers at the initiation of a pulse or otherwise. Similarly, the measurement resistance should be chosen to be low enough so as not to detract from the corresponding bias voltages, but large enough to provide additional amplification via Ohm's law. Much in the same manner that TLP probe diameters and exposed probe lengths are iterated to find an ideal design for a given plume, the TLP bias circuit may also have to go through several design iterations before arriving at a configuration suitable for the specific plume.

5.3 RPA Design Development for Small-scale Unsteady Plasma Thruster Plumes

The second goal of this research entailed the validation of two new RPA designs capable of characterizing the ion parameters of small-scale unsteady plasmas. The collimating RPA designs have been proven as viable alternatives to traditional gridded RPAs which have been known to be susceptible to space charge limitations and breakdown phenomena. Both the SC-RPA and the MC-μRPA have been successfully validated using data from the gridded RPA as a benchmark. The gridded RPA data yields indication of space charge limiting plasma

contributing to a lower than desired ion decelerating voltage and a slightly elevated set of collector plate currents. The SC-RPA indicates possible slight space charge effects, if any, but more importantly demonstrates the successful implementation of a collimating channel in conjunction with a grid series. The theory developed for the collimating design most accurately accounts for the plasma flux limitations occurring within both apertures. The SC-RPA has the added benefit of presenting the incident plasma with a more than 1000x reduction in cross-sectional area, thus minimizing any possible shock effects and density gradients. The MC-μRPA provides more severe collimation and has also been validated as an applicable design, provided that the acute signal reduction is compensated for using appropriate amplification methods (i.e. operational amplifiers, larger measurement resistances, etc…).

The necessary ion parameter extraction methods were reviewed and where applicable, developed. Nonlinear least squares fitting provide a limited ability to reliably solve for macroscopic ion parameters from I-V data only when the applicable theory can be fully analytically integrated. When this is not the case, iterative methods using a fuzzy logic set of rules can be applied. These iterative methods were demonstrated for the basic case of the classical RPA current collection theory, the separation approximation theory, and the fully comprehensive collimating RPA current collection theory for each of the three RPA designs. Computational errors and Maxwellian distribution plots were also calculated and output. These analyses were limited to a single species approximation and as such, a weighted mass was subsequently assumed.

The cumbersome process of the collimating IPEM function requires for each iteration double nested numeric integration across speed ratios to arrive at a transmission fraction, recalculation of the ion distribution function, and additional integration of the non-Maxwellian

collimated distribution to arrive at a collector plate current value corresponding to one effective ion retarding potential.

5.4 Recommendations for Future RPA Designs and Data Reduction

Since the collimating IPEM program is computationally intensive, and since this process has been shown to closely approximate the separation approximation IPEM for large ion retarding potentials, it can therefore be substituted by the separation IPEM when using only the I-V-t data corresponding to the high energy tail of the distributions. A visual inspection of the integration areas of the Maxwellian and non-Maxwellian distributions can be performed using the output plots available from the IPEM to ensure that they are identical.

The collimating IPEM program was inherently based on an approximation of the collimating transmission fraction based on the speed ratio of a Maxwellian plasma species. Further accuracy in the reduction program could be attained by performing the necessary double numeric integration of the cylindrical channel flux formula (Patterson, 1971) for monoenergetic beams of plasma to generate a true transmission fraction curve. Each monoenergetic value considered would represent an individual point on the peculiar velocity-transmission fraction curve. The curve itself would represent a specific channel geometry and could then be applied to the Maxwellian distribution much in the same manner as that of the speed ratio approximation used in the present version of the collimating IPEM.

The RPA data reduction techniques were also limited to a single-species approximation. A MATLAB polyfit polynomial degree greater than 2 yields the dual local maxima characteristic of a multispecies plasma and would be more conducive to a multispecies characterization. This would require an additional set of fuzzy logic rules to influence the additional unknowns for the

generation of comparative I-V-t curves. Iteration convergence would more than likely take considerably longer.

MCP dimensions could also be optimized. An ideal MCP would have as many channels as possible, with diameter to length ratios as low as possible. It would be recommended to procure MCPs with channel diameters roughly equal to the MCP thickness to minimize collimation effects. The MCP thickness is also constrained with respect to rigidity. As thickness of the molybdenum MCP is reduced below 100 μm it is considered a foil, and would become difficult to install and maintain.

Another possible method of characterizing the ion speed ratio of a plasma plume entails the implementation of numerous collimators of varying aspect ratio. The analysis of the collimating effects as the channels become more directional could give further insight towards both the collimating behavior of the channels, as well as a curve fit approximation of the true ion speed ratio.

Bibliography

Allen, J.E., "Probe Theory – The Orbital Motion Approach," *Physica Scripta*, 1402-4896/45/5/013, Vol. 45, pp. 497-503, 1992.

Antonsen, E.L., Burton, R.L., & Rysanek, F., "Energy Measurements in a Coaxial Electromagnetic Pulsed Plasma Thruster," AIAA 99-2292, *35th AIAA/ASME/SAE/ASEE* Joint Propulsion Conference and Exhibit, 35th, Los Angeles, CA, June 20-24, 1999.

Awadallah, R.S., Freund, D.E., & Simon, D.H., "Electrostatic Emission Modeling for Micro Pulsed Plasma Thrusters," AIAA-2005-3698, *41st AIAA/ASME/SAE/ASEE Joint Propulsion Conference & Exhibit*, July 10-13, 2005, Tucson, AZ.

Barakat, A.R. & Schunk, R.W., "Momentum and Energy Exchange Collision Terms for Interpreting Bi-Maxwellian Gases," *Journal of Physics D: Applied Physics*, Vol. 14, pp. 421-438, 1981.

Begun, M. & Guman, W.J., "Pulsed Plasma Radio Frequency Interference Studies," AFPRL-TR-77-85, Final Report for the Period 17 June 1976-1 September 1977, Fairchild Industries, Inc. and the Air Force Rocket Propulsion Laboratory, September 1977.

Benson, S.W., Arrington, L.A., & Hoskins, W.A., "Development of a PPT for the EO-1 Spacecraft," AIAA-99-2276, *35th AIAA/ASME/SAE/ASEE* Joint Propulsion Conference and Exhibit, 35th, Los Angeles, CA, June 20-24, 1999.

Beonig, H.V., Plasma Science and Technology, Cornell University Press: New York, 1989.

Bevington, P. R., Data Reduction and Error Analysis for the Physical Sciences, McGraw-Hill Book Company, 1969.

Bird, G.A., Molecular Gas Dynamics and the Direct Simulation of Gas Flows, Clarendon Press, 1994.

Burr-Brown Research Corporation, Handbook of Operational Amplifiers, Burr-Brown Research Corporation, Tucson, AZ, 1963.

Burton, T.A., Parker, K., & Shumlak, U., "Exhaust Plume Characterization of a Mini-PPT using a Time-of-Flight/Gridded Energy Analyzer," AIAA-2002-4122, *38th AIAA/ASME/SAE/ASEE Joint Propulsion Conference & Exhibit*, July 7-10, 2002, Indianapolis, IN.

Busek Co. Inc. Press Release, "Hall Thruster and Micropropulsion Technology," Natick, MA, 2007.

Chapman, S. & Cowling, T.G., The Mathematical Theory of Non-Uniform Gases, Cambridge University Press, 1939.

Chen, F.F., "Lecture Notes on Langmuir Probe Diagnostics," Electrical Engineering Department, University of California, Los Angeles, Mini-Course on Plasma Diagnostics, IEEE-ICOPS, Jeju, Korea, June 5, 2003.

Chen, S. & Sekiguchi, T., "Instantaneous Direct-display System of Plasma Parameters by Means of a Triple Probe," J*ournal of Applied Physics*, Vol. 26., No. 8, August, 1965.

Chen, S., "Studies of the Effect of Ion Current on Instantaneous Triple-Probe Measurements," *Journal of Applied Physics*, Vol. 42, No. 1, January, 1971.

Chung, P.M., Talbot, L., & Touryan, K.J., "Electric Probes in Stationary and Flowing Plasmas: Part 1. Collisionless and Transitional Probes," *AIAA Journal*, Vol. 12, No. 2, 1974.

Clausing, P., "The Flow of Highly Rarefied Gases through Tubes of Arbitrary Length," Ann. Physik, Vol.5, No.12, pp. 961-973, 1932.

Djogo, G. & Osmokrovic, P., "Statistical Properties of Electrical Breakdown in Vacuum," *IEEE Transactions on Electrical Insulation*, Vol. 24, Issue 6, December 1989, pp. 949-953.

Dolbec, R.E., "RFI Measurements on a LES-7 Prototype Pulsed Plasma Thruster," *Journal of Spacecraft and Rockets*, Vol. 7, No. 7, July 1970, pp. 889-890.

Eckman, R.F., Byrne, L., Gatsonis, N.A., & Pencil, E.J., "Triple Langmuir Probe Measurements in the Plume of a Pulsed Plasma Thruster," *Journal of Propulsion and Power*, Vol. 17, No. 4, 2001.

Emhoff, J., "Progress in Thrust Measurements from Micro Pulsed Plasma Discharges," AIAA-2007-5299, *43rd AIAA/ASME/SAE/ASEE Joint Propulsion Conference*, July 8-11, 2007, Cincinnati, OH.

Engeln, R., Mazouffre, S., Vankan, P., Bakker, I, & Schram, D.C., "Plasma Expansion, Fundamentals and Applications," *Plasma Sources Science and Technology*, Vol. 11, pp. A100-A104, January, 2002.

Evans, J.D., Zawalski, W., & Chen, F.F., "Evaluation of Langmuir Probe Ion Density Measurement in Weakly Ionized Discharges Using Plasma Oscillation Probes and Microwave Interferometry," LTP-111, Low Temperature Plasma Technology Laboratory Technical Notes, 2001.

Fridman, A. & Kennedy, L.A., Plasma Physics and Engineering, Taylor and Francis Books: Great Britain, 2004.

Gatsonis, N.A., Byrne, L.T., Zwahlen, J.C., Pencil, E.J., & Kamhawi, H., "Current-Mode Triple and Quadruple Langmuir Probe Methods with Applications to Flowing Pulsed Plasmas," IEEE Transactions on Plasma Science, Vol. 32, No. 5, pp. 2118-2129, October, 2004.

Gatsonis, N.A, Zwahlen, J., Wheelock, A., Pencil, E.J., & Kamhawi, H., "Pulsed Plasma Thruster Plume Characterization Using a Current-Mode Quadruple Langmuir Probe Method", *Journal of Propulsion and Power*, Vol. 20, No. 2, pp. 243-254, March-April, 2004.

Gatsonis, N. A. & Yin, X., "Hybrid (Particle/Fluid) Modeling of Pulsed Plasma Thruster Plumes," Journal of Propulsion and Power, Vol. 17, No. 5, pp. 945-958, Sept-Oct. 2001.

Giffin, G. B., "Analysis of the Ion Current Collection in the Plasma Wake During the Charging Hazards and Wake Studies (CHAWS) Experiment," Master of Science Thesis, Massachusetts Institute of Technology, December 1996.

Green, T. S., "Space Charge Effects in Plasma Particle Analyzers," Plasma Physics, Vol.12, 1970.

Gulczinski III, F.S., Dulligan, M.J., Lake, J.P., & Spanjers, G.G., "Micropropulsion Research at AFRL," AIAA 2000-3255, *36th AIAA/ASME/SAE/ASEE Joint Propulsion Conference & Exhibit*, July 16-19, 2000, Huntsville, AL.

Guman, W.J. & Nathanson, D.M., "Pulsed Plasma Microthruster Propulsion System for Synchronous Orbit Satellite," *Journal of Spacecraft*, Vol. 7, No. 4, 1970.

Hohmann, K., "Radio Frequency Micro Ion Thruster for Precision Propulsion," NASA SBIR 2004 Solicitation, Proposal No. 04-II S3.01-7863, 2004.

Hanson, W. B., Zuccaro, D. R., Lippincott, C. R., & Sanatani, S., "The Retarding-Potential Analyzer on Atmosphere Explorer," *Radio Science*, Vol. 8, No. 4, 1973.

Hastings Jr., C., Approximations for Digital Computers, Princeton University Press, Princeton, NJ, 1955.

Heelis, R. A. & Hanson, W. B., "Measurements of Thermal Ion Drift Velocity and Temperature Using Planar Sensors," Measurement Techniques in Space Plasmas: Particles, American Geophysical Union, 1998.

Hutchinson, I.H., Principles of Plasma Diagnostics, Cambridge University Press, 2002.

Huba, J.D., NRL Plasma Formulary, NRL/PU/6790—04-477, Naval Research Laboratory, 2004 Edition.

Hughes, P. C. & de Leeuw, J. H., "Theory for the Free Molecule Impact Probe at an Angle of Attack," Rarefied Gas Dynamics, Vol.1, 1965.

Igarashi, M., Kumagai, N., Sato, K., Tamura, K., Takegahara, H., Okamoto, H., Wakizono, & T., Hashimoto, H., "Performance Improvements of Pulsed Plasma Thruster for Micro Satellite," IEPC-01-152, *27th International Electric Propulsion Conference*, October 15-19, 2001, Pasadena, CA.

Kanal, M., "Theory of Current Collection of Moving Cylindrical Probes," *Journal of Applied Physics*, Vol. 35, No. 6, June, 1964.

Kelley, M.C., The Earth's Ionosphere: Plasma Physics and Electrodynamics, Academic Press, Inc., 1989.

Ketsdever, A.D., Wadsworth, D.C., & Muntz, E.P., "Predicted Performance and Systems Analysis of the Free Molecule Micro-resistojet," Micropropulsion for Small Spacecraft, *Progress in Astronautics and Aeronautics*, Vol. 187, American Institute of Aeronautics and Astronautics, Inc., 2000.

King, L. B. & Gallimore, A. D., "Gridded Retarding Pressure Sensor for Ion and Neutral Particle Flux in Flowing Plasmas", AIAA-96-2983, 32nd AIAA/ASME/SAE/ASEE Joint Propulsion Conference, July 1-3, 1996, Lake Buena Vista, FL.

Koizumi, H., Ryosuke, N., Komurasaki, K., & Arakawa, Y., "Plasma Acceleration Processes in an Ablative Pulsed Plasma Thruster," *Physics of Plasmas*, Vol. 14, No. 3, 2007.

LabVIEW, Ver. 7.1, National Instruments, 2004.

Laframboise, J., "Theory of Cylindrical and Spherical Langmuir Probes in a Collisionless Plasma at Rest," UTIS Rept. 100, Univ. of Toronto, Inst. Of Aerospace Studies, National Technical Information Service Document AD 634596, Springfield, Virginia, June, 1966.

Laframboise, J.G. & Sonmor, L.J., "Current Collection by Probes and Electrodes in Space Magnetoplasmas: A Review," *Journal of Geophysical Research*, Vol. 98, No. A1, pp. 337-357, January, 1993.

Lam, S.H., "Unified Theory for the Langmuir Probe in a Collisionless Plasma," *The Physics of Fluids*, Vol. 8, No. 1, January, 1965.

Lee, R.H., Taylor L.C., Muntz, E.P. & Ketsdever, A.D., "Free Molecule Micro-Resistojet: Nanosatellite Propulsion," AFRL Report OMB No. 0704-0188, 1998.

Markusic, T.E., & Spores, R.A., "Spectroscopic Emission Measurements of a Pulsed Plasma Thruster Plume," AIAA 97-2924, *33rd AIAA/ASME/SAE/ASEE Joint Propulsion Conference & Exhibit*, July 6-9, 1997, Seattle, WA.

Marrese, C. M., Majumdar, N., Haas, J., Williams, G., King, L. B., & Gallimore, A. D., "Development of a Single-orifice Retarding Potential Analyzer for Hall Thruster Plume Characterization," IEPC-97-066, 25th International Electric Propulsion Conference, August 1997, Cleveland, OH.

Mathcad 2001i Professional, MathSoft Engineering and Education, Inc., 2001.

MATLAB, Ver. 7.2.0.232 Release 2006a, The Mathwork, Inc., 2006.

Maynard, E. P., "Direct Simulation Monte Carlo Analysis of Rarefied Gas Flow in Tubes," Master of Science Thesis, Worcester Polytechnic Institute, May 1996.

Mitchner, M., & Kruger, C.H., Jr., Partially Ionized Gases, John Wiley & Sons, Inc., 1973.

Mora, P., "Plasma Expansion into a Vacuum," *Physical Review Letters*, Vol. 90, No., 18, May, 2003.

Myers, R.M. and Arrington, L.A., "Pulsed Plasma Thruster Contamination", AIAA-96-2729, *32nd AIAA/ASME/ SAE/ASEE Joint Propulsion Conference*, July 1-3, 1996, Lake Buena Vista, FL.

Mueller, J., Pyle, D., Chakraborty, I., Ruiz, R., Tang, W., Marrese, C., and Lawton, R., "Electric Breakdown Characteristics of Silicon Dioxide Films for Use in Microfabricated Ion Engine Accelerator Grids," Micropropulsion for Small Spacecraft, Progress in Astronautics and Aeronautics, Vol. 187, edited by Micci, M. and Ketsdever, A., AIAA, Reston, VA, 2000.

Ordonez, C.A. & Molina, M.I., "Evaluation of the Coulomb Logarithm Using Cutoff and Screened Coulomb Interaction Potentials," *Physics of Plasmas*, Vol. 1, No. 8, August, 1994.

Partridge, J. & Gatsonis, N.A., "Characterization of High-Density Flowing Plasmas Using a Directional Micro-Retarding Potential Analyzer," *29th International Electric Propulsion Conference*, October 31-November 4, 2005, Princeton, NJ.

Partridge, J. & Gatsonis, N.A., "Preliminary Design and Analysis of a Directional Micro-Retarding Potential Analyzer for High-Density Plumes," AIAA-2003-5172, *39th AIAA/ASME/SAE/ASEE Joint Propulsion Conference & Exhibit*, July 20-23, 2003, Huntsville, AL.

Partridge, J. & Gatsonis, N.A., "Validation of a Directional Micro-Retarding Potential Analyzer for High-Density Plumes," AIAA-2005-3533, *41st AIAA/ASME/SAE/ASEE Joint Propulsion Conference & Exhibit*, Tucson, AZ. July 10-13, 2005.

Patterson, G.N., Introduction to the Kinetic Theory of Gases, University of Toronto Press, Toronto, 1971.

Pencil, E.J. & Kamhawi, H., "Alternate Propellant Evaluation for 100-joule-class Pulsed Plasma Thrusters," AIAA-2003-5171, AIAA-2003-5022, *39th AIAA/ASME/SAE/ASEE Joint Propulsion Conference & Exhibit*, July 20-23, 2003, Huntsville, AL.

Peterson, E.W. & Talbot, L., "Collisionless Electrostatic Single-Probe and Double Probe Measurements," AIAA Journal, Vol. 8, No. 12, pp. 2215-2219, December, 1970.

Press, W.H., Teukolsky, S.A., Vetterling, W.T., & Flannery, B.P., Numerical Recipes in FORTRAN: The Art of Scientific Computing, Second Edition, Cambridge University Press, 1992.

Robin, M.R., Brogan, T.R., & Cardiff, E.H., "An Ammonia Microresistojet (MRJ) for Micro Satellites," AIAA-2008-5288, 44th *AIAA/ASME/SAE/ASEE Joint Propulsion Conference & Exhibit*, July 21 – 23, 2008, Hartford, CT.

Sakabe, S. & Yasukazu, I., "Cross Sections for Resonant Charge Transfer Between Atoms and Their Positive Ions: Collision Velocity $\leq$ 1 a.u.," *Atomic Data and Nuclear Data Tables*, Vol. 49, No. 2, November, 1991.

Scharlemann, C.A. & York, T.M., "Pulsed Plasma Thruster Using Water Propellant, Part I: Investigation of Thrust Behavior and Mechanism," AIAA-2003-5022, *39th AIAA/ASME/SAE/ASEE Joint Propulsion Conference & Exhibit*, July 20-23, 2003, Huntsville, AL.

Scharlemann, C.A. & York, T.M., "Pulsed Plasma Thruster Using Water Propellant, Part II: Thruster Operation and Performance Evaluation," AIAA-2003-5023, *39th AIAA/ASME/SAE/ASEE Joint Propulsion Conference & Exhibit*, July 20-23, 2003, Huntsville, AL.

Shumlak, U., Burton, T.A., & Parker, K.M., "Mass Characterization Measurements of a Mini-PPT Exhaust Plasma," AIAA-2003-5169, *39th AIAA/ASME/SAE/ASEE Joint Propulsion Conference & Exhibit*, July 20-23, 2003, Huntsville, AL.

Sicotte, R.L., "RFI Measurements at UHF on a Pulsed Plasma Thruster," *Journal of Spacecraft and Rockets*, Engineering Notes, March 1970, pp. 337-338.

Siefring, C.L., Amatucci, W.E., & Rodriguez, P., "Fast Electron Temperature Measurements with Langmuir Probes: Considerations for Space Flight and Initial Laboratory Tests," Measurement Techniques in Space Plasmas: Particles, The American Geophysical Union, 1998.

Simon, D.H. & Deal, D., Aerospace Micro-Technologies Fact Sheet, 07-00963-AMT, Johns Hopkins University Applied Physics Laboratory, March, 2007.

Simon, D.H., Land III, H. B., & Emhoff, J., "Experimental Evaluation of a Micro Pulsed Plasma Thruster Concept," AIAA-2006-4330, *42nd AIAA/ASME/SAE/ASEE Joint Propulsion Conference & Exhibit*, July 9-12, 2006, Sacremento, CA.

Simon, D.H. & Land III, H. B., "Instrumentation Development for Micro Pulsed Plasma Thruster Experiments," AIAA-2005-4264, *41st AIAA/ASME/SAE/ASEE Joint Propulsion Conference & Exhibit*, July 10-13, 2005, Tucson, AZ.

Simon, D.H. & Land, H.B., "Pulsed Plasma Thrusters for Micropropulsion," AIAA-2003-5170, *39th AIAA/ASME/SAE/ASEE Joint Propulsion Conference & Exhibit*, July 20-23, 2003, Huntsville, AL.

Sovey, J.S., Zana, L.M., & Knowles, S.C., "Electromagnetic Emission Experiences Using Electric Propulsion Systems- A Survey, AIAA-87-2028, *AIAA/SAE/ASME/ASEE 23rd Joint Propulsion Conference*, June 29 – July 2, 1987, San Diego, CA.

Spirkin, A. & Gatsonis, N. A., "Unstructured 3D PIC Simulation of Plasma Flow in a Segmented Microchannel," AIAA-2003-3896, *36th AIAA Thermophysics Conference*, July 23-26, 2003, Orlando, FL.

Thomassen, K.I., "Radiation from Pulsed Electric Thrusters," *Journal of Spacecraft and Rockets*, Vol. 10, No. 10, October 1973, pp. 679-680.

Tsay, M.M., "Direct Numerical Modeling of a Radio-frequency Micro Ion Thruster," Master of Science Thesis, Massachusetts Institute of Technology, May 2006.

Wirz, R.E., “Discharge Plasma Processes of Ring-Cusp Ion Thrusters,” Doctoral Thesis, California Institute of Technology, April 2005.

Wirz, R., Polk, J., Marresse, C., Mueller, J., Escobedo, J., & Sheehan, P., “Development and Testing of a 3cm Electron Bombardment Micro-Ion Thruster,” IEPC-01-343, *27th International Electric Propulsion Conference*, October 15-19, 2001, Pasadena, CA.

Wong, J., Reed, H., & Ketsdever, A., “University Micro-/Nanosatellite as a Micropropulsion Testbed,” Micropropulsion for Small Spacecraft, *Progress in Astronautics and Aeronautics*, Vol. 187, American Institute of Aeronautics and Astronautics, Inc., 2000.

Yin, X., “Axisymmetric Hybrid Numerical Modeling of Pulsed Plasma Thruster Plumes,” Doctor of Philosophy Dissertation, Worcester Polytechnic Institute, May, 1999.

Zakrzwski, C., Davis, M., & Sarmiento, C., “Addressing EO-1 Spacecraft Pulsed Plasma Thruster EMI Concerns,” AIAA-2001-3641, *37th AIAA/ASME/SAE/ASEE Joint Propulsion Conference*, July 8-11, 2001, Salt Lake City, Utah.

Appendix A. Data Acquisition and Averaging vi Schematics

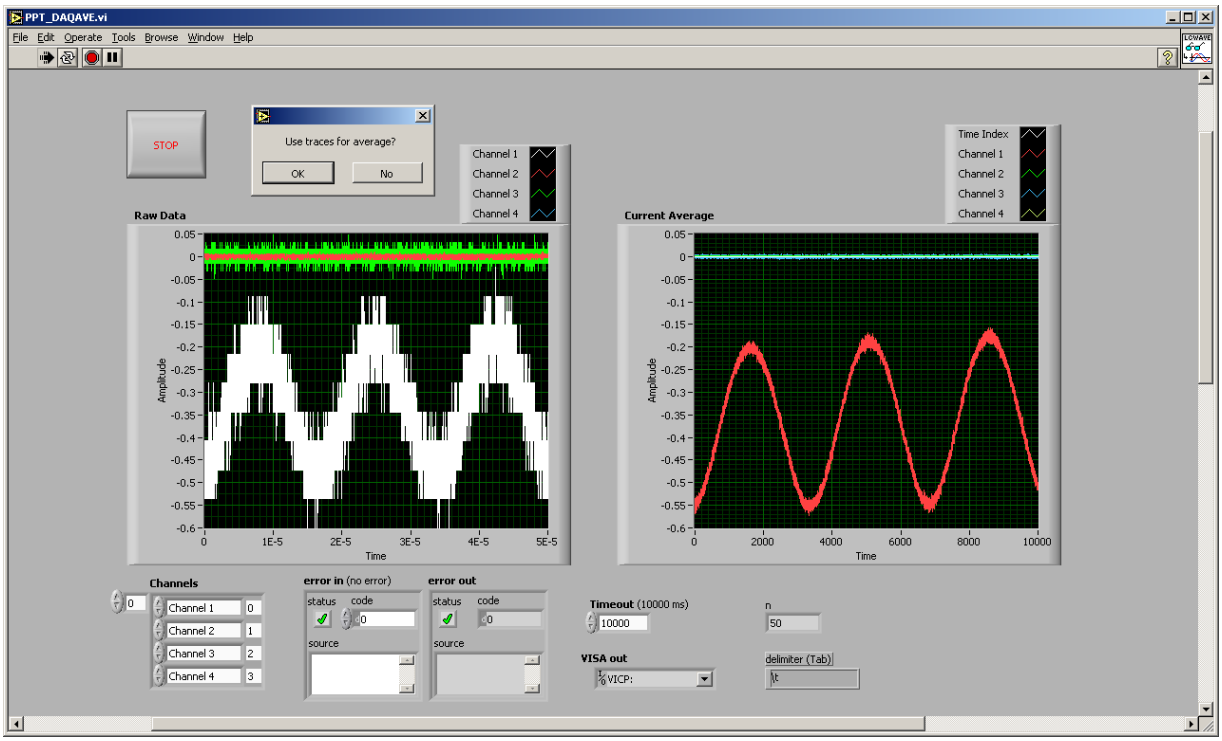

Figure 81. Front panel of the MiLiPulT data acquisition and averaging LabVIEW vi.

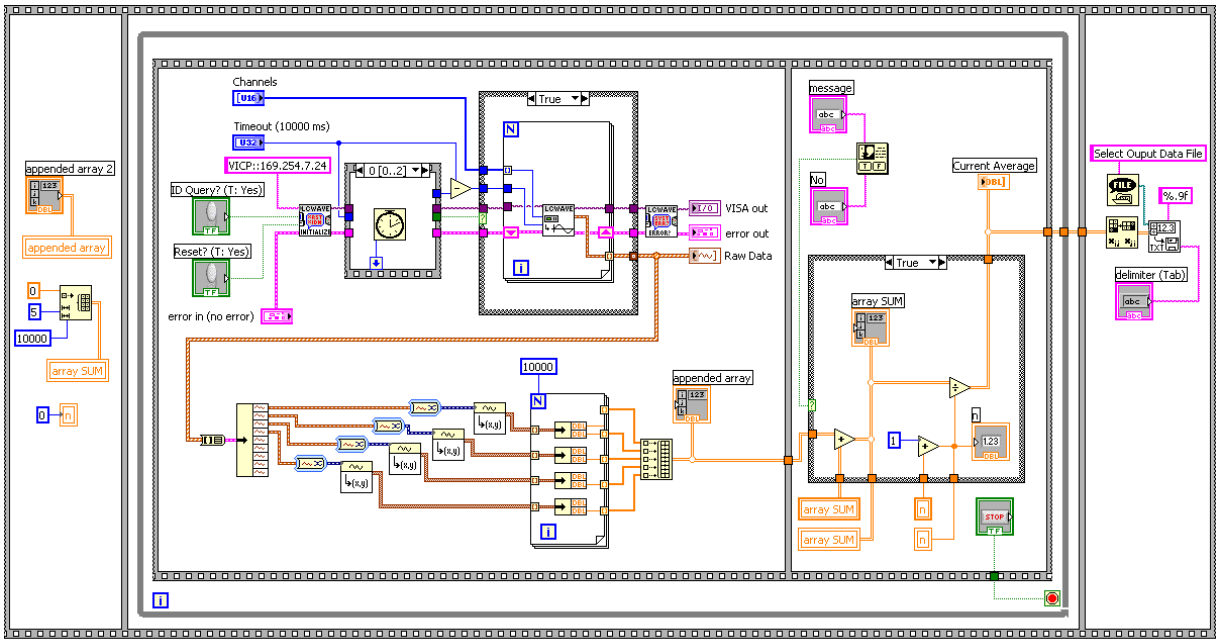

Figure 82. Block diagram of the MiLiPulT data acquisition and averaging LabVIEW vi.

Appendix B. Triple and Quadruple Langmuir Probe Fabrication

Overview:

The purpose of this manual is to provide a record of the various design improvements and fabrication techniques developed over the many iterations of both shielded and unshielded Langmuir probes used throughout the aforementioned research. Since TLP and QLP design is heavily dependent upon the plume properties (electron number density, electron temperature, ion speed ratio, frequency, plume size, etc…), a priori calculations are recommended in order to provide a correctly tailored probe. Specific materials are recommended, in addition to dimensions. The ceramic and probe wire cutting processes are discussed in detail. Angled joints are demonstrated through the bending of the probe wires and application of a binding ceramic paste. Wiring, shielding, and installation are also reviewed. The probe described here is a QLP with a right angle joint, as it is more complex to fabricate than a TLP or a QLP/TLP without a right angle joint. The probe wire diameter is 1.4 mm with an exposed parallel probe length of 10.0 mm and an exposed cross-probe length of 30.0 mm to increase collection area. This probe was designed for a particularly large and relatively low-density plasma and would not be suitable for microplume applications. Other TLP and QLP designs are shown at the end of this appendix in

A Priori Calculations:

If the approximate magnitudes of the electron number density and temperature are not known, the TLP/QLP implementation can be quite an iterative process, where a probe designed for an initial estimation of plasma properties is fabricated and tested. Future redesign is then performed based on the previous probe's readings, even if it received no current signals at all.

Ideally, one should determine an approximate plasma operating envelope, and build two probes; one for each extreme value of the Debye length.

Materials:

While alumina has slightly superior durability, it may be difficult to procure at the appropriate dimensions. McMaster-Carr currently has but one size of four bore tubing (0.188" O.D.). However, four bore glass tubing can be purchased from Wale Apparatus in several sizes. Probe wires are typically made from tungsten rods, which can be brittle and do not respond well to soldering. Polysilica tubing is typically used to sheath the tungsten wires, which prevent plasma from traveling upstream into the ceramic housing, thus ensuring that the exposed probe wire area is accurate.

Cutting the Ceramic:

The first step entails cutting or scoring the ceramic tubing in order to form pieces of the correct length for the 90° angle joint. Since the ceramic is extremely brittle, every precaution should be taken for both safety and to prevent undesired fractures in the ceramic, particularly when the probe is near completion or if you are on a limited budget. Eye protection is recommended when cutting, scoring, or snapping. Additionally, constantly keep the ceramic over and close to the work surface in case it is dropped. Store the ceramic and /or probes in a safe, undisturbed place.

Although the dimensions of the QLP are application dependent, it is recommended that the parallel ceramic tube be 20 cm, with the perpendicular piece being 10 cm. This length minimizes the disturbance to the plasma, while keeping it from being excessively awkward to

build, handle, transport, and install. This also allows a probe to be made from purchasing one linear foot of original ceramic, and requires making only one cut.

If the ceramic is glass, it can be cut to the proper length using a Dremel® equipped with a diamond or carbide circular blade. Be sure to cut so that at least one long piece (recommended > 20 cm) piece left will have the manufacturer's original flat orthogonal tip. Since using a clamp or a vise could crush the ceramic, tape the piece to a flat surface approved for and capable of incurring damage, such as a workbench. Tape it in four places: One at each end, and one on either side of the cut location, as shown in Figure 83. Cut into the glass at a relatively high Dremel speed (> 15,000 rpm) until the glass is either fractured or scored to roughly a millimeter. If it is not yet fully broken, lay the piece on a sharp edge of the work surface, with the score directed upwards and located at the edge. Snap the ceramic in two by holding it just past the edge and pulling down while holding the other portion to the table. Again, eye protection and hand protection such as work gloves are recommended. Be sure not to drop either piece when it breaks.

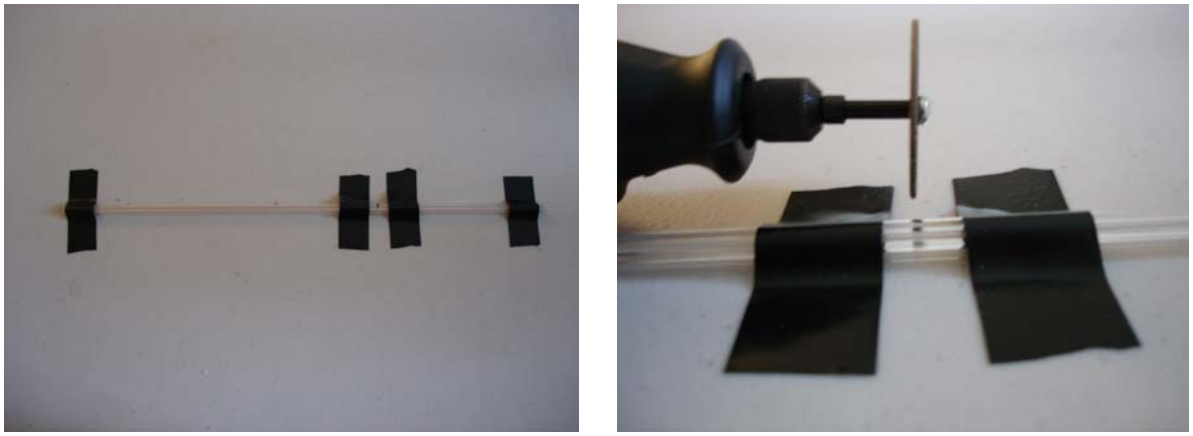

Figure 83. Proper taping and Dremel-cutting of fused quartz four-bore glass tubing.

If the ceramic is alumina, the aforementioned method of snapping at desired lengths can be performed, without scoring. It is acceptable if the ceramic did not break evenly across the cross section. These tips can comprise the inner tips to the right angle joint.

Cutting the Probe Wires:

Next, it is necessary to cut the probe wires to length. Use a high speed Dremel or a small carbide blade chop saw on a vise/fence with a cutting angle of 90° to ensure orthogonal flat probe tips. Cutting tungsten wire any thicker than ~0.3 mm wire with pliers or any other scissor-like tool will split the wire at the tips. Cut four wire segments, each to be long enough to accommodate the two ceramic pieces, with at least 3 cm to spare at the tip end, at least 3 cm to comprise the right angle joint, and more than 5 cm at the connection end. It is also recommended that the four wires vary in length by roughly 3 cm each. This ensures that the connections will occupy less axial space relative the perpendicular ceramic tube.

For example, the illustrated QLP consists of a parallel ceramic tube length of 20 cm and a perpendicular ceramic tube of 10 cm. Therefore, the four wires should be cut to no less than 41, 43, 45, and 47 cm in length. Depending on the tip effect calculations, it may be convenient to make the cross probe wire slightly longer than the parallel probe wires to increase the perpendicular collection area. File the wires using a fine metal file just enough to remove any burrs.

Insulating Tubing:

Ideally, the inner bore diameter of the ceramic is only slightly larger than the outer diameter of the wires, within tolerance. If not, insulating polysilica tubing is required to prevent

the wire from moving or bending within the ceramic. Eventually, 'potting' of the probe tips with a ceramic paste is performed. This potting would deteriorate due to movement of the probe lines, resulting in a much larger exposed probe area and inaccurate current measurements. Tubing such as Kapton or polysilica with an inner diameter slightly larger than the wire diameter and with an outer diameter slightly smaller than the ceramic bore diameter can be used. Snap or cut four pieces to exactly the same length as the parallel ceramic tube and four to the exact length of the perpendicular tube. Depending on the tolerances, it might be easier to slide them onto the wires first, or in the other case, into the ceramic. In either case, proceed as though the insulating tubing is now part of the wire or ceramic, respectively.

Wire Bending:

Bend each of the four wires to a 90° angle at the appropriate length. In this case, that length is 24.5 cm from one end. Slide both ceramic tubes into the four wires so that both are approximately 1-2 cm from the right angle joint. Then, with the parallel ceramic tube pushed up to the right angle joint, bend another 90° angle into one of the probe tips to act as the cross probe. Caution should be taken to minimize the amount of repeated bending required to reach exactly 90°, as the Tungsten wire may snap off. Now push the parallel ceramic tube up to the cross probe joint.

Ceramic Paste Application:

The probe is now ready for several coats of a ceramic paste to comprise the right angle joint. If the tungsten wires are smaller than ~0.4 mm, this joint will provide the rigidity the probe needs. While thicker wires can hold the right angle without the aid of ceramic paste, the

paste also serves to electrically isolate the four probe lines from each other. Zirconium oxide paste applied at a thickness of roughly 2 mm takes roughly 24 hours to dry. Multiple thin coats are required since applying more than a few millimeters in only one coat will not dry for several days if at all. Be sure to coat the space between the probe wires, as shown in Figure 84.

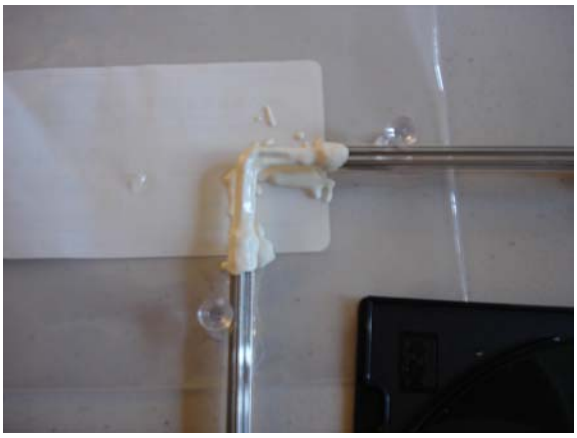

Figure 84. Zirconium ceramic paste application at a right angle TLP/QLP joint.

Also at this stage, apply a thin layer to the parallel ceramic tip which is to be exposed to the plasma. Avoid applying paste on the exposed wires, as this would reduce the effective probe area. This process, known as potting, is critical to ensuring accurate values for exposed probe areas and eventual current measurement. Potting can also be applied to the ceramic tip on the connection end, but is not required.

Shielding:

Once the right angle joint and potting has dried, wrap the ceramic in an electrically conductive material, such as the wire sheathing used in coaxial cables, or with conductive adhesive copper tape. Ensure that the shielding and probe wires are not in contact by leaving roughly 5 mm between the shielding and the ceramic tips, as shown in Figure 85.

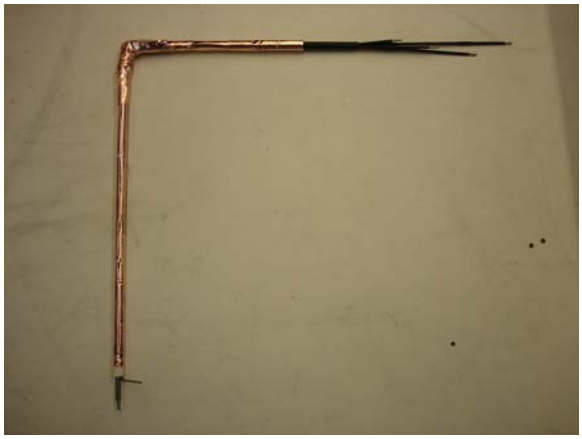

Figure 85. Electrical shielding of the QLP/TLP leaving a sufficiently exposed ceramic area at the tip.

Next, electrically isolate all but a few millimeters of the connection ends of the wire with an insulator. The use of Kapton tape and heat shrink is shown in Figure 86. Heat shrink can be used in addition to or instead of Kapton tape. Only one section of the shielding should be left exposed so that it can eventually be grounded its respective electrical connection without the introduction of ground loops.

Figure 86. Insulation of probe wire connections using heat shrink and Kapton tape leaving one shielding section exposed for eventual grounding.

Continue by wrapping the conductive material around the individual connection leads. Similar to the exposed probe tip, leave several millimeters between the conductive material and the exposed wire.

Further Shielding and Connections:

The fabrication process will diverge here depending on the types of connection used to provide the four lines a means out of the chamber. In this case, female BNC crimp connections were used since the vacuum chamber for this application had four BNC feedthroughs.

Whatever the connection type, the priority here is to insulate the entire probe while grounding the conductive shield to only one connection (avoiding ground loops). Also, the continuity of the probe lines and the rigidity of the connections are critical.

For BNC crimp connections, solder the probe wires to the center pins, as shown in Figure 86. Typical center pins have a hole to insert the soldered wire for a stronger connection. Before sliding the connection casings onto the center pins, slide on the crimp tube onto each lead, followed by a piece of heat shrink, preferably of different colors, as shown in Figure 87. This will help with connecting the probe to the correct lines later.

Figure 87. BNC crimp tubes and colored heat shrink used to secure and identify the probe lines, respectively.

Now wrap the entire probe from ceramic probe tip up to exposed wire with an insulator, such as Kapton tape. However, leave exposed roughly 5 mm of the conductive shielding on only one of the probe wires (it doesn't matter which one) so that it will make contact with one of the grounded shielded connections. Solder the connection casing to the shield. Then insulate the

area, heat shrink, and crimp it. Heat shrink and crimp the other three leads as well. It is also recommended that the entire probe excluding the exposed probe wires be coated with another layer of Kapton tape. The end product is shown in Figure 88.

Figure 88. Shielded right angle QLP with BNC electrical connections.

Figure 89 shows other QLPs designed for various points of an expected operational envelope of a plasma. Note that the QLP on the right was left unshielded. The advantage to this design is that it presents the plasma with a smaller oblique surface area, but it is more susceptible to EMI/RFI noise and is considerably weaker structurally.

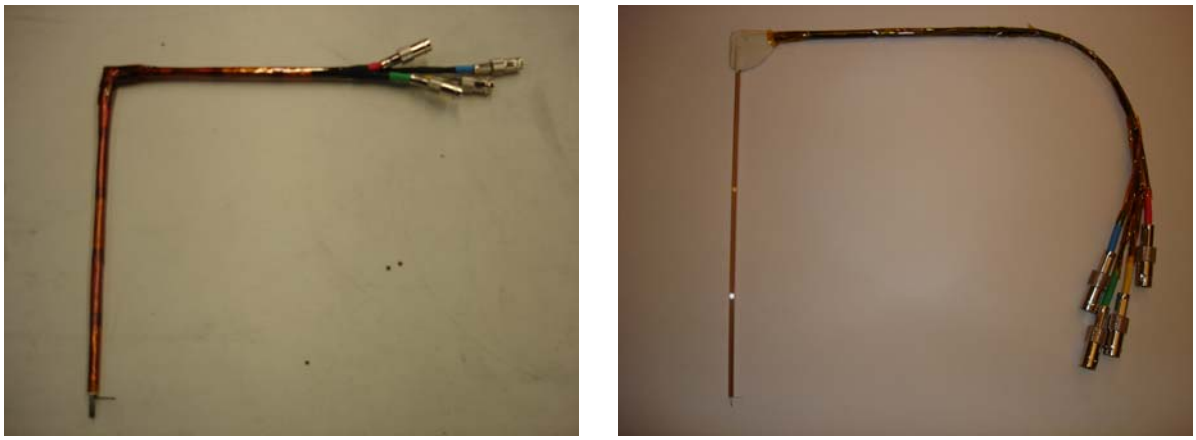

Figure 89. Right angle QLPs designed for opposite corners of an expected operating envelope: Shielded (left) and unshielded right).

Right angle joints are used for TLPs and QLPs to remove the electrical connections of the probe away from the plume. This feature is not always necessary, particularly for plume ballistic testing or small-scale plasma characterization where the electrical connections will be shielded or secured by a mount of some kind. Examples of these Langmuir probes are shown in Figure 90.

Figure 90. QLPs and TLPs designed for ballistic plume tests (unshielded with D-pin connections and no right angle joints).

At this point, check for continuity of each probe wire. Also, check for isolation of each probe wire from each other, as well as from the shield. Check that the shield is grounded to only the one connector casing.

Make a note of which probe line corresponds to which heat shrink color, particularly the cross probe. Also by now, the three perpendicular probe wires may have adjusted in position, resulting in different probe lengths. If the wires are thicker than ~0.4 mm in diameter, *carefully* cut all three at once in the Dremel or chop saw with a diamond or carbide blade. If the wires are smaller, use pliers, as the chop saw would bend the wires. Again, file any burrs with a fine metal file. Check for proper continuity and isolation a second time. Take accurate measurements of the final probe wire lengths.

Probe Stand:

The primary design constraint of the stand is that it provides a robust standoff where the wire connections can be secured. This prevents shear forces due to the weight of the cables from breaking the probe. If the QLP is not to be mounted to a linear traverse or other type of translation stage, building the stand out of a threaded rod allows the user to adjust the height and position of the probe while the chamber is vented.

Installation:

It is recommended that all four wires have an identification system, such as color or the application of Kapton tape strips in 0, 1, 2 and 3 segments on each end of each cable, respectively. Connect the four wires to the inner chamber feedthroughs, and check for continuity to the outside of the chamber. Mounting the probe with two pieces of Kapton tape and a tie-wrap was effective and reversible method.

Also, if significant work is being done in the vacuum chamber, remove the QLP, as it is likely the probe could be irreparably damaged.

Appendix C. Bell Jar System Diagram & Operating Procedures

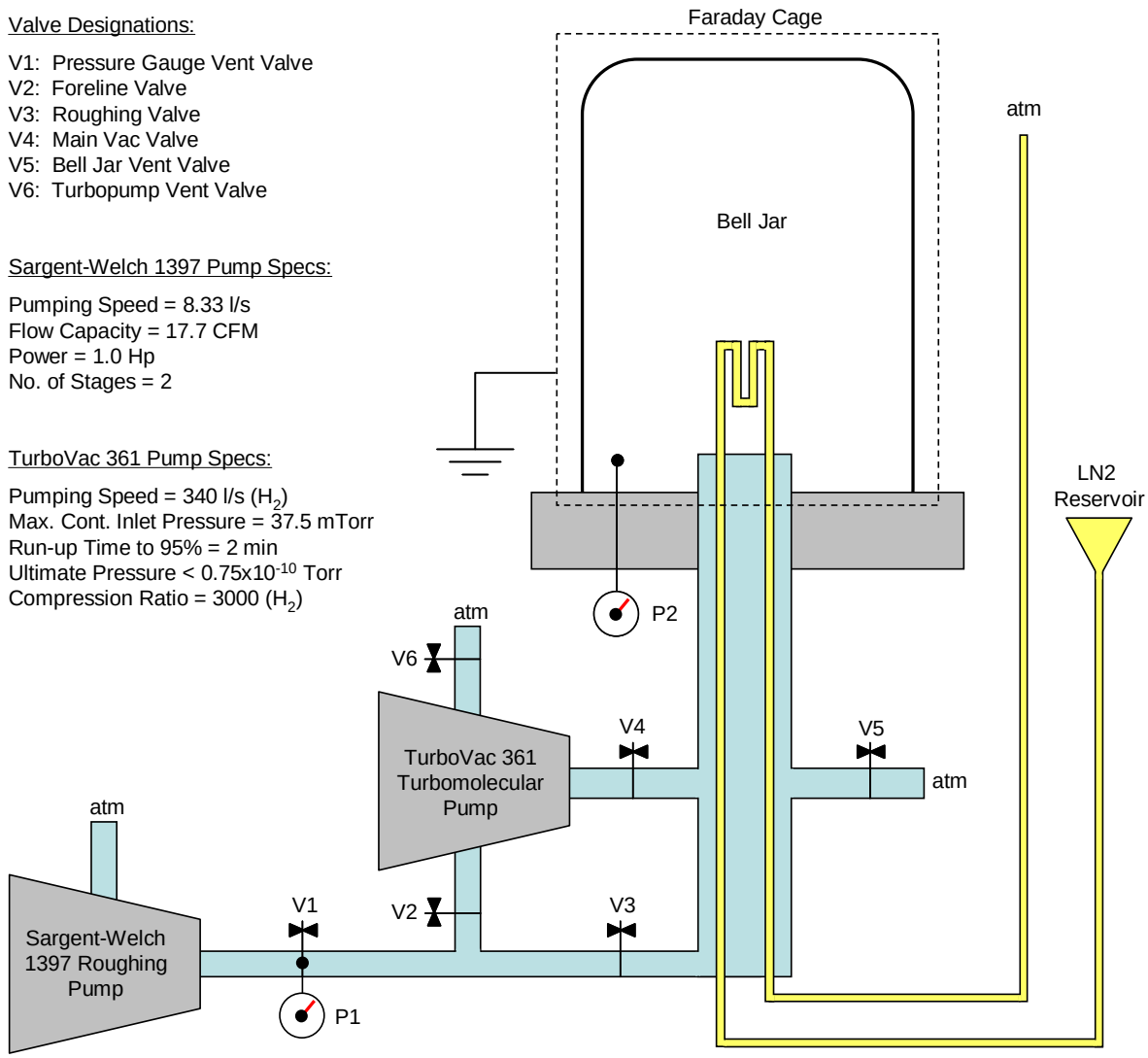

Figure 91. Bell jar system pump specifications, flow diagram, and valve designations.

Bell Jar Vacuum Pump-down Procedure:

1. Ensure that the turbopump vent valve (V6) is closed.

2. Vent the bell jar to atmosphere by opening the bell jar vent valve (V5). This will avoid pressure differentials across valves V2, V3, and V4 later.

3. Close V5.

4. Ensure that the pressure gauge vent valve (V1) is open.

4. Turn on/ plug in the roughing pump.
5. Wait at least 2 minutes for the roughing pump to get to full speed. Completely open the roughing valve (V3) slowly. Not waiting the two minutes before applying a load to the roughing pump has been known to trip the circuit breaker.
6. Monitor the foreline pressure via P1. When the foreline pressure is below 50 mTorr (~10 minutes), turn on the turbopump again making sure the turbopump vent valve (V6) is closed.
7. Open the foreline valve (V2) and the main vacuum valve (V4) completely. There will be a slight increase in pressure.
8. When both the foreline pressure (P1) and tank pressure (P2) drops below 50 mTorr (~15 minutes), turn on the turbopump. There will be another rise in pressure before it drops to roughly $2x10^{-4}$ Torr.
9. Add LN2 into the cold trap to obtain pressures below $1x10^{-4}$ Torr and to absorb latent water molecules within the bell jar. Replenish LN2 as necessary.

Bell Jar Vent-up to Atmosphere Procedure:

1. Shut off all power supplies related to the thruster or application within the bell jar. Ensure that the motion control stepper motors are powered off (heat dissipation concerns while under vacuum).
2. Close the main vacuum valve (V4).
3. Turn off the turbopump.
4. Close the foreline valve (V2).
5. Vent the turbopump via the turbopump vent valve (V6). Open V6 by no more than 5 full rotations and leave it at atmosphere until the next pump-down.

6. Turn off/ unplug the roughing pump. Remaining LN2 in the cold trap can be allowed to boil off.

Notes:

- It is considered good practice to leave the bell jar and its contents under vacuum between pump-down procedures.
- As a general rule, do not open valves which are under a significant pressure differential. The exception to this rule is the bleed or vent valve (V5), which is used to bring the bell jar back up to atmosphere.
- The pressure gauge valve (V1) is typically not used and is left open.

Running the turbopump only (alternative operation):

1. Close all valves V1 through V6.
2. Turn on the turbopump.
3. Slowly open the pressure gauge vent valve (V1) or have V1 open already provided that the roughing valve (V3) is closed.
4. Slowly open the roughing valve (V3).
5. Vent back up by closing the roughing valve (V3) and powering off the turbopump. Be sure to vent the turbopump via V6.

Appendix D. RPA IPEM MATLAB Code

```
% RPA_IPEM.m
%
% Extracts ion number density, ion temperature, and ion speed ratio
% from I-V curve data based on fuzzy logic iterative methods using
% the choice of one of the following methods for curve generation:
%
% Classic: Applies classical RPA CCT calculations from Kelley (1989).
%
% Separation: Calculates collimator transmission fraction using numeric
%             integration & directly multiplies it with the
%             classical RPA CCT.
%
% Collimating:  Calculates collimator transmission fraction using numeric
%               integration, generates collimated distribution function,
%               & numerically integrates the distribution function to find
%               the collected current
%
%
% Assumptions: known ion mass,
%              known RPA geometry,
%              Maxwellian ion distribution,
%              single species

clear all
format long

% Input initial guesses
ni=1.0E17
T=2.0
S=2.0

%Define physical constants & RPA parameters
Pi=3.14159265358979323846264;
Boltz=1.381E-23;
q=1.602E-19;
m=8.505*1.673E-27; %Species mass
cm=sqrt(2*Boltz*T*11604/m); %Most probable ion velocity
beta=1/cm;
A=1.14e-5; %Entrance area
Chi_grid=0.32; %Grid transmission fraction

% Input polyfit number of degrees, maximum iterations before hardstop
polyfit_n=2;
maxit=500;

% Input voltage resoltuion & maximum voltage
phi_res=5;
phi_max=100;
phi_length=(phi_max/phi_res)+1

% Check to make sure phi_length is an integer
if mod(phi_length,1.0)~=0.0
```

```
    'Phi_length must be an integer.'
    break
end

% Initialize basic parameters and errors
iteration=0;
cyclestart=0;
phieff=0;
I=0.0;
error(phi_length,2)=0;
odd_error(phi_length,2)=0;
even_error(phi_length,2)=0;
total_error=1.0;
average_error=1.0;

% Initialize polyfit parameters
I_XLS=0;
length=0;
width=0;
p=0;
Structure=0;
voltagevals=0;
currentvals=0;
f=0;
fit_error=0;
table=0;

% Initialize I-V curve parameters
I_ACT(phi_length,2)=0;
I_TNI(phi_length,2)=0;
I_TNI_first(phi_length,2)=0;
I_TNI_previous(phi_length,2)=0;
I_TNI_old(phi_length,2)=0;
difference(phi_length,2)=0;
slope(2,2)=0;

% Write Potentials 0V through phi_max by phi_res
for i=1:phi_length
    I_ACT(i,1)=(i-1)*phi_res;
    I_TNI(i,1)=(i-1)*phi_res;
end

% Write I_TNI zero potential as 0.0001V to avoid TNI divide by zero
I_TNI(1,1)=0.0001;
I_ACT(1,1)=0.0001;

% Input I-V curve data for polyfit
I_XLS=xlsread('ivcurvedata1.xls')

% Define the 'x' and 'y' of the data matrix
[length,width]=size(I_XLS);
for i=1:length
    voltagevals(i,1)=I_XLS(i,1);
    currentvals(i,1)=I_XLS(i,2);
end
```

```
% Take polyfit of data matrix
[p,Structure]=polyfit(voltagevals,currentvals,polyfit_n);
p
Structure

% Determine fit error, output if needed
f=polyval(p,voltagevals);
for i=1:length
    fit_error(i,1)=(currentvals(i,1)-f(i,1))/currentvals(i,1);
end
table=[voltagevals currentvals f fit_error];

% generate polyfit I-V curve
for i=1:phi_length
    I_ACT(i,2)=polyval(p,I_ACT(i,1));
end
I_ACT

% Plot ('plot' for linear scale, 'semilogy' for log plot)
  figure(1)
  semilogy(voltagevals,currentvals,'o',I_ACT(1:phi_length,1),...
      I_ACT(1:phi_length,2),'-r');
  title('I-V Curve Data vs. Polyfit')
  xlabel('Effective Retarding Potential (V)')
  ylabel('Collector Plate Current (A)')
  legend('Curve Data','Polyfit')

% Iterate to convergence
while total_error > 0.0001
    iteration=iteration+1

%   Store old TNI curves for plotting purposes
    I_TNI_old=I_TNI_previous;
    I_TNI_previous=I_TNI;

%   Run (overwrite) TNI at phieff=0.00001
    I_TNI(1,2)=classic(0.0001,ni,T,S);
                % or classic or collimating

%   Run TNI over rest of phieff range
    for i=2:phi_length
        phieff=(i-1.0)*phi_res

        %Choosing the classic method:
        %I=classic(phieff,ni,T,S)

        %Choosing the separation method:
        I=separation(phieff,ni,T,S)

        %Choosing the collimating method:
        %I=collimating(phieff,ni,T,S)

        I_TNI(i,2)=I;
```

```
    end

%   Store first TNI curve for plotting purposes
    if iteration==1
        I_TNI_first=I_TNI;
    end

%   Display newly generated TNI curve
    I_TNI

%   Compute Differences
    for i=1:phi_length
        difference(i,2)=I_ACT(i,2)-I_TNI(i,2);
    end

%   Store previous error matrix for use in determining convergence
    if mod(iteration,2)==1
       for i=1:phi_length
           odd_error(i,2)=error(i,2);
       end
    elseif mod(iteration,2)==0
       for i=1:phi_length
           even_error(i,2)=error(i,2);
       end
    end

%   Compute Slopes
    slope(1,1)=(I_TNI(2,2)-I_TNI(1,2))/(I_TNI(2,1)-I_TNI(1,1));
    slope(1,2)=(I_ACT(2,2)-I_ACT(1,2))/(I_ACT(2,1)-I_ACT(1,1));
    slope(2,1)=(I_TNI(phi_length,2)-I_TNI(phi_length-1,2))/...
        (I_TNI(phi_length,1)-I_TNI(phi_length-1,1));
    slope(2,2)=(I_ACT(phi_length,2)-I_ACT(phi_length-1,2))/...
        (I_ACT(phi_length,1)-I_ACT(phi_length-1,1));

%   Compute New Error Matrix & Total Error
    for i=1:phi_length
       error(i,2)=abs(difference(i,2)/I_ACT(i,2));
    end

    total_error=0.0;

    for i=1:phi_length
       total_error=total_error+error(i,2);
    end
    average_error=total_error/phi_length;

%   Display Total Error & Iteration
    iteration, total_error

%   Check for convergence
    if error==odd_error % Possibility of converged cycling
        cyclestart=iteration;
    end
    if iteration == cyclestart+1 % Confirm converged cycling
        if error==even_error
```

```
            'Iteration has converged (cycling detected).'
            iteration=maxit  % Break iterations if cycling confirmed
        end
    end

%   Fuzzy Logic Toolbox/ Compute Next Iteration values for ni, T, & S
    if difference(1,2)>0
        ni=ni+1.0E15
    elseif difference(1,2)<0
        ni=ni-1.0E15
    end

    if slope(2,1)>slope(2,2)
        T=T+0.01
    else
        T=T-0.01
    end

    if slope(1,1)>slope(1,2)
        S=S-0.01
    else
        S=S+0.01
    end

%   Plot ('plot' for linear scale, 'semilogy' for log plot)
    figure(2)
    semilogy(I_ACT(1:phi_length,1),I_ACT(1:phi_length,2),'-r',...
        I_TNI(1:phi_length,1),I_TNI(1:phi_length,2),'--b',...
        I_TNI_previous(1:phi_length,1),...
        I_TNI_previous(1:phi_length,2),'--b',...
        I_TNI_old(1:phi_length,1),I_TNI_old(1:phi_length,2),':b',...
        I_TNI_first(1:phi_length,1),I_TNI_first(1:phi_length,2),'-.g',...
        'linewidt',1.3);
%   Sample curve is solid, red
%   Most recent curve is solid, blue
%   Previous (two iterations ago) curve is dashed, blue
%   Old (three iterations ago) curve is dotted, blue
%   First (based on initial guess) curve is centerline, green
    title('RPA Extraction: I-V Curve Data and TNI Iterations')
    xlabel('Effective Retarding Potential (V)')
    ylabel('Collector Plate Current (A)')
    legend('Experimental Curve','TNI Iteration RECENT',...
        'TNI Iteration PREVIOUS','TNI Iteration OLD','TNI Iteration FIRST')

%   Allow plotting refresh by pausing for 2 seconds
    pause(2)

%   Hard Stop at maxit # of iterations
    if iteration==maxit
        'Iteration has hard stopped.'
        break
    end
 end

% Output of ni[final], T[final], S[final], error
```

```
ni
T
S
total_error
average_error


-------------------------------------------------------------------------------

function y = classic(phieff,ni,T,S)

Pi=3.14159265358979323846264;
m=8.505*1.673E-27;
Boltz=1.381E-23;
q=1.602E-19;
cm=sqrt(2*Boltz*T*11604/m);
beta=1/cm;
A=2.01e-10;
Chi_grid=0.32;
V=sqrt(2*1.602E-19*phieff/m)*beta;

y=(q*A*Chi_grid*ni/(2*sqrt(Pi)))*((exp(-(V-S)*(V-S))/beta)+(S/beta)...
    *sqrt(Pi)*(1-erf(V-S)))


-------------------------------------------------------------------------------

function z = separation(phieff,ni,T,S)

% Define physical constants and known RPA parameters
Pi=3.14159265358979323846264;
m=8.505*1.673E-27;
Boltz=1.381E-23;
q=1.602E-19;
cm=sqrt(2*Boltz*T*11604/m);
beta=1/cm;
A=2.01e-10;
Chi_grid=0.32;
V=sqrt(2*1.602E-19*phieff/m)*beta;
Dee=0.02;  %0.08          %MC-microRPA vs. SC-RPA

% Calculate the parameters of the collimation from Patterson (1971).
Chi=exp(-S*S)+(S*sqrt(Pi)*(1+erf(S)));
Psi=(2/(Dee*Dee))*(sqrt(1+(Dee*Dee))-1);

% To calculate Eta(S,Dee), need to use nested double numeric integration
% using Simpson's rule approximation
%
% Define outermost integral bounds and resolution
a2=0;
b2=1;
n2=4000;
h2=(b2-a2)/n2;

for(j=1:n2)
```

```
    y(j)=a2+j*h2;

    % Calc inner integral contribution
    % Define outermost integral bounds and resolution
    a1=0;
    b1=atan(sqrt(1-y(j)*y(j)));
    %b1=y(j)*y(j);  % Test Expression
    n1=4000;
    h1=(b1-a1)/n1;

    % Evaluate the inner function at each interval
    for(i=1:n1-1)
        x(i)=a1+i*h1;
        f(i)=eta_integrand(x(i),S);
    end

    % Sum the two interval endpoints
    sum=(h1/3)*(eta_integrand(a1,S)+eta_integrand(b1,S));

    % Sum the middle intervals based on Simpson's composite rule
    for(i=1:n1-1)
        if (mod(i,2)==0)
            sum=sum+(h1/3)*4*eta_integrand(x(i),S);
        else
            sum=sum+(h1/3)*2*eta_integrand(x(i),S);
        end
    % End inner integral Sum
    end

    %Pass the integral sum to the outer integrand value
    g(j)=sum;
    sum=0;
end

% Sum the outer integral
total=(h2/3)*g(n2);
for(k=1:n2-1)
    if (mod(k,2)==0)
        total=total+(h1/3)*4*g(k);
    else
        total=total+(h1/3)*2*g(k);
    end
end

% Calculate true eta(S,Dee)
Eta=total/Dee;

% Calculate numerator of collimating transmission fraction (terms in front
% will cancel out with those in the denominator, so they can be excluded...)
Ncc1=Chi-(Psi*exp(-S*S))-(4*S/sqrt(Pi))*Eta;

% Calculate collimating transmission fraction
Chi_c=Ncc1/Chi

% Calculate collector plate current assuming Maxwellian distribution
```

```
% exiting the collimator (i.e. the separation approximation).
z=(q*A*Chi_grid*Chi_c*ni/(2*sqrt(Pi)))*((exp(-(V-S)*(V-S))/beta)+(S/beta)...
    *sqrt(Pi)*(1-erf(V-S)))


-------------------------------------------------------------------------------

function y = eta_integrand(x,S)

y=(1+erf(S*cos(x)))*cos(x)*exp(-S*S*sin(x)*sin(x));
%y=x*x; % Test Expression

-------------------------------------------------------------------------------
```